CHALMERS UNIVERSITY OF TECHNOLOGY
Gothenburg, Sweden
www.chalmers.se

PHD THESIS

6G networks are set to transform the way we connect and navigate the world. Beyond just faster internet, 6G will combine communication and precise positioning to enable technologies like self-driving cars, delivery drones, and smarter cities. It will provide seamless connectivity and accuracy, even in remote areas or environments where today's networks fall short.

This work focuses on three technologies that will make this possible. Massive multiple-input multiple-output (MIMO) uses large arrays of antennas to boost network performance and handle thousands of devices efficiently. Smart surfaces, known as reconfigurable intelligent surface (RIS), can direct signals like mirrors for better coverage and pinpoint accuracy, even in crowded or tricky spaces. Satellites, working alongside ground networks, bring connectivity and positioning to places where traditional systems can not, like deep oceans or isolated mountains.

Together, these innovations are shaping a future where connectivity is everywhere, reliable, and perfectly in sync with our increasingly digital lives. With 6G, the world will feel smaller, smarter, and more connected than ever before.

YASAMAN ETTEFAGH • Positioning, Synchronization, and Communication in 6G: Insights from Massive MIMO, RIS, and NTN • 2025

WATERMARK

CHALMERS
UNIVERSITY OF TECHNOLOGY

Positioning, Synchronization, and Communication in 6G: Insights from Massive MIMO, RIS, and NTN

YASAMAN ETTEFAGH

DEPARTMENT OF ELECTRICAL ENGINEERING
CHALMERS UNIVERSITY OF TECHNOLOGY
Gothenburg, Sweden 2025
www.chalmers.se

THESIS FOR THE DEGREE OF DOCTOR OF PHILOSOPHY

Positioning, Synchronization, and Communication in 6G: Insights from Massive MIMO, RIS, and NTN

Yasaman Ettefagh

Department of Electrical Engineering
Chalmers University of Technology
Gothenburg, Sweden, 2025

Positioning, Synchronization, and Communication in 6G: Insights from Massive MIMO, RIS, and NTN

Yasaman Ettefagh
ISBN: 978-91-8103-202-4

Doktorsavhandlingar vid Chalmers tekniska högskola
Ny serie nr 5660
ISSN 0346-718X
This thesis has been prepared using LaTeX.

Department of Electrical Engineering
Chalmers University of Technology
SE-412 96 Gothenburg, Sweden
Phone: +46 (0)31 772 1000
www.chalmers.se

Printed by Chalmers Digital Printing
Gothenburg, Sweden, 2025

To my beloved ones
and to future me, as a reminder

Abstract

Sixth-generation (6G) wireless networks aim to transform communication and localization by enabling precise positioning and seamless connectivity for advanced applications like autonomous systems, augmented reality, and smart cities. Technologies like massive multiple-input multiple-output (MIMO), reconfigurable intelligent surface (RIS), and non-terrestrial networks (NTNs) play a critical role in achieving these objectives by addressing challenges in capacity, coverage, and synchronization in diverse environments.

This thesis investigates the use of massive MIMO technology to optimize communication architectures by analyzing the interplay between the number of antennas and quantizer resolution. This work identifies massive MIMO configurations that balance performance and complexity across varying signal-to-noise ratios (SNRs). The study contributes to the design of robust and scalable architectures for next-generation communication systems.

Moving on to the localization topic, this thesis also explores a frugal RIS-enabled localization and synchronization setup designed to provide precise positioning in cost-effective deployments. A scenario with one base station (BS) and two RISs is studied to localize a stationary user equipment (UE), despite the presence of an unknown carrier frequency offset (CFO) between the UE and the BS. This work highlights the potential of RIS technology to enhance localization accuracy and reduce infrastructure requirements.

Another emerging direction in localization is the use of NTNs, driven by their potential for large-scale deployment. This thesis investigates an integrated LEO-cellular network for NTN-based localization and synchronization. A hybrid system with one BS and one low Earth orbit (LEO) satellite is analyzed to estimate the UE's position, velocity, clock bias, and CFO under synchronization challenges. The results highlight NTN's potential for robust localization in areas with limited terrestrial infrastructure.

By tackling key challenges in communication and localization, this thesis contributes to the design of efficient solutions for 6G networks, supporting their practical deployment in next-generation wireless systems.

Keywords: 6G, communication, localization, massive multiple-input multiple-output (MIMO), non-terrestrial networks (NTNs), reconfigurable intelligent surfaces (RIS), synchronization.

List of Publications

This thesis is based on the following publications:

[A] **Y. Ettefagh**, S. Rezaei Aghdam, G. Durisi, S. Jacobsson, M. Coldrey, and C. Studer, "Performance of Quantized Massive MIMO with Fronthaul Rate Constraint over Quasi-Static Channels". *IEEE Access*, vol. 11, pp. 56935–56947, June 2023.

[B] **Y. Ettefagh**, MF. Keskin, K. Kheykhosravi, G. Seco-Granados, and H. Wymeersch, "Frugal RIS-aided 3D Localization with CFO under LoS and NLoS Conditions". *Submitted to IEEE Transactions on Vehicular Technology.*

[C] **Y. Ettefagh**, S. Saleh, MF. Keskin, H. Chen, G. Seco-Granados, and H. Wymeersch, "Integrated Cellular and LEO-based Positioning and Synchronization under User Mobility". *Submitted to IEEE Transactions on Vehicular Technology.*

Other publications by the author, not included in this thesis, are:

[D] **Y. Ettefagh**, S. Jacobsson, A. Hu, G. Durisi, and C. Studer, "All-digital massive MIMO uplink and downlink rates under a fronthaul constraint". *Proc. Asilomar Conf. Signals, Syst., Comput.*, Pacific Grove, CA, USA, Nov. 2019, pp 416-420.

[E] S. Jacobsson, **Y. Ettefagh**, G. Durisi, and C. Studer, "All-digital massive MIMO with a fronthaul constraint". *Proc. IEEE Statistical Sig. Pro. Workshop*, Freiburg, Germany, Jun. 2018.

[F] S. Saleh, P. Zheng, X. Liu, H. Chen, MF. Keskin, B. Priyanto, M. Beale, **Y. Ettefagh**, G. Seco-Granados, T. Y. Al-Naffouri, H. Wymeersch, "Integrated 6G TN and NTN Localization: Challenges, Opportunities, and Advancements". accepted for publication in IEEE Communications Standards Magazine.

Acknowledgments

Doing a PhD is indeed a journey, often filled with ups and downs—mine was no exception! In many ways, it resembles a small-scale version of life itself: starting out young and naïve, full of energy, going through tough times in the middle while searching for meaning, and finally reaching the end, hopefully wiser, more knowledgeable ... and maybe a bit tired! With this reflection in mind, I would now like to acknowledge those whose presence made this journey what it was.

I would like to start by thanking the key people who supported me during the early part of this journey. I am deeply grateful to my examiner, Prof. Giuseppe Durisi, for his valuable guidance. I also wish to express my appreciation to Dr. Sina Rezaei and Dr. Sven Jacobsson for their collaboration and contributions throughout this experience.

A special thanks goes to my supervisor, Prof. Henk Wymeersch. Through his endless support and unique approach to making research both challenging and enjoyable, I learned to trust myself. I always valued our discussions and meetings, and I am truly grateful for his patience and for going beyond technical supervision, offering support in every way.

I would also like to express my gratitude to all my collaborators: Prof. Gonzalo Seco-Granados, Dr. Furkan Keskin, Dr. Sharief Saleh, and Dr. Hui Chen. A special thanks to my collaborator and friend, Dr. Kamran Keykhosravi, for all the insightful discussions we had. It has been a privilege to work with such a brilliant and inspiring team, and I will always be grateful for this opportunity.

I am also thankful to the E2 department, especially Prof. Fredrik Brannström and Prof. Erik Ström for the support throughout this journey. Additionally, I want to express my appreciation to my colleagues at Volvo Trucks—your support, flexibility, and the friendly environment we shared were key to reaching this point.

I have been fortunate to be surrounded by many wonderful friends. A heartfelt thank you to my dear friend Mohammad Hossein, for always being there for me and for our continued friendship. I am also grateful to Zahra, Mohammad Ali (Manzar), Marziyeh, Fazeleh, Maryam, Masoud and all my other friends who made Gothenburg feel like home. A special thank you to my dearest friend Elham—no matter how far apart we live, your presence in my life always warms my heart.

To my family—thank you. Mom and Dad, your unwavering belief in me has been my greatest source of strength. Thank you, Ehsan, Shirin, Tahsin, Alireza, Hana and Ava for being my emotional anchors through it all.

Finally, my deepest gratitude goes to the person who has always supported me, lifted me up in difficult moments, and stood by my side with unconditional love. Thank you, Andreas, for being in my life.

Sincerely,
Yasaman Ettefagh,
Göteborg, 2025

Acronyms

AD:	autonomous driving
ADAS:	advanced driver-assistance systems
ADC:	analog to digital converter
AR:	augmented reality
AWGN:	additive white Gaussian noise
BB:	baseband
BBU:	baseband unit
BS:	base station
CFO:	carrier frequency offset
CSI:	channel state information
DA-MMSE:	distortion-aware minimum mean square error
DAC:	digital to analog converter
FWA:	fixed wireless access
GPS:	global positioning system
IoT:	internet of things
LMMSE:	linear minimum mean square error
LoS:	line-of-sight
MF:	matched-filtering
MIMO:	multiple-input multiple-output
MMSE:	minimum mean square error
MU:	multi-user

MUI:	multi-user interference
NMSE:	normalized mean square error
NTN:	non-terrestrial networks
OFDM:	orthogonal frequency division multiplexing
RF:	radio frequency
RIS:	reconfigurable intelligent surfaces
RRH:	remote radio head
RTT:	round trip time
SINDR:	signal to interference plus noise plus distortion ratio
SISO:	single-input single-output
SNR:	signal to noise ratio
TA:	timing advance
TDD:	time division duplex
TDoA:	time difference of arrival
ToA:	time of arrival
UE:	user equipment
VR:	virtual reality
ZF:	zero-forcing

Contents

Abstract i

List of Papers iii

Acknowledgements v

Acronyms vii

I Overview 1

1 Introduction 3

1.1 Background 3

1.1.1 Massive MIMO 4

1.1.2 From Communication to Localization 6

1.1.3 RIS-aided Localization 7

1.1.4 Localization: Integration with NTN 8

1.2 Organization of the Thesis 8

1.3 Notation 9

2 Quantized Massive MIMO in Communication **11**
2.1 Data Converters 11
2.1.1 Linearization using Bussgang Theorem 12
2.1.2 Covariance Matrix of Distortion 13
2.1.3 Stochastic Resonance and Dithering for 1-Bit analog to digital converters (ADCs) 14
2.2 Multi-user Massive MIMO 14
2.2.1 Channel Model 16
2.2.2 Uplink Transmission 16
2.2.3 Downlink Transmission 19

3 Terrestrial and Non-Terrestrial Localization **21**
3.1 Cellular-based Localization 21
3.1.1 Topology and Configuration 22
3.1.2 Channel Model 23
3.1.3 Synchronization and Coverage Consideration 23
3.2 Reconfigurable Intelligent Surfaces in Localization 24
3.2.1 Topology and Configuration 24
3.2.2 Channel Model 26
3.2.3 Synchronization and Coverage Consideration 26
3.3 Non-Terrestrial Networks in Localization 27
3.3.1 Topology and Configuration 28
3.3.2 Channel Model 28
3.3.3 Synchronization and Coverage Consideration 29

4 Summary of the Appended Papers, and Contributions **31**
4.1 Paper A 31
4.2 Paper B 32
4.3 Paper C 33

References **35**

II Papers **43**

A Performance of Quantized Massive MIMO with Fronthaul Rate Constraint over Quasi-Static Channels **A1**

1 Introduction A4
1.1 Prior Art A5
1.2 Contributions A6
1.3 Paper Outline A7
1.4 Notation A8
2 System Model A8
2.1 Uplink Transmission A10
2.2 Downlink Transmission A11
3 Analysis of the Achievable Error Probability A12
3.1 Preliminary Result A12
3.2 Linearization Via Bussgang's Theorem A13
3.3 The Actual Error-Probability Bound A15
3.4 Asymptotic Limits and Useful Approximations A17
4 Numerical Results A22
4.1 Simulation Setup A23
4.2 Channel-Estimation Performance A26
4.3 Accuracy of the Proposed Large-Blocklength Approximations A28
4.4 Impact of Dithering A30
4.5 Optimal Number of Pilot Symbols A31
4.6 Number of Antennas vs. Data-Converter Resolution . . A32
5 Conclusions A33
References A36

B Frugal RIS-aided 3D Localization with CFO under LoS and NLoS Conditions **B1**

1 Introduction B3
2 System Model B8
2.1 Scenario B8
2.2 Geometric Relations B8
2.3 Signal Model B8
2.4 Joint Localization and Frequency Synchronization Problem B11

3 RIS Profile Design B11
3.1 Hadamard-based Design B12
3.2 Example B13
4 High-level Algorithm Description B14
4.1 Channel-domain Parameter Estimation B14
4.2 Localization B16
4.3 Joint line-of-sight (LoS) Detection and Localization . . B17
5 Channel Parameter Estimation B18
5.1 Channel Parameter Estimation under LoS B19
5.2 Channel Parameter Estimation without LoS B21
5.3 Complexity Analysis B24
6 Numerical Results B25
6.1 Scenario, Performance Metric and Simulation Setup . . B25
6.2 Localization under LoS B27
6.3 Localization without LoS B29
6.4 Joint LoS Detection and localization B32
6.5 Comparison with Existing Methods B33
6.6 Sensitivity Analysis to Uncontrolled Multipath B34
6.7 Sensitivity Analysis to UE Velocity B38
6.8 Analysis on Ergodic Capacity B39
6.9 Analysis of Localization Bound with Increasing Number of RISs B40
7 Conclusion B41
1 RIS Phase Profile - Temporal Coding B43
2 Fisher Information Matrix Analysis B44
3 Received signal model in the presence of multi-path components B45
References B46

C Integrated Cellular and LEO-based Positioning and Synchronization under User Mobility C1
1 Introduction C3
2 System Model C7
2.1 Scenario C7
2.2 Signal and Channel Model C8
2.3 Geometric Relations C10
2.4 Problem Statement C11

3 Generative and Simplified Models C11
3.1 Clock and Frequency Offset C11
3.2 Generative Model C11
3.3 Simplified Models C19
4 Estimation Algorithms C21
4.1 Channel Parameter Estimation C22
4.2 Location, Clock Offset, Velocity and CFO Estimation . C28
4.3 Complexity Analysis C30
5 Simulation Results C31
5.1 Simulation Setup and Theoretical Bounds C31
5.2 Results and Discussion C32
6 Concluding Remarks C39
1 Derivation of continuous-time generative model C40
2 Linearizing the delay propagation C40
3 FIM and Bias Term in MRCB C42
References C43

Part I

Overview

CHAPTER 1

Introduction

1.1 Background

Wireless communication has become an indispensable necessity of the modern networked society, enabling seamless connectivity across the globe. From mobile phones to internet of things (IoT) devices, the main function of these technologies is to facilitate the exchange of information. Enabled by this capability, numerous applications in different areas such as augmented reality (AR), virtual reality (VR), smart cities , autonomous systems and telemedicine have been developed. The total mobile traffic is predicted to reach 313EB/m [1] in 2029 [1], while this number is less than 150EB/m in 2025. To realize such a considerable requirement, future communication technologies must deliver significantly higher throughput, lower latency, and enhanced reliability. The 6G networks are expected to provide higher capacity and ubiquitous connectivity due to ever-increased IoT ecosystem, as well as enhanced energy efficiency due to sustainability purposes.

While the primary objective of these technologies is to provide reliable and seamless communication, with the help of the existing infrastructure designed

[1] 1 EB (exabyte) is one quintillion, or 10^{18}

for communication, it is possible to develop improved radio localization services as well [2]. Accurate localization services are essential in a wide range of applications, from autonomous driving (AD) and advanced driver-assistance systems (ADAS) to AR and precise navigation. The ability to determine an object's position with high precision enables safer transportation systems, enhances user experiences in AR, and facilitates efficient navigation in complex environments. Current localization technologies, while advanced, still face challenges in terms of accuracy, coverage, and robustness, particularly in urban canyons and indoor environments. The demand for precise localization is growing, with the autonomous vehicle market was valued at $60.3 billion in 2025 and expected to reach a value of $448.6 billion by 2030, according to Allied Market Research [3]. To achieve the necessary precision for AD/ADAS, localization systems are required to provide accuracy within centimeter level for 95% of the time [4]. These future expectations underscore the critical need to develop new technology enablers that can enhance the precision, reliability, and scalability of localization systems.

To unlock the futuristic use cases of 6G mentioned above, both in communication and localization, a number of technology enablers are being developed such as massive MIMO, RIS, NTN, utlization of tera-hertz (THz) frequency bands, etc. The first three technologies and their roles in communication and localization are briefly discussed below.

1.1.1 Massive MIMO

Massive MIMO is a key technology in modern wireless communication systems that involves the use of a large number of antennas at the BS to serve multiple user equipment UE simultaneously [5]. By employing hundreds or even thousands of antennas, massive MIMO systems can significantly enhance both communication and localization capabilities [6]. The large array of antennas allows for precise beamforming, which directs energy towards intended users, thereby improving signal strength and coverage. This boost in energy efficiency translates into higher spectral efficiency, as more data can be transmitted over the same frequency spectrum. Moreover, massive MIMO's spatial resolution capabilities enable more accurate localization of users, as the direction and range of incoming signals can be precisely estimated. This dual improvement in communication and localization is essential for the development of the aformentioned advanced applications, where both high data rates

and precise positioning are required.

Two main architecture for realizing massive MIMO systems have been proposed in the literature, namely fully-digital and hybrid architectures. In fully-digital architecture, each antenna is connected to an individual radio frequency (RF) chain, containing mixers, power amplifiers, etc., as well as a pair of data converters. This results in full flexibility in beamforming and high spectral efficiency, with the challenge of high implementation cost and high power consumption. On the other hand, in hybrid architecture, antennas are connected to fewer RF chains through a network of phase shifters so that a combination of analog and digital beamforming can be implemented. This results in limited flexibility in beamforming and necessitates antenna calibration. However, hybrid architectures are more energy efficient and cost effective compared to their all-digital counterparts. In this thesis, we focus on a fully-digital architecture because it offers remarkable benefits in terms of reconfigurability, accessibility, and ease of maintenance.

In an all-digital massive MIMO setup, one of the main contributors to high power consumption is high resolution data converters. Therefore one solution is to leverage low resolution data converters which will cause non-linear distortion to their input signals. In [7]–[10], it is shown that architectures with few bit data converters and enough number of antennas and depending on the number of UEs, can approach to the performance of infinite-precision data converters.

In some deployments of massive MIMO systems, the remote radio head (RRH), which houses the antennas and the RF chains, and the base-band unit (BBU) are physically separated and are connected through a link, known as the fronthaul link, which has a limited capacity. The amount of raw data transfering through this link is directly proportional to the number of antennas and the resolution of data converters, therefore a limited fronthaul capacity poses a trade-off between the number of antennas and the resolution of data converters.

With this introduction, the first research question is as follows: Given a constrained fronthaul capacity, what is the optimal massive MIMO architecture in terms of the number of antennas and the resolution of data converters? In Paper A, we developed an analytical framework to evaluate this trade-off.

1.1.2 From Communication to Localization

Localization is predominantly performed using the Global Positioning System (GPS), a satellite-based navigation system that determines a user's position based on time of arrival (ToA) measurements [11]. GPS requires an unobstructed LoS to at least four satellites, with the satellites and the user positioned such that they are not collinear. The system consists of a constellation of at least 24 satellites orbiting the Earth, along with ground control stations and GPS receivers. These satellites continuously transmit signals, which receivers use to compute their precise location through multilateration of the time delays from multiple satellites.

Despite its widespread deployment, GPS has several limitations. One of the most significant drawbacks is its reliance on direct LoS between the user and the satellites. This dependency makes GPS vulnerable in obstructed environments, such as urban canyons, dense forests, and indoor settings, where signal blockage and multipath effects degrade localization accuracy. Moreover, Global Navigation Satellite System (GNSS) constellations are managed by individual countries or coalitions, such as the European Union's Galileo. As a result, access to these services is subject to policy decisions by the operating entities, which may lead to restrictions under certain circumstances. This aspect highlights the importance of considering system availability and resilience in critical applications. Additionally, GPS accuracy can be affected by signal multipath, where signals reflect off surfaces before reaching the receiver, causing errors in position calculations. More over, GPS-based positioning is vulnerable to spoofing and jamming, which pose serious risks in safety-critical applications [12]. In jamming attacks, the signal is intentionally blocked or overwhelmed, preventing the receiver from obtaining a valid position. In spoofing, an attacker transmits counterfeit signals that mislead the receiver into estimating an incorrect location or time. Since GPS is a passive, one-way system, it lacks the ability to detect such attacks, making receiver-side detection or complementary systems essential for reliable operation in adversarial environments.

An alternative solution is to use cellular networks. Each new generation of mobile communications comes with new features that make localization more accurate [2]. In 2G networks, a rough positioning can be done using the cell-ID technique, in which the location of the closest BS is used to estimate the position of the mobile device. This technique can be improved by combining

them with ranging-based measurements of timing advance (TA) and signal strength measurements. Experimental results show that this combination can achieve localization accuracy better than 100 m [13]. However, such accuracy was initially insufficient for emergency call localization, as it did not meet the regulatory requirements in some countries, such as the E911 mandate by the FCC in the U.S. In 3G, cell-ID technique can be combined with round trip time (RTT) measurements from three BSs, which can achieve localization accuracy of 70 to 90 m. In 3G and 4G networks, the location of the user can be estimated using the time difference of arrival (TDoA) measurements from multiple BSs and multilateration. This results in uncertainty in the order of 20 to 50m. In 5G networks, the adoption of mmWave frequencies and beamforming techniques improved the accuracy of positioning [14]–[16]. In 6G networks, the use of RISs and NTN is expected to further enhance the accuracy and reliability of cellular-based localization [17]–[22].

1.1.3 RIS-aided Localization

RISs are an emerging technology in wireless communication systems, consisting of a multitude of passive elements that can dynamically adjust their properties to control electromagnetic waves. These elements can be programmed to redirect intercepted signals towards specific locations, thereby enhancing signal strength and coverage. This redirection capability leads to significant improvements in energy efficiency, as signals can be effectively steered to their intended destinations with minimal loss [23]. The improved energy efficiency not only enhances communication by boosting signal quality and data throughput but also benefits localization by enabling more precise control over signal paths [17]. By utilizing RISs, additional measurements can be incorporated without introducing extra unknowns, thanks to their synchronization and knowledge of their location and orientation. Furthermore, optimizing the propagation environment through RIS technology supports advanced applications that require both robust communication and accurate positioning, making it a crucial component in the evolution of next-generation wireless networks.

Building on the potential of RISs for precise localization, we now address the second research question: "Using RISs, what is the minimal required architecture to accurately position a user?" In Paper B, we investigate this question in detail.

1.1.4 Localization: Integration with NTN

Next, we turn our attention to NTNs, which represent a transformative approach in wireless communication, incorporating satellite systems into the traditional terrestrial network (TN) infrastructure. NTN was introduced to address various challenges faced by cellular networks, such as coverage limitations in remote areas, high latency, and insufficient localization accuracy. Initial 3GPP releases, like Release 16, laid the groundwork by outlining the integration of satellite communication to enhance connectivity and extend network reach. Release 17 further advanced this by incorporating NTN elements, including LEO satellites, which offer significant benefits over traditional geostationary satellites [24]. Due to their lower altitude, LEO satellites reduce latency and provide improved signal quality, thereby enhancing communication reliability and real-time data transfer. These advancements ensure that NTN contributes substantially to the evolution of global communication and precise location-based services.

Integration of terrestrial and NTNs offers immense potential in enhancing localization by leveraging the complementary strengths of terrestrial base stations and non-terrestrial platforms like LEO satellites. This synergy provides robust solutions to challenges in traditional localization systems, including limited coverage and high latency in remote or urban environments [25]. As highlighted in previous studies, combining TN and NTN elements enables global coverage, improved signal availability, and enhanced accuracy, even in complex scenarios [21], [22].

Building on these advancements, the final research question investigates how we can benefit from the integration of one terrestrial BS and one LEO satellite in positioning and synchronization of a moving UE considering realistic synchronization effects. Paper C explores this question.

1.2 Organization of the Thesis

Part I of this thesis is organized as follows.

- In Chapter 2, data converters and a mathematical tool to simplify the derivations are introduced together with a review of the quantized multi-user (MU) massive MIMO setup.
- In Chapter 3, a brief summary of traditional localization techniques

together with an introduction to more advanced RIS and NTN-based localization techniques are presented.

- Chapter 4 contains a summary of the appended papers appearing in Part II.

1.3 Notation

Lowercase and uppercase boldface letters and lowercase letters denote column vectors, matrices and scalars, respectively. The set of real numbers and complex numbers are indicated by $\mathbb{R}$ and $\mathbb{C}$ respectively. The notations $(.)^{\mathsf{T}}$ and $(.)^{\mathsf{H}}$ indicate transpose and hermitian transpose, respectively. The operators $\mathbb{E}[.]$ and $\text{diag}(\boldsymbol{X})$ denote the mathematical expectation over the specified random variable and the diagonal elements of a square matrix $\boldsymbol{X}$, respectively. An all-zero vector of dimension N is denoted by $\mathbf{0}_N$. The complex-valued N-dimensional circularly-symmetric Gaussian probability density function with zero mean and covariance $\mathbf{K}$ is expressed as $\mathcal{CN}(\mathbf{0}_N, \mathbf{K})$. The real and imaginary parts of a signal are indicated by $\Re(.)$ and $\Im(.)$.

CHAPTER 2

Quantized Massive MIMO in Communication

In this section, we discuss the modeling of data converters and use the well-known Bussgang theorem to linearize the input-output relation. Then we use conventional precoder and combiner techniques to derive signal to interference plus noise plus distortion ratio (SINDR) and ergodic sum-rate in a multi-user quantized uplink and downlink massive MIMO scenario.

2.1 Data Converters

In a practical communication system, data converters are essential for converting signals from analog to digital domain and vise versa. For the uplink, ADCs at the BS convert the incoming analog signal into a digital signal, making it ready for digital processing in the BBU. On the downlink, digital to analog converters (DACs) handle the reverse process, turning digital signals into analog form for transmission over the wireless channel. In this chapter and Paper A, it is assumed that the users have infinite-resolution data converters, while the BS is equipped with low-resolution data converters. Data converters as non-linear devices cause irreversible distortion to the input signal which is increased by lowering the resolution, on the other hand the power

consumption of data converters scales exponentially with their resolution [26]. In this section, we explore a mathematical tool used to linearize the effects of data converters, making the derivations more straightforward. Additionally, we discuss a phenomenon known as stochastic resonance, which occurs with single-bit resolution data converters at high SNR.

2.1.1 Linearization using Bussgang Theorem

In this thesis, uniform, symmetric and mid-rise quantizers are used. Considering the input $r \in \mathbb{R}$, the quantized signal $\mathcal{Q}(r)$ is defined as

$$y = \mathcal{Q}(r) = \begin{cases} \frac{\Delta}{2}(1 - 2^Q) & \text{if } r < -\frac{\Delta}{2}2^Q \\ \Delta\lfloor \frac{r}{\Delta} \rfloor + \frac{\Delta}{2} & \text{if } -\frac{\Delta}{2}2^Q < r < \frac{\Delta}{2}2^Q \\ \frac{\Delta}{2}(2^Q - 1) & \text{if } r \geq \frac{\Delta}{2}2^Q. \end{cases} \tag{2.1}$$

Here, Q and Δ represent the resolution and step size of the quantizer respectively. To simplify the notation, the quantization labels are represented by the set $\mathcal{L} = \{l_0, ..., l_{L-1}\}$ where $L = 2^Q$ denotes the total number of quantization levels. The quantization thresholds are defined by the set $\mathcal{T} = \{\tau_0, ..., \tau_L\}$ where $\tau_0 = -\infty$ and $\tau_L = +\infty$. For a complex input to the quantizer, $\mathbf{z} \in \mathbb{C}^n$, the real and imaginary parts of $\boldsymbol{z}$ are quantized separately using two independent quantizers. To linearize the input-output relationship, the quantized signal can be expressed as the sum of the linear minimum mean square error (LMMSE) estimate of the output and an uncorrelated distortion term. The LMMSE estimate provides a practical way to approximate the relationship, and when $\mathbf{z}$ follows a Gaussian distribution, a mathematical tool known as Bussgang theorem [27] can be applied to further simplify and characterize this linearization.

Theorem 1. *The cross-correlation of two Gaussian signals, when one of them has undergone a non-linear transformation, is the same as the cross-correlation of them before the non-linear transformation except for a scaling factor called Bussgang gain.*

As a result of Bussgang theorem, the linearized input-output relationship

for $\mathbf{y} = \mathcal{Q}(\mathbf{z})$, where $\mathbf{z} \sim \mathcal{CN}(\mathbf{0}, \mathbf{C_z})$ can be expressed as follows:

$$\begin{aligned} \mathbf{y} &= \mathbf{G}\mathbf{z} + \mathbf{d}, \\ \mathbf{G} &= \mathbb{E}\left[\mathcal{Q}(\mathbf{z})\mathbf{z}^{\mathrm{H}}\right] \mathbb{E}\left[\mathbf{z}\mathbf{z}^{\mathrm{H}}\right]^{-1} = \mathbf{C_{yz}}\mathbf{C_z}^{-1}. \end{aligned} \tag{2.2}$$

Here, $\mathbf{C_{yz}} = \mathbb{E}[\mathbf{y}\mathbf{z}^{\mathrm{H}}]$ denotes the covariance between $\mathbf{y}$ and $\mathbf{z}$. The distortion term $\mathbf{d}$ is a non-Gaussian, zero-mean random vector that is uncorrelated with $\mathbf{z}$. The covariance matrix of $\mathbf{d}$ plays an important role in subsequent analyses, particularly those involving achievable rates. For the case of the mid-rise quantizer function described in (2.1), the Bussgang matrix is given by [8], [28]

$$\mathbf{G} = \frac{\Delta}{\sqrt{\pi}} \mathrm{diag}(\mathbf{C_z})^{-1/2} \sum_{i=1}^{L-1} \exp\left(-\frac{\Delta^2}{2}(i - L/2)^2 \mathrm{diag}(\mathbf{C_z})^{-1}\right). \tag{2.3}$$

2.1.2 Covariance Matrix of Distortion

According to (2.2), the covariance matrix of distortion takes the following form:

$$\mathbf{C_d} = \mathbb{E}\left[(\mathbf{y} - \mathbf{G}\mathbf{z})(\mathbf{y} - \mathbf{G}\mathbf{z})^{\mathrm{H}}\right] = \mathbf{C_y} - \mathbf{G}\mathbf{C_z}\mathbf{G}. \tag{2.4}$$

Note that since $\mathbf{G}$ is a real diagonal matrix, it satisfies $\mathbf{G}^{\mathrm{H}} = \mathbf{G}$. To compute $\mathbf{C_d}$, it is necessary to determine the covariance matrix of the quantized signal $\mathbf{y}$. The diagonal elements of $\mathbf{C_y}$ are given by [29]

$$[\mathbf{C_y}]_{p,p} = 2\mathbb{E}[y_p^R y_p^R] = \frac{\Delta^2}{2}(L-1)^2 - 4\Delta^2 \sum_{i=1}^{L-1} \left(i - \frac{L}{2}\right) \Phi\left(\frac{\sqrt{2}}{\sigma_p}\left(i - \frac{L}{2}\right)\right). \tag{2.5}$$

Here, $\sigma_p = [\mathbf{C_z}]_{p,p}^{1/2}$ and $\Phi(x) = \sqrt{1/2\pi}\int_{-\infty}^{x} e^{-t^2/2}dt$ represents the cumulative distribution function (CDF) of the standard normal random variable. For $Q > 1$, there is no closed-form expression available for the off-diagonal elements of $\mathbf{C_y}$. However, in the special case of 1-bit data converters, the covariance matrix can be expressed in closed-form using the arcsine law as follows [30]

$$\mathbf{C_y} = \frac{2}{\pi}\left[\arcsin\left(\mathrm{diag}(\mathbf{C_z})^{-\frac{1}{2}} \mathbf{C_z} \mathrm{diag}(\mathbf{C_z})^{-\frac{1}{2}}\right)\right]. \tag{2.6}$$

For $Q > 1$, some approximations have been proposed in the literature including the diagonal approximation [29]. This approximation relies on the observation that the diagonal elements of $\mathbf{C_y}$ can be computed exactly [29]. By modeling the distortion introduced by the quantizers as a white process, the off-diagonal elements of the distortion matrix are assumed to be zero. Under this assumption $\mathbf{C_d}$ can be approximated as follows:

$$\begin{aligned}\mathbf{C}_{\mathbf{d}}^{\text{diag}} &= \text{diag}\left(\mathbf{C_y}\right) - \mathbf{G}\text{diag}\left(\mathbf{C_z}\right)\mathbf{G}^{\text{H}} \qquad (2.7)\\ &= \frac{\Delta^2}{2}(L-1)^2\mathbf{I}_n - 4\Delta^2\sum_{i=1}^{L-1}\left(i-\frac{L}{2}\right)\Phi\left(\sqrt{2}\left(i-\frac{L}{2}\right)\text{diag}\left(\mathbf{C_z}\right)^{-1/2}\right).\end{aligned}$$

2.1.3 Stochastic Resonance and Dithering for 1-Bit ADCs

Single-bit resolution ADCs operate as comparators, and they do not preserve the amplitude information of the input signal. This means that for 1-bit quantizers, the output of $\mathcal{Q}(r)$ and $\mathcal{Q}(\alpha r)$ are identical for $\alpha > 0$. Now suppose that our observations to be quantized are noisy. At low and medium SNR levels, the additive noise turns out to be beneficial as it alters quantized output, effectively encoding some amplitude information of the input signal. As a result, when multiple noisy observations of the desired signal are available, it becomes possible to partially recover its amplitude. This phenomenon is referred to as stochastic resonance [31], [32].

In high SNR, stochastic resonance no longer occurs because the additive noise term becomes negligible and does not significantly affect the quantized output. Therefore, 1-bit ADCs suffer from loss of amplitude information at high SNR. To address this limitation, it is possible to add artificial noise to effectively reduce the SNR operating point. This technique is called dithering and is being used to improve the performance of 1-bit data converters [33], [34]. For this reason, we used dithering in high SNR regime in Paper A.

2.2 Multi-user Massive MIMO

The objective of this section is to derive lower bounds on the uplink and downlink achievable rates in an all-digital low-resolution MU massive MIMO system. This thesis considers a single-cell scenario where a BS with B antennas communicates with $U \ll B$ single-antenna UEs using the same time and

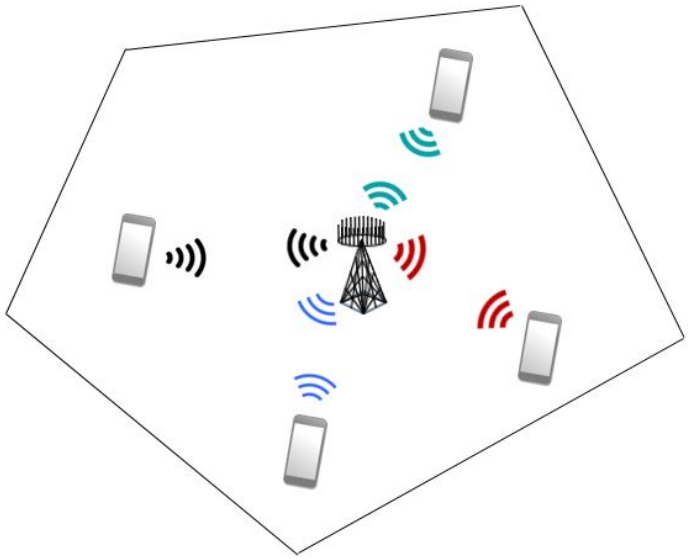

Figure 2.1: A single cell scenario in which a B-antenna BS serves U UEs on the same time and frequency resource.

frequency resource via spatial multiplexing, as illustrated in Fig. 2.1. Each antenna at the BS is connected to a pair of data converters that independently quantize the real and imaginary parts of the input signal. The wireless channel is represented by $\mathbf{H}^{B\times U}$ and is modeled as a block-fading channel, remaining constant during the transmission of a codeword.

In practical scenarios, the BS and UEs lack knowledge of the channel state information (CSI), necessitating channel estimation. It is assumed that the system operates in time division duplex (TDD) mode, where uplink and downlink transmissions share the same frequencies but occur in different time intervals. Under this assumption, the estimated channel from the uplink can also be used for the downlink. In this chapter, to focus on deriving the lower bounds on achievable rates, the BS and UEs are assumed to have full knowledge of CSI. This assumption is relaxed in Paper A. Additionally, this chapter reviews the derivations of the commonly used ergodic capacity, whereas Paper A emphasizes outage capacity, which is better suited for block-fading channels and short packet transmissions.

2.2.1 Channel Model

In this subsection, we review the channel model used in Paper A. Our focus is on mm-wave propagation, where the wireless channel exhibits sparsity in the angular domain. This sparsity allows the channel behavior to be represented as the superposition of a small number of propagation paths. A widely-used channel model that aligns well with the sparse nature of mm-wave wireless channels is the clustered channel model [35]–[37]. In this model, N_{cl} clusters of scatterers are considered, with each cluster contributing N_{ray} propagation paths. The discrete-time narrow-band multi-user channel impulse response for the uplink is given by $\mathbf{H} = [\mathbf{h}_1, \mathbf{h}_2, ..., \mathbf{h}_U] \in \mathbb{C}^{B\times U}$ where $\mathbf{h}_u$ can be written as

$$\mathbf{h}_u = \sqrt{\frac{1}{N_{\text{cl}}N_{\text{ray}}}} \sum_{n=1}^{N_{\text{cl}}} \sum_{m=1}^{N_{\text{ray}}} \alpha_{n,m}^u \mathbf{a}(\theta_{n,m}^u). \tag{2.8}$$

Here, the fading coefficients $\alpha_{n,m}^u$ are i.i.d. complex random variables following $\mathcal{CN}(0, \sigma_u^2)$, where σ_u^2 represents the pathloss experienced by the u^{th} UE. The term $\mathbf{a}(\theta_{n,m}^u)$ denotes the array response vector of the uniform linear array (ULA) at the BS in the far field, expressed as:

$$\mathbf{a}(\theta_{n,m}^u) = \left[1, e^{-j2\pi\theta_{n,m}^u}, ..., e^{-j2\pi(B-1)\theta_{n,m}^u}\right]^{\text{T}}, \tag{2.9}$$

where $\theta_{n,m}^u = d\sin(\phi_{n,m}^u)/\lambda$, d represents the antenna spacing, $\phi_{n,m}^u$ denotes the angle-of-arrival (AoA) (spatial angle) measured from the boresight of the ULA, and λ is the wavelength of the signal.

2.2.2 Uplink Transmission

In the uplink, U UEs transmit signals to the BS. The received signal $\mathbf{y}^{\text{ul}} \in \mathbb{C}^B$ at the BS at time instant k can be expressed as:

$$\mathbf{y}_k^{\text{ul}} = \sqrt{\rho^{\text{ul}}}\mathbf{H}\mathbf{s}_k^{\text{ul}} + \mathbf{n}_k^{\text{ul}}, \tag{2.10}$$

where $\mathbf{n}_k^{\text{ul}} \sim \mathcal{CN}(\mathbf{0}_B, \mathbf{I}_B)$ represents the additive noise, and the transmit signal vector is $\mathbf{s}k^{\text{ul}} = [s_{k,1}^{\text{ul}}, \ldots, s_{k,U}^{\text{ul}}] \in \mathbb{C}^U$. Each signal $s_{k,u}^{\text{ul}}$, for $u = 1, \ldots, U$, is independently drawn from $\mathcal{CN}(0, 1)$, and ρ^{ul} denotes the uplink SNR. The received signal $\mathbf{y}_k^{\text{ul}}$ at the BS passes through an automatic gain controller circuit (AGC) circuit and a pair of Q-bit quantizers at each antenna. The

purpose of the AGC circuit is to adjust the dynamic range of the input signal to the quantizer such that the probability of overload remains below a specified threshold. The resulting quantized signal can be expressed as:

$$\mathbf{r}_k^{\mathrm{ul}} = \mathcal{Q}(\mathbf{A}(\sqrt{\rho^{\mathrm{ul}}}\mathbf{H}\mathbf{s}_k^{\mathrm{ul}} + \mathbf{n}_k^{\mathrm{ul}})), \tag{2.11}$$

where $\mathbf{A}$ models the AGC circuit and $\mathcal{Q}(.)$ is the quantizer function given in (2.1). Following the derivations of Bussgang linearization in Sect. 2.1.1, (2.11) can be written as

$$\mathbf{r}_k^{\mathrm{ul}} = \mathbf{G}^{\mathrm{ul}}\mathbf{A}(\sqrt{\rho^{\mathrm{ul}}}\mathbf{H}\mathbf{s}_k^{\mathrm{ul}} + \mathbf{n}_k^{\mathrm{ul}}) + \mathbf{d}_k^{\mathrm{ul}}, \tag{2.12}$$

Here, $\mathbf{G}^{\mathrm{ul}}$ is the Bussgang matrix (2.3) and $\mathbf{d}^{\mathrm{ul}}$ is a non-Gaussian quantization noise that is uncorrelated to $\mathbf{y}^{\mathrm{ul}}$. The distortion covariance $\mathbf{C}_{\mathbf{d}}^{\mathrm{ul}}$ can be found by arcsine law when $Q = 1$ and diagonal approximation when $Q > 1$ as explained in Sec. 2.1.2. The covariance of the input to the quantizer $\mathbf{z}_k^{\mathrm{ul}} = \mathbf{A}\mathbf{y}_k^{\mathrm{ul}}$ is $\mathbf{C}_{\mathbf{z}}^{\mathrm{ul}} = \mathbf{A}\mathbf{C}_{\mathbf{y}}^{\mathrm{ul}}\mathbf{A}$.

In this thesis, we employ sub-optimal linear processing at the BS due to its simplicity. When the number of BS antennas is large, linear processing becomes nearly optimal under favorable propagation conditions [38], [39]. The idea of linear processing in the uplink is to determine a matrix $\mathbf{W}$, referred to as the combiner matrix, which is then applied to the received signal. This operation yields an estimate of each user's data stream, as shown below:

$$\hat{\mathbf{s}}_k^{\mathrm{ul}} = \mathbf{W}^{\mathrm{H}}\mathbf{r}_k^{\mathrm{ul}} = \mathbf{W}^{\mathrm{H}}\left(\mathbf{G}^{\mathrm{ul}}\mathbf{A}(\sqrt{\rho^{\mathrm{ul}}}\mathbf{H}\mathbf{s}_k^{\mathrm{ul}} + \mathbf{n}_k^{\mathrm{ul}}) + \mathbf{d}_k^{\mathrm{ul}}\right). \tag{2.13}$$

The ergodic sum-rate is lower bounded by

$$R_{\mathrm{sum}}^{\mathrm{ul}} = \mathbb{E}_{\mathbf{H}}\left[\sum_{u=1}^{U}\log(1+\gamma_u^{\mathrm{ul}})\right], \tag{2.14}$$

where γ_u^{ul} is the received SINDR at the uth UE, given by

$$\gamma_u^{\mathrm{ul}} = \frac{\rho^{\mathrm{ul}}|\mathbf{w}_u^{\mathrm{H}}\mathbf{G}^{\mathrm{ul}}\mathbf{A}\mathbf{h}_u|^2}{\rho^{\mathrm{ul}}\sum_{v\neq u}|\mathbf{w}_u^{\mathrm{H}}\mathbf{G}^{\mathrm{ul}}\mathbf{A}\mathbf{h}_v|^2 + \mathbf{w}_u^{\mathrm{H}}\mathbf{C}_{\mathrm{d}}^{\mathrm{ul}}\mathbf{w}_u + ||\mathbf{A}\mathbf{G}^{\mathrm{ul}}\mathbf{w}_u||^2} \tag{2.15}$$

This lower bound is found by treating the residual multi-user interference (MUI) and the quantization noise as an independent Gaussian noise to reflect

the worst-case scenario [40, App B] and is achieved by Gaussian signaling.

Three widely used linear combiners are matched filtering (MF), zero-forcing (ZF), and minimum mean square error (MMSE). The MF combiner is designed to maximize the per-user SNR, but its primary limitation is its inability to handle multi-user interference (MUI). As a result, the MF combiner performs well in the low SNR regime but struggles in the high SNR regime due to interference. On the other hand, the ZF combiner eliminates MUI by placing nulls in the directions of non-intended users. However, it does not account for additive white Gaussian noise (AWGN), leading to noise enhancement and poor performance at low SNR, while excelling at high SNR. The MMSE combiner, in contrast, minimizes the mean-square error between the estimated signal $\hat{\mathbf{s}}$ and the actual signal $\mathbf{s}$. It also maximizes the received SINR, making it superior to both ZF and MF combiners.

The classical MF, ZF, and MMSE combiners do not consider the impact of quantization distortion. To address this, distortion-aware (DA) versions of the MMSE combiner were introduced in [41] and [42], which aim to maximize the received SINDR. The definitions of the ZF, MF, and DA-MMSE combiners are provided below.

$$\mathbf{W} = \begin{cases} \mathbf{G}^{\mathrm{ul}}\mathbf{A}\mathbf{H} & \text{for MF,} \\ \left(\mathbf{G}^{\mathrm{ul}}\mathbf{A}\mathbf{H}\right)\left(\left(\mathbf{G}^{\mathrm{ul}}\mathbf{A}\mathbf{H}\right)^{\mathrm{H}}\mathbf{G}^{\mathrm{ul}}\mathbf{A}\mathbf{H}\right)^{-1} & \text{for ZF,} \end{cases} \tag{2.16}$$

and for DA-MMSE combiner [42]

$$\mathbf{w}_u = \left(\rho^{\mathrm{ul}}\left(\sum_{v\neq u}\mathbf{G}^{\mathrm{ul}}\mathbf{A}\mathbf{h}_v\left(\mathbf{G}^{\mathrm{ul}}\mathbf{A}\mathbf{h}_v\right)^{\mathrm{H}}\right) + \mathbf{G}^{\mathrm{ul}}\mathbf{A}(\mathbf{G}^{\mathrm{ul}}\mathbf{A})^{\mathrm{H}} + \mathbf{C}_{\mathrm{d}}^{\mathrm{ul}}\right)^{-1} \tag{2.17}$$

$$\times\left(\rho^{\mathrm{ul}}\mathbf{G}^{\mathrm{ul}}\mathbf{A}\mathbf{h}_u\right), \tag{2.18}$$

where $\mathbf{w}_u, u = 1, ..., U$ are columns of the combiner matrix $\mathbf{W}$. In Paper A, we leverage DA-MMSE combiner.

2.2.3 Downlink Transmission

The U-dimensional discrete-time received signal at time instant k at UEs can be written as

$$\mathbf{y}_k^{\mathrm{dl}} = \mathbf{H}^{\mathrm{T}} \alpha \mathcal{Q}\left(\mathbf{z}_k^{\mathrm{dl}}\right) + \mathbf{n}_k^{\mathrm{dl}}, \tag{2.19}$$

where $\mathcal{Q}(.)$ denotes the quantizer function given in (2.1). The vector $\mathbf{n}_k^{\mathrm{dl}} \sim \mathcal{CN}(\mathbf{0}_U, \mathbf{I}_U)$ represents the AWGN at the UEs' side and the transmit signal is shown by $\mathbf{z}_k^{\mathrm{dl}}$. The factor α is a power-normalization parameter used to ensure that the transmit power satisfies the constraint ρ^{dl}. This constraint is determined by treating the input to the quantizer as a complex Gaussian random variable, as shown below:

$$\alpha = \frac{\sqrt{\rho^{\mathrm{dl}}/2}}{\sqrt{\sum_{i=0}^{L-1} l_i^2 \left(Q(\sqrt{2}\tau_i) - Q(\sqrt{2}\tau_{i+1})\right)}}. \tag{2.20}$$

Here, $Q(x) = \sqrt{1/2\pi} \int_x^{\infty} e^{-t^2/2} dt$ denotes the Q-function. Similar to the uplink, we use linear processing for downlink. The signals intended to UEs are represented as $\mathbf{s}_k^{\mathrm{dl}} = [s_{1,k}^{\mathrm{dl}}, ..., s_{U,k}^{\mathrm{dl}}] \in \mathbb{C}^U$ where $\mathbb{E}[|s_{u,k}^{\mathrm{dl}}|^2] = 1$ for $u = 1, \ldots, U$. The downlink precoded signals $\mathbf{z}_k^{\mathrm{dl}}$ using the precoding matrix $\mathbf{P}$ are expressed as below

$$\mathbf{z}_k^{\mathrm{dl}} = \mathbf{P}\mathbf{s}_k^{\mathrm{dl}}. \tag{2.21}$$

The purpose of using precoders is to design the (unquantized) transmitted signal $\mathbf{z}_k^{\mathrm{dl}}$ in such a way that minimal processing is required on the UE side to obtain a soft estimate $\hat{\mathbf{s}}_k^{\mathrm{dl}}$. Three widely used precoders are ZF, MF, and MMSE. These precoders are dual versions of their corresponding combiners, sharing the same objectives and properties. Assuming a non-quantized setup, the formulations of these precoders are given as follows:

$$\mathbf{P} = \begin{cases} \beta \mathbf{H}^* & \text{for MF,} \\ \beta \mathbf{H}^* \left(\mathbf{H}^{\mathrm{T}} \mathbf{H}^*\right)^{-1} & \text{for ZF,} \\ \beta \mathbf{H}^* \left(\mathbf{H}^{\mathrm{T}} \mathbf{H}^* + \frac{U}{\rho^{\mathrm{dl}}} \mathbf{I}_U\right)^{-1} & \text{for MMSE.} \end{cases} \tag{2.22}$$

Here, the factor β is chosen such that $\mathbb{E}[||\mathbf{P}\mathbf{s}_k^{\mathrm{dl}}||^2] = B$. Similar to the uplink, by applying Bussgang linearization, (2.2), (2.19) can be reformulated as

$$\mathbf{y}_k^{\mathrm{dl}} = \mathbf{H}^{\mathrm{T}}\mathbf{G}^{\mathrm{dl}}\left(\mathbf{P}\mathbf{s}_k^{\mathrm{dl}}\right) + \mathbf{H}^{\mathrm{T}}\mathbf{d}_k^{\mathrm{dl}} + \mathbf{n}_k^{\mathrm{dl}}. \tag{2.23}$$

Here, $\mathbf{G}^{\mathrm{dl}}$ represents the Bussgang matrix defined in (2.3) and $\mathbf{d}_k^{\mathrm{dl}}$ denotes a non-Gaussian quantization distortion which is uncorrelated with $\mathbf{s}_k^{\mathrm{dl}}$. The covariance matrix of the distortion $\mathbf{C}_{\mathrm{d}}^{\mathrm{dl}}$ can be computed in closed-form for $Q = 1$ using the arcsine law or approximated for higher resolutions of quantizers, as discussed in Sec. 2.1.2. The covariance of the input to the quantizer is given by $\mathbf{C}_{\mathbf{z}}^{\mathrm{dl}} = \mathbf{P}\mathbf{P}^{\mathrm{H}}$. Assuming that the u^{th} UE has knowledge of its effective channel gain $\left([\mathbf{H}^{\mathrm{T}}\mathbf{G}^{\mathrm{dl}}\mathbf{P}]_{u,u}\right)$, it can recover its intended stream as

$$\hat{s}_{u,k}^{\mathrm{dl}} = \left([\mathbf{H}^{\mathrm{T}}\mathbf{G}^{\mathrm{dl}}\mathbf{P}]_{u,u}\right)^{-1} y_{u,k}^{\mathrm{dl}}. \tag{2.24}$$

Similar to the uplink, the ergodic sum-rate can be lower bounded by

$$R_{\mathrm{sum}}^{\mathrm{dl}} = \mathbb{E}_{\mathbf{H}}\left[\sum_{u=1}^{U}\log(1+\gamma_u^{\mathrm{dl}})\right], \tag{2.25}$$

where γ_u^{dl} is the received SINDR at the uth UE, given by

$$\gamma_u^{\mathrm{dl}} = \frac{|\mathbf{h}_u^{\mathrm{T}}\mathbf{G}^{\mathrm{dl}}\mathbf{p}_u|^2}{\sum_{v\neq u}|\mathbf{h}_u^{\mathrm{T}}\mathbf{G}^{\mathrm{dl}}\mathbf{p}_v|^2 + \mathbf{h}_u^{\mathrm{T}}\mathbf{C}_{\mathrm{d}}^{\mathrm{dl}}\mathbf{h}_u^{*} + 1} \tag{2.26}$$

CHAPTER 3

Terrestrial and Non-Terrestrial Localization

In this chapter, the usage of terrestrial and non-terrestrial networks in localization will be reviewed. The chapter starts with investigating the usage of cellular networks as well as RISs for localization. We explore the infrastructure required to perform positioning in traditional cellular networks as well as how RISs can reduce these requirements. Next, the chapter continues with an introduction to NTNs, investigating their role in localization. Key considerations such as synchronization and coverage are analyzed and compared across these technologies. Finally, the chapter sheds light on how NTNs coordinate with cellular systems to enhance localization accuracy and reliability.

3.1 Cellular-based Localization

Cellular positioning methods requires a sufficient number of base stations to achieve accurate localization. These methods rely on measurements from the transmitted reference signals as well as the known BS positions and can be network-based or mobile-based, depending on if the location estimation is done in the uplink or the downlink [2]. The most common conventional cellular positioning methods are based on measurements such as ToA, TDoA,

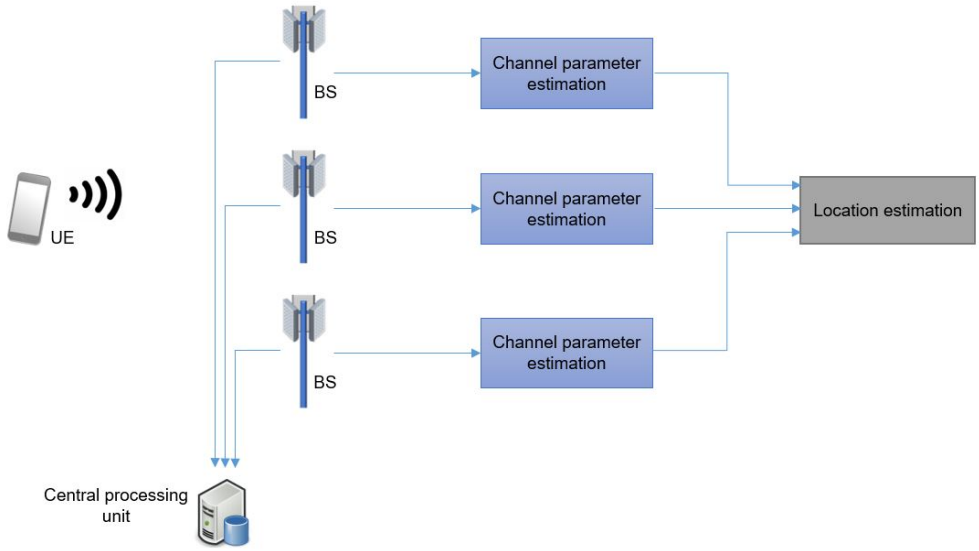

Figure 3.1: A cellular network performing localization

angle-of-departure (AoD), AoA, etc [43]. In 4G, the UE estimates the ToA for each BS, which depends on the distance to the BS and the UE's clock bias. By estimating four ToA through LoS link, the user can estimate three TDoA and solve for its 3D position and clock bias by trilateration. This technique can be implemented in downlink as well as uplink. In this method, all four BSs need to be tightly synchronized by a central processing unit.

In 5G systems operating at mmWave frequencies, both UEs and BSs can be equipped with multiple antennas. This allows the channel to be characterized not only by delays but also by angles, including both AoD and AoA, in both azimuth and elevation planes [44]. Therfore, the UE can determine its location by triangulating the AoD measurements from two BSs.

3.1.1 Topology and Configuration

As mentioned above, when clock offsets or oscillator mismatches are considered, additional base stations are often necessary. These discrepancies introduce errors into the measurements, particularly in ToA and TDoA techniques,

as timing inaccuracies propagate into the calculated distances. This additional measurement improves the robustness of the localization system, ensuring accurate positioning even in the presence of synchronization challenges. Figure 3.1, illustrates a network-based cellular positioning system, employing a number of synchronized BSs. Different channel parameter estimation algorithms have been proposed in the literature, including delay-based [45]–[47], angular-based [48], or a combination of both [49]–[51], etc.

3.1.2 Channel Model

Here, we consider a cellular localization approach. Considering B multi-antenna BSs, each with ULA of N antennas and a single antenna UE, the wideband uplink channel at b^{th} BS and k^{th} subcarrier $\mathbf{h}_{b,k} \in \mathbb{C}^N$ can be expressed as:

$$\mathbf{h}_{b,k} = \sum_{l=0}^{L-1} \alpha_{b,l}\mathbf{a}(\theta_{b,l})e^{-j2\pi\Delta_f k\tau_{b,l}},\ b = 1, \cdots, B,\ k = 1, \cdots, K, \tag{3.1}$$

where the channel comprises a LoS path and $L-1$ uncontrolled multipaths components. Here, $\theta_{b,0}$, $\tau_{b,0}$ and $\alpha_{b,0}$ denote the AoA, delay and the channel gain of the LoS path, and $\theta_{b,l}$, $\tau_{b,l}$ and $\alpha_{b,l}$ where $l \neq 0$ express the AoAs, delays and path gains the uncontrolled multipath components, corresponding to the b^{th} BS. The array steering vector is given by $\boldsymbol{a}(\theta) = [1, e^{-j2\pi/\lambda d\sin\theta}, \cdots, e^{-j2\pi/\lambda d(N-1)\sin\theta}]^{\mathsf{T}}$, where d is the antenna spacing. In this scenario, the geometric information is contained in θ_0 and τ_0, assuming these paths are present. The AoA estimates together with the known orientation of the BSs provides directional information to determine the UE position. Meanwhile, the ToA estimates offer UE positional information and clock bias by determining the range between BSs and the UE.

3.1.3 Synchronization and Coverage Consideration

In real-world cellular networks, environmental factors such as multipath propagation and signal blockages can significantly impact positioning accuracy. These challenges often necessitate deploying additional base stations (BSs) to provide redundancy and ensure the reliability of localization systems.

Synchronization among BSs plays a critical role in achieving precise posi-

tioning. In 4G systems, tight synchronization is required to enable accurate time-of-arrival (ToA) and time-difference-of-arrival (TDoA) measurements, as the clock offsets directly influence the estimation accuracy [51]. The tight synchronization requirements ensure that the localization process remains robust, even in challenging environments. While 5G systems leverage advanced technologies like mmWave frequencies and massive multiple-input multiple-output (MIMO) arrays to enhance angular and distance-based measurements, these improvements come with trade-offs. The reliance on mmWave frequencies reduces the coverage area due to higher path loss and susceptibility to blockages compared to 4G systems. However, techniques such as angular measurements can partially mitigate these limitations by requiring fewer infrastructure elements for accurate positioning.

3.2 Reconfigurable Intelligent Surfaces in Localization

RISs represent a recent significant technology in wireless communication and localization. These surfaces consist of programmable elements that can dynamically manipulate electromagnetic waves without leveraging any power amplification [23]. Instead, by adjusting the phase, amplitude, or polarization of reflected signals, RISs enable precise control over the propagation environment, creating a smart and controllable environment tailored for optimal communication and localization [52].

RISs are particularly valuable for extending coverage and enhancing signal quality, especially in areas affected by blockages or signal attenuation due to multipath propagation. They can be integrated into existing infrastructure, such as walls or buildings, reducing deployment complexity [53]. By strategically shaping signal paths, RISs contribute to reduced power consumption and greater coverage, making them a key enabler for sustainable and efficient localization solutions in future networks [23].

3.2.1 Topology and Configuration

The number and placement of RISs and BSs required for effective localization depend on the specific use case and operational scenario. In conventional localization systems, multiple BSs are often needed to ensure adequate coverage

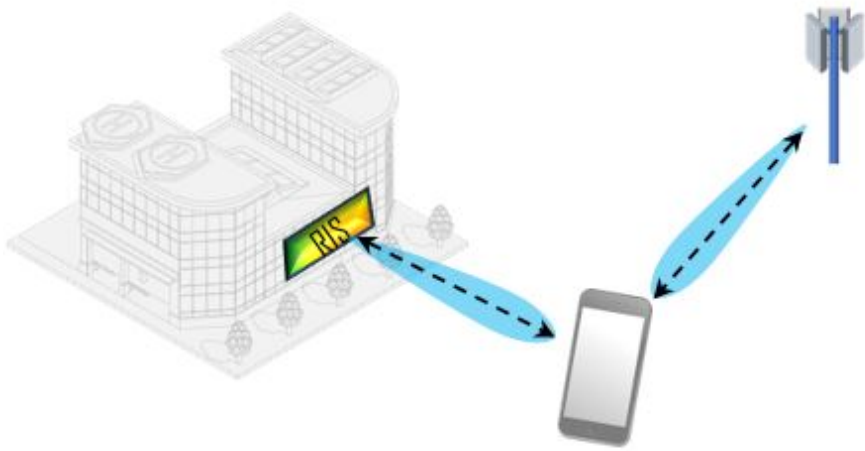

Figure 3.2: A RIS-aided network performing localization

and accuracy, particularly in complex environments such as urban canyons, as highlighted in the previous section. However, integrating RISs can significantly reduce this requirement by enabling precise signal redirection and beamforming.

RISs can drastically lower the infrastructure needed for scenarios where traditional localization might be infeasible [54]. For instance, in single-input single-output (SISO) configurations, 3D localization can be achieved with one BS and one RIS using wideband signals [55] as illustrated in Fig. 3.2. This contrasts with the conventional need for four BSs in a similar scenario without RISs.

Moreover, by exploiting the angular information (e.g., AoD) provided by RISs, the system can identify the UE location with fewer active components. In another example, considering multiple antennas at the BS and single antenna UE, accurate 3D localization can be performed via 1 BS and 1 RIS, by intersecting two half lines found by estimating 2 AoDs [56].

These examples illustrate how RISs not only reduce the number of BSs required for localization but also expand the feasibility of localization to scenarios previously considered impractical.

3.2.2 Channel Model

The uplink channel for the scenario depicted in Fig. 3.2 can be expressed as follows

$$\mathbf{h}_k[t] = \sum_{l=0}^{L-1} \alpha_l \boldsymbol{a}(\theta_l) e^{-j2\pi\Delta_f k\tau_l} + \alpha_{\text{RIS}} \mathbf{a}(\theta_{\text{RIS}}) \boldsymbol{a}_{\text{RIS}}^{\mathsf{T}}(\phi) \boldsymbol{\Omega}[t] \boldsymbol{a}_{\text{RIS}}(\psi) e^{-j2\pi\Delta_f k\tau_{\text{RIS}}}, \tag{3.2}$$

which generalizes the single BS cellular channel given in 3.1 by adding a RIS path. The RIS path consists of two segments: UE-to-RIS transmission and RIS-to-BS transmission. Here, θ_{RIS} represents the AoA in the RIS-BS path, ϕ denotes the RIS-BS AoD, ψ is RIS-UE AoA, τ_{RIS} shows ToA which captures the combined effect of the UE-RIS and RIS-BS distances as well as the clock bias and α_{RIS} represents the combined UE-RIS-BS channel gain. The RIS array steering vector for the m^{th} element is $[\boldsymbol{a}(\boldsymbol{\theta}(t))]_m = e^{j(2\pi/\lambda)\boldsymbol{v}^{\mathsf{T}}\boldsymbol{q}_m}$, $(m = 1, \cdots, M)$ where $\boldsymbol{q}_m$ is the known position of the m^{th} element. In this model, the parameters θ_{RIS} and ϕ are known, since the BS and RIS locations are predetermined. The UE's location information is encoded in ψ and τ_{RIS}. The RIS configurations $\boldsymbol{\Omega}[t]$ must be time-varying to enable estimation of AoA and to mitigate interference from uncontrolled multipath components.

3.2.3 Synchronization and Coverage Consideration

Synchronization is essential for maintaining the integrity of time-based localization techniques. Accurate synchronization between the BS, RIS, and UE is required to minimize timing errors that could otherwise degrade localization accuracy. This is particularly challenging in dynamic environments where clock drifts or delays might occur. Advanced signal processing techniques, such as joint estimation of timing offsets and localization parameters, are often employed to address these challenges [56], [57].

As discribed previously, RISs expand the coverage by introducing synthesized and controllable paths, therefore in case of limited LoS connectivity, such as urban canyons or indoor environments or weak signal reception due to multipath environment, deploying RISs can boost the coverage area accordingly. This allows localization systems to extend their coverage to areas previously inaccessible with traditional infrastructure. As an example, in configurations

without access to BSs, RISs can enable localization through techniques such as RTT and angle-based measurements. By utilizing a single RIS and the UE's ability to process reflected signals, sufficient data can be collected for self-localization [58]. This makes RISs particularly valuable in remote or challenging environments where deploying traditional BSs is impractical.

In paper B, we will explore the minimal infrastructure, both in terms of hardware and spectral resources, to enable RIS-aided localization and UE synchronization.

3.3 Non-Terrestrial Networks in Localization

NTN is an umbrella term referring to communication systems that rely on airborne and spaceborne platforms to provide connectivity in areas where terrestrial infrastructure is limited or unavailable [24]. Airborne platforms include high altitude platform stations (HAPSs) and unmanned aerial vehicles (UAVs) while spaceborne platforms in NTN include geostationary Earth orbit (GEO), medium Earth orbit (MEO), and LEO satellites. HAPSs are stratospheric platforms that operate at altitudes of 18 to 50 km, they provide localized coverage and are particularly useful for disaster recovery and rural connectivity. UAVs are flexible and mobile, and can act as temporary network nodes or relays, supporting localized or on-demand communication needs. GEO satellites are located approximately at altitude of 36,000 km above the Earth and provide continuous coverage to fixed regions, making them ideal for broadcasting and long-distance communication. MEO satellites orbit at altitudes between 8,000 km and 20,000 km and provide balance between coverage and latency. LEO satellites operate at altitudes of 500 to 2,000 km, and they offer low-latency and high-bandwidth services, compared to GEO and MEO satellites, and frequently deployed in mega constellations to ensure global coverage [59], [60]. Comparing to MEO and GEO, LEO satellites offer much stronger signals with lower construction and launching costs as well [61]. Therefore, the focus of the remainder of this section will be on LEO satellites.

3.3.1 Topology and Configuration

A number of studies have examined how localization can be effectively achieved in NTNs [62]. For instance, In [63], an integrated LEO-GPS positioning method is proposed which uses LEO to help GPS navigation using Doppler measurements and they concluded that leveraging LEO positioning can extend localization coverage when less than 4 GPS satellites are in view. In [64], the presented framework utilizes carrier Doppler shift measurements to estimate 3D position, 3D velocity, receiver clock offset and clock offset rate. However for this technique to work, at least 8 measured Doppler shift are required which means that at least 8 LEO satellite need to be simultaneously visible. In [65] an NTN-based localization method emphasizing signal interference modeling and mitigation strategies have been studied. The scenario requires at least four satellites in view for accurate 3D positioning using positioning reference signal (PRS). In [66], a multi-LEO localization method is investigated that relies on ToA measurements and at least 4 LEO satellites to achieve accurate 3D localization precision.

In [61], integration of LEO satellites and cellular networks are considered which is believed to enhance localization and communication performance in 5G and beyond. Through this integration, global coverage with high chance of availability, low latency, high reliability, and affordable cost can be ensured, while challenges such as handover management due to high mobility still need to be addressed.

3.3.2 Channel Model

In Fig. 3.3 an integrated LEO and cellular-based localization scenario together with a moving UE is depicted as an example. The BS and the satellite are synchronized while an unknown CFO between the BS and the UE is considered. The downlink wideband channel can be modeled as below

$$h_k[t] = \sum_{l=0}^{L-1} \alpha_l \mathbf{a}^\top(\theta_l)\mathbf{f}(t)e^{-j2\pi\Delta_f k\tau_l} + \alpha_{\mathrm{s}} e^{-j2\pi\Delta_f k\tau_{\mathrm{s}}} e^{j2\pi\gamma_{\mathrm{s}}t} \tag{3.3}$$

where γ_{s} captures the Doppler of the satellite and the CFO, τ_{s} denotes the time delay, α_{s} is the satellite-UE channel gain and $\mathbf{f}(t)$ is the BS time-varying precoder, which enables the UE to estimate the BS LoS AoD, θ_0. UE's location information is encoded in θ_0, τ_0, τ_{s} and marginally in γ_{s}, and γ_{s} contains UE's

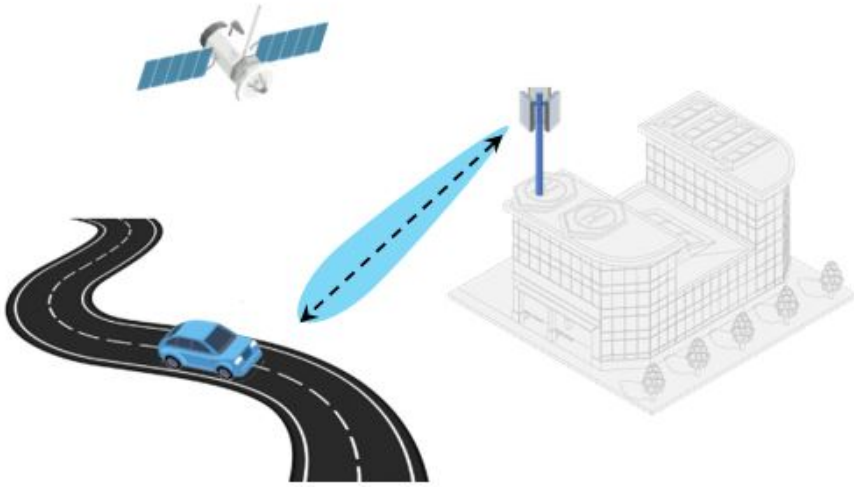

Figure 3.3: An NTN-aided network performing localization

velocity information.

3.3.3 Synchronization and Coverage Consideration

One of the key advantages of NTNs, or in particular, LEO satellites, is their ability to deliver robust global coverage, ensuring reliable connectivity even in remote and challenging environments [67]. This makes them particularly suitable for real-time applications such as video streaming and the IoT [68]. However, the high mobility of LEO satellites introduces frequent handovers, causing a significant challenge for seamless communication. This challenge can be mitigated by employing mega-constellations with inter-satellite links, which enable continuous communication and efficient data routing even as satellites move out of a region [69].

Synchronization in LEO satellite systems presents unique challenges due to significantly larger propagation delays and high Doppler shifts compared to terrestrial networks. A typical LEO satellite at an altitude of 600 km experiences a one-way propagation delay of approximately 2 ms, which is orders of magnitude greater than the 30μs delay in terrestrial networks where the dis-

tance between the UE and the BS is up to 10 km in rural areas. Additionally, LEO satellites exhibit high relative velocities of up to 8 km/s, resulting in significant Doppler shifts. These shifts can vary rapidly and can reach values much higher than those in terrestrial systems, which can further complicates synchronization [70].

These characteristics of LEO systems create critical challenges to synchronization. The high propagation delay complicates uplink and downlink time synchronization, while the substantial Doppler shifts cause severe inter-carrier interference (ICI) in widely used orthogonal frequency division multiplexing (OFDM)-based transmissions, which are highly sensitive to timing and frequency errors. As a result, insufficient time and frequency synchronization can degrade spectral efficiency and disrupt system performance [70].

To address these challenges, advanced solutions are employed. For time synchronization, techniques like TA compensate for the propagation delay by using the satellite's trajectory and position relative to the user [70], [71]. For Doppler shift mitigation, pre-compensation methods leverage known satellite and Earth velocities to remove a significant portion of the shift, leaving a smaller residual offset to be corrected at the receiver.

In Paper C, we investigate an integrated NTN-cellular localization and synchronization setup to position a moving UE, considering the lack of synchronization between the UE and the network. The system accounts for large propagation delays and significant Doppler shifts, incorporating these factors into the model to enable accurate localization and synchronization.

CHAPTER 4

Summary of the Appended Papers, and Contributions

This section outlines the three appended papers, each introduced with a research question. The summary of each paper is presented as a response to its respective question, along with a description of the contributions made by the various authors.

4.1 Paper A

Ettefagh, Y., Aghdam, S. R., Durisi, G., Jacobsson, S., Coldrey, M., & Studer, C. (2023). Performance of Quantized Massive MIMO With Fronthaul Rate Constraint Over Quasi-Static Channels. IEEE Access, 11, 56935-56950.

Research question 1: Which architecture, in terms of the number of antennas and the resolution of data converters, is most suitable in a fully digital massive MIMO scenario, given a limited fronthaul link capacity?

In paper A, we investigate the performance of a fully digital massive MIMO system equipped with low-resolution data converters and operating under a constrained fronthaul rate in quasi-static channels. Unlike traditional approaches focusing on the ergodic scenario, this study develops a novel, rigorous framework for analyzing error probabilities in uplink and downlink communications under finite-blocklength conditions. By considering imperfect channel state information and incorporating the effects of pilot transmission and hardware limitations, the paper characterizes the trade-off between the number of BS antennas and the resolution of data converters. Extensive numerical results highlight optimal configurations under varying power levels and CSI accuracy, providing valuable insights for designing efficient massive MIMO architectures that balance spectral efficiency and hardware complexity.

Contributions: Giuseppe Durisi (GD) proposed the problem and the methodology. Yasaman Ettefagh (YE) derived the system model. Sven Jacobsson (SJ) contributed to the system model. YE derived the theoretical limits in Sec. IV.D, conducted the simulations, performed the analysis, and wrote the paper. GD derived the theoretical bounds in Sec. III.C, contributed to the derivation of theoretical limits in Sec. IV.D, supported the analysis, and revised the paper. Sina Rezaei Aghdam (SR) assisted with the simulations and analysis. SR, SJ, Mikael Coldrey (MC), and Christoph Studer (CS) reviewed the paper and provided feedback.

4.2 Paper B

Ettefagh, Y., Keskin, M. F., Keykhosravi, K., Seco-Granados, G., & Wymeersch, H. Frugal RIS-aided 3D Localization with CFO under LoS and NLoS Conditions. Under Revision, IEEE Transactions on Vehicular Technology.

Research Question: Considering a frugal scenario with limited bandwidth and single-antenna transmitter and receiver, how can RISs support user localization?

In paper B we explore a frugal approach to 3D localization and frequency synchronization for stationary UE using RISs in a narrowband (SISO) scenario. We address challenges such as LoS blockage and unknown CFO by

proposing efficient algorithms for LoS detection, channel parameter estimation, and localization under both LoS and non-LoS conditions. Our study develops low-complexity estimators and evaluates their performance against theoretical bounds, demonstrating robustness even under multi-path interference and CFO uncertainty. By utilizing minimal spectrum and antenna resources, the study demonstrates the feasibility of achieving high-accuracy positioning in a cost-effective and energy-efficient manner, aligning with the sustainability objectives of 6G.

Contributions: Henk Wymeersch (HW), Gonzalo Seco-Granados (GS), and Furkan Keskin (FK) proposed the problem. YE conducted the literature study, derived the mathematical models, derived the estimators, implemented them, analyzed the results, and authored the paper. HW, GS, FK, and Kamran Keykhosravi (KK) supported in the design of the estimators through discussions. All authors provided feedback to the paper.

4.3 Paper C

Ettefagh, Y., Saleh, S., Keskin, M. F., Chen, H., Seco-Granados, G., & Wymeersch, H. Integrated Cellular and LEO-based Positioning and Synchronization under User Mobility. In Preparation, IEEE Transactions on Vehicular Technology.

Research Question: How can the integration of a terrestrial base station and a LEO satellite support positioning of a mobile UE in the presence of reasonable synchronization and Doppler effects?

In paper C, we examine the integration of terrestrial cellular networks with NTNs, such as LEO satellites, to enhance the localization, velocity estimation, and synchronization of a mobile UE. It presents a comprehensive system model along with a hierarchy of simplified models, each tailored to different levels of computational complexity. The study develops estimation algorithms for these models to enable efficient and accurate parameter estimation, with simulations validating their performance across a range of scenarios. The results underscore the potential of integrated terrestrial and NTN systems

to optimize the trade-off between computational complexity and positioning accuracy, offering significant advancements for 6G localization and synchronization technologies.

Contributions: YE proposed the research question and applied for Vinnova funding to support this work toward her PhD. HW supported in writing the funding application and focusing of the problem scope. YE derived all signal models and estimators, implemented the generative model and applied the estimators, performed all simulations and analysis, and wrote the paper. Sharief Saleh (SS) supported in the design of the estimators. FK contributed to the analysis. Hui Chen (HC) supported with the performance metric and the evaluation methodology. Gonzalo Seco-Granados (GS) supported with the analysis. All the authors reviewed the paper and provided feedback.

References

[1] Ericsson, "Ericsson mobility report," Nov. 2024.

[2] J. A. del Peral-Rosado, R. Raulefs, J. A. López-Salcedo, and G. Seco-Granados, "Survey of cellular mobile radio localization methods: From 1G to 5G," *IEEE Communications Surveys & Tutorials*, vol. 20, no. 2, pp. 1124–1148, 2017.

[3] Allied Market Research, *Autonomous vehicle market by level of autonomy, component, application, and region: Global opportunity analysis and industry forecast, 2021–2030*, Online; accessed 8 January 2025, Forecast data: Market valued at $76.13 billion in 2020, projected to reach $2,161.79 billion by 2030., 2022.

[4] T. G. Reid, S. E. Houts, R. Cammarata, *et al.*, "Localization requirements for autonomous vehicles," *SAE International Journal of Connected and Automated Vehicles*, vol. 2, no. 12-02-03-0012, pp. 173–190, 2019.

[5] H. Q. Ngo, E. G. Larsson, and T. L. Marzetta, "Energy and spectral efficiency of very large multiuser MIMO systems," *IEEE Transactions on Communications*, vol. 61, no. 4, pp. 1436–1449, 2013.

[6] N. Garcia, H. Wymeersch, E. G. Larsson, A. M. Haimovich, and M. Coulon, "Direct localization for massive MIMO," *IEEE Transactions on Signal Processing*, vol. 65, no. 10, pp. 2475–2487, 2017.

[7] S. Jacobsson, G. Durisi, M. Coldrey, T. Goldstein, and C. Studer, "Quantized precoding for massive MU-MIMO," *IEEE Trans. Commun.*, vol. 65, no. 11, pp. 4670–4684, Nov. 2017.

[8] S. Jacobsson, G. Durisi, M. Coldrey, U. Gustavsson, and C. Studer, "Throughput analysis of massive MIMO uplink with low-resolution ADCs," *IEEE Trans. Wireless Commun.*, vol. 16, no. 6, pp. 4038–4051, Jun. 2017.

[9] C. Mollén, J. Choi, E. G. Larsson, and R. W. Heath, "Achievable uplink rates for massive MIMO with coarse quantization," in *2017 IEEE International Conference on Acoustics, Speech and Signal Processing (ICASSP)*, IEEE, 2017, pp. 6488–6492.

[10] K. Roth, H. Pirzadeh, A. L. Swindlehurst, and J. A. Nossek, "A comparison of hybrid beamforming and digital beamforming with low-resolution adcs for multiple users and imperfect CSI," *IEEE Journal of Selected Topics in Signal Processing*, vol. 12, no. 3, pp. 484–498, 2018.

[11] J. J. Spilker Jr, P. Axelrad, B. W. Parkinson, and P. Enge, *Global positioning system: theory and applications, volume I.* American Institute of Aeronautics and Astronautics, 1996.

[12] T. E. Humphreys, "Detection strategy for cryptographic gnss anti-spoofing," *IEEE Transactions on Aerospace and Electronic Systems*, vol. 49, no. 2, pp. 1073–1090, 2013.

[13] M. A. Spirito, S. Poykko, and O. Knuuttila, "Experimental performance of methods to estimate the location of legacy handsets in GSM," in *IEEE 54th Vehicular Technology Conference. VTC Fall 2001. Proceedings (Cat. No. 01CH37211)*, IEEE, vol. 4, 2001, pp. 2716–2720.

[14] L. Italiano, B. C. Tedeschini, M. Brambilla, H. Huang, M. Nicoli, and H. Wymeersch, "A tutorial on 5G positioning," *arXiv preprint arXiv:2311.10551*, 2023.

[15] F. Wen, H. Wymeersch, B. Peng, W. P. Tay, H. C. So, and D. Yang, "A survey on 5G massive MIMO localization," *Digital Signal Processing*, vol. 94, pp. 21–28, 2019.

[16] A. Shahmansoori, G. E. Garcia, G. Destino, G. Seco-Granados, and H. Wymeersch, "Position and orientation estimation through millimeter-wave MIMO in 5G systems," *IEEE Transactions on Wireless Communications*, vol. 17, no. 3, pp. 1822–1835, 2017.

[17] H. Wymeersch, J. He, B. Denis, A. Clemente, and M. Juntti, "Radio localization and mapping with reconfigurable intelligent surfaces: Challenges, opportunities, and research directions," *IEEE Vehicular Technology Magazine*, vol. 15, no. 4, pp. 52–61, 2020.

[18] A. Behravan, V. Yajnanarayana, M. F. Keskin, *et al.*, "Positioning and sensing in 6G: Gaps, challenges, and opportunities," *IEEE Vehicular Technology Magazine*, vol. 18, no. 1, pp. 40–48, 2022.

[19] D.-R. Emenonye, H. S. Dhillon, and R. M. Buehrer, "Fundamentals of RIS-aided localization in the far-field," *IEEE Transactions on Wireless Communications*, 2023.

[20] J. He, F. Jiang, K. Keykhosravi, J. Kokkoniemi, H. Wymeersch, and M. Juntti, "Beyond 5G RIS mmwave systems: Where communication and localization meet," *IEEE Access*, vol. 10, pp. 68 075–68 084, 2022.

[21] A. Gonzalez-Garrido, J. Querol, and S. Chatzinotas, "5G positioning reference signal configuration for integrated terrestrial/non-terrestrial network scenario," in *2023 IEEE/ION Position, Location and Navigation Symposium (PLANS)*, IEEE, 2023, pp. 1136–1142.

[22] J. Ma, P. Zheng, X. Liu, Y. Zhang, and T. Y. Al-Naffouri, "Integrated positioning and communication via LEO satellites: Opportunities and challenges," *arXiv preprint arXiv:2411.14360*, 2024.

[23] C. Huang, A. Zappone, G. C. Alexandropoulos, M. Debbah, and C. Yuen, "Reconfigurable intelligent surfaces for energy efficiency in wireless communication," *IEEE transactions on wireless communications*, vol. 18, no. 8, pp. 4157–4170, 2019.

[24] X. Lin, S. Rommer, S. Euler, E. A. Yavuz, and R. S. Karlsson, "5G from space: An overview of 3GPP non-terrestrial networks," *IEEE Communications Standards Magazine*, vol. 5, no. 4, pp. 147–153, 2021.

[25] S. Saleh, P. Zheng, X. Liu, *et al.*, "Integrated 6g tn and ntn localization: Challenges, opportunities, and advancements," *arXiv preprint arXiv:2501.13488*, 2025.

[26] R. H. Walden, "Analog-to-digital converter survey and analysis," *IEEE J. Sel. Areas Commun.*, vol. 17, no. 4, pp. 539–550, 1999.

[27] J. J. Bussgang, "Crosscorrelation functions of amplitude-distorted Gaussian signals," Res. Lab. Elec., Cambridge, MA, Tech. Rep. 216, Mar. 1952.

[28] S. Jacobsson, Y. Ettefagh, G. Durisi, and C. Studer, "All-digital massive MIMO with a fronthaul constraint," in *Proc. IEEE Statistical Sig. Pro. Workshop*, Freiburg , Germany, Jun. 2018.

[29] S. Jacobsson, G. Durisi, M. Coldrey, and C. Studer, "Linear precoding with low-resolution DACs for massive MU-MIMO-OFDM downlink," *IEEE Trans. Wireless Commun.*, vol. 18, no. 3, pp. 1595–1609, Mar. 2019.

[30] A. Mezghani and J. A. Nossek, "Capacity lower bound of MIMO channels with output quantization and correlated noise," in *Proc. IEEE Int. Symp. Inf. Theory*, 2012, pp. 1–5.

[31] M. D. McDonnell, N. G. Stocks, C. E. M. Pearce, and D. Abbo, "Stochastic resonance - from suprathreshold stochastic resonance to stochastic signal quantization," in *Stochastic Resonance - From Suprathreshold Stochastic Resonance to Stochastic Signal Quantization*. Cambridge University Press, 2008.

[32] J. Mo, P. Schniter, N. G. Prelcic, and R. W. Heath, "Channel estimation in millimeter wave MIMO systems with one-bit quantization," in *Proc. Asilomar Conf. Signals, Syst., Comput.,*, Pacific Grove, CA, USA, Apr. 2014, pp. 957–961.

[33] O. Dabeer and U. Madhow, "Channel estimation with low-precision analog-to-digital conversion," in *Proc. IEEE Int. Conf. Commun. (ICC)*, 2010, pp. 1–6.

[34] J. Mo and R. W. Heath, "High SNR capacity of millimeter wave MIMO systems with one-bit quantization," in *2014 Information Theory and Applications Workshop (ITA)*, IEEE, 2014, pp. 1–5.

[35] O. El Ayach, S. Rajagopal, S. Abu-Surra, Z. Pi, and R. W. Heath, "Spatially sparse precoding in millimeter wave MIMO systems," *IEEE Trans. Wireless Commun.*, vol. 13, no. 3, pp. 1499–1513, Mar. 2014.

[36] A. Alkhateeb, O. El Ayach, G. Leus, and R. W. Heath, "Channel estimation and hybrid precoding for millimeter wave cellular systems," *IEEE J. Select. Areas Commun.*, vol. 8, no. 5, pp. 831–846, Jul. 2014.

[37] R. W. Heath, N. Gonzalez-Prelcic, S. Rangan, W. Roh, and A. M. Sayeed, "An overview of signal processing techniques for millimeter wave MIMO systems," *IEEE J. Select. Areas Commun.*, vol. 10, no. 3, pp. 436–453, Feb. 2016.

[38] T. L. Marzetta, "Noncooperative cellular wireless with unlimited numbers of base station antennas," *IEEE Trans. Wireless Commun.*, vol. 9, no. 11, pp. 3590–3600, 2010.

[39] F. Rusek, D. Persson, B. K. Lau, *et al.*, "Scaling up MIMO: Opportunities and challenges with very large arrays," *IEEE Signal Process. Mag.*, vol. 30, no. 1, pp. 40–60, 2012.

[40] A. Lapidoth and S. Shamai (Shitz), "Fading channels: How perfect need 'perfect side information' be?" *IEEE Trans. Inf. Theory*, vol. 48, no. 5, pp. 1118–1134, May 2002.

[41] E. Bjornson, L. Sanguinetti, and J. Hoydis, "Can hardware distortion correlation be neglected when analyzing uplink se in massive MIMO?" In *2018 IEEE 19th International Workshop on Signal Processing Advances in Wireless Communications (SPAWC)*, IEEE, 2018, pp. 1–5.

[42] E. Björnson, L. Sanguinetti, and J. Hoydis, "Hardware distortion correlation has negligible impact on UL massive MIMO spectral efficiency," *IEEE Trans. Commun.*, vol. 67, no. 2, pp. 1085–1098, Feb. 2019, ISSN: 0090-6778, 1558-0857.

[43] I. K. Adusei, K. Kyamakya, and K. Jobmann, "Mobile positioning technologies in cellular networks: An evaluation of their performance metrics," in *MILCOM 2002. Proceedings*, IEEE, vol. 2, 2002, pp. 1239–1244.

[44] R. M. Buehrer, H. Wymeersch, and R. M. Vaghefi, "Collaborative sensor network localization: Algorithms and practical issues," *Proceedings of the IEEE*, vol. 106, no. 6, pp. 1089–1114, 2018.

[45] W. Wang, G. Wang, F. Zhang, and Y. Li, "Second-order cone relaxation for TDOA-based localization under mixed LOS/NLOS conditions," *IEEE Signal Processing Letters*, vol. 23, no. 12, pp. 1872–1876, 2016.

[46] N. Xia and M. A. Weitnauer, "TDOA-based mobile localization using particle filter with multiple motion and channel models," *IEEE Access*, vol. 7, pp. 21 057–21 066, 2019.

[47] Y. Zou, H. Liu, W. Xie, and Q. Wan, "Semidefinite programming methods for alleviating sensor position error in TDOA localization," *IEEE Access*, vol. 5, pp. 23 111–23 120, 2017.

[48] S. Wang, X. Jiang, and H. Wymeersch, "Cooperative localization in wireless sensor networks with AOA measurements," *IEEE Transactions on Wireless Communications*, vol. 21, no. 8, pp. 6760–6773, 2022.

[49] C. L. F. Mayorga, F. Della Rosa, S. A. Wardana, *et al.*, "Cooperative positioning techniques for mobile localization in 4G cellular networks," in *IEEE international conference on pervasive services*, IEEE, 2007, pp. 39–44.

[50] Y. Liu, X. Shi, S. He, and Z. Shi, "Prospective positioning architecture and technologies in 5G networks," *IEEE Network*, vol. 31, no. 6, pp. 115–121, 2017.

[51] S. Fan, W. Ni, H. Tian, Z. Huang, and R. Zeng, "Carrier phase-based synchronization and high-accuracy positioning in 5G new radio cellular networks," *IEEE Transactions on Communications*, vol. 70, no. 1, pp. 564–577, 2021.

[52] C. Pan, H. Ren, K. Wang, *et al.*, "Reconfigurable intelligent surfaces for 6G systems: Principles, applications, and research directions," *IEEE Communications Magazine*, vol. 59, no. 6, pp. 14–20, 2021.

[53] Y. Liu, X. Liu, X. Mu, *et al.*, "Reconfigurable intelligent surfaces: Principles and opportunities," *IEEE communications surveys & tutorials*, vol. 23, no. 3, pp. 1546–1577, 2021.

[54] K. Keykhosravi, B. Denis, G. C. Alexandropoulos, *et al.*, "Leveraging RIS-enabled smart signal propagation for solving infeasible localization problems: Scenarios, key research directions, and open challenges," *IEEE Vehicular Technology Magazine*, vol. 18, no. 2, pp. 20–28, 2023.

[55] K. Keykhosravi, M. F. Keskin, G. Seco-Granados, P. Popovski, and H. Wymeersch, "RIS-enabled SISO localization under user mobility and spatial-wideband effects," *IEEE Journal of Selected Topics in Signal Processing*, vol. 16, no. 5, pp. 1125–1140, 2022.

[56] A. Fascista, M. F. Keskin, A. Coluccia, H. Wymeersch, and G. Seco-Granados, "RIS-aided joint localization and synchronization with a single-antenna receiver: Beamforming design and low-complexity estimation," *IEEE Journal of Selected Topics in Signal Processing*, vol. 16, no. 5, pp. 1141–1156, 2022.

[57] A. Fascista, A. Coluccia, H. Wymeersch, and G. Seco-Granados, "RIS-aided joint localization and synchronization with a single-antenna mmwave receiver," in *ICASSP 2021-2021 IEEE International Conference on Acoustics, Speech and Signal Processing (ICASSP)*, IEEE, 2021, pp. 4455–4459.

[58] K. Keykhosravi, G. Seco-Granados, G. C. Alexandropoulos, and H. Wymeersch, "RIS-enabled self-localization: Leveraging controllable reflections with zero access points," in *ICC 2022-IEEE International Conference on Communications*, IEEE, 2022, pp. 2852–2857.

[59] Q. Ye, C. Lo, J. Jeon, *et al.*, "5G new radio and non-terrestrial networks: Reaching new heights," in *2022 IEEE International Conference on Communications Workshops (ICC Workshops)*, IEEE, 2022, pp. 538–543.

[60] F. Rinaldi, H.-L. Maattanen, J. Torsner, *et al.*, "Non-terrestrial networks in 5G & beyond: A survey," *IEEE access*, vol. 8, pp. 165 178–165 200, 2020.

[61] S. Liu, Z. Gao, Y. Wu, *et al.*, "LEO satellite constellations for 5G and beyond: How will they reshape vertical domains?" *IEEE Communications Magazine*, vol. 59, no. 7, pp. 30–36, 2021.

[62] F. S. Prol, R. M. Ferre, Z. Saleem, *et al.*, "Position, navigation, and timing (PNT) through low earth orbit (LEO) satellites: A survey on current status, challenges, and opportunities," *IEEE Access*, vol. 10, pp. 83 971–84 002, 2022.

[63] W.-H. Hsu and S.-S. Jan, "Assessment of using doppler shift of LEO satellites to aid GPS positioning," in *2014 IEEE/ION Position, Location and Navigation Symposium-PLANS 2014*, IEEE, 2014, pp. 1155–1161.

[64] M. L. Psiaki, "Navigation using carrier doppler shift from a LEO constellation: Transit on steroids," *Navigation*, vol. 68, no. 3, pp. 621–641, 2021.

[65] A. Gonzalez-Garrido, J. Querol, H. Wymeersch, and S. Chatzinotas, "Interference analysis and modeling of positioning reference signals in 5G ntn," *IEEE Open Journal of the Communications Society*, 2024.

[66] A. M. Graff and T. E. Humphreys, "OFDM-based positioning with unknown data payloads: Bounds and applications to LEO PNT," *arXiv preprint arXiv:2407.19106*, 2024.

[67] S. Xia, Q. Jiang, C. Zou, and G. Li, "Beam coverage comparison of LEO satellite systems based on user diversification," *IEEE access*, vol. 7, pp. 181 656–181 667, 2019.

[68] H. Zhou, L. Liu, and H. Ma, "Coverage and capacity analysis of LEO satellite network supporting internet of things," in *ICC 2019-2019 IEEE International Conference on Communications (ICC)*, IEEE, 2019, pp. 1–6.

[69] H. Xie, Y. Zhan, G. Zeng, and X. Pan, "LEO mega-constellations for 6G global coverage: Challenges and opportunities," *IEEE Access*, vol. 9, pp. 164 223–164 244, 2021.

[70] L. Ma, C. Park, X. Wang, P. Gaal, and A. R. Alvarino, "Uplink time synchronization for non-terrestrial networks," *IEEE Communications Magazine*, vol. 61, no. 7, pp. 114–118, 2023.

[71] W. Liu, X. Hou, J. Wang, L. Chen, and S. Yoshioka, "Uplink time synchronization method and procedure in release-17 nr ntn," in *2022 IEEE 95th Vehicular Technology Conference:(VTC2022-Spring)*, IEEE, 2022, pp. 1–5.

Part II

Papers

PAPER A

Performance of Quantized Massive MIMO with Fronthaul Rate Constraint over Quasi-Static Channels

Y. Ettefagh, S. Rezaei Aghdam, G. Durisi, S. Jacobsson, M. Coldrey, and C. Studer

Published in IEEE Access, June 2023,
vol. 11, pp. 56935–56947
 DOI: 10.1109/ACCESS.2023.3282369

The layout has been revised.

Abstract

We provide a rigorous framework for characterizing and numerically evaluating the error probability achievable in the uplink and downlink of a fully digital quantized multiuser multiple-input multiple-output (MIMO) system. We assume that the system operates over a quasi-static channel that does not change across the finite-length transmitted codewords, and only imperfect channel state information (CSI) is available at the base station (BS) and at the user equipments. The need for the novel framework developed in this paper stems from the fact that, for the quasi-static scenario, commonly used signal-to-interference-and-distortion-ratio expressions that depend on the variance of the channel estimation error are not relatable to any rigorous information-theoretic achievable-rate bound. We use our framework to investigate how the performance of a fully digital massive MIMO system subject to a fronthaul rate constraint, which imposes a limit on the number of samples per second produced by the analog-to-digital and digital-to-analog converters (ADCs and DACs), depends on the number of BS antennas and on the precision of the ADCs and DACs. In particular, we characterize, for a given fronthaul constraint, the trade-off between the number of antennas and the resolution of the data converters, and discuss how this trade-off is influenced by the accuracy of the available CSI. Our framework captures explicitly the cost, in terms of spectral efficiency, of pilot transmission—an overhead that the outage capacity, the classic asymptotic metric used in this scenario, cannot capture. We present extensive numerical results that validate the accuracy of the proposed framework and allow us to characterize, for a given fronthaul constraint, the optimal number of antennas and the optimal resolution of the converters as a function of the transmitted power and of the available CSI.

1 Introduction

Massive multiple-input multiple-output (MIMO) is a key technology enabler of 5G. Indeed, the large number of active antennas available at the base station (BS) in multiuser massive MIMO architectures results in significant spectral and energy efficiency gains compared to traditional, small-scale MIMO architectures. Furthermore, these gains can be achieved by means of low-complexity spatial processing [1].

In this paper, we focus on fully-digital massive MIMO architectures in which the radio-frequency (RF) frontend, which we will refer to as remote radio head (RRH) and which hosts the RF circuitry, mixers, and data converters, is not colocated with the baseband unit (BBU), in which digital signal processing is performed. Separating these two units is convenient for accessibility, maintenance, and reconfigurability purposes. We are specifically interested in the scenario in which the RRH is equipped with a massive antenna array.[1] One challenge in such architectures is that the RRH and BBU need to be connected via a finite-capacity fronthaul link—a limitation that is important to take into account when designing massive MIMO systems, especially the ones operating over the large bandwidths available in the millimeter-wave (mm-wave) part of the spectrum. To understand the scale of this interconnect problem, consider for example a massive MIMO base-station (BS) equipped with 100 active antenna branches, each connected to two 16-bit resolution data converters, one for the real and one for the imaginary part of the base-band signal, operating at 1 GS/s. Such an architecture produces 3.2 Tb/s of raw baseband data, which is difficult to transfer using current fronthaul standards. One possible, low-complexity approach to circumvent this issue is to reduce the resolution of the data converters. We are then left with the following natural question. How should one choose the sampling rate, the number of antennas, and the resolution of the data converters, given a constraint on the product of these three quantities, which reflects the fronthaul capacity? In this paper, we will shed light on this question by characterizing the trade-off between the number of antennas and the resolution of the data converters for a fixed sampling rate.

[1] We will not consider the distributed massive MIMO scenario in which the BBU is connected to multiple spatially distributed RRHs [2].

1.1 Prior Art

The problem of designing wireless systems in the presence of a fronthaul constraint has been studied extensively in the context of cloud radio access networks (see, e.g., [3] and references therein). However, the focus of this line of work is on solutions where significant signal-processing capabilities are available at the RRHs, which can then execute sophisticated multiterminal compression techniques. In contrast, the focus of this paper is on low-complexity solutions enabling low-cost RRHs. Specifically, we consider a simpler approach for reducing the required fronthaul rate, which involves lowering the precision of the converters at the RRH.

A large body of literature is concerned with the performance achievable with multiuser massive MIMO systems in which the BS is equipped with low-resolution data converters. Existing works include the derivation of information-theoretic achievable rates in the ergodic scenario with Gaussian codebooks [4]–[10], the design of channel estimation and data-detection algorithms [11]–[16], of linear and nonlinear precoders [7], [17]–[19], and of low-complexity equalization techniques [20]. All of these results reveal that satisfactory performance can be achieved even when using 1-bit converters at the RRHs, and that, by using 3-to-5-bit converters, one can approach closely the performance achievable in the infinite-precision case. Extensions of these works to the case of distributed massive MIMO, with focus on the spectral and energy efficiency achievable in the ergodic setting, have been provided in [21]–[25].

The focus of this paper is on the analysis of the rate achievable in the less studied *quasi-static scenario*, in which, differently from the commonly analyzed ergodic setting, the channel remains constant for the duration of each transmitted codeword. This scenario is relevant in propagation conditions with limited time and frequency diversity. It is also relevant when short codewords are transmitted, which occurs in control channels, during the initial-access phase, and in machine-type communications involving stringent latency requirements and limited bandwidth.

For the case in which low-precision data converters are used at the BS, it is crucial to assume that the BS has at its disposal only imperfect channel-state information (CSI), typically acquired in massive MIMO systems via uplink pilot transmission. Indeed, the presence of low-precision converters makes acquiring perfect CSI challenging, even when the number of transmitted pilot symbols is large. As illustrated recently in [26] in the context of short-

packet transmissions over infinite-precision massive MIMO links, analyses for the quasi-static case in the presence of imperfect CSI are nontrivial. Indeed, one cannot simply take the ergodic-rate signal-to-interference-and-noise ratio (SINR) expressions reported in, e.g., [27, Thm. 4.1] for the uplink and account for the quasi-static nature of the channel by evaluating the cumulative distribution function of the SINR to determine the outage probability as a function of the transmission rate. This is not correct even in the asymptotic regime of large blocklength, since the resulting expression cannot be related to any rigorous notion of outage probability. Similarly, one cannot insert these ergodic SINR expressions into normal-approximation formulas [28, Eq. 223] to obtain approximations on the rate achievable in the finite-blocklength regime. Unfortunately, both approaches are commonly found in the literature. This highlights the need for a rigorous framework—built from first principles—to analyze the quasi-static scenario.

1.2 Contributions

In this paper, we provide such a rigorous framework, and use it to characterize the uplink and downlink packet error probability achievable in the quasi-static scenario, for the case in which a BS, equipped with a large antenna array and low-precision converters, serves in the same time-frequency resources multiple user equipments (UEs). Our framework leverages three fundamental ingredients: (i) the random-coding union bound with parameter s (RCUs) from finite-blocklength information theory [29] to capture the finite length of the transmission packets; (ii) a scaled nearest-neighbor mismatch decoder [30] to account for the imperfect CSI available at the BS and at the UEs, as well as for the low-complexity, suboptimal processing performed at both transmitters and receivers; (iii) Bussgang's decomposition [31] to deal with the nonlinearity introduced by the low-resolution converters. These ingredients have been used separately in the literature before. However, their combination, which is required to address the key design question formulated in this paper, is novel and nontrivial. We also show how to approximate the obtained error probability bounds with simpler asymptotic expressions that are in terms of the so-called generalized mutual information (GMI).[2] The resulting approximation is shown to be very accurate for packet error probabilities in the range

[2]This quantity was previously used in performance analyses of low-precision massive MIMO architectures in, e.g., [9].

$[10^{-3}, 10^{-1}]$.

We then use the packet error-probability bounds developed in the paper to obtain engineering insights into the optimal design of multiuser massive MIMO systems with low-precision converters, operating under a fronthaul constraint. Specifically, focusing on a realistic clustered channel model, and considering the quantization-aware channel-estimation algorithm proposed in [12], we determine, for a given fronthaul constraint, the optimal number of antennas and the resolution of the quantizers that maximize the rate at which uplink and downlink communications can be sustained with a packet error probability not exceeding 10%. For the parameters considered in our numerical simulations, which pertain a scenario with 8 users and a fronthaul constraint of 512 bit/s/Hz, our analysis reveals that the highest performing BS architecture involves a large antenna array (from 64 to 256 antenna elements, depending on the SNR) connected to low-precision data converters (from 1 to 4 bits, depending on the SNR). A solution involving 1-bit data converters and 256 antennas turns out to be optimal from a bi-directional communication perspective for low transmitted-power levels, whereas for high transmitted-power levels, a solution involving 4-bit data converters and 64 antennas is preferable. Increasing the precision of the converters beyond these values, at the cost of a reduction in the number of antennas, turns out to be deleterious, once the impact of imperfect CSI is accounted for. Interestingly, these conclusions are different from the ones derived by performing a perfect-CSI analysis. Indeed, in the perfect-CSI case, the use of architectures involving higher-precision quantizers and fewer antennas is preferable.

1.3 Paper Outline

In Section 2, we introduce the system model, the fronthaul constraint, and the linear spatial processing that will be considered in the rest of the paper. In Section 3, we present our nonasymptotic framework for the characterization of the packet error probability, as well as asymptotic limits and approximations that will be useful to obtain system-design guidelines. In Section 4, we describe our numerical-simulation setup and conduct experiments to determine (i) the impact of a fronthaul constraint on the channel-estimation accuracy obtainable via pilot transmission, (ii) the optimal number of pilot symbols, and (iii) the effect on performance of nonsubtractive dithering in the 1-bit quantization case. We then shed light on the fronthaul-induced trade-off be-

tween number of antennas at the BS and resolution of the quantizers. Some concluding remarks are provided in Section 5.

1.4 Notation

Lower-case bold letters are used for vectors and upper-case bold letters for matrices. We denote by $\mathcal{CN}(\mathbf{0}_N, \boldsymbol{R})$, where $\mathbf{0}_N$ stands for the all-zero vector of size N, the distribution of an N-dimensional circularly-symmetric complex-valued Gaussian vector with zero mean and $N \times N$ covariance matrix $\boldsymbol{R}$. We use $\mathbf{I}_N$ to denote the $N \times N$ identity matrix, and $\mathbb{E}[\cdot]$, $\mathbb{V}[\cdot]$, $\mathbb{P}[\cdot]$ to denote the expectation, variance, and probability operators, respectively. The natural logarithm is denoted by $\log(\cdot)$, the Gaussian Q-function by $Q_G(\cdot)$, the indicator function by $\mathbb{1}\{\cdot\}$, and the floor function by $\lfloor \cdot \rfloor$. Finally, the notation $f(n) = \mathcal{O}(g(n))$, $n \to \infty$ means that $\limsup_{n\to\infty} \left| f(n)/g(n) \right| < \infty$.

2 System Model

We consider a single-cell massive multiuser MIMO scenario, in which a BS equipped with B antennas, serves $U \ll B$ single-antenna UEs in the same time-frequency resources. As depicted in Fig. 1, the BS consists of a RRH and a BBU that are connected via a rate-constrained fronthaul interface. Each antenna is equipped with a pair of Q-bit data converters, one for the in-phase and one for the quadrature component. We consider a time division duplexing (TDD) scenario. In the uplink, the data-transmission phase is preceded by a pilot-transmission phase, which allows the BS to acquire (imperfect) CSI. The signal transmitted by the U UEs is quantized at the B BS antennas using the low-precision data converters. The quantized signal is then transferred to the BBU via the fronthaul link, where channel estimation, linear combining, and decoding are performed. In the downlink, the linearly precoded signal is quantized at the BBU and transferred over the fronthaul link, where it is converted into the analog domain and transmitted over the B antennas. It follows that an architecture with B active antennas and Q-bit converters, operating at the Nyquist sampling rate, requires a fronthaul interface able to support a rate of $2BQ$ bit/s/Hz.

We assume uniform, symmetric, mid-rise quantizers with step size Δ and Q-bit resolution. Specifically, let $r \in \Re$ be the input of the quantizer. Then,

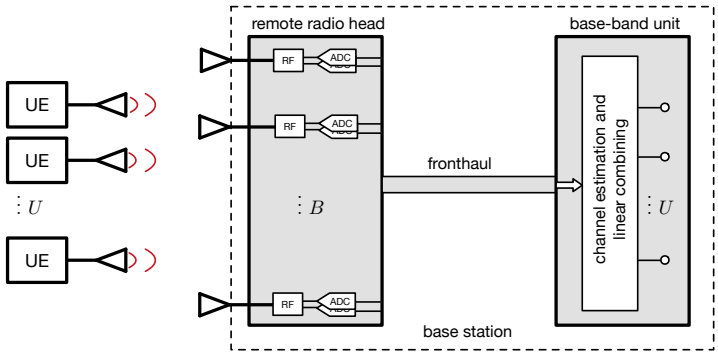

(a) Uplink

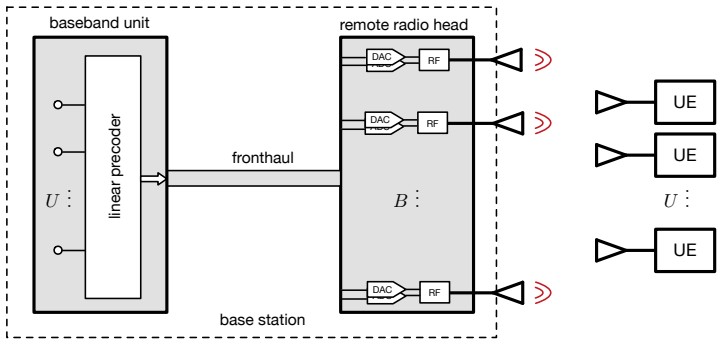

(b) Downlink

Figure 1: Overview of the fully digital BS architecture considered in the paper. A B-antenna BS serves U users over the same time-frequency resources. Each antenna is connected to a pair of quantizers with Q-bit resolution. The BS consists of a BBU and an RRH that are connected via a rate-constrained fronthaul interface.

the output $\mathcal{Q}(r)$ is given by

$$\mathcal{Q}(r) = \begin{cases} \frac{\Delta}{2}(1-L), & \text{if } r < -\frac{\Delta}{2}L \\ \Delta\left\lfloor \frac{r}{\Delta} \right\rfloor + \frac{\Delta}{2}, & \text{if } -\frac{\Delta}{2}L \leq r < \frac{\Delta}{2}L \\ \frac{\Delta}{2}(L-1), & \text{if } r \geq \frac{\Delta}{2}L. \end{cases} \tag{A.1}$$

Here, $L = 2^Q$ denotes the number of quantization levels. For a complex-valued input z, we let $\mathcal{Q}(z) = \mathcal{Q}(\Re\{z\}) + j\mathcal{Q}(\Im\{z\})$. For a vector $\mathbf{z}$, we denote by $\mathcal{Q}(\mathbf{z})$ the result of applying $\mathcal{Q}(\cdot)$ entry-wise to its elements.

2.1 Uplink Transmission

We consider a TDD transmission protocol in which an uplink frame consisting of n_{ul} channel uses is followed by a downlink frame of n_{dl} channel uses. The fading process is assumed to stay constant over the duration of the $n_{\text{ul}} + n_{\text{dl}}$ channel uses. Furthermore, we assume that reciprocity holds, so that the channel estimated in the uplink can be used by the BS in downlink transmission.

In the uplink, we model the B-dimensional discrete-time, complex-valued, base-band signal received at the BS at time instant k as follows:

$$\mathbf{y}^{\text{ul}}[k] = \mathbf{H}\mathbf{s}^{\text{ul}}[k] + \mathbf{n}^{\text{ul}}[k], \quad k = 1, \ldots, n_{\text{ul}}. \tag{A.2}$$

Here, $\mathbf{s}^{\text{ul}}[k] = \left[s_1^{\text{ul}}[k], s_2^{\text{ul}}[k], \ldots, s_U^{\text{ul}}[k]\right]^{\mathsf{T}} \in \mathbb{C}^U$ is the signal transmitted by the U UEs at time instant k, the $B \times U$ matrix $\mathbf{H}$ represents the fading channel, and $\mathbf{n}^{\text{ul}}[k] \sim \mathcal{CN}(\mathbf{0}_B, N_0\mathbf{I}_B)$ denotes the additive white Gaussian noise at the BS, which we assume to be independent across k, and independent also of the transmitted signal and the fading matrix. The first n_p channel uses in the uplink are reserved for the transmission of pilot symbols, used by the BS to estimate $\mathbf{H}$. The remaining $n_d = n_{\text{ul}} - n_p$ channel uses are reserved for data transmission. Note that, so far, we have so far not provided any statistical model for the fading channel $\mathbf{H}$. This is because the information theoretic bounds we shall provide in Section 3 hold for arbitrary quasi-static fading models.

At the receiver, the signal $\mathbf{y}^{\text{ul}}[k]$ is passed through an automatic gain control (AGC) circuit, which scales each of the entries of $\mathbf{y}^{\text{ul}}[k]$ so as to match the

dynamic range of the quantizer. Then, a linear combiner $\boldsymbol{W} \in \mathbb{C}^{\times B \times U}$, which is computed by the BS on the basis of the CSI acquired via the n_p pilot symbols, is used to obtain an estimate $\hat{\mathbf{s}}^{\mathrm{ul}}[k] \in \mathbb{C}^{\times U}$ of the transmitted signal $\mathbf{s}^{\mathrm{ul}}[k]$ on the basis of the quantizer output. Mathematically, we have the following model:

$$\hat{\mathbf{s}}^{\mathrm{ul}}[k] = \boldsymbol{W}^{\mathsf{H}} \mathcal{Q}(\boldsymbol{A}\mathbf{y}^{\mathrm{ul}}[k]), \quad k = n_p + 1, \ldots, n_{\mathrm{ul}}. \tag{A.3}$$

Here, the diagonal matrix $\boldsymbol{A}$ models the AGC operation. Note that we have not specified how pilot transmission is performed or which channel estimator and linear combiner are used. Again, this is because the information-theoretic bounds we shall provide in Section 3 hold for arbitrary pilot transmission schemes and channel estimators.

2.2 Downlink Transmission

The acquired CSI in the uplink phase is used by the BS to compute the linear precoder $\mathbf{P}$. The resulting precoded signal is then passed through a Q-bit quantizer to satisfy the fronthaul-rate requirements. As a consequence, the U-dimensional discrete-time received signal at the UEs can be modeled as follows:

$$\mathbf{y}^{\mathrm{dl}}[k] = \mathbf{H}^{\mathsf{T}} \alpha \mathcal{Q}(\mathbf{P}\mathbf{s}^{\mathrm{dl}}[k]) + \mathbf{n}^{\mathrm{dl}}[k] \tag{A.4}$$

for $k = n_{\mathrm{ul}} + 1, \ldots, n_{\mathrm{ul}} + n_{\mathrm{dl}}$. Here, $\mathbf{s}^{\mathrm{dl}}[k] = \left[s_1^{\mathrm{dl}}[k], \ldots, s_U^{\mathrm{dl}}[k]\right]^{\mathsf{T}}$ contains the signal intended to each of the U UEs, and the vector $\mathbf{n}^{\mathrm{dl}}[k] \sim \mathcal{CN}(\mathbf{0}_U, N_0 \mathbf{I}_U)$ is the AWGN at the UEs' side. This vector is independent across k and does not depend on the transmitted signal or the fading matrix. In (A.4), the parameter α is a normalization factor used to enforce the power constraint $\mathbb{E}[\|\alpha \mathcal{Q}(\mathbf{P}\mathbf{s}^{\mathrm{dl}}[k])\|^2] = \rho^{\mathrm{dl}}$. Note that when the resolution of the quantizer is very low (e.g., for a 1-bit quantizer), significant throughput gains can be achieved by adopting more sophisticated *nonlinear* precoders, which depend on the transmitted data (see, e.g., [7], [18], [19]). In this paper, we focus on linear precoders because they are the de-facto standard in commercial massive MIMO BS. Similarly to the uplink, the information-theoretic bounds we shall provide in Section 3 hold for an arbitrary linear precoder $\mathbf{P}$. We shall assume that the UEs are equipped with high-resolution converters. Hence, we will not model quantization distortion at the UEs in uplink and downlink.

3 Analysis of the Achievable Error Probability

We will now provide a nonasymptotic, i.e., finite-blocklength, upper bound on the error probability achievable for a given transmission rate in both the uplink and the downlink for the system model described in Section 2. From this result, one can directly obtain a lower bound on the achievable rates for a given target error probability. Our derivation is based on an information-theoretic random-coding argument. Specifically, we will provide a characterization of the average error probability, averaged over the so-called i.i.d Gaussian codebook ensemble, in which each symbol of the transmitted codewords is generated independently from the same zero-mean Gaussian distribution. The main components of our analysis are the mismatch-decoding framework [32] and the RCUs from finite-blocklength information theory [29]. Both tools will be described in detail in the following sections.

3.1 Preliminary Result

As a preliminary result, we shall state the desired bound on the error probability for the following simpler infinite-precision, single-antenna, single-UE nonfading channel model:

$$v[k] = gq[k] + z[k], \quad k = 1, \dots, n. \tag{A.5}$$

Here, g is a deterministic complex-valued coefficient and $\{z[k]\}_{k=1}^{n}$ is a sequence of i.i.d $\mathcal{CN}(0, \sigma^2)$ random variables. Note that we allow σ^2 to depend on g. This will turn out to be important to apply the bound on the error probability obtained when analyzing (A.5) to the input-output relations of interest in this paper, i.e., (A.3) and (A.4). The bound reported in this section is derived under the following crucial assumptions:

(i) The receiver has access to a noisy estimate $\hat{g}$ of g, which the receiver treats as perfect. Specifically, since the additive noise is Gaussian, the receiver operates according to the so-called scaled-nearest neighbor principle [30], i.e., it seeks the n-dimensional transmitted codeword $[\hat{q}[1], \dots, \hat{q}[n]]^{\mathsf{T}}$ that, after scaling by $\hat{g}$, is closest to the receiver vector $[v[1], \dots, v[n]]^{\mathsf{T}}$ in Euclidean norm.

(ii) The average packet error probability is averaged over the ensemble of Gaussian i.i.d codebooks. Specifically, the input signals $q[k]$ in (A.5) are

drawn independently from a $\mathcal{CN}(0, \rho)$ distribution. Here, ρ denotes the transmit power.

Under these assumptions, as proven for example in [26, Thm. 1], one can establish the existence of a coding scheme with rate R and packet error probability $\epsilon = \mathbb{P}\Big[\big[\hat{q}[1], \ldots, \hat{q}[n]\big]^{\mathsf{T}} \neq \big[q[1], \ldots, q[n]\big]^{\mathsf{T}}\Big]$ that is upper-bounded by

$$\epsilon \leq \inf_{s>0} \mathbb{P}\left[\frac{\log f}{n} + \frac{1}{n}\sum_{k=1}^{n} \imath_s(q[k], v[k]) \leq R\right]. \tag{A.6}$$

Here, f is a random variable that is uniformly distributed on the interval $[0, 1]$ and

$$\begin{aligned}\imath_s(q[k], v[k]) = -s\big|v[k] - \hat{g}q[k]\big|^2 + \frac{s\big|v[k]\big|^2}{1 + s\rho\big|\hat{g}\big|^2} \\ + \log\big(1 + s\rho\big|\hat{g}\big|^2\big)\end{aligned} \tag{A.7}$$

is the so-called *generalized information density* [29]. The bound in (A.6) is an instantiation (for a given channel model and a given mismatch-decoding rule) of a more general bound, commonly referred to as RCUs [29]. This bound is, in turn, a relaxation and generalization to mismatch decoding of the random-coding union bound proposed in [28, Thm. 16]. The bound in (A.6) is optimized over the parameter $s > 0$, which originates from the Chernoff-bound step used to relax the random-coding union bound. Note, though, that any choice of $s > 0$ results in a valid (although potentially looser) bound.

3.2 Linearization Via Bussgang's Theorem

One obstacle in the direct application of the bound (A.7) to the uplink and downlink channel input-output-relations (A.3) and (A.4) is the presence of the nonlinear operator $\mathcal{Q}(\cdot)$, which prevents the direct use of the mismatch-decoding framework. Indeed, the mismatch-decoding operation that results in the information density (A.7) relies on the linearity of (A.5). Bussgang's theorem [31], which has been used extensively in the massive MIMO literature to analyze the impact of hardware impairments [5], [10], [33], [34], provides a simple approach to overcome this issue. Specifically, Bussgang's theorem yields a simple way to compute the correlation between two Gaussian vectors,

after one of the two vectors is passed through a nonlinearity (in our case, the quantization operation (A.1)). This theorem, combined with a standard linear minimum mean square error (LMMSE) decomposition, allows us to obtain the desired linearization.

3.2.1 Uplink

Let us start by considering the uplink input-output relation after spatial combining given in (A.3). Throughout, we shall assume, in agreement with what stated in Section 3.1, that the input signals $s_u^{\mathrm{ul}}[k]$, $u = 1, \ldots, U$, $k = n_p+1, \ldots, n_{\mathrm{ul}}$, are drawn independently from a $\mathcal{CN}(0, \rho^{\mathrm{ul}})$ distribution, where ρ^{ul} denotes the uplink transmit power, which we assume being the same for all UEs. It is convenient to write the output $\mathbf{r}^{\mathrm{ul}}[k] = \mathcal{Q}\big(\boldsymbol{A}\mathbf{y}^{\mathrm{ul}}[k]\big)$ of the quantizer as the sum of the LMMSE estimate of $\mathbf{r}^{\mathrm{ul}}[k]$ given the input $\boldsymbol{A}\mathbf{y}^{\mathrm{ul}}[k]$ of the quantizer, plus the uncorrelated, non-Gaussian estimation error $\mathbf{d}^{\mathrm{ul}}[k]$ as follows:

$$\mathbf{r}^{\mathrm{ul}}[k] = \mathbf{G}^{\mathrm{ul}}\mathbf{y}^{\mathrm{ul}}[k] + \mathbf{d}^{\mathrm{ul}}[k] \quad k = n_p + 1, \ldots, n_{\mathrm{ul}}. \tag{A.8}$$

Here, $\mathbf{G}^{\mathrm{ul}}$ is the LMMSE-filter matrix. Since the input $\boldsymbol{A}\mathbf{y}^{\mathrm{ul}}[k]$ of the quantizer is conditionally Gaussian given the channel matrix $\mathbf{H}$, this filter takes on a particularly simple form. Specifically, it follows from Bussgang's theorem that $\mathbf{G}^{\mathrm{ul}}$ is diagonal and given by [17]

$$\begin{aligned}\mathbf{G}^{\mathrm{ul}} = \frac{\Delta}{\sqrt{\pi}}&\mathrm{diag}\big(\boldsymbol{A}\mathbf{C}_{\mathbf{y}^{\mathrm{ul}}}\boldsymbol{A}\big)^{-1/2} \\ &\times \sum_{i=1}^{L-1} \exp\big(-\Delta^2(i - L/2)^2 \mathrm{diag}\big(\boldsymbol{A}\mathbf{C}_{\mathbf{y}^{\mathrm{ul}}}\boldsymbol{A}\big)^{-1}\big)\end{aligned} \tag{A.9}$$

where $\mathbf{C}_{\mathbf{y}^{\mathrm{ul}}} = \mathbb{E}[\mathbf{y}^{\mathrm{ul}}\mathsf{H}(\mathbf{y}^{\mathrm{ul}})]$. Substituting (A.9) into (A.8) and then (A.8) into (A.3), we obtain the desired linearized input-output relation, to which we can apply the error-probability bound (A.6).

3.2.2 Downlink

We shall assume that the downlink input signals $\mathbf{s}^{\mathrm{dl}}[k]$ are drawn independently from a $\mathcal{CN}(\mathbf{0}_U, \mathbf{I}_U)$ distribution. Similar to the uplink, it follows from

Bussgang's theorem that (A.4) can be equivalently expressed as

$$\mathbf{y}^{\mathrm{dl}}[k] = \mathbf{H}^{\mathrm{T}}\alpha\left(\mathbf{G}^{\mathrm{dl}}\mathbf{P}\mathbf{s}^{\mathrm{dl}}[k] + \mathbf{d}^{\mathrm{dl}}[k]\right) + \mathbf{n}^{\mathrm{dl}}[k] \tag{A.10}$$

for $k = n_{\mathrm{ul}} + 1, \ldots, n_{\mathrm{ul}} + n_{\mathrm{dl}}$, where $\mathbf{d}^{\mathrm{dl}}[k]$ is the non-Gaussian quantization noise, which is uncorrelated with $\mathbf{s}^{\mathrm{dl}}[k]$, and where the LMMSE-filter matrix $\mathbf{G}^{\mathrm{dl}}$ has the same form as $\mathbf{G}^{\mathrm{ul}}$ in (A.9), with $\boldsymbol{A}\mathbf{C}_{\mathbf{y}^{\mathrm{ul}}}\boldsymbol{A}$ replaced by $\mathbf{P}\mathbf{P}^{\mathsf{H}}$.

3.3 The Actual Error-Probability Bound

3.3.1 Uplink

We let $\hat{s}_u^{\mathrm{ul}}[k]$ denote the uth entry of the vector $\hat{\mathbf{s}}^{\mathrm{ul}}[k]$ in (A.3), and the vectors $\mathbf{w}_u$ and $\mathbf{h}_u$ denote the uth columns of the $B \times U$ combining matrix $\boldsymbol{W}$ and channel matrix $\mathbf{H}$. Substituting (A.8) into (A.3), we can write the estimate $\hat{s}_u^{\mathrm{ul}}[k]$ of the kth data symbol from user u as

$$\begin{aligned}\hat{s}_u^{\mathrm{ul}}[k] = {} & \mathbf{w}_u{}^{\mathsf{H}}\mathbf{G}^{\mathrm{ul}}\boldsymbol{A}\mathbf{h}_u s_u^{\mathrm{ul}}[k] + \sum_{\substack{v=1 \\ v\neq u}}^{U}\mathbf{w}_u{}^{\mathsf{H}}\mathbf{G}^{\mathrm{ul}}\boldsymbol{A}\mathbf{h}_v s_v^{\mathrm{ul}}[k] \\ & + \mathbf{w}_u{}^{\mathsf{H}}\mathbf{G}^{\mathrm{ul}}\boldsymbol{A}\mathbf{n}^{\mathrm{ul}}[k] + \mathbf{w}_u{}^{\mathsf{H}}\mathbf{d}^{\mathrm{ul}}[k]\end{aligned} \tag{A.11}$$

for $k = n_p + 1, \ldots, n_{\mathrm{ul}}$ and $u = 1, \ldots, U$. The first term in (A.11) denotes the useful signal. The remaining terms comprise the residual multiuser interference, the additive noise, and the quantization noise. The BS is not aware of the effective channel gain $g_u^{\mathrm{ul}} = \mathbf{w}_u{}^{\mathsf{H}}\mathbf{G}^{\mathrm{ul}}\boldsymbol{A}\mathbf{h}_u$. However, it can use the n_p pilot symbols to obtain the estimate $\hat{g}^{\mathrm{ul}} = \mathbf{w}_u{}^{\mathsf{H}}\mathbf{G}^{\mathrm{ul}}\boldsymbol{A}\hat{\mathbf{h}}_u$, where $\hat{\mathbf{h}}_u$ denotes the uth column of the channel estimate matrix $\widehat{\mathbf{H}}$.

Since $\mathbf{H}$, and, hence $\widehat{\mathbf{H}}$, are assumed to stay constant over the entire transmission duration, which involves $n_{\mathrm{ul}} + n_{\mathrm{dl}}$ channel uses, we can obtain a mismatch-decoding upper bound on the per-user error probability ϵ_u^{ul}, $u = 1, \ldots, U$, by applying (A.6) to the linearized input-output relation (A.11) for each realization of $\mathbf{H}$ and $\widehat{\mathbf{H}}$ and then by averaging over $\mathbf{H}$ and $\widehat{\mathbf{H}}$. Specifically, by setting $q[k] = s_u^{\mathrm{ul}}[k]$, $v[k] = \hat{s}_u^{\mathrm{ul}}[k]$, $g = g_u^{\mathrm{ul}}$, $\hat{g} = \hat{g}_u^{\mathrm{ul}}$, and $\rho = \rho^{\mathrm{ul}}$ in (A.6) and (A.7), and by accounting for the pilot-transmission overhead, we

can upper-bound the uplink per-user error probability as

$$\epsilon_u^{\mathrm{ul}} \leq \mathbb{E}_{\mathbf{H},\widehat{\mathbf{H}}}\left[\inf_{s>0}\mathbb{P}\left[\frac{\log f}{n_{\mathrm{ul}}} + \frac{1}{n_{\mathrm{ul}}}\sum_{k=n_p+1}^{n_{\mathrm{ul}}} \imath_s(s_u^{\mathrm{ul}}[k], \hat{s}_u^{\mathrm{ul}}[k]) \leq R \,\middle|\, \mathbf{H}, \widehat{\mathbf{H}}\right]\right]. \tag{A.12}$$

In (A.12), the probability inside the expectation is computed with respect to the transmitted symbols, the additive noise, and the uniform random variable f.

3.3.2 Downlink

We let $s_u^{\mathrm{dl}}[k]$, $n_u^{\mathrm{dl}}[k]$, and $y_u^{\mathrm{dl}}[k]$ denote the uth entry of the symbol vector $\mathbf{s}^{\mathrm{dl}}[k]$, noise vector $\mathbf{n}^{\mathrm{dl}}[k]$, and received vector $\mathbf{y}^{\mathrm{dl}}[k]$, respectively. Furthermore, let $\mathbf{p}_u$ denote the uth column of the precoding matrix $\mathbf{P}$. It then follows from (A.10) that

$$y_u^{\mathrm{dl}}[k] = \alpha \mathbf{h}_u^{\mathrm{T}} \mathbf{G}^{\mathrm{dl}} \mathbf{p}_u s_u^{\mathrm{dl}}[k] + \sum_{\substack{v=1 \\ v\neq u}}^{U} \alpha \mathbf{h}_u^{\mathrm{T}} \mathbf{G}^{\mathrm{dl}} \mathbf{p}_v s_v^{\mathrm{dl}}[k] + \alpha \mathbf{h}_u^{\mathrm{T}} \mathbf{d}^{\mathrm{dl}}[k] + n_u^{\mathrm{dl}}[k] \tag{A.13}$$

for $k = n_{\mathrm{ul}}+1, \ldots, n_{\mathrm{ul}}+n_{\mathrm{dl}}$, and $u = 1, \ldots, U$. We assume that the uth UE is not aware of the effective channel $g_u^{\mathrm{dl}} = \alpha \mathbf{h}_u^{\mathrm{T}} \mathbf{G}^{\mathrm{dl}} \mathbf{p}_u$ but it is aware of its mean $\hat{g}_u^{\mathrm{dl}} = \alpha \mathbb{E}[\mathbf{h}_u^{\mathrm{T}} \mathbf{G}^{\mathrm{dl}} \mathbf{p}_u]$. This setup is often considered in the massive MIMO literature and yields, in the asymptotic ergodic setting, the so-called hardening bound [27, Thm. 4.6]. In our quasi-static setup, we will treat $\hat{g}_u^{\mathrm{dl}}$ simply as the imperfect CSI used by the scaled-nearest neighbor decoder at the uth UE, hence providing an operational interpretation to the hardening bound. By setting $q[k] = s_u^{\mathrm{dl}}[k]$, $v[k] = y_u^{\mathrm{dl}}[k]$, $g = g_u^{\mathrm{dl}}$, $\hat{g} = \hat{g}_u^{\mathrm{dl}}$, and $\rho = 1$ in (A.6)

and (A.7), we can upper-bound the downlink per-user error probability as

$$\epsilon_u^{\mathrm{dl}} \leq \mathbb{E}_{\mathbf{H},\widehat{\mathbf{H}}}\left[\inf_{s>0}\mathbb{P}\left[\frac{\log(f)}{n_{\mathrm{dl}}} + \frac{1}{n_{\mathrm{dl}}}\sum_{k=n_{\mathrm{ul}}+1}^{n_{\mathrm{ul}}+n_{\mathrm{dl}}} \imath_s(s_u^{\mathrm{dl}}[k], y_u^{\mathrm{dl}}[k]) \leq R \,\middle|\, \mathbf{H}, \widehat{\mathbf{H}}\right]\right]. \tag{A.14}$$

The probability in (A.14) is computed with respect to the symbols transmitted by the BS and the additive noise. This probability depends on the channel estimate $\widehat{\mathbf{H}}$ indirectly through the precoding matrix $\mathbf{P}$.

3.4 Asymptotic Limits and Useful Approximations

The error-probability bounds provided in (A.12) and (A.14) are difficult to evaluate. Indeed not only the expectations, but also the conditional probability terms within the bounds can in general not be obtained in closed form, and need to be evaluated numerically, which is especially challenging if one targets low error probabilities. Furthermore, the minimization over s, which is required to tighten the bounds, needs also to be performed numerically for each realization of $\mathbf{H}$ and $\widehat{\mathbf{H}}$.[3]

As we shall discuss next, it turns out that, when one operates in the moderate error-probability regime (i.e., packet error probability in the range $[10^{-3}, 10^{-1}]$), one can obtain asymptotic approximations on the error-probability bounds in (A.12) and (A.14) that are much simpler to evaluate numerically. After demonstrating their accuracy, we will use these approximations in Section 4 to provide insights on the optimal system design.

3.4.1 A Normal Approximation

To introduce the first approximation, we start with the uplink bound (A.12). Note that, given $\mathbf{H}$ and $\widehat{\mathbf{H}}$, the conditional probability term in (A.12) involves the linear combination of $n_{\mathrm{ul}} - n_p + 1$ independent random variables (the $n_{\mathrm{ul}} - n_p$ information-density terms, which are actually also identically distributed, and the $\log(f)$ term). Fix an arbitray integer $k \in [n_p + 1, n_{\mathrm{ul}}]$. It will turn

[3] In practice, one can loosen the bounds by moving the minimization outside the expectation, which alleviates somewhat the numerical complexity of this optimization step.

out convenient to let

$$I_{s,u}^{\mathrm{ul}} = \mathbb{E}[\imath_s(s_u^{\mathrm{ul}}[k], \hat{s}_u^{\mathrm{ul}}[k])] \tag{A.15}$$

$$= -s\Big(\big|g_u^{\mathrm{ul}} - \hat{g}_u^{\mathrm{ul}}\big|^2 \rho^{\mathrm{ul}} + \sigma_{u,\mathrm{ul}}^2\Big) + s\frac{\rho^{\mathrm{ul}}\big|g_u^{\mathrm{ul}}\big|^2 + \sigma_{u,\mathrm{ul}}^2}{1 + s\rho^{\mathrm{ul}}\big|\hat{g}_u^{\mathrm{ul}}\big|^2}$$
$$+ \log\Big(1 + s\rho^{\mathrm{ul}}\big|\hat{g}_u^{\mathrm{ul}}\big|^2\Big) \tag{A.16}$$

where the expectation in (A.15) is computed only with respect to the transmitted symbols and the additive noise (i.e., $\mathbf{H}$ and $\widehat{\mathbf{H}}$ are fixed). In (A.16), we let $\sigma_{u,\mathrm{ul}}^2$ denote the conditional variance, given $\mathbf{H}$ and $\widehat{\mathbf{H}}$, of the total additive noise in (A.11), which includes also residual multiuser interference and quantization noise. Specifically, we have that

$$\sigma_{u,\mathrm{ul}}^2 = \sum_{\substack{v=1 \\ v\neq u}}^{U} \big|\mathbf{w}_u{}^{\mathsf{H}}\mathbf{G}^{\mathrm{ul}}\boldsymbol{A}\mathbf{h}_v\big|^2 + N_0\|\mathbf{w}_u^{\mathsf{H}}\mathbf{G}^{\mathrm{ul}}\boldsymbol{A}\|^2$$
$$+ \mathbf{w}_u{}^{\mathsf{H}}\mathbf{C}_{\mathbf{d}^{\mathrm{ul}}}\mathbf{w}_u \tag{A.17}$$

where $\mathbf{C}_{\mathbf{d}^{\mathrm{ul}}} = \mathbb{E}[\mathbf{d}^{\mathrm{ul}}\big(\mathbf{d}^{\mathrm{ul}}\big)^{\mathsf{H}}]$ denotes the correlation matrix of the uplink quantization distortion. To obtain (A.17) we have used that the transmitted symbols are independent across users and that the quantization noise and the transmitted symbols are uncorrelated as a consequence of the LMMSE decomposition. The random variable $I_{s,u}^{\mathrm{ul}}$ in (A.16) is usually referred to as the GMI.

Let us also set $V_{s,u}^{\mathrm{ul}} = \mathbb{V}[\imath_s(s_u^{\mathrm{ul}}[k], \hat{s}_u^{\mathrm{ul}}[k])]$. This quantity is a generalization to the mismatch-decoding setup of the so-called *channel dispersion* in finite-blocklength information theory (see, e.g., [28, Def. 1]).

Let us now assume that $n_{\mathrm{ul}} - n_p \gg 1$. Since the random variable $\log(f)$ has finite moments, we can approximate the error probability in (A.12) using

the Berry-Essen central-limit theorem [35, Ch. XVI.5] and conclude that

$$\mathbb{P}\left[\frac{\log f}{n_{\mathrm{ul}}}+\frac{1}{n_{\mathrm{ul}}}\sum_{k=n_p+1}^{n_{\mathrm{ul}}}\imath_s(s_u^{\mathrm{ul}}[k],\hat{s}_u^{\mathrm{ul}}[k])\le R\,\middle|\,\mathbf{H},\widehat{\mathbf{H}}\right] = Q_G\left(\frac{\left(1-\frac{n_p}{n_{\mathrm{ul}}}\right)I_{u,s}^{\mathrm{ul}}-R}{\sqrt{\left(1-\frac{n_p}{n_{\mathrm{ul}}}\right)\frac{V_{u,s}^{\mathrm{ul}}}{n_{\mathrm{ul}}}}}\right)+\mathcal{O}\left(\frac{1}{\sqrt{n_{\mathrm{ul}}-n_p}}\right). \quad \text{(A.18)}$$

We shall refer to the approximation on the conditional error probability on the left-hand side of (A.18) obtained by neglecting the $\mathcal{O}\big(1/\sqrt{n_{\mathrm{ul}}-n_p}\big)$ term on the right-hand side of (A.18) as *normal approximation*.

A similar approximation can be derived for the conditional probability term in the downlink error probability bound provided in (A.14). Specifically, let[4] for an arbitrary integer $k\in[n_{\mathrm{ul}}+1,n_{\mathrm{ul}}+n_{\mathrm{dl}}]$

$$I_{s,u}^{\mathrm{dl}}=\mathbb{E}[\imath_s(s_u^{\mathrm{dl}}[k],y_u^{\mathrm{dl}}[k])] \quad \text{(A.19)}$$

$$=-s\Big(\big|g_u^{\mathrm{dl}}-\hat{g}_u^{\mathrm{dl}}\big|^2+\sigma_{u,\mathrm{dl}}^2\Big)+s\frac{\big|g_u^{\mathrm{dl}}\big|^2+\sigma_{u,\mathrm{dl}}^2}{1+s\big|\hat{g}_u^{\mathrm{dl}}\big|^2} +\log\Big(1+s\big|\hat{g}_u^{\mathrm{dl}}\big|^2\Big) \quad \text{(A.20)}$$

where

$$\sigma_{u,\mathrm{dl}}^2=\sum_{v\neq u}\alpha^2\big|\mathbf{h}_u^{\mathrm{T}}\mathbf{G}^{\mathrm{dl}}\mathbf{p}_v\big|+\alpha^2\mathbf{h}_u^{\mathrm{T}}\mathbf{C}_{\mathbf{d}^{\mathrm{dl}}}{\mathbf{h}_u}^*+N_0 \quad \text{(A.21)}$$

with $\mathbf{C}_{\mathbf{d}^{\mathrm{dl}}}=\mathbb{E}[\mathbf{d}^{\mathrm{dl}}\big(\mathbf{d}^{\mathrm{dl}}\big)^{\mathsf{H}}]$. Let $V_{s,u}^{\mathrm{dl}}=\mathbb{V}[\imath_s(s_u^{\mathrm{dl}}[k],y_u^{\mathrm{dl}}[k])]$. Then,

$$\mathbb{P}\left[\frac{\log f}{n_{\mathrm{dl}}}+\frac{1}{n_{\mathrm{dl}}}\sum_{k=n_{\mathrm{ul}}+1}^{n_{\mathrm{ul}}+n_{\mathrm{dl}}}\imath_s(s_u^{\mathrm{dl}}[k],y_u^{\mathrm{dl}}[k])\le R\,\middle|\,\mathbf{H},\widehat{\mathbf{H}}\right] = Q_G\left(\frac{I_{u,s}^{\mathrm{dl}}-R}{\sqrt{\frac{V_{u,s}^{\mathrm{dl}}}{n_{\mathrm{dl}}}}}\right)+\mathcal{O}\left(\frac{1}{\sqrt{n_{\mathrm{dl}}}}\right). \quad \text{(A.22)}$$

[4] Note that (A.20) depends on the transmit power ρ^{dl} indirectly, through the normalization parameter α, which appears in the definitions of g_u^{dl}, $\hat{g}_u^{\mathrm{dl}}$, and $\sigma_{u,\mathrm{dl}}^2$.

3.4.2 The Outage-Probability Limit

Neglecting the $\mathcal{O}(\cdot)$ terms in (A.18) and (A.22) and then substituting (A.18) into (A.12) and (A.22) into (A.14), one obtains approximations on the uplink and downlink error probabilities that are accurate when $n_{\mathrm{ul}} - n_p \gg 1$ and $n_{\mathrm{dl}} \gg 1$, and easier to evaluate, since the probability term is given in closed form.

However, the resulting expressions are still challenging to evaluate numerically. Indeed, the first issue is that both $V_{u,s}^{\mathrm{ul}}$ and $V_{u,s}^{\mathrm{dl}}$ depend on the expectation of the product of powers of the input signal and the quantization distortion in the LMMSE decomposition of the quantized signal. These terms do not admit, in general, an analytical characterization. The second issue is that, even after the above-mentioned substitutions, the optimization over s, which is needed to tighten bounds, cannot be performed analytically.

To avoid both of these issues, we next present an alternative, looser, asymptotic approximation in terms of outage probability. Starting from the uplink, we assume that $n_{\mathrm{ul}} \to \infty$ and that $\lim_{n_{\mathrm{ul}}\to\infty} n_p/n_{\mathrm{ul}} = p \in [0,1]$, where p is the rate penalty due to pilot transmission. It follows from (A.18) that

$$\lim_{n_{\mathrm{ul}}\to\infty} \mathbb{P}\left[\frac{\log f}{n_{\mathrm{ul}}} + \frac{1}{n_{\mathrm{ul}}} \sum_{k=n_p+1}^{n_{\mathrm{ul}}} \imath_s(s_u^{\mathrm{ul}}[k], \hat{s}_u^{\mathrm{ul}}[k]) \le R \,\middle|\, \mathbf{H}, \widehat{\mathbf{H}}\right]$$

$$= \begin{cases} 1, & \text{if } (1-p) I_{u,s}^{\mathrm{ul}} < R \\ 0, & \text{otherwise} \end{cases} \tag{A.23}$$

$$= \mathbb{1}(1-p) I_{u,s}^{\mathrm{ul}} < R. \tag{A.24}$$

Using (A.24) in (A.12), we conclude that

$$\lim_{n_{\mathrm{ul}}\to\infty} \mathbb{E}_{\mathbf{H},\widehat{\mathbf{H}}}\left[\inf_{s>0} \mathbb{P}\left[\frac{\log f}{n_{\mathrm{ul}}} + \frac{1}{n_{\mathrm{ul}}} \sum_{k=n_p+1}^{n_{\mathrm{ul}}} \imath_s(s_u^{\mathrm{ul}}[k], \hat{s}_u^{\mathrm{ul}}[k]) \le R \,\middle|\, \mathbf{H}, \widehat{\mathbf{H}}\right]\right]$$

$$= \mathbb{E}[\inf_{s>0} \mathbb{1}(1-p) I_{u,s}^{\mathrm{ul}} < R] \tag{A.25}$$

$$= \mathbb{P}\left[(1-p)\left(\sup_{s>0} I_{u,s}^{\mathrm{ul}}\right) < R\right]. \tag{A.26}$$

We shall refer to (A.26) as uplink GMI-based outage bound. It turns out that the maximization over $s > 0$ in (A.26) can be performed analytically. Specifically, let s_{opt} the value of s that maximizes the GMI $I^{\mathrm{ul}}_{u,s}$. Then, proceeding similar to [30, App. A], one can show that

$$s_{opt} = \frac{-2c + b + \sqrt{b^2 + 4ac}}{2bc} \tag{A.27}$$

where $a = \rho^{\mathrm{ul}} \left| g^{\mathrm{ul}}_u \right|^2 + \sigma^2_{u,\mathrm{ul}}$, $b = \rho^{\mathrm{ul}} \left| \hat{g}^{\mathrm{ul}}_u \right|^2$, and $c = \rho^{\mathrm{ul}} \left| g^{\mathrm{ul}}_u - \hat{g}^{\mathrm{ul}}_u \right|^2 + \sigma^2_{u,\mathrm{ul}}$.

It is worth noting that in the perfect CSI case, in which $\hat{g}^{\mathrm{ul}}_u = g^{\mathrm{ul}}_u$, we have that $a = b + c$. Using this equality in (A.27), we obtain that

$$s_{opt} = \frac{1}{c} = \frac{1}{\sigma^2_{u,\mathrm{ul}}}. \tag{A.28}$$

This implies that, in the perfect CSI case,

$$\sup_{s>0} I^{\mathrm{ul}}_{u,s} = \log\left(1 + \frac{\rho^{\mathrm{ul}} \left| g^{\mathrm{ul}}_u \right|^2}{\sigma^2_{u,\mathrm{ul}}}\right) \tag{A.29}$$

and (A.26) reduces to the familiar outage-probability formula

$$\mathbb{P}\left[\log\left(1 + \frac{\rho^{\mathrm{ul}} \left| g^{\mathrm{ul}}_u \right|^2}{\sigma^2_{u,\mathrm{ul}}}\right) < R\right]. \tag{A.30}$$

This provides further evidence that (A.26) is the natural extension of (A.30) to the case of imperfect CSI. It is worth stressing that, in the imperfect CSI case, the expression for the outage probability obtained by substituting in (A.26) the optimal value of s given in (A.28), does not take the form given in (A.30), with the SINR in (A.30) replaced by a SINR term including also the variance of the channel estimation error. This means that the ergodic SINR expression for the imperfect CSI case reported in e.g., [27, Thm. 4.1] should not be used in the quasi-static setting considered in this paper.

With steps similar to the ones leading to (A.26), one can show that, in the

downlink,

$$\lim_{n_{\mathrm{dl}}\to\infty} \mathbb{E}_{\mathbf{H},\widehat{\mathbf{H}}}\left[\inf_{s>0} \mathbb{P}\left[\frac{\log f}{n_{\mathrm{dl}}} + \frac{1}{n_{\mathrm{dl}}} \sum_{k=n_{\mathrm{ul}}+1}^{n_{\mathrm{ul}}+n_{\mathrm{dl}}} \imath_s(s_u^{\mathrm{dl}}[k], y_u^{\mathrm{dl}}[k]) \leq R \,\middle|\, \mathbf{H}, \widehat{\mathbf{H}}\right]\right] = \mathbb{P}\left[\left(\sup_{s>0} I_{u,s}^{\mathrm{dl}}\right) < R\right] \tag{A.31}$$

where the value of s maximizing $I_{u,s}^{\mathrm{dl}}$ is given by (A.27), with $a = \left|g_u^{\mathrm{dl}}\right| + \sigma_{u,\mathrm{dl}}^2$, $b = \left|\hat{g}_u^{\mathrm{dl}}\right|^2$, and $c = \left|g_u^{\mathrm{dl}} - \hat{g}_u^{\mathrm{dl}}\right|^2 + \sigma_{u,\mathrm{dl}}^2$. We shall refer to (A.31) as downlink GMI-based outage bound. Similar to the uplink, if we assume that the UEs have perfect knowledge of the effective channel g_u^{dl}, then

$$\sup_{s>0} I_{u,s}^{\mathrm{dl}} = \log\left(1 + \frac{\left|g_u^{\mathrm{dl}}\right|^2}{\sigma_{u,\mathrm{ul}}^2}\right) \tag{A.32}$$

and (A.31) reduces to the familiar outage formula

$$\mathbb{P}\left[\log\left(1 + \frac{\left|g_u^{\mathrm{dl}}\right|^2}{\sigma_{u,\mathrm{dl}}^2}\right) < R\right]. \tag{A.33}$$

4 Numerical Results

We present numerical simulations to demonstrate the accuracy of the approximations on the error-probability bounds presented in Section 3. We will then use these approximations—more specifically (A.26) for the uplink and (A.31) for the downlink—to investigate the trade-off between the number of antennas and the resolution of the converters in the fully digital massive MIMO architecture described in Section 2. We will also study how this trade-off is influenced by the quality of the available CSI. Before presenting our numerical experiments, we detail in the next section the scenario that will be considered throughout, as well as the system parameters and the algorithm used for channel estimation.

4.1 Simulation Setup

4.1.1 Propagation Scenario

We consider a small-cell scenario where a BS, which is equipped with a uniform linear array of B equispaced antennas, serves $U = 8$ users, uniformly distributed within a disc centered around the BS, with inner radius of 5 meters and outer radius of 150 meters. The propagation channel between each UE and the BS is modeled according to a standard clustered channel model (previously considered within the context of massive MIMO architectures with low precision quantizers in, e.g., in [36]–[38]). This channel model involves N_{cl} clusters, with each cluster contributing to N_{ray} propagation paths. According to this model, each column $\mathbf{h}_u$, $u = 1, \ldots, U$, of the channel matrix $\mathbf{H}$ can be written as

$$\mathbf{h}_u = \sqrt{\frac{1}{N_{\mathrm{cl}} N_{\mathrm{ray}}}} \sum_{n=1}^{N_{\mathrm{cl}}} \sum_{m=1}^{N_{\mathrm{ray}}} \alpha_{n,m}^{u} \mathbf{a}(\theta_{n,m}^{u}). \tag{A.34}$$

Here, the fading coefficients $\alpha_{n,m}^{u}$ are i.i.d $\mathcal{CN}(0, \sigma_u^2)$ complex random variables, with σ_u^2 modeling the path loss experienced by the uth UE. Furthermore, $\mathbf{a}(\theta_{n,m}^{u})$ is the array response vector of the uniform linear array at the BS in far field

$$\mathbf{a}(\theta_{n,m}^{u}) = \left[1, e^{-j2\pi\theta_{n,m}^{u}}, \ldots, e^{-j2\pi(B-1)\theta_{n,m}^{u}}\right]^{\mathrm{T}} \tag{A.35}$$

where $\theta_{n,m}^{u} = d \sin(\phi_{n,m}^{u})/\lambda$, with d being the antenna spacing, $\phi_{n,m}^{u}$ the angle of arrival or spatial angle measured from the boresight of the uniform linear array, and λ is the wavelength.

Throughout our simulations, we assume $N_{cl} = 2$ and $N_{ray} = 4$ and fix the antenna spacing to $\lambda/2$. As pathloss model, we assume that $10 \log_{10} \sigma_u^2 = -72 - 29.2 \log_{10}(d_u)$, where d_u denotes the distance between the uth UE and the BS. The angle of arrival $\phi_{n,m}^{u}$ is modeled as $\phi_{n,m}^{u} = \phi_n^u + \phi_{offset}$, where $\phi_n^u \sim \mathcal{U}[-\pi/3, \pi/3]$ and $\phi_{\mathrm{offset}} \sim \mathcal{U}[-\pi/24, \pi/24]$.

4.1.2 System Parameters

The noise spectral density N_0 is assumed to be $-174\,\mathrm{dBm/Hz}$, the carrier frequency is 30 GHz, and the transmitted signal has a bandwidth equal to 50 MHz. In the channel estimation phase, we assume that each user transmits concurrently orthogonal pilot sequences, obtained by cyclically shifting a

Zadoff-Chu sequence [12] of length n_p. Let $\mathbf{T} \in \mathbb{C}^{\times U \times n_p}$ with $\mathbf{T}\mathbf{T}^{\mathsf{H}} = n_p \rho^{\mathrm{ul}} \mathbf{I}_U$ be the matrix containing the pilot symbols transmitted by all UEs. Let the $B \times n_p$ received signal at the BS during the pilot phase be

$$\mathbf{Y}^p = \mathbf{H}\mathbf{T} + \mathbf{N}^p \tag{A.36}$$

where $\mathbf{N}^p \in \mathbb{C}^{\times B \times n_p}$ denotes the additive noise. We use the signal received in the pilot phase to determine the AGC diagonal matrix $\boldsymbol{A}$ when computing $\hat{g}_u^{\mathrm{ul}}$. Specifically, we set

$$\boldsymbol{A} = \mathrm{diag}\left(\widehat{\mathbf{C}}_{\mathbf{y}^{\mathrm{ul}}}\right)^{-1/2} \tag{A.37}$$

where

$$\widehat{\mathbf{C}}_{\mathbf{y}^{\mathrm{ul}}} = \frac{1}{n_p}\mathbf{Y}^p(\mathbf{Y}^p)^{\mathsf{H}}. \tag{A.38}$$

We also use $\widehat{\mathbf{C}}_{\mathbf{y}^{\mathrm{ul}}}$ as an estimate of $\mathbf{C}_{\mathbf{y}^{\mathrm{ul}}}$ when evaluating the Bussgang filter $\mathbf{G}^{\mathrm{ul}}$ in the computation of $\hat{g}_u^{\mathrm{ul}}$.

To set the parameter Δ in (A.1), we treat the input of the quantizer as a complex Gaussian random variable of zero mean and unit variance and we require that the clipping probability does not exceed 10^{-4}. This yields

$$\Delta = \frac{\sqrt{2}}{L} Q_G^{-1}\left(\frac{10^{-4}}{2}\right). \tag{A.39}$$

Let now, $\tau_i = \Delta(i - L/2)$ for $i = 1, \ldots, L-1$ and $\tau_0 = -\infty$, $\tau_L = \infty$ denote the quantization thresholds. Furthermore, let $\ell_i = \Delta(i - L/2 + 1/2)$ for $i = 0, \ldots, L-1$ be the quantization labels. Treating again the input of the quantizer as a complex Gaussian random variable, we set the downlink power-normalization parameter α in (A.4) to

$$\alpha = \frac{\sqrt{\rho^{\mathrm{dl}}/2}}{\sqrt{\sum_{i=0}^{L-1} \ell_i^2 \left(Q_G\left(\sqrt{2}\tau_i\right) - Q_G\left(\sqrt{2}\tau_{i+1}\right)\right)}}. \tag{A.40}$$

For the 1-bit case, we compute the correlation of the uplink and downlink quantization distortion $\mathbf{C}_{\mathbf{d}^{\mathrm{ul}}}$ and $\mathbf{C}_{\mathbf{d}^{\mathrm{dl}}}$ using the so called arc-sine law [39] (see [17, Eqs. (34) and (43)]). When $Q > 1$, we use the diagonal approximation proposed in [17, Sec. IV.C].

Throughout this section, we set $n_{\mathrm{ul}} = n_{\mathrm{dl}} = 500$ and assume that the

fronthaul interface can support a rate no larger than 512 bit/s/Hz . For a 50 MHz transmitted-signal bandwidth, this implies a fronthaul rate of about 25.6 Gbit/s, which is in the range of what can be supported with current technologies. This constraint implies that $2BQ \leq 512$ bit/s/Hz. As a consequence, the largest number of BS antennas that is compatible with the use of quantizers with $Q = 1, 2, 3, 4, 5, 6, 7, 8$ bits of resolution is $B = 256, 128, 85, 64, 51, 42, 36, 32$, respectively.

4.1.3 Channel Estimation

To estimate the channel, we use the CSI-acquisition algorithm proposed in [12]. In this algorithm, the clustered channel generated according to (A.34) is estimated in the angle domain. Since in this representation the channel is approximately sparse, the channel estimation problem can be reduced to a quantized compressive-sensing reconstruction problem. The approach followed in [12] is to solve this problem using a method that combines expectation maximization with approximate message passing.

4.1.4 Linear Combiner and Precoder

The available CSI at the BS is used to construct a linear combiner and a linear precoder. Throughout this section, we will consider the distortion-aware MMSE combiner proposed in [6, Eq. 13] for which

$$\mathbf{w}_u = \left(\rho^{\mathrm{ul}} \left(\sum_{v \neq u} \mathbf{G}^{\mathrm{ul}} \mathbf{A} \hat{\mathbf{h}}_v \left(\mathbf{G}^{\mathrm{ul}} \mathbf{A} \hat{\mathbf{h}}_v \right)^{\mathrm{H}} \right) + N_0 \mathbf{G}^{\mathrm{ul}} \mathbf{A} (\mathbf{G}^{\mathrm{ul}} \mathbf{A})^{\mathrm{H}} + \mathbf{C}_{\mathbf{d}^{\mathrm{ul}}} \right)^{-1} \left(\rho^{\mathrm{ul}} \mathbf{G}^{\mathrm{ul}} \mathbf{A} \hat{\mathbf{h}}_u \right) \tag{A.41}$$

and a MMSE precoder (which ignores quantization effects)

$$\mathbf{P} = \beta \widehat{\mathbf{H}}^{*} \left(\widehat{\mathbf{H}}^{\mathrm{T}} \widehat{\mathbf{H}}^{*} + \frac{U N_0}{\rho^{\mathrm{dl}}} \mathbf{I}_{\mathrm{U}} \right)^{-1} \tag{A.42}$$

where the normalization factor β is chosen so that $\mathbb{E}[\|\mathbf{P}\mathbf{s}^{\mathrm{ul}}\|^2] = B$. Some remarks on the performance achievable with the simpler maximum ratio combiner in the uplink and maximum ratio precoder in the downlink are provided

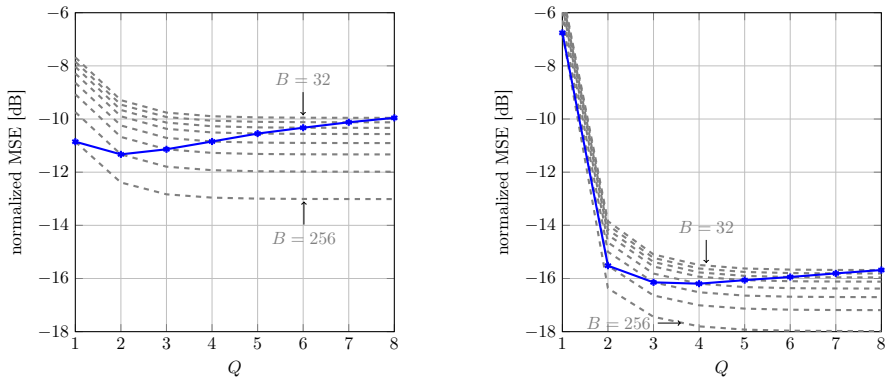

(a) $\rho^{\mathrm{ul}} = 16$ **(b)** $\rho^{\mathrm{ul}} = 24$

Figure 2: Channel estimation normalized MSE as a function of the resolution of the quantizers and the number of BS antennas. The points marked in blue are obtained by considering the largest number of BS antennas that is compatible with a fronthaul constraint of 512 bit/s/Hz.

in Section 4.6.

4.2 Channel-Estimation Performance

Before analyzing the trade-off between the number of antennas and the resolution of the converters for a given fronthaul constraint in Section 4.6, we start by providing in this section some insights on the choice of the pilot-sequence length for the clustered channel model (A.34) and the channel-estimation algorithm described in Section 4.1.3. We will then discuss in Section 4.3 the accuracy of the simple-to-evaluate error-probability approximations provided in (A.26) and (A.31), and analyze in Section 4.4 the impact of dithering in both uplink and downlink for the case $Q = 1$. We start by investigating the normalized MSE of the channel estimate[5] obtained at the BS as a function of the resolution Q of the data converters for the case in which $U = 8$ users transmit simultaneously pilot sequences of length $n_p = 48$ as described in Section 4.1.2. As we shall discuss in Section 4.5, for the error-probability

[5]This quantity is defined as the average of the ratio between the square of the channel estimation error and the square of the norm of the channel.

values considered therein, this choice for n_p strikes a good balance between accuracy of the channel estimate and pilot overhead. Note that, because of the fronthaul constraint, the number of BS antennas decreases as Q is increased, as described in Section 4.1.2. To investigate the impact of quantization on the accuracy of the channel estimates obtainable at the BS, we consider two values of transmit power: a low transmit-power value of 16 dBm, and a high transmit-power value of 24 dBm.[6] The grey lines in Fig 2 illustrate the channel-estimation normalized MSE as a function of Q, for a fixed number of transmit antennas $B \in \{32, 36, 42, 51, 64, 85, 128, 256\}$. The MSE values marked in blue are the ones corresponding to the largest number of antennas that is compatible with the fronthaul constraint, for the corresponding value of Q. We note that for the low transmit-power value, the lowest MSE value is obtained when $Q = 2$ and $B = 128$, whereas, for the high transmit-power value, $Q = 4$ and, hence, $B = 64$ results in the lowest MSE. Increasing the transmit power turns out beneficial in terms of MSE for all Q values except $Q = 1$, for which the MSE deteriorates as the transmit power is increased. This behavior is common in the 1-bit case and has been noticed before for a variety of channel models and channel-estimation algorithms [11], [40]–[43]. To shed further light on this phenomenon, we plot in Fig. 3 the channel-estimation normalized MSE for $(Q, B) \in \{(1, 256), (2, 128), (3, 85)\}$. Note that the MSE curve decreases monotonically with ρ^{ul} when $Q = 2, 3$. On the contrary, when $Q = 1$, the MSE curve achieves a global minimum at $\rho^{\text{ul}} \approx 20$ dBm. The reason is as follows: although a single-bit quantizer preserves only the sign of the input signal, with a sufficient amount of noise, amplitude information about the input signal can be recovered via multiple measurements. This well-known phenomenon, known as stochastic resonance, can be enforced also in the high-SNR regime via the use of nonsubtractive dithering at the receiver, prior to quantization [44]. We will investigate the beneficial effects of dithering in the high-SNR regime for the case $Q = 1$ in Section 4.4. Note that the two transmit-power values chosen in Fig. 2 are to the left and to the right of the transmit-power value minimizing the normalized MSE in Fig. 3, i.e., $\rho^{\text{ul}} = 20$ dBm.

[6] As we shall clarify shortly, these two values allow us to analyze the impact of dithering for the 1-bit quantization case.

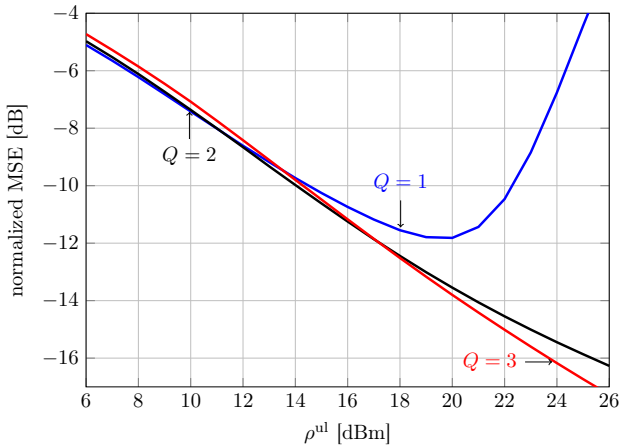

Figure 3: Channel-estimation normalized MSE as a function of ρ^{ul} for the (Q, B) pairs $\{(1, 256), (2, 128), (3, 85)\}$ satisfying the fronthaul constraint of 512 bit/s/Hz .

4.3 Accuracy of the Proposed Large-Blocklength Approximations

In Section 3.4, we proposed two large-blocklength approximations to the RCUs bounds (A.12) and (A.14). Focusing on the uplink, we shall now discuss the accuracy of these approximations. Specifically, we compare the error probability bound given by (i) the RCUs bound (A.12), (ii) the normal approximation (A.18), (iii) the GMI-based outage probability (A.26) (computed for $p = n_p/n_{\mathrm{ul}}$), and (iv) the perfect-CSI outage probability (A.30). In Fig. 4, we present this comparison for the case $Q = 1$, $n_{\mathrm{ul}} = 500$, and $U = 8$. Specifically, we report the error probability as predicted by the different bounds/approximations, versus the number of transmit antennas B when each user transmits at a rate R of 0.5 bit/s/Hz. As in Section 4.2, we consider two values for the transmit power. The reported error probability bounds are optimized over the number of transmitted pilots n_p. Furthermore, the bound (A.12) and the normal approximation (A.18) are optimized over the parameter s. As shown in the figure, for the range of error probabilities considered here, the predictions obtained using the RCUs bound (A.12) and

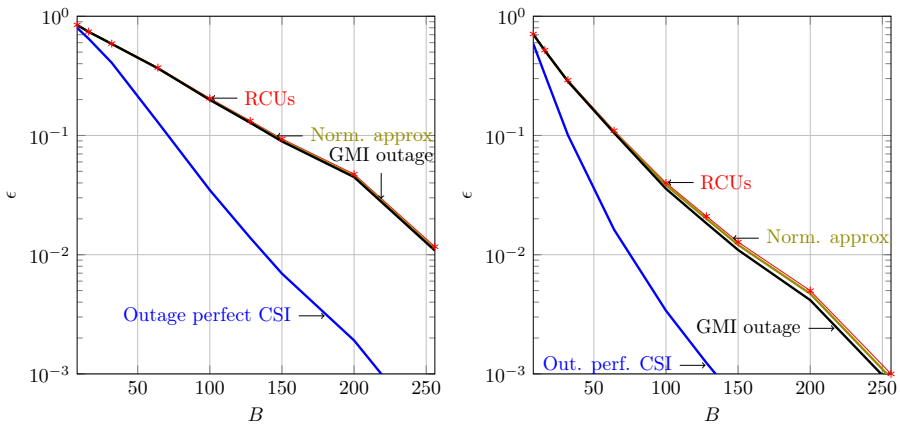

(a) $\rho^{\mathrm{ul}} = 16$ dBm **(b)** $\rho^{\mathrm{ul}} = 24$ dBm

Figure 4: Comparison between the proposed bounds and approximations on the uplink packet-error probability achievable for the case $Q = 1$, $U = 8$, $n_{\mathrm{ul}} = 500$, and $R = 0.5\,\mathrm{bit/s/Hz}$. The error probability curves are optimized over the number of transmitted pilots.

the normal approximation (A.18) match the ones obtained using the GMI-based outage probability (A.16). On the contrary, the predictions based on the perfect-CSI outage-probability approximation provided in (A.30) turn out to highly underestimate the error probability. The optimal number of pilot symbols in Fig. 4 is around 48 for higher values of the error probability, and increases to around 56 for error probability values around 10^{-2} and below. A similar result holds for the other values of quantizer resolution Q considered in this section as well as for the downlink.

Based on these results, we shall use the GMI-based outage bounds (A.26) and (A.31) as performance metrics when conducting the system-optimization investigations reported in the following two sections.

4.4 Impact of Dithering

We now focus on the case $Q = 1$ and investigate the impact of dithering on both uplink and downlink performance. We set $B = 256$, $n_p = 48$, and investigate the impact of dithering on the GMI-based outage bounds (A.26) and (A.31). The other system parameters are as in the previous sections. Dithering is only used in the channel-estimation phase. Indeed, for the parameters considered in this section, dithering in the data-transmission phase does not yield any benefits. The reason is that the residual multiuser interference after linear spatial processing acts as dithering and is sufficient to induce stochastic resonance. We model dithering by assuming that the smallest channel-estimation MSE achievable for the case $Q = 1$, which is achieved by transmitting pilot symbols at a power of around 20 dBm (see Fig. 3) can be maintained for all values of $\rho^{\mathrm{ul}} \geq 20\,\mathrm{dBm}$. We also assume that the uplink operates at a much lower power than the downlink. Specifically, the channel estimate used to generate the downlink precoder is obtained via a pilot-transmission uplink phase in which the pilot symbols are transmitted at a power level that is 26 dB less than the downlink power ρ^{dl}.

In Fig. 5, we depict the maximum achievable rate compatible with a GMI-based outage probability not exceeding 0.1. As shown in the figure, dithering in the channel estimation phase is beneficial in the uplink. Indeed, without dithering the rate drops rapidly as the transmit power is increased beyond 20 dBm, whereas, with dithering, the achievable rate does not decrease with the transmit power, apart from a small rate reduction at 21 dBm, which is the power level at which dithering is first introduced. Interestingly, using dither-

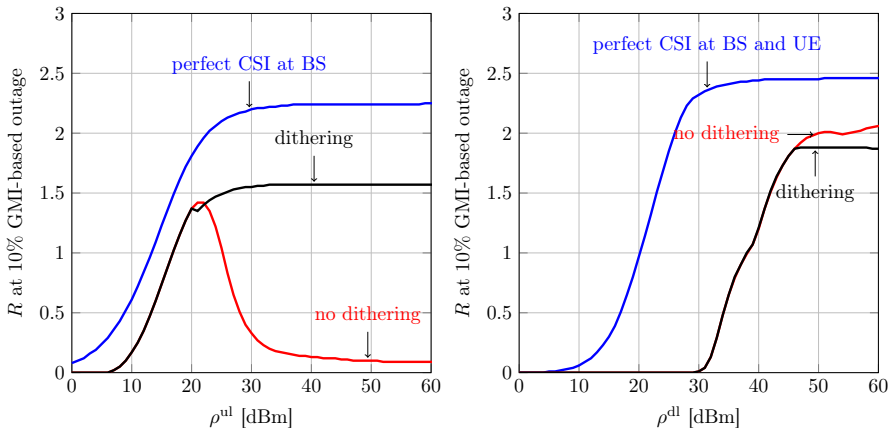

(a) Uplink **(b)** Downlink

Figure 5: Impact of dithering during the channel-estimation phase on the uplink and downlink performance.

ing in the channel-estimation phase has no benefits in the downlink, for the range of transmitted-power values considered in the figure. The reason is as follows: although, both in the uplink and in the downlink, the decoder operates according to the scaled nearest-neighbor principle, the scaling parameter in the two setups is different. In the uplink, we use the scaling parameter $\hat{g}_u^{\mathrm{ul}} = \mathbf{w}_u{}^{\mathsf{H}}\mathbf{G}^{\mathrm{ul}}\boldsymbol{A}\hat{\mathbf{h}}_u$ whereas in the downlink we use the hardening-bound-inspired scaling parameter $\hat{g}_u^{\mathrm{dl}} = \alpha\mathbb{E}[\mathbf{h}_u^{\mathrm{T}}\mathbf{G}^{\mathrm{dl}}\mathbf{p}_u]$. It turns out that the explicit dependence of $\hat{g}^{\mathrm{ul}}$ on $\hat{\mathbf{h}}_u$ makes this bound sensitive to the lack of stochastic resonance occurring when ρ^{ul} exceeds 20 dBm.

4.5 Optimal Number of Pilot Symbols

We consider again as performance metric the maximum rate that is compatible with a GMI-based uplink outage probability not exceeding 0.1, and investigate the optimal number of pilot symbols for different values of Q and B chosen so as to satisfy the fronthaul constraint. In Table 1 and 2, we report, for both $\rho^{\mathrm{ul}} = 16\,\mathrm{dBm}$ and $\rho^{\mathrm{ul}} = 24\,\mathrm{dBm}$, the optimal number of pilots as well as the rate penalty incurred when setting $n_p = 48$, which is the value we considered

Table 1: Optimal value of n_p and rate penalty when n_p is set to 48: $\rho^{\mathrm{ul}} = 16$ dBm.

(Q, B)	$(1, 256)$	$(2, 128)$	$(3, 85)$	$(4, 64)$	$(5, 51)$	$(6, 42)$	$(7, 38)$	$(8, 32)$
$n_p^\star$	64	60	60	60	128	128	128	128
Rate pen. [%]	4.34	4.41	4.83	4.83	5.88	14.70	17.85	20.83

Table 2: Optimal value of n_p and rate penalty when n_p is set to 48: $\rho^{\mathrm{ul}} = 24$ dBm; dithering is used for the pair $(1, 256)$.

(Q, B)	$(1, 256)$	$(2, 128)$	$(3, 85)$	$(4, 64)$	$(5, 51)$	$(6, 42)$	$(7, 38)$	$(8, 32)$
$n_p^\star$	48	36	36	40	36	40	40	48
Rate pen. [%]	0	0	0	0	0	0	0	0

in Figs. 2, 3, and 5. As shown in the tables, this rate penalty is negligible for $\rho^{\mathrm{ul}} = 24\,\mathrm{dBm}$. Indeed, for this transmit-power value the rate curve as a function of the number of pilot symbols is flat around its maximum. The rate penalty is also small for $\rho^{\mathrm{ul}} = 16\,\mathrm{dBm}$ for small Q values, but it increases for larger Q values.

4.6 Number of Antennas vs. Data-Converter Resolution

Finally, we investigate how one should select the number of antennas and the resolution of the quantizers to maximize the uplink and downlink rates given a GMI-based outage constraint of 0.1, hence addressing the central question that motivated our investigation. In Fig. 6, we report the uplink and the downlink rates for the pair $\rho^{\mathrm{ul}} = 16\,\mathrm{dBm}$, $\rho^{\mathrm{dl}} = 42\,\mathrm{dBm}$, as well as for the pair $\rho^{\mathrm{ul}} = 24\,\mathrm{dBm}$, $\rho^{\mathrm{dl}} = 50\,\mathrm{dBm}$, as a function of the resolution Q of the quantizers, for a fronthaul rate of $512\,\mathrm{bit/s/Hz}$. Motivated by machine-type communications where an uplink data-collection phase is followed by the transmission of a control command on the downlink, we also report the bi-directional rate, which we define as the largest rate R for which the bi-directional outage probability

$$\mathbb{P}\left[\min\left\{(1-p)\left(\sup_{s>0} I_{u,s}^{\mathrm{ul}}\right), \left(\sup_{s>0} I_{u,s}^{\mathrm{dl}}\right)\right\} < R\right] \tag{A.43}$$

does not exceed 0.1. The uplink rates are optimized over the choice of n_p; the channel estimates obtained using the resulting number of pilots is used to determine the downlink precoder. For the case $Q = 1$, dithering in the

channel-estimation phase is introduced whenever beneficial. We see from the figure that, in the perfect-CSI case (Figs. 6a and 6b), the system is uplink-limited and the bi-directional rate curve follows closely the uplink-rate curve. In the uplink, for both transmit power values considered in the figure, the rate is maximized when $Q = 1$, which yields a BS with $B = 256$ antennas. Indeed, since the system is power-limited in the uplink, the array gain resulting from the deployment of additional antennas, offsets the increased quantization noise resulting from the choice of 1-bit converters. On the contrary, the choice $Q = 1$ is suboptimal in the downlink, where, instead, the rate is maximized when $Q = 5$ and $Q = 6$, respectively. Here, the reduction in quantization noise and, hence, also multiuser interference (recall that we use a quantization-unaware linear precoder) resulting from this choice of Q, which yields $B = 51$ and $B = 42$, respectively, offsets the reduction in array gain.

The picture changes when one considers the case of pilot-assisted transmission and accounts for the inaccurate channel estimate available at the BS. Indeed, as shown in Fig. 6c and 6d, imperfect CSI yields a significant reduction in the downlink rates, although the system still remains uplink limited. Similarly to the perfect-CSI case, for both values of transmitted power considered in the figures, the downlink rate is maximized when $Q = 5$. In the uplink, however, the value $Q = 1$ is optimal only for the pair $\rho^{\mathrm{ul}} = 16$ dBm and $\rho^{\mathrm{dl}} = 42$ dBm, whereas for the pair $\rho^{\mathrm{ul}} = 24$ dBm and $\rho^{\mathrm{dl}} = 50$ dBm, the uplink rate is maximizes when $Q = 3$ and the bi-directional rate when $Q = 4$.

Finally, we report in Fig. 7 the performance achievable using maximum-ratio combiner in the uplink and maximum-ratio beamformer in the downlink. As shown in the figure, the downlink performance reduces significantly so that no positive rate can be achieve in the bidirectional-transmission case, for the acquired-CSI scenario.

5 Conclusions

We have considered the problem of designing a multiuser massive MIMO architecture where the BS is equipped with low-precision converters and a fronthaul constraint limits the amount of data that can be exchanged between the RRH and the BBU. Furthermore, we have assumed that the communication link is used to exchange short packets over a quasi-static fading channels that

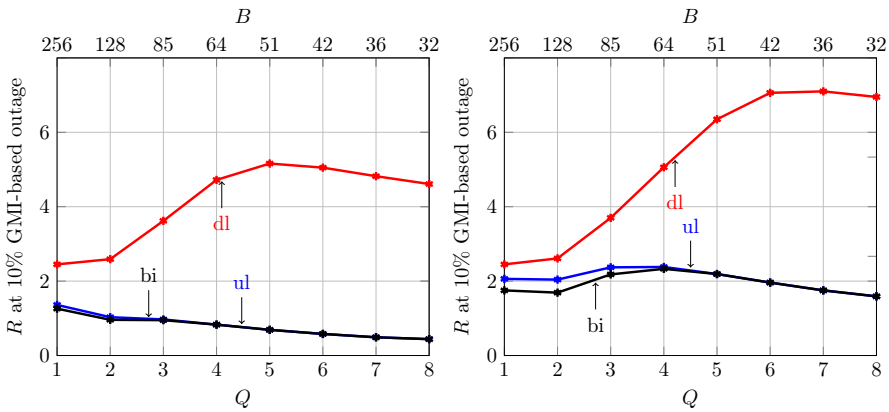

(a) $\rho^{\mathrm{ul}} = 16\,\mathrm{dBm}$, $\rho^{\mathrm{dl}} = 42\,\mathrm{dBm}$, perfect CSI **(b)** $\rho^{\mathrm{ul}} = 24\,\mathrm{dBm}$, $\rho^{\mathrm{dl}} = 50\,\mathrm{dBm}$, perfect CSI

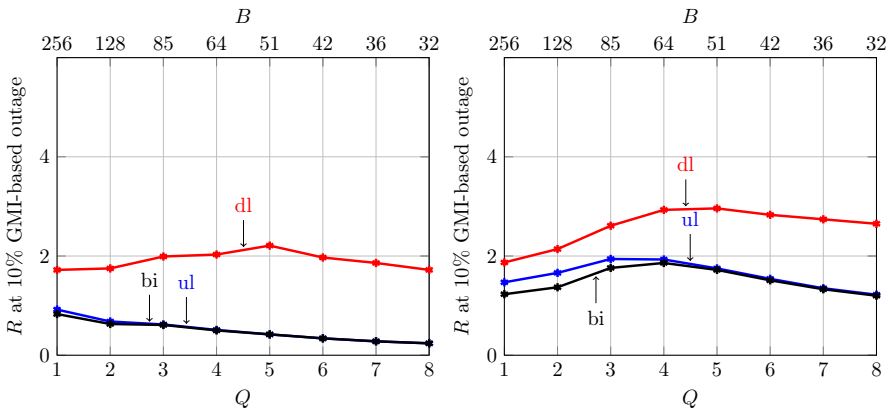

(c) $\rho^{\mathrm{ul}} = 16\,\mathrm{dBm}$, $\rho^{\mathrm{dl}} = 42\,\mathrm{dBm}$, acquired CSI **(d)** $\rho^{\mathrm{ul}} = 24\,\mathrm{dBm}$, $\rho^{\mathrm{dl}} = 50\,\mathrm{dBm}$, acquired CSI

Figure 6: Achievable rate at 10% GMI-based outage probability as a function of the quantizer resolution Q, for a fronthaul constraint of 512 bit/s/Hz.

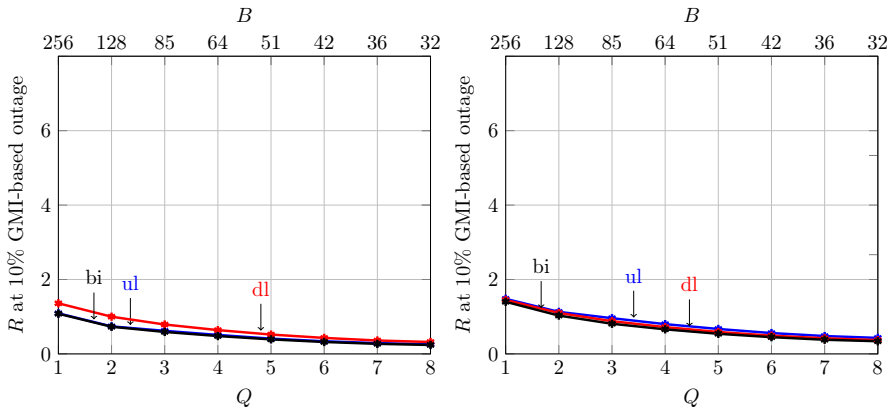

(a) $\rho^{\mathrm{ul}} = 16\,\mathrm{dBm}$, $\rho^{\mathrm{dl}} = 42\,\mathrm{dBm}$, perfect CSI **(b)** $\rho^{\mathrm{ul}} = 24\,\mathrm{dBm}$, $\rho^{\mathrm{dl}} = 50\,\mathrm{dBm}$, perfect CSI

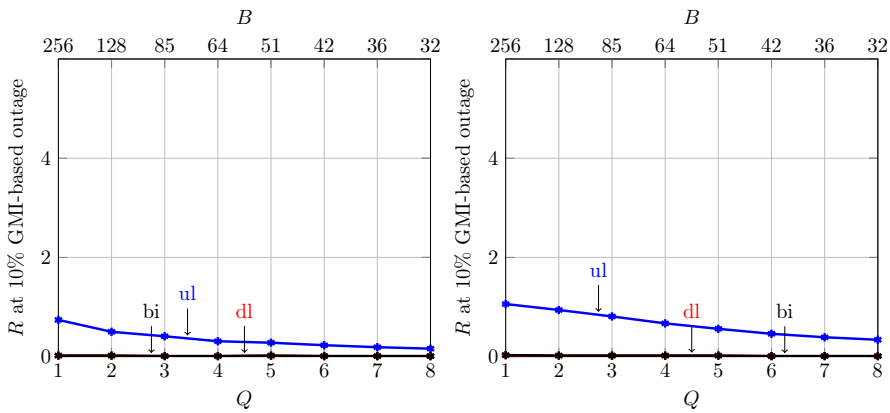

(c) $\rho^{\mathrm{ul}} = 16\,\mathrm{dBm}$, $\rho^{\mathrm{dl}} = 42\,\mathrm{dBm}$, acquired CSI **(d)** $\rho^{\mathrm{ul}} = 24\,\mathrm{dBm}$, $\rho^{\mathrm{dl}} = 50\,\mathrm{dBm}$, acquired CSI

Figure 7: Achievable rate at 10% GMI-based outage probability as a function of the quantizer resolution Q, for a fronthaul constraint of 512 bit/s/Hz; Maximum ratio combiner and maximum ratio precoder.

is not known a priori to the BS and the UEs and is estimated via uplink pilots. Our main contribution is a general framework for the characterization of the error probability in this setup, which relies on the RCUs bound from finite-blocklength information theory, a scaled nearest-neighbor decoder, and the use of Bussgang decomposition. We present both finite-blocklength bounds, and asymptotic approximations based on the GMI, which turn out to be accurate for moderate error-probability targets (see Fig. 4).

Using our bounds, we have conducted a number of experiments that shed light on the optimal design of the considered system. In particular, we have shown that when the lack of accuracy in the acquired CSI is accounted for, architectural solutions involving large antenna arrays connected to 1-bit to 4-bit converters, depending on the transmit-power values, are preferable.

References

[1] L. Lu, G. Y. Li, A. L. Swindlehurst, A. Ashikhmin, and R. Zhang, "An overview of massive MIMO: Benefits and challenges," vol. 8, no. 5, pp. 742–758, Apr. 2014.

[2] Ö. T. Demir, E. Björnson, and L. Sanguinetti, *Foundations of user centric cell-free massive MIMO* (Foundations and Trends in Signal Processing 3-4). 2020, vol. 14.

[3] S.-H. Park, O. Simeone, O. Sahin, and S. Shamai Shitz, "Fronthaul Compression for Cloud Radio Access Networks: Signal processing advances inspired by network information theory," *IEEE Signal Process. Mag.*, vol. 31, no. 6, pp. 69–79, Nov. 2014, ISSN: 1558-0792.

[4] S. Jacobsson, G. Durisi, M. Coldrey, U. Gustavsson, and C. Studer, "Throughput analysis of massive MIMO uplink with low-resolution ADCs," *IEEE Trans. Wireless Commun.*, vol. 16, no. 6, pp. 4038–4051, Jun. 2017.

[5] C. Mollén, J. Choi, E. G. Larsson, and R. W. Heath, "Uplink performance of wideband massive MIMO with one-bit ADCs," *IEEE Trans. Wireless Commun.*, vol. 16, no. 1, pp. 87–100, Jan. 2017, ISSN: 1536-1276.

[6] E. Björnson, L. Sanguinetti, and J. Hoydis, "Hardware distortion correlation has negligible impact on UL massive MIMO spectral efficiency," *IEEE Trans. Commun.*, vol. 67, no. 2, pp. 1085–1098, Feb. 2019, ISSN: 0090-6778, 1558-0857.

[7] S. Jacobsson, G. Durisi, M. Coldrey, T. Goldstein, and C. Studer, "Quantized precoding for massive MU-MIMO," *IEEE Trans. Commun.*, vol. 65, no. 11, pp. 4670–4684, Nov. 2017.

[8] Y. Li, C. Tao, A. L. Swindlehurst, A. Mezghani, and L. Liu, "Downlink achievable rate analysis in massive MIMO systems with one-bit dacs," *IEEE Commun. Lett.*, vol. 21, no. 7, pp. 1669–1672, Mar. 2017.

[9] N. Liang and W. Zhang, "Mixed-ADC massive MIMO," *IEEE J. Sel. Areas Commun.*, vol. 34, no. 4, pp. 983–997, Apr. 2016.

[10] A. K. Saxena, I. Fijalkow, and A. L. Swindlehurst, "Analysis of one-bit quantized precoding for the multiuser massive MIMO downlink," *IEEE Trans. Signal Processing*, vol. 65, no. 17, pp. 4624–4634, Jun. 2017.

[11] Y. Li, C. Tao, G. Seco-Granados, A. Mezghani, A. L. Swindlehurst, and L. Liu, "Channel estimation and performance analysis of one-bit massive MIMO systems," *IEEE Trans. Signal Process.*, vol. 65, no. 15, pp. 4075–4089, Aug. 2017.

[12] J. Mo, P. Schniter, and R. W. Heath, "Channel estimation in broadband millimeter wave MIMO systems with few-bit ADCs," *IEEE Trans. Signal Processing*, vol. 66, no. 5, pp. 1141–1154, Mar. 2017.

[13] C. Studer and G. Durisi, "Quantized massive MU-MIMO-OFDM uplink," *IEEE Trans. Commun.*, vol. 64, no. 6, pp. 2387–2399, Jun. 2016.

[14] L. V. Nguyen, A. L. Swindlehurst, and D. H. N. Nguyen, "SVM-based channel estimation and data detection for one-Bit massive MIMO systems," *IEEE Trans. Signal Process.*, vol. 69, pp. 2086–2099, Mar. 2021, ISSN: 1941-0476.

[15] S. S. Thoota and C. R. Murthy, "Massive MIMO-OFDM Systems with low resolution ADCs: Cramér-Rao bound, sparse channel estimation, and soft symbol decoding," *IEEE Trans. Signal Process.*, vol. 70, pp. 4835–4850, 2022, ISSN: 1941-0476.

[16] L. V. Nguyen, D. H. N. Nguyen, and A. L. Swindlehurst, "Deep learning for estimation and pilot signal design in few-bit massive MIMO systems," *IEEE Trans. Wireless Commun.*, vol. 22, no. 1, pp. 379–392, Jan. 2023, ISSN: 1558-2248.

[17] S. Jacobsson, G. Durisi, M. Coldrey, and C. Studer, "Linear precoding with low-resolution DACs for massive MU-MIMO-OFDM downlink," *IEEE Trans. Wireless Commun.*, vol. 18, no. 3, pp. 1595–1609, Mar. 2019.

[18] Y. Khorsandmanesh, E. Björnson, and J. Jaldén, "Quantisation-aware precoding for MU-MIMO with limited-capacity fronthaul," in *Proc. IEEE Int. Conf. Acoust., Speech, Signal Process. (ICASSP)*, Singapore, May 2022.

[19] A. S. Nedelcu, F. Steiner, and G. Kramer, "Low-resolution precoding for multi-antenna downlink channels and OFDM," *Entropy*, vol. 24, no. 4, p. 504, Apr. 2022, ISSN: 1099-4300.

[20] O. Castañeda, S. Jacobsson, G. Durisi, T. Goldstein, and C. Studer, "Finite-alphabet MMSE equalization for all-digital massive MU-MIMO mmWave communications," *IEEE J. Sel. Areas Commun.*, vol. 38, no. 9, Sep. 2020.

[21] M. Bashar, K. Cumanan, A. G. Burr, H. Q. Ngo, E. G. Larsson, and P. Xiao, "Energy efficiency of the cell-free Massive MIMO Uplink with optimal uniform quantization," *IEEE Trans. Green Commun. Netw.,*, vol. 3, no. 4, pp. 971–987, Dec. 2019, ISSN: 2473-2400.

[22] Y. Zhang, M. Zhou, X. Qiao, H. Cao, and L. Yang, "On the performance of cell-free massive MIMO with low-resolution ADCs," *IEEE ACCESS*, vol. 7, pp. 117 968–117 977, 2019, ISSN: 2169-3536.

[23] X. Hu, C. Zhong, X. Chen, W. Xu, H. Lin, and Z. Zhang, "Cell-free Massive MIMO systems with low resolution ADCs," *IEEE Trans. Commun.*, vol. 67, no. 10, pp. 6844–6857, Oct. 2019, ISSN: 1558-0857.

[24] G. Femenias and F. Riera-Palou, "Fronthaul-constrained cell-free massive MIMO with low resolution ADCs," *IEEE Access*, vol. 8, pp. 116 195–116 215, 2020, ISSN: 2169-3536.

[25] M. Bashar, P. Xiao, R. Tafazolli, K. Cumanan, A. G. Burr, and E. Björnson, "Limited-fronthaul cell-free massive MIMO with local MMSE receiver under Rician fading and phase shifts," *IEEE Wireless Commun. Lett.*, vol. 10, no. 9, Sep. 2021, ISSN: 2162-2345.

[26] J. Östman, A. Lancho, G. Durisi, and L. Sanguinetti, "URLLC with massive MIMO: Analysis and design at finite blocklength," *IEEE Trans. Wireless Commun.*, vol. 20, no. 10, pp. 6387–6401, Apr. 2021.

[27] E. Björnson, J. Hoydis, and L. Sanguinetti, "Massive MIMO networks: Spectral, energy, and hardware efficiency," *Found. Trends Signal Process.*, vol. 11, no. 3-4, pp. 154–655, 2017.

[28] Y. Polyanskiy, H. V. Poor, and S. Verdú, "Channel coding rate in the finite blocklength regime," *IEEE Trans. Inform. Theory*, vol. 56, no. 5, pp. 2307–2359, Apr. 2010.

[29] A. Martinez and A. Guillén i Fàbregas, "Saddlepoint approximation of random–coding bounds," in *Proc. Inf. Theory Applicat. Workshop (ITA)*, San Diego, CA, U.S.A., Feb. 2011.

[30] A. Lapidoth and S. Shamai (Shitz), "Fading channels: How perfect need 'perfect side information' be?" *IEEE Trans. Inf. Theory*, vol. 48, no. 5, pp. 1118–1134, May 2002.

[31] J. J. Bussgang, "Crosscorrelation functions of amplitude-distorted Gaussian signals," Res. Lab. Elec., Cambridge, MA, Tech. Rep. 216, Mar. 1952.

[32] A. Ganti, A. Lapidoth, and I. Telatar, "Mismatched decoding revisited: General alphabets, channels with memory, and the wide-band limit," *IEEE Trans. Inf. Theory*, vol. 46, no. 7, pp. 2315–2328, Nov. 2000, ISSN: 0018-9448.

[33] S. Jacobsson, U. Gustavsson, G. Durisi, and C. Studer, "Massive MU-MIMO-OFDM uplink with hardware impairments: Modeling and analysis," in *Proc. Allerton Conf. Commun., Contr., Comput.*, Pacific Grove CA, U.S.A., Nov. 2018.

[34] O. T. Demir and E. Björnson, "The Bussgang decomposition of nonlinear systems: Basic theory and MIMO extensions [Lecture Notes]," *IEEE Signal Process. Mag.*, vol. 38, no. 1, pp. 131–136, Jan. 2021, ISSN: 1558-0792.

[35] W. Feller, *An Introduction to Probability Theory and its Applications*, 2nd ed. New York, NY, USA, 1971, vol. II.

[36] O. El Ayach, S. Rajagopal, S. Abu-Surra, Z. Pi, and R. W. Heath, "Spatially sparse precoding in millimeter wave MIMO systems," *IEEE Trans. Wireless Commun.*, vol. 13, no. 3, pp. 1499–1513, Mar. 2014.

[37] A. Alkhateeb, O. El Ayach, G. Leus, and R. W. Heath, "Channel estimation and hybrid precoding for millimeter wave cellular systems," *IEEE J. Select. Areas Commun.*, vol. 8, no. 5, pp. 831–846, Jul. 2014.

[38] R. W. Heath, N. Gonzalez-Prelcic, S. Rangan, W. Roh, and A. M. Sayeed, "An overview of signal processing techniques for millimeter wave MIMO systems," *IEEE J. Select. Areas Commun.*, vol. 10, no. 3, pp. 436–453, Feb. 2016.

[39] J. H. Van Vleck and D. Middleton, "The spectrum of clipped noise," *Proc. IEEE*, vol. 54, no. 1, pp. 2–19, Jan. 1966.

[40] J. Mo, P. Schniter, N. G. Prelcic, and R. W. Heath, "Channel estimation in millimeter wave MIMO systems with one-bit quantization," in *Proc. Asilomar Conf. Signals, Syst., Comput.,*, Pacific Grove, CA, USA, Apr. 2014, pp. 957–961.

[41] Y. Ettefagh, S. Jacobsson, A. Hu, G. Durisi, and C. Studer, "All-digital massive MIMO uplink and downlink rates under a fronthaul constraint," in *Proc. Asilomar Conf. Signals, Syst., Comput.,*, Pacific Grove, CA, USA, Nov. 2019, pp. 416–420.

[42] N. J. Myers, K. N. Tran, and R. W. Heath Jr., "Low-rank MMWAVE MIMO channel estimation in one-bit receivers," in *IEEE Int. Conf. Acoust., Speech, Signal Process. (ICASSP)*, Barcelona, Spain, May 2020, pp. 5005–5009.

[43] R. Zhou, H. Du, and D. Zhang, "Millimeter wave MIMO channel estimation with one-bit receivers," *IEEE Commun. Lett.*, vol. 26, no. 1, pp. 158–162, Jan. 2022.

[44] O. Dabeer and A. Karnik, "Signal parameter estimation using 1-bit dithered quantization," *IEEE Trans. Inform. Theory*, vol. 52, no. 12, pp. 5389–5405, Dec. 2006.

PAPER B

Frugal RIS-aided 3D Localization with CFO under LoS and NLoS Conditions

Y. Ettefagh, MF. Keskin, K. Kheykhosravi, G. Seco-Granados, and H. Wymeersch

Submitted to IEEE Transactions on Vehicular Technology

The layout has been revised.

Abstract

In this paper, we investigate 3-D localization and frequency synchronization with multiple RISs in the presence of CFO for a stationary UE. In line with the 6G goals of sustainability and efficiency, we focus on a *frugal* communication scenario with minimal spatial and spectral resources (i.e., narrowband single-input single-ouput system), considering both the presence and blockage of the LoS path between the BS and the UE. We design a generalized likelihood ratio test (GLRT)-based LoS detector, channel parameter estimation and localization algorithms, with varying complexity. To verify the efficiency of our estimators, we compare the root mean-squared error (RMSE) to the Cramér-Rao bound (CRB) of the unknown parameters. We also evaluate the sensitivity of our algorithms to the presence of uncontrolled multi-path components (MPC) and various levels of CFO. Simulation results showcase the effectiveness of the proposed algorithms under minimal hardware and spectral requirements, and a wide range of operating conditions, thereby confirming the viability of RIS-aided frugal localization in 6G scenarios.

1 Introduction

ACCURATE positioning is a pre-requisite for many modern use-cases, finding applications in various areas such as autonomous driving, augmented reality, navigation, etc. [1]. While Global Positioning System (GPS) stands out as the ubiquitous solution for navigation, its efficacy is often compromised in scenarios where a direct line of sight to satellites is obstructed, such as in tunnels, dense urban environments and indoors. An alternative solution is to use cellular networks. Cellular networks have been used for positioning since the first generation (1G) of mobile networks [2]. In 4G networks, time difference of arrival (TDoA) and angle-of-arrival (AoA)-based techniques were introduced, which rely on multiple base stations to estimate the position of a mobile device. These techniques proved to be more accurate than the previous ones, but required additional infrastructure and were not

suitable for indoor environments. In 5G networks, the adoption of mmWave frequencies and beamforming techniques improved the accuracy of positioning [3]–[5]. In 6G networks, the use of reconfigurable intelligent surfaces (RISs) is expected to further enhance the accuracy and reliability of cellular-based localization [6]–[9].

In advancement of wireless communications through successive generations, achieving sustainability and improving energy and spectral efficiency has always been a central objective, and the upcoming 6G is no exception [10]. As pointed out, 4G networks succeeded in improving positioning by putting a minimum requirement on hardware resources and 5G managed to progress further in positioning by accessing large chunks of bandwidth in mmWave and large antenna arrays. Therefore, the question remains whether 6G will continue this trend or if there could be another solution to achieve improved positioning without leveraging more resources. The use of RISs appears to be a key point in this regard.

RISs constitute one of the key-technology enablers for 6G [11], providing an additional, controllable path between the base station (BS) and the user equipment (UE). Primarily, RISs are designed as a cost-effective and energy-efficient solution to address signal blockage challenges without the need to densify the network with more BSs. This approach is favored due to the simpler hardware requirements and lower maintenance costs associated with RIS [12], [13]. RISs consist of a large number of small elements that can be manipulated to reflect incident waves in desired directions [14]. Deploying RISs in an environment allows for the engineering of the propagation medium, enhancing signal strength and reducing interference at targeted locations [15]. This ultimately enhances communication rate and coverage [16] while providing significant gains in localization performance [17].

The use of RISs in radio localization has been extensively studied in the literature, with numerous works exploring the potential of RISs to improve UE localization thanks to the additional reflected paths [18]–[21]. Notable contributions include [6], [18], [19], which discuss the challenges, opportunities, and research directions related to RIS-aided positioning. Since localization often comes as a by-product of cellular communication systems, it is advantageous if it is *frugal* with resources, such as antennas and time-frequency allocations, to avoid compromising the quality and infrastructure requirements of wireless communications—so far the primary objective of cellular networks. Along this

line, RIS-based narrowband (NB) localization was discussed in [22], where a NB RIS-based multiple-input single-output (MISO) localization approach for a single-antenna UE was investigated. RIS-enabled localization with single BS and single antenna is discussed in [23], [24]. In [23], a localization and clock-synchronization approach to single-input single-output (SISO), single RIS wideband (WB) case was introduced. In [24], authors propose a method for single-antenna receiver 2-D localization and achieve centimeter-level localization accuracy with fingerprinting the RIS-phases over time. A broader perspective on frugal localization was taken in [25], which conducted an analysis on UE localization scenarios with minimal required number of BS and RISs, showing that it is possible to estimate the UE's position with one BS and two RISs under NB communication even without a direct path from the BS to the UE.

A common weakness in the above works is that they ignore the presence of carrier frequency offset (CFO) between the BS and the UE. Since both CFO and the use of diverse RIS phase profiles [26] (i.e., beam sweeping for angle-of-departure (AoD) estimation from the RIS using beamspace measurements at the UE [22], [27]) over time lead to phase variations across consecutive transmissions, the impacts of CFO and RIS profile variation add up together in the time-series of phase shifts, resulting in the so-called *angle-Doppler/CFO coupling effect*, as noted in [28], [29]. In real systems, accurate estimation and compensation of CFO are vital for localization and communication performance. Techniques vary by application; for instance, in [30] a pilot-based approach using orthogonal pilots and a Hadamard matrix structure allows efficient CFO estimation and compensation, enhancing localization accuracy by reducing phase distortions. Similarly, [31] employs a synthetic aperture method to jointly estimate AoD and CFO, improving resolution in multi-path environments. From an experimental perspective, [25] demonstrates SISO localization of a stationary UE with one BS and two RISs in the absence of a CFO. However, this study has the impractical requirement that the BS and UE share a common oscillator to eliminate CFO issues. Moreover, the approach relies on using directional RIS beams to sweep potential locations and estimate AoDs from the RISs. This method is ineffective with random RIS phase profiles, which are commonly used in RIS-aided communications when UE locations are unknown, e.g., [32]–[34]. Overall, no systematic study has been conducted to address the problem of *frugal localization* and frequency

synchronization with the help of RISs under angle/CFO coupling effect and when employing random RIS phase configurations. Therefore, in light of the existing literature, two crucial questions emerge that remain unanswered: *(i)* is it possible to perform joint 3-D downlink localization and frequency synchronization in the challenging NB (i.e., single-carrier) SISO scenario with multiple RISs employing random phase configurations?; and *(ii)* can efficient and low-complexity algorithms be developed for line-of-sight (LoS) presence detection, channel parameter/CFO estimation and localization in both the presence and absence of the direct LoS path between the BS and the UE?

In an attempt to address the identified shortcomings of existing studies on RIS-aided localization and fill the corresponding research gaps, we consider the frugal localization problem of a UE in case of NB SISO signaling via one BS and several RISs employing random phase profiles. The novel contributions of this paper can be summarized as follows.

- **Frugal localization under CFO:** We formalize the problem of NB RIS-aided SISO localization and frequency synchronization under the assumption of CFO between the transmitter and the receiver with parsimonious usage of resources. We develop novel low-complexity estimators of the unknowns, including the CFO and AoDs, which enable us to perform localization. Different estimation algorithms under various circumstances are designed, including one estimation algorithm in case the direct LoS between the BS and the UE is present, as well as two estimation algorithms in case of blocked LoS between the BS and UE. Our estimators achieve the theoretical bounds at moderate to high transmit power. Simulation results show the efficiency of the estimator with respect to theoretical bounds.

- **LoS detection:** We design a generalized likelihood ratio test (GLRT)-based detector to determine if the LoS exists or not, which complements the above contribution to a full localization and synchronization algorithm. Our proposed algorithm is capable of attaining the theoretical bounds at a moderate to high transmit power.

- **Sensitivity analysis:** We assess the sensitivity of our algorithm to multi-path components (MPC), which shows that our algorithm quickly converges to the achievable bounds with Rician factor as small as 10. We also study the sensitivity of location estimation under UE motion. More-

over, we compare the performance of our algorithm with prior works in which CFO is not compensated for by ignoring CFO as an unknown. The performance drastically deteriorates at CFO values much smaller than values typically found in UE, suggesting the importance of accurate estimation of the CFO. These analyses provide us insight about the applicability of our algorithm, therefore they are listed as contributions of this work.

- **Resource Efficiency:** We prove that with a minimalistic spectral and BS/UE hardware configuration, including a single antenna and single subcarrier and sufficient number of RISs, it is possible to perform accurate positioning. Therefore, our approach sets a new benchmark for resource efficiency in communication systems, potentially reducing the cost and complexity of deployment, which is in accordance with 6G objectives.

The paper is structured as follows. In Sec. 2, the system setup is detailed. Sec. 3 describes orthogonal RIS profile design to facilitate per-RIS AoD and CFO estimation. Sec. 4 describes the overall flow of the algorithm, including channel parameter estimation under LoS and non-line-of-sight (NLoS), localization under LoS and NLoS, and detection of if the LoS is present or not. Channel parameter turns out to be the main challenge and low-complexity methods are derived in Sec. 5: in Sec. 5.1, estimation algorithms in case the direct link between the BS and UE (LoS) exists will be explained. Sec. 5.2 sheds light on estimation algorithms in the more challenging scenario in which the LoS path does not exist. The performance of the estimators and detector are shown and discussed in Sec. 6. Finally, Sec. 7 concludes the findings of the paper.

Notation

Vectors and matrices are shown by bold-face lower-case and bold-face upper-case letters respectively. The notations $(.)^{\mathsf{T}}$ and $(.)^{\mathsf{H}}$ indicate transpose and hermitian transpose. All one vector with size n denoted by $\mathbf{1}_n$ and the identity matrix with size n is represented by $\mathbf{I}_n$. The L2 norm of a vector is shown by $\|.\|$. The matrix $\boldsymbol{R}_z(\theta)$ denotes the 3-D rotation matrix by an angle θ about the z-axis. The Kronecker product and the Hadamard product are shown by $\otimes$ and $\odot$ respectively.

2 System Model

In this section, we describe the proposed localization system that promotes the parsimonious use of spatial and spectral resources for joint location and frequency offset estimation of a static user.

2.1 Scenario

Consider a RIS-aided downlink (DL) localization system with a single-antenna BS, R identical N-element RISs, and a single-antenna UE, as shown in Fig. 1. The BS and the RISs are located at known positions $\boldsymbol{p}_{\mathrm{b}} \in \mathbb{R}^3$ and $\boldsymbol{p}_{\mathrm{RIS},r} \in \mathbb{R}^3$, $r = 1, \cdots, R$ (denoting the RIS centers) respectively, while the UE has an unknown position $\boldsymbol{p} \in \mathbb{R}^3$. The RISs are assumed to have known orientations, represented by the unitary rotation matrices $\boldsymbol{R}_r \in \mathrm{SO}(3) \subset \mathbb{R}^{3\times 3}$, $r = 1, \cdots, R$, that map the global frame of reference to the local coordinate systems of the RISs. The UE is considered stationary. Moreover, due to oscillator inaccuracies, the UE is not perfectly frequency-synchronized to the BS, which leads to an unknown CFO $\nu \in \mathbb{R}$ at the UE with respect to the BS [35], [36].

2.2 Geometric Relations

The AoD from the r^{th} RIS to the UE is denoted by $\boldsymbol{\theta}_r = \left[[\boldsymbol{\theta}_r]_{\mathrm{az}}, [\boldsymbol{\theta}_r]_{\mathrm{el}}\right]^{\mathsf{T}} \in \mathbb{R}^2$, where

$$[\boldsymbol{\theta}_r]_{\mathrm{az}} = \operatorname{atan2}\left([\boldsymbol{r}_r]_2, [\boldsymbol{r}_r]_1\right), \tag{B.1}$$

$$[\boldsymbol{\theta}_r]_{\mathrm{el}} = \arccos\left(\frac{[\boldsymbol{r}_r]_3}{\|\boldsymbol{p} - \boldsymbol{p}_{\mathrm{RIS},r}\|}\right), \tag{B.2}$$

with $\boldsymbol{r}_r = \boldsymbol{R}_r(\boldsymbol{p} - \boldsymbol{p}_{\mathrm{RIS},r})$ representing the vector extending from the r^{th} RIS to the UE in the local frame of reference of the r^{th} RIS.

2.3 Signal Model

The BS transmits NB pilot symbols $\boldsymbol{s} = [s_0 \cdots s_{M-1}]^{\mathsf{T}} \in \mathbb{C}^M$ over M transmission instances with sampling period T_s and a power constraint P such that $\|\boldsymbol{s}\|^2 = MP$. Assuming the absence of uncontrolled multipath (i.e., due to reflection or scattering off passive objects) as in [22], [23], [32], [37], [38], the

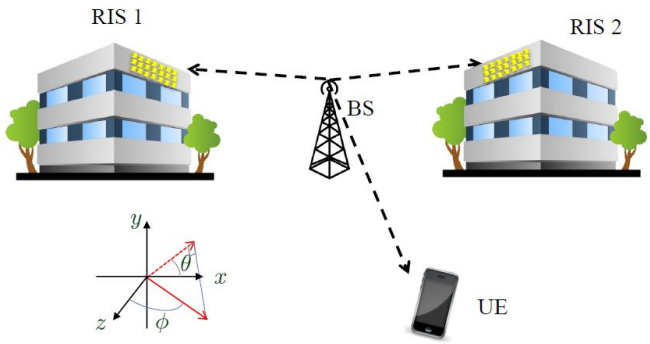

Figure 1: Frugal localization scenario involving one single-antenna BS, $R = 2$ RISs and one single-antenna user with NB (single-carrier) communication.

received complex baseband signal at the UE associated to the m^{th} transmission is given by

$$y_m = h_m e^{j2\pi m T_s \nu} s_m + n_m, \tag{B.3}$$

where $T_s \in \mathbb{R}$ is the symbol duration, the term $e^{j2\pi m T_s \nu}$ results from the CFO (ν) between the BS and the UE, $n_m \in \mathbb{C}$ denotes circularly symmetric complex Gaussian noise with $n_m \sim \mathcal{CN}(0, \sigma^2)$, and $h_m \in \mathbb{C}$ represents the overall BS-UE channel for the m^{th} transmission involving both the LoS path and the NLoS paths through the RISs, i.e.,[1]

$$h_m = h_{\text{LoS},m} + h_{\text{RIS},m}. \tag{B.4}$$

In (B.4), $h_{\text{LoS},m} \in \mathbb{C}$ is the LoS (i.e., direct) channel between the BS and the UE, written as

$$h_{\text{LoS},m} = \alpha_0, \tag{B.5}$$

where $\alpha_0 \in \mathbb{C}$ denotes the channel gain. As to the NLoS channel in (B.4), it

[1] In a section of the simulation results (Sec. 6.6), uncontrolled MPC will be incorporated into the channel model as part of a sensitivity analysis.

can be defined as

$$h_{\mathrm{RIS},m} = \sum_{r=1}^{R} \alpha_r \, \boldsymbol{a}^{\mathsf{T}}(\boldsymbol{\theta}_r) \mathrm{diag}(\boldsymbol{\gamma}_{r,m}) \boldsymbol{a}(\boldsymbol{\phi}_r), \tag{B.6}$$

where $\alpha_r \in \mathbb{C}$ is the channel gain over the BS-(r^{th} RIS)-UE path and $\boldsymbol{\phi}_r \in \mathbb{R}^2$ denotes the known AoA from the BS at the r^{th} RIS (given the known positions and orientations of the BS and the RISs). In addition, $\boldsymbol{\gamma}_{r,m} \in \mathbb{C}^N$ represents the phase profile of the r^{th} RIS at time m and $\boldsymbol{a}(\cdot) \in \mathbb{C}^N$ is the RIS steering vector, given by [23]

$$[\boldsymbol{a}(\boldsymbol{\psi})]_n = \exp\left(j \boldsymbol{k}^{\mathsf{T}}(\boldsymbol{\psi}) \boldsymbol{q}_n\right), \tag{B.7}$$

for a generic $\boldsymbol{\psi}$ where $\boldsymbol{q}_n \in \mathbb{R}^3$ denotes the known position of the n^{th} RIS element with respect to the RIS center in the local coordinate system of the RIS, and

$$\boldsymbol{k}(\boldsymbol{\psi}) = \frac{2\pi}{\lambda} \left[\sin([\boldsymbol{\psi}]_{\mathrm{el}}) \cos([\boldsymbol{\psi}]_{\mathrm{az}}),\, \sin([\boldsymbol{\psi}]_{\mathrm{el}}) \sin([\boldsymbol{\psi}]_{\mathrm{az}}),\, \cos([\boldsymbol{\psi}]_{\mathrm{el}})\right]^{\mathsf{T}} \tag{B.8}$$

is the wavenumber vector defined for a given angle $\boldsymbol{\psi}$. Let

$$\boldsymbol{W}_r \triangleq [\boldsymbol{a}(\boldsymbol{\phi}_r) \odot \boldsymbol{\gamma}_{r,0} \;\; \cdots \;\; \boldsymbol{a}(\boldsymbol{\phi}_r) \odot \boldsymbol{\gamma}_{r,M-1}] \in \mathbb{C}^{N \times M}, \tag{B.9}$$

$$\boldsymbol{b}(\nu) \triangleq [1 \;\; e^{j2\pi T_s \nu} \;\; \cdots \;\; e^{j2\pi (M-1) T_s \nu}]^{\mathsf{T}} \in \mathbb{C}^M. \tag{B.10}$$

Then, using (B.4)–(B.6) and (B.9)–(B.10), the aggregated observations in (B.3) over M transmissions can be written as [2]

$$\boldsymbol{y} = \sqrt{P}\Big(\alpha_0 \, \boldsymbol{b}(\nu) + \sum_{r=1}^{R} \alpha_r \, \boldsymbol{x}_r(\boldsymbol{\theta}_r) \odot \boldsymbol{b}(\nu)\Big) + \boldsymbol{n}, \tag{B.11}$$

where $\boldsymbol{y} \triangleq [y_0 \; \cdots \; y_{M-1}]^{\mathsf{T}} \in \mathbb{C}^M$, $\boldsymbol{x}_r(\boldsymbol{\theta}_r) = \boldsymbol{W}_r^{\mathsf{T}} \boldsymbol{a}(\boldsymbol{\theta}_r)$ and $\boldsymbol{n} \in \mathbb{C}^M$ is the noise component with $\boldsymbol{n} \sim \mathcal{CN}(\boldsymbol{0}, \sigma^2 \mathbf{I})$. In (B.11), we have set $s_m = \sqrt{P}$, $\forall m$ for simplicity.

[2] In Sec. 6.7, we extend the received signal model to account for UE motion with velocity $\boldsymbol{v}$. When the condition $|MT_s(\boldsymbol{p}_i - \boldsymbol{p})^{\mathsf{T}} \boldsymbol{v} / (\lambda \|\boldsymbol{p}_i - \boldsymbol{p}\|)| < 1/8$ holds (where $i \in \mathrm{b}, R_1, ..., R_r$), the Doppler-induced phase variation over the M transmissions is negligible [39].

2.4 Joint Localization and Frequency Synchronization Problem

The goal is to estimate the position $\boldsymbol{p}$ and the CFO ν of the UE from the observation $\boldsymbol{y}$ in (B.11). For this estimation problem, the unknown channel-domain parameters are given by

$$\boldsymbol{\eta}_{\text{ch}}^{\text{LoS}} = [\alpha_{\text{R},0}\ \alpha_{\text{I},0}\ \cdots\ \alpha_{\text{R},R}\ \alpha_{\text{I},R}\ \nu\ \boldsymbol{\theta}_1^{\mathsf{T}}\ \cdots\ \boldsymbol{\theta}_R^{\mathsf{T}}] \in \mathbb{R}^{4R+3}, \tag{B.12}$$

while the unknown location-domain parameter vector is

$$\boldsymbol{\eta}^{\text{LoS}} = [\alpha_{\text{R},0}\ \alpha_{\text{I},0}\ \cdots\ \alpha_{\text{R},R}\ \alpha_{\text{I},R}\ \nu\ \boldsymbol{p}^{\mathsf{T}}]^{\mathsf{T}} \in \mathbb{R}^{2R+6}. \tag{B.13}$$

Here, $\alpha_{\text{R},r} \triangleq \Re\{\alpha_r\}$ and $\alpha_{\text{I},r} \triangleq \Im\{\alpha_r\}$, $r = 0, \cdots, R$. The superscript 'LoS' is used to highlights that the LoS path exists. Clearly, in case no LoS exists between the UE and the BS, the channel-domain vector and the location-domain vector would change into $\boldsymbol{\eta}_{\text{ch}}^{\text{NLoS}} = [\alpha_{\text{R},1}\ \alpha_{\text{I},1}\ \cdots\ \alpha_{\text{R},R}\ \alpha_{\text{I},R}\ \nu\ \boldsymbol{\theta}_1^{\mathsf{T}}\ \cdots\ \boldsymbol{\theta}_R^{\mathsf{T}}] \in \mathbb{R}^{4R+1}$, and $\boldsymbol{\eta}^{\text{NLoS}} = [\alpha_{\text{R},1}\ \alpha_{\text{I},1}\ \cdots\ \alpha_{\text{R},R}\ \alpha_{\text{I},R}\ \nu\ \boldsymbol{p}^{\mathsf{T}}]^{\mathsf{T}} \in \mathbb{R}^{2R+4}$, respectively. The superscripts 'NLoS' is used to denote that the LoS path does not exist.

It should be noted that the LoS path does not directly convey positional information because the UE's position is a function of the AoDs according to (B.1)–(B.2). In our formulation, the LoS component appears solely as a complex scalar whose phase evolves over time according to the CFO, and does not include any AoD-dependent terms. However, as we will see in Sec. 6, the accuracy of CFO estimation is improved if the LoS is present, and as a result, the residual error in RIS path separation[3] decreases as discussed in Sec. 3, simplifying also the AoD estimation algorithm.

3 RIS Profile Design

Estimating the channel-domain parameters in (B.12) requires a complex high-dimensional optimization, which is cumbersome even in the case of $R = 2$. To circumvent this, we leverage the controllability offered by the RIS by designing an orthogonal temporal-coding for RIS phase profiles [40]. In the absence of CFO, the contributions from $R + 1$ paths in (B.11) can be separated and the

[3] To be able to estimate AoDs separately from each RIS, signal components corresponding to different RISs in (B.11) need to be separated.

unknowns from each RIS path can be estimated separately.

3.1 Hadamard-based Design

The idea involves using the rows of the Hadamard matrix to encode the phase profiles of the RISs, followed by a simple post processing at the receiver to retrieve the contributions from each path [40].

We first divide the total transmissions into $L \geq 2^{\lceil \log_2(R+1) \rceil}$ equal-sized blocks. Choose L such that it is a factor of M. We next define $\boldsymbol{P}_r \in \mathbb{C}^{N \times (M/L)}$, $r = 1, \cdots, R$ as a set of *base phase profiles* of length M/L for each RIS. These profiles may be random in case there is no prior information about the UE location, or directional in case partial information about the UE location is available.

We take R rows of the Hadamard matrix[4] of length L (except for the first row, which is constant) as the coding vectors $\mathbf{c}_r \in \mathbb{R}^L$ for the r^{th} RIS, $r = 1, \cdots, R$. Then we then form the full phase profile of each RIS at transmission $m = kL + l$, $k = 0, \cdots, M/L - 1$,

$$\boldsymbol{\gamma}_{r,kL+l} = ([\mathbf{c}_r]_l)\, \boldsymbol{P}_{r[:,k]}, \tag{B.14}$$

where $\boldsymbol{P}_{r[:,k]}$ denotes the k^{th} column of $\boldsymbol{P}_r$, $[\mathbf{c}_r]_l$ denotes the l^{th} element of $\mathbf{c}_r$, and $l = 0, \cdots, L-1$. This indexing structure is used to map the two indices (k, l) into a single index m, where $1 \leq m \leq M$.

At the receiver side, to extract the r^{th} RIS components from (B.11), it is enough to reshape the received signal $\boldsymbol{y} \in \mathbb{C}^M$ as

$$\mathbf{Y} = [\boldsymbol{y}_{0:L-1} | \boldsymbol{y}_{L:2L-1} | \cdots | \boldsymbol{y}_{M-L:M-1}] \in \mathbb{C}^{L \times (M/L)}, \tag{B.15}$$

and then compute

$$\boldsymbol{y}_r = \frac{1}{L} \mathbf{Y}^{\mathsf{T}} \mathbf{c}_r, \; r = 1, \cdots, R. \tag{B.16}$$

where $\boldsymbol{y}_r \in \mathbb{C}^{M/L}$ is the filtered signal containing the r^{th} RIS components. It is possible to separate the LoS component using $\boldsymbol{y}_0 = 1/L \mathbf{Y}^{\mathsf{T}} \mathbf{c}_0$, where $\mathbf{c}_0 = \mathbf{1}_L$. As a result, despite the RIS-reflected paths having significantly lower energy

[4]Recall that a Hadamard matrix $\mathbf{C}$ of length L is an $L \times L$ matrix, is made up of entries in $\{-1, +1\}$, and satisfies $\mathbf{C}\mathbf{C}^{\top} = L\mathbf{I}$. The amplitude constraint is compatible with the RIS profile constraint.

than the LoS path due to the approximately random phase configuration, the use of orthogonal temporal coding for RIS phase profiles ensures their extraction through coherent integration. The details of this extraction are provided in the next subsection, with an example.

3.2 Example

As an example, we fix the number of RISs to $R = 2$. Note that to separate the contributions from the three paths (LoS, RIS 1 and RIS 2), the minimum required coding length is $L = 4$. We take $\mathbf{c}_0 = [1, 1, 1, 1]^\mathsf{T}$, $\mathbf{c}_1 = [1, -1, 1, -1]^\mathsf{T}$ and $\mathbf{c}_2 = [1, 1, -1, -1]^\mathsf{T}$. The vectors $\boldsymbol{z}_0 = \sqrt{P}\alpha_0\, \boldsymbol{b}(\nu)$ and $\boldsymbol{z}_r = \sqrt{P}\alpha_r\, \boldsymbol{x}_r(\boldsymbol{\theta}_r) \odot \boldsymbol{b}(\nu)$, $r = 1, 2$ and $l = 0, 1, 2, 3$ represent the noise-free received signal contributions from the LoS and RIS paths, respectively. These vectors capture the signal components corresponding to each path before noise is introduced.

We can express the 4 consecutive noise-free samples of each path as follows:

$$[\boldsymbol{z}_0]_{4k+l} = \sqrt{P}\alpha_0 e^{j2\pi(4k+l)T_s\nu}, \tag{B.17}$$

$$[\boldsymbol{z}_1]_{4k+l} = \sqrt{P}\alpha_1 \left([\mathbf{c}_r]_l\ g_1(\boldsymbol{\phi}_1, \boldsymbol{\theta}_1, k)\right) e^{j2\pi(4k+l)T_s\nu}, \tag{B.18}$$

$$[\boldsymbol{z}_2]_{4k+l} = \sqrt{P}\alpha_2 \left([\mathbf{c}_2]_l\ g_2(\boldsymbol{\phi}_2, \boldsymbol{\theta}_2, k)\right) e^{j2\pi(4k+l)T_s\nu}, \tag{B.19}$$

where $g_r(\boldsymbol{\phi}_r, \boldsymbol{\theta}_r, k) = (\boldsymbol{a}(\phi_r) \odot \boldsymbol{P}_{r[:,k]})^\mathsf{T}\boldsymbol{a}(\boldsymbol{\theta}_r)$, $r = 1, 2$. Then, by applying (B.16) and in the case of $\nu = 0$, the filtered measurements $\boldsymbol{y}_0$, $\boldsymbol{y}_1$ and $\boldsymbol{y}_2$ will be as follows

$$[\boldsymbol{y}_0]_k = \sqrt{P}\alpha_0 + [\tilde{\boldsymbol{n}}_0]_k, \tag{B.20}$$

$$[\boldsymbol{y}_1]_k = \sqrt{P}\alpha_1 g_1(\boldsymbol{\phi}_1, \boldsymbol{\theta}_1, k) + [\tilde{\boldsymbol{n}}_1]_k, \tag{B.21}$$

$$[\boldsymbol{y}_2]_k = \sqrt{P}\alpha_2 g_2(\boldsymbol{\phi}_2, \boldsymbol{\theta}_2, k) + [\tilde{\boldsymbol{n}}_2]_k, \tag{B.22}$$

where $[\tilde{\boldsymbol{n}}_r]_k = 1/4 \sum_{l=0}^{3} [\mathbf{c}_r]_l [\boldsymbol{n}]_{4k+l}$ (see App. 1). Therefore, $\boldsymbol{y}_r$, $r = 1, 2$ contain the contribution from the r^{th} RIS and $\boldsymbol{y}_0$ contain the LoS contribution without any interference from the other RISs. However, if $\nu \neq 0$, this coding would result in some residual inter-RIS interference and the separation cannot be done perfectly. The solution is to first estimate the CFO ($\hat{\nu}$) and remove it

from the observations by $\tilde{\boldsymbol{y}} = \boldsymbol{y} \odot \boldsymbol{b}(-\hat{\nu})$, then proceed with this coding. Hence in the following sections, we proceed with estimating the CFO and cancel it out from the received signal.

4 High-level Algorithm Description

In this section, we provide a high-level description of the proposed joint localization and synchronization algorithm to tackle the problem in Sec. 2.4, covering both the channel-domain parameter estimation and localization.

4.1 Channel-domain Parameter Estimation

The maximum-likelihood (ML) estimate of the channel-domain parameters from (B.11) can be obtained by solving the following optimization problems:

$$[\hat{\nu}, \hat{\boldsymbol{\theta}}_1, \cdots, \hat{\boldsymbol{\theta}}_R, \hat{\alpha_0}, \hat{\alpha}_1, \cdots, \hat{\alpha}_R] = \tag{B.23}$$
$$\underset{\substack{\nu, \boldsymbol{\theta}_1, \cdots, \boldsymbol{\theta}_R, \\ \alpha_0, \alpha_1, \cdots, \alpha_R}}{\arg\min} \left\| \boldsymbol{y} - \sqrt{P}\alpha_0 \boldsymbol{b}(\nu) - \sqrt{P} \sum_{r=1}^{R} \alpha_r \boldsymbol{x}_r(\boldsymbol{\theta}_r) \odot \boldsymbol{b}(\nu) \right\|^2,$$

if LoS exists, which we will refer to as LoS scenario, and

$$[\hat{\nu}, \hat{\boldsymbol{\theta}}_1, \cdots, \hat{\boldsymbol{\theta}}_R, \hat{\alpha}_1, \cdots, \hat{\alpha}_R] = \tag{B.24}$$
$$\underset{\substack{\nu, \boldsymbol{\theta}_1, \cdots, \boldsymbol{\theta}_R \\ \alpha_1, \cdots, \alpha_R}}{\arg\min} \left\| \boldsymbol{y} - \sqrt{P} \sum_{r=1}^{R} \alpha_r \boldsymbol{x}_r(\boldsymbol{\theta}_r) \odot \boldsymbol{b}(\nu) \right\|^2,$$

if LoS is blocked, which we will refer to as NLoS scenario.

4.1.1 Conditional Channel Gain Estimation

The ML estimate of the path gains can be derived easily in closed-form as a function of the estimated CFO and AoDs as follows. First, we start by writing the received signal in the below form

$$\boldsymbol{y} = \boldsymbol{A}(\boldsymbol{\chi}_{\text{ch}})\boldsymbol{\alpha} + \boldsymbol{n}, \tag{B.25}$$

where $\boldsymbol{\chi}_{\text{ch}} = [\nu, \boldsymbol{\theta}_1^{\mathsf{T}}, \cdots, \boldsymbol{\theta}_R^{\mathsf{T}}]^{\mathsf{T}}$, $\boldsymbol{A}(\boldsymbol{\chi}_{\text{ch}}) = \sqrt{P}[\boldsymbol{b}(\nu)\ \boldsymbol{x}_1(\boldsymbol{\theta}_1) \odot \boldsymbol{b}(\nu)\ \cdots\ \boldsymbol{x}_R(\boldsymbol{\theta}_R) \odot \boldsymbol{b}(\nu)]$ and $\boldsymbol{\alpha} = [\alpha_0\ \alpha_1\ \cdots\ \alpha_R]^{\mathsf{T}}$, in case LoS exists and $\boldsymbol{A}(\boldsymbol{\chi}_{\text{ch}}) = \sqrt{P}[\boldsymbol{x}_1(\boldsymbol{\theta}_1) \odot \boldsymbol{b}(\nu)\ \cdots\ \boldsymbol{x}_R(\boldsymbol{\theta}_R) \odot \boldsymbol{b}(\nu)]$ and $\boldsymbol{\alpha} = [\alpha_1\ \cdots\ \alpha_R]^{\mathsf{T}}$ in case LoS is obstructed. Accordingly, the path gains can be estimated in closed-form as

$$\hat{\boldsymbol{\alpha}}(\boldsymbol{\chi}_{\text{ch}}) = (\boldsymbol{A}(\boldsymbol{\chi}_{\text{ch}})^{\mathsf{H}} \boldsymbol{A}(\boldsymbol{\chi}_{\text{ch}}))^{-1} \boldsymbol{A}(\boldsymbol{\chi}_{\text{ch}})^{\mathsf{H}} \boldsymbol{y}. \tag{B.26}$$

4.1.2 Compressed Channel Parameter Estimation

We can now plug the channel gain estimates in (B.26) back into (B.23) and (B.24) to derive the compressed ML cost functions, reducing their dimensionality to $(2R + 1)$ (which, however, still lead to very high computational complexity):

$$[\hat{\nu}, \hat{\boldsymbol{\theta}}_1, \cdots, \hat{\boldsymbol{\theta}}_R] = \underset{\nu, \boldsymbol{\theta}_1, \cdots, \boldsymbol{\theta}_R}{\arg\min} \tag{B.27}$$
$$\left\| \boldsymbol{y} - \sqrt{P}\hat{\alpha}_0(\boldsymbol{\chi}_{\text{ch}})\boldsymbol{b}(\nu) - \sqrt{P}\sum_{r=1}^{R} \hat{\alpha}_r(\boldsymbol{\chi}_{\text{ch}})\boldsymbol{x}_r(\boldsymbol{\theta}_r) \odot \boldsymbol{b}(\nu) \right\|^2.$$

in case LoS exists, and

$$[\hat{\nu}, \hat{\boldsymbol{\theta}}_1, \cdots, \hat{\boldsymbol{\theta}}_R] = \tag{B.28}$$
$$\underset{\nu, \boldsymbol{\theta}_1, \cdots, \boldsymbol{\theta}_R}{\arg\min} \left\| \boldsymbol{y} - \sqrt{P}\sum_{r=1}^{R} \hat{\alpha}_r(\boldsymbol{\chi}_{\text{ch}})\boldsymbol{x}_r(\boldsymbol{\theta}_r) \odot \boldsymbol{b}(\nu) \right\|^2.$$

in case LoS is obstructed.

As discussed in Sec. 3, it is possible to significantly simplify the optimization problems (B.27) and (B.28) with time-orthogonal RIS phase profiles, assuming a good estimate of the CFO is available. Sec. 5 will provide a detailed explanation of how to solve these two optimization problems with reasonable complexity, leveraging the orthogonal RIS profile design.

4.2 Localization

The direct ML approach to solve the localization and synchronization problem in in Sec. 2.4 is as follows:

$$[\hat{\nu},\ \hat{\boldsymbol{p}}] = \arg\min_{\nu,\boldsymbol{p}} \big\|\boldsymbol{y} - \sqrt{P}\hat{\alpha}_0(\boldsymbol{\chi}_{\mathrm{p}})\boldsymbol{b}(\nu) - \sqrt{P}\sum_{r=1}^{R}\hat{\alpha}_r(\boldsymbol{\chi}_{\mathrm{p}})\boldsymbol{x}_r(\boldsymbol{p})\odot\boldsymbol{b}(\nu)\big\|^2, \tag{B.29}$$

in LoS scenario, and

$$[\hat{\nu},\ \hat{\boldsymbol{p}}] = \arg\min_{\nu,\boldsymbol{p}} \big\|\boldsymbol{y} - \sqrt{P}\sum_{r=1}^{R}\hat{\alpha}_r(\boldsymbol{\chi}_{\mathrm{p}})\boldsymbol{x}_r(\boldsymbol{p})\odot\boldsymbol{b}(\nu)\big\|^2, \tag{B.30}$$

in NLoS scenario, where $\hat{\alpha}_0(\boldsymbol{\chi}_{\mathrm{p}})$ and $\hat{\alpha}_r(\boldsymbol{\chi}_{\mathrm{p}})$ can be found from (B.26) by replacing $\boldsymbol{\chi}_{\mathrm{p}} = [\nu, \boldsymbol{p}^{\mathsf{T}}]$ with $\boldsymbol{\chi}_{\mathrm{ch}}$ using
$\boldsymbol{A}(\boldsymbol{\chi}_{\mathrm{p}}) = \sqrt{P}[\boldsymbol{b}(\nu)\ \ \boldsymbol{x}_1(\boldsymbol{\theta}_1(\boldsymbol{p}))\odot\boldsymbol{b}(\nu)\ \ \cdots\ \ \boldsymbol{x}_R(\boldsymbol{\theta}_R(\boldsymbol{p}))\odot\boldsymbol{b}(\nu)]$, (B.1) and (B.2). Both problems can be solved using a gradient descent method, starting from an initial estimate of ν and $\boldsymbol{p}$. The initial estimate of ν is provided directly by the channel parameter estimator in (B.27) or (B.28), while the initial estimate of $\boldsymbol{p}$ can be obtained from the AoD estimates in (B.27) or (B.28). This coarse position estimation problem can be solved by using geometric arguments by finding the least-squares intersection of the lines extending from the $\boldsymbol{p}_{\mathrm{RIS},r}$ towards the UE with estimated AoD $\hat{\boldsymbol{\theta}}_r$, through

$$\boldsymbol{p}_r = \boldsymbol{p}_{\mathrm{RIS},r} + \beta_r\mathbf{u}_r,\ r = 1, \cdots, R, \tag{B.31}$$

where $\mathbf{u}_r = \boldsymbol{R}_r^{\mathsf{T}}\boldsymbol{k}(\hat{\boldsymbol{\theta}}_r)/\big\|\boldsymbol{R}_r^{\mathsf{T}}\boldsymbol{k}(\hat{\boldsymbol{\theta}}_r)\big\|$ is the unitary direction vector and β_r is unknown.

In order to locate the UE, we need to find the closest point in the 3-D space to these lines. The least-square problem for the intersection of R lines can be written as [41]

$$\hat{\boldsymbol{p}} = \arg\min_{\boldsymbol{p}} \sum_{r=1}^{R}\big\|(\boldsymbol{p} - \boldsymbol{p}_{\mathrm{RIS},r}) - ((\boldsymbol{p} - \boldsymbol{p}_{\mathrm{RIS},r})^{\mathsf{T}}\mathbf{u}_r)\mathbf{u}_r\big\|^2. \tag{B.32}$$

It follows that [42]

$$\hat{\boldsymbol{p}} = \Big(\sum_{r=1}^{R} \big(\mathbf{I} - \mathbf{u}_r \mathbf{u}_r^{\mathsf{T}} \big) \Big)^{-1} \Big(\sum_{r=1}^{R} \big(\mathbf{I} - \mathbf{u}_r \mathbf{u}_r^{\mathsf{T}} \big) \boldsymbol{p}_{\mathrm{RIS},r} \Big). \tag{B.33}$$

4.3 Joint LoS Detection and Localization

In practice, the UE may not know if the LoS between itself and the BS is blocked. To address this, we will introduce a GLRT-based method to perform LoS detection. Once the presence or absence of the LoS path is known, we can choose the correct set of estimations.We formulate a hypothesis testing problem as follows:

$$\boldsymbol{y} = \begin{cases} \boldsymbol{y}_{\mathrm{NLoS}}(\boldsymbol{\zeta}, \nu) + \boldsymbol{n}, & \text{under } \mathcal{H}_0 \\ \boldsymbol{y}_{\mathrm{LoS}}(\alpha_0, \nu) + \boldsymbol{y}_{\mathrm{NLoS}}(\boldsymbol{\zeta}, \nu) + \boldsymbol{n}, & \text{under } \mathcal{H}_1 \end{cases}, \tag{B.34}$$

where $\boldsymbol{\zeta} = [\alpha_{\mathrm{R},1} \ \alpha_{\mathrm{I},1} \ \cdots \ \alpha_{\mathrm{R},R} \ \alpha_{\mathrm{I},R} \ \boldsymbol{\theta}_1^{\mathsf{T}} \ \cdots \ \boldsymbol{\theta}_R^{\mathsf{T}}]^{\mathsf{T}}$. The null hypothesis $\mathcal{H}_0$ refers to the case where the LoS path is blocked in (B.11), while the alternate hypothesis $\mathcal{H}_1$ refers to the case in which the LoS path exists in (B.11). In (B.34),

$$\boldsymbol{y}_{\mathrm{LoS}}(\alpha_0, \nu) \triangleq \sqrt{P} \alpha_0 \, \boldsymbol{b}(\nu), \tag{B.35}$$

$$\boldsymbol{y}_{\mathrm{NLoS}}(\boldsymbol{\zeta}, \nu) \triangleq \sum_{r=1}^{R} \sqrt{P} \alpha_r \, \boldsymbol{x}_r(\boldsymbol{\theta}_r) \odot \boldsymbol{b}(\nu). \tag{B.36}$$

The GLRT for the problem in (B.34) can be expressed as [43]

$$\mathcal{L}(\boldsymbol{y}) = \frac{\max_{\alpha_0, \boldsymbol{\zeta}, \nu} p(\boldsymbol{y} \,|\, \mathcal{H}_1; \alpha_0, \boldsymbol{\zeta}, \nu)}{\max_{\boldsymbol{\zeta}, \nu} p(\boldsymbol{y} \,|\, \mathcal{H}_0; \boldsymbol{\zeta}, \nu)} \underset{\mathcal{H}_0}{\overset{\mathcal{H}_1}{\gtrless}} \psi, \tag{B.37}$$

Algorithm 1 Joint LoS Detection and Parameter Estimation Algorithm

Input: Received signal $\boldsymbol{y} \in \mathbb{C}^M$ in (B.11).

Output: Estimates $\hat{\nu}, \hat{\boldsymbol{\theta}}_1, \cdots, \hat{\boldsymbol{\theta}}_R$

1: Solve under $\mathcal{H}_0$: Estimate $\hat{\nu}_{\text{NLoS}}, \hat{\boldsymbol{\zeta}}_{\text{NLoS}}$ (see Section 5.2)

2: Solve under $\mathcal{H}_1$: Estimate $\hat{\nu}_{\text{LoS}}, \hat{\boldsymbol{\zeta}}_{\text{LoS}}$ and $\hat{\alpha}_0$ (see Section 5.1)

3: LoS detection via (B.38): $\mathcal{L}^{\log}(\boldsymbol{y}) \underset{\mathcal{H}_0}{\overset{\mathcal{H}_1}{\gtrless}} \sigma^2 \log \psi$.

4: Based on the result, choose the final set of estimates accordingly.

where ψ is a threshold. Writing the log-likelihood ratio $\mathcal{L}^{\log}(\boldsymbol{y}) \triangleq \sigma^2 \log \mathcal{L}(\boldsymbol{y})$, we obtain

$$\begin{aligned}\mathcal{L}^{\log}(\boldsymbol{y}) = \frac{1}{2} \Bigg(& \min_{\boldsymbol{\zeta},\nu} \left\| \boldsymbol{y} - \boldsymbol{y}_{\text{NLoS}}(\boldsymbol{\zeta}, \nu) \right\|^2 - \\ & \min_{\alpha_0,\boldsymbol{\zeta},\nu} \left\| \boldsymbol{y} - \boldsymbol{y}_{\text{LoS}}(\alpha_0, \nu) - \boldsymbol{y}_{\text{NLoS}}(\boldsymbol{\zeta}, \nu) \right\|^2 \Bigg) \\ & \underset{\mathcal{H}_0}{\overset{\mathcal{H}_1}{\gtrless}} \psi' = \sigma^2 \log \psi. \end{aligned} \tag{B.38}$$

There are two separate optimization problems to tackle in (B.38), identical to (B.23) and (B.24), which will be solved in Sec. 5: under LoS in Sec. 5.1 and NLoS in Sec. 5.2. We can plug-in the resulting estimated LoS and NLoS parameter values into (B.38) to perform LoS detection. The algorithm is summarized in Algorithm 1.

5 Channel Parameter Estimation

In this section, we elaborate on the channel parameter estimation procedures that solve (B.27) and (B.28). First, we start under the assumption that LoS exists in Sec. 5.1, tackling (B.27), then we continue with blocked LoS assumption in Sec. 5.2, focusing on (B.28). The section concludes with a complexity analysis in Section 5.3.

5.1 Channel Parameter Estimation under LoS

In this scenario, the LoS path is the dominant path as the RIS-induced paths are usually very weak. Hence, we treat the RIS paths as noise for CFO estimation, and then recover the signal per RIS, by harnessing the orthogonal RIS profiles.

5.1.1 CFO Estimation

We form the NLoS-ML estimation of CFO with the assumption that the contribution from the RIS paths is negligible. Under this assumption, we can rewrite the NLoS-ML problem in (B.27) as follows:

$$\hat{\nu} = \arg\min_{\nu} \left\| \boldsymbol{y} - \sqrt{P}\hat{\alpha}_0(\nu)\boldsymbol{b}(\nu) \right\|^2 = \arg\max_{\nu} |\boldsymbol{b}^{\mathsf{H}}(\nu)\boldsymbol{y}|^2, \tag{B.39}$$

which is a 1-D line search over the interval $-1/(2T_s) < \nu < 1/(2T_s)$ to find coarse estimates. Then we can implement a 1-D quasi-Newton algorithm to find refined estimates of CFO.

5.1.2 RIS Separation

Using the estimated CFO $\hat{\nu}$, we wipe off its effect from the original observation in (B.11) as

$$\tilde{\boldsymbol{y}} = \boldsymbol{y} \odot \boldsymbol{b}(-\hat{\nu}). \tag{B.40}$$

Then, assuming the residual CFO $\nu - \hat{\nu}$ is negligible, we separate each RIS path by first forming the reshaped CFO-removed signal $\tilde{\mathbf{Y}}$ using (B.15) and then filtering it using (B.16):

$$\tilde{\boldsymbol{y}}_r = \frac{1}{L}\tilde{\mathbf{Y}}^{\mathsf{T}}\mathbf{c}_r, \ r = 1, \cdots, R. \tag{B.41}$$

The CFO-removed, filtered contribution from the r^{th} RIS can then be modeled explicitly as

$$\tilde{\boldsymbol{y}}_r = \sqrt{P}\alpha_r \bar{\boldsymbol{x}}_r(\boldsymbol{\theta}_r) + \boldsymbol{n}_r. \tag{B.42}$$

Here, $\boldsymbol{n}_r$ contains noise plus any residual interference (due to residual CFO). The term $\bar{\boldsymbol{x}}_r(\boldsymbol{\theta}_r) = \bar{\boldsymbol{W}}_r^{\mathsf{T}}\boldsymbol{a}(\boldsymbol{\theta}_r) \in \mathbb{C}^{M/L}$, and $\bar{\boldsymbol{W}}_r \in \mathbb{C}^{N\times M/L}$ contains the uncoded RIS phase profiles, i.e.,

$$\bar{\boldsymbol{W}}_r \triangleq [\boldsymbol{a}(\boldsymbol{\phi}_r)\odot\boldsymbol{\gamma}_{r,0}\ \boldsymbol{a}(\boldsymbol{\phi}_r)\odot\boldsymbol{\gamma}_{r,L}\ \cdots\ \boldsymbol{a}(\boldsymbol{\phi}_r)\odot\boldsymbol{\gamma}_{r,M-L}]. \tag{B.43}$$

5.1.3 AoD Estimation per RIS

For CFO-free r^{th} RIS contribution in (B.42), we can formulate the corresponding ML problem as

$$[\hat{\alpha}_r, \hat{\boldsymbol{\theta}}_r] = \underset{\alpha_r,\boldsymbol{\theta}_r}{\arg\min} \left\|\tilde{\boldsymbol{y}}_r - \sqrt{P}\alpha_r\bar{\boldsymbol{x}}_r(\boldsymbol{\theta}_r)\right\|^2. \tag{B.44}$$

The path gain can be estimated in closed-form as a function of $\boldsymbol{\theta}_r$ as follows:

$$\hat{\alpha}_r(\boldsymbol{\theta}_r) = \frac{\bar{\boldsymbol{x}}_r^{\mathsf{H}}(\boldsymbol{\theta}_r)\tilde{\boldsymbol{y}}_r}{\sqrt{P}\left\|\bar{\boldsymbol{x}}_r(\boldsymbol{\theta}_r)\right\|^2}. \tag{B.45}$$

Plugging (B.45) into (B.44) yields

$$\hat{\boldsymbol{\theta}}_r = \underset{\boldsymbol{\theta}_r}{\arg\min} \left\|\tilde{\boldsymbol{y}}_r - \bar{\boldsymbol{x}}_r(\boldsymbol{\theta}_r)\frac{\bar{\boldsymbol{x}}_r^{\mathsf{H}}(\boldsymbol{\theta}_r)\tilde{\boldsymbol{y}}_r}{\left\|\bar{\boldsymbol{x}}_r(\boldsymbol{\theta}_r)\right\|^2}\right\|^2 \tag{B.46}$$

$$= \underset{\boldsymbol{\theta}_r}{\arg\min}\ \tilde{\boldsymbol{y}}_r^{\mathsf{H}}\left(\mathbf{I} - \frac{\bar{\boldsymbol{x}}_r(\boldsymbol{\theta}_r)\bar{\boldsymbol{x}}_r^{\mathsf{H}}(\boldsymbol{\theta}_r)}{\left\|\bar{\boldsymbol{x}}_r(\boldsymbol{\theta}_r)\right\|^2}\right)\tilde{\boldsymbol{y}}_r. \tag{B.47}$$

Therefore, the ML problem in (B.44) reduces to

$$\hat{\boldsymbol{\theta}}_r = \underset{\boldsymbol{\theta}_r}{\arg\max} \frac{|\tilde{\boldsymbol{y}}_r^{\mathsf{H}}\bar{\boldsymbol{x}}_r(\boldsymbol{\theta}_r)|^2}{\left\|\bar{\boldsymbol{x}}_r(\boldsymbol{\theta}_r)\right\|^2}. \tag{B.48}$$

For each RIS r, this problem is solved separately by first performing a 2-D grid search for coarse estimation and then refining by applying a 2-D quasi-Newton algorithm with the coarse estimate as the starting point.

The overall algorithm to solve (B.27) is summarized in Algorithm 2.

Algorithm 2 LoS Estimation Algorithm to Solve (B.27)

Input: Received signal $\boldsymbol{y} \in \mathbb{C}^M$ in (B.11).
Output: Estimates $\hat{\nu}, \hat{\boldsymbol{\theta}}_1, \cdots, \hat{\boldsymbol{\theta}}_R$.

$\hat{\nu} = \arg\max_{\nu} \boldsymbol{b}(\nu)^{\mathsf{H}} \boldsymbol{y}$.
$\tilde{\boldsymbol{y}} = \boldsymbol{y} \odot \boldsymbol{b}(-\hat{\nu})$.
$\tilde{\mathbf{Y}} = \text{reshape}(\tilde{\boldsymbol{y}}, L, M/L)$ via (B.15).
for $r = 1, \cdots, R$ **do**
  $\tilde{\boldsymbol{y}}_r = 1/L \ \tilde{\mathbf{Y}}^{\mathsf{T}} \mathbf{c}_r$.
  $\hat{\boldsymbol{\theta}}_r = \arg\max_{\boldsymbol{\theta}} |\tilde{\boldsymbol{y}}_r^{\mathsf{H}} \bar{\boldsymbol{x}}_r(\boldsymbol{\theta})|^2 / \|\bar{\boldsymbol{x}}_r(\boldsymbol{\theta})\|^2$.
end for

5.2 Channel Parameter Estimation without LoS

In (B.28), the challenge is that unlike the previous scenario (B.27), in which there exists a dominant LoS path, here the CFO and AoDs are coupled in the received signal (as the CFO cannot be estimated using the LoS path therefore its effect remains in the time-domain phase shifts). In this section, we present two low-complexity approaches to tackle this problem: the first one consists of R 3-D searches, each including 1-D CFO and 2-D RIS AoD search for each RIS. The second one involves a single 1-D CFO estimation, followed by R individual 2-D AoD estimations.

5.2.1 ML Estimation

This approach is based on the observation that by conducting a 1-D search over the CFO, there will be an optimal value where all per-RIS observations can be decoupled. The approach operates as follows. For each trial value of the CFO $\nu \in \mathbb{C}_v$, we compute $\tilde{\boldsymbol{y}}(\nu) = \boldsymbol{y} \odot \boldsymbol{b}(-\nu)$ as in (B.40), where we make the dependence on ν explicit. Similarly, we compute $\tilde{\boldsymbol{y}}_r(\nu)$ as in (B.41). We then estimate the AoD from each RIS $\hat{\boldsymbol{\theta}}_1(\nu), \cdots, \hat{\boldsymbol{\theta}}_R(\nu)$ using (B.48). Finally, we find the optimal ν (and AoDs as a result) from (B.28) as

$$\hat{\nu} = \arg\min_{\nu} \left\| \boldsymbol{y} - \sqrt{P} \sum_{r=1}^{R} \hat{\alpha}_r(\nu) \boldsymbol{x}_r(\hat{\boldsymbol{\theta}}_r(\nu)) \odot \boldsymbol{b}(\nu) \right\|^2. \tag{B.49}$$

The overall algorithm to solve (B.28) is summarized in Algorithm 3.

Algorithm 3 NLoS Estimation Algorithm to Solve (B.28) - ML Estimation

Input: Received signal $\boldsymbol{y} \in \mathbb{C}^M$ in (B.11).
Output: Estimates $\hat{\nu}, \hat{\boldsymbol{\theta}}_1, \cdots, \hat{\boldsymbol{\theta}}_R$

for $\nu \in \mathbb{C}_v$ **do**
  $\tilde{\boldsymbol{y}}(\nu) = \boldsymbol{y} \odot \boldsymbol{b}(-\nu)$.
  $\tilde{\mathbf{Y}}(\nu) = \text{reshape}(\tilde{\boldsymbol{y}}(\nu), L, M/L)$ via (B.15).
  for $r = 1, \cdots, R$ **do**
    $\tilde{\boldsymbol{y}}_r(\nu) = 1/L\ \tilde{\mathbf{Y}}^{\mathsf{T}}(\nu)\mathbf{c}_r$.
    $\hat{\boldsymbol{\theta}}_r(\nu) = \arg\max_{\boldsymbol{\theta}} |\tilde{\boldsymbol{y}}_r^{\mathsf{H}}(\nu)\bar{\boldsymbol{x}}_r(\boldsymbol{\theta})|^2 / \|\bar{\boldsymbol{x}}_r(\boldsymbol{\theta})\|^2$.
  end for
end for
$\hat{\nu} = \arg\min_{\nu \in \mathbb{C}_v} \left\| \boldsymbol{y} - \sqrt{P} \sum_{r=1}^{R} \alpha_r(\nu) \boldsymbol{x}_r(\hat{\boldsymbol{\theta}}_r(\nu)) \odot \boldsymbol{b}(\nu) \right\|^2$.

5.2.2 Low-complexity Unstructured Estimation

The NLoS-ML estimation in (B.49) requires a 3-D search and is thus computationally expensive. The motivation of this second approach is to de-couple the effect of CFO and AoDs so as to estimate the CFO with a 1-D search. To do so, we can express into $\mathbf{Y} \in \mathbb{C}^{L \times (M/L)}$ in (B.15) as

$$\mathbf{Y} = \mathbf{D}(\nu)\mathbf{C}\mathbf{H}(\boldsymbol{\chi}_{\text{ch}}) + \mathbf{N}, \tag{B.50}$$

where $\boldsymbol{\chi}_{\text{ch}} = [\nu, \boldsymbol{\theta}_1^{\mathsf{T}}, \cdots, \boldsymbol{\theta}_R^{\mathsf{T}}]^{\mathsf{T}}$, $\mathbf{D}(\nu) = \text{diag}[1\, e^{j2\pi T_s \nu}, \ldots, e^{j2\pi(L-1)T_s\nu}] \in \mathbb{C}^{L \times L}$ and the matrix $\mathbf{C} \in \mathbb{C}^{L \times R}$ is the coding matrix which is composed of the coding vectors with length L as below

$$\mathbf{C} = [\mathbf{c}_1, \cdots, \mathbf{c}_R] \in \mathbb{R}^{L \times R}\ . \tag{B.51}$$

In addition, the matrix $\mathbf{H}(\boldsymbol{\chi}_{\text{ch}}) \in \mathbb{C}^{R \times (M/L)}$ is a function of both CFO and AoD with elements $h_{r,\ell} = [\mathbf{H}(\boldsymbol{\chi}_{\text{ch}})]_{r,\ell}$, $(r = 1, \cdots, R, \ell = 1, \cdots, M/L)$ as follows:

$$h_{r,\ell} = \sqrt{P}\alpha_r(\boldsymbol{a}^{\mathsf{T}}(\boldsymbol{\phi}_r) \odot \boldsymbol{P}_{r[:,\ell-1]}^{\mathsf{T}})\boldsymbol{a}(\boldsymbol{\theta}_r)e^{j2\pi(\ell-1)LT_s\nu}, \tag{B.52}$$

and $\mathbf{N} \in \mathbb{C}^{L \times (M/L)}$ is the reshaped noise. With this re-modeling and ignoring the dependence of $\mathbf{H}(\boldsymbol{\chi}_{\text{ch}})$ on the CFO, we de-couple the effect of CFO and AoDs in the measurement model by factoring out matrix $\mathbf{D}(\nu)$, which is a

function of only CFO, and treating the matrix $\mathbf{H}(\boldsymbol{\chi}_{\text{ch}})$ as an unstructured matrix. Therefore, it is enough to apply a 1-D grid search to estimate the CFO through $\mathbf{D}(\nu)$, without the need to estimate AoDs jointly. We will drop the dependence of $\mathbf{H}$ on $\boldsymbol{\chi}_{\text{ch}}$ to simplify the notation.

To formulate the NLoS-ML estimator of the CFO under the model (B.50), we vectorize the observation as

$$\boldsymbol{y} = \text{vec}(\mathbf{Y}) = (\mathbf{I}_{M/L} \otimes (\mathbf{D}(\nu)\mathbf{C}))\mathbf{h} + \mathbf{n} = \mathbf{E}(\nu)\mathbf{h} + \mathbf{n}, \tag{B.53}$$

where we used the property of the Kronecker product (eq. 520 in[44]). Here, $\mathbf{h} = \text{vec}(\mathbf{H}) \in \mathbb{C}^{RM/L}$ and $\mathbf{E}(\nu) = (\mathbf{I}_{M/L} \otimes (\mathbf{D}(\nu)\mathbf{C})) \in \mathbb{C}^{M\times(RM/L)}$. Then, we can form the NLoS-ML estimator to estimate ν and $\mathbf{h}$ accordingly as

$$[\hat{\nu}, \hat{\mathbf{h}}] = \underset{\nu,\mathbf{h}}{\arg\min} \left\|\boldsymbol{y} - \mathbf{E}(\nu)\mathbf{h}\right\|^2, \tag{B.54}$$

where the conditional estimate of $\mathbf{h}$ is derived in closed form as

$$\hat{\mathbf{h}}(\nu) = (\mathbf{E}^{\mathsf{H}}(\nu)\mathbf{E}(\nu))^{-1}\mathbf{E}^{\mathsf{H}}(\nu)\mathbf{y} = \frac{1}{L}\mathbf{E}^{\mathsf{H}}(\nu)\mathbf{y}, \tag{B.55}$$

since $\mathbf{E}^{\mathsf{H}}(\nu)\mathbf{E}(\nu) = L\mathbf{I}_{RM/L}$. Hence, we can write the estimate of ν as

$$\begin{aligned}
\hat{\nu} &= \underset{\nu}{\arg\min} \left\|\boldsymbol{y} - \frac{1}{L}\mathbf{E}(\nu)\mathbf{E}^{\mathsf{H}}(\nu)\boldsymbol{y}\right\|^2 \\
&= \underset{\nu}{\arg\min} \left\| \left(\mathbf{I}_M - \frac{1}{L}\mathbf{E}(\nu)\mathbf{E}^{\mathsf{H}}(\nu)\right)\boldsymbol{y}\right\|^2 \\
&= \underset{\nu}{\arg\max} \left\|\mathbf{E}^{\mathsf{H}}(\nu)\boldsymbol{y}\right\|^2.
\end{aligned} \tag{B.56}$$

We can rewrite the objective function in matrix form using

$$\text{unvec}\left(\mathbf{E}^{\mathsf{H}}(\nu)\boldsymbol{y}\right) = (\mathbf{D}(\nu)\mathbf{C})^{\mathsf{H}}\mathbf{Y} = \mathbf{C}^{\mathsf{H}}\mathbf{D}^{\mathsf{H}}(\nu)\mathbf{Y}. \tag{B.57}$$

Here, the operator $\text{unvec}(\boldsymbol{a}) = \boldsymbol{A}$ transforms the vector $\boldsymbol{a} \in \mathbb{C}^{RM/L}$ to the matrix $\boldsymbol{A} \in \mathbb{C}^{R\times(M/L)}$. Hence, the optimization problem will be

$$\hat{\nu} = \underset{\nu}{\arg\max} \left\|\mathbf{C}^{\mathsf{H}}\mathbf{D}^{\mathsf{H}}(\nu)\mathbf{Y}\right\|_{\text{F}}^2, \tag{B.58}$$

where $\|\cdot\|_{\text{F}}$ stands for the Frobenius norm.

Algorithm 4 NLoS Estimation Algorithm to Solve (B.28) - Low-complexity Unstructured Estimation

Input: Received signal $\boldsymbol{y} \in \mathbb{C}^M$ in (B.11).

Output: Estimates $\hat{\nu}, \hat{\boldsymbol{\theta}}_1, \cdots, \hat{\boldsymbol{\theta}}_R$

$\mathbf{Y} = \text{reshape}(\boldsymbol{y}, L, M/L)$ via (B.15)

$\hat{\nu} = \arg\max_{\nu} \left\| \mathbf{C}^{\mathsf{H}} \mathbf{D}^{\mathsf{H}}(\nu) \mathbf{Y} \right\|^2$

$\tilde{\boldsymbol{y}} = \boldsymbol{y} \odot \boldsymbol{b}(-\hat{\nu})$

$\tilde{\mathbf{Y}}(\nu) = \text{reshape}(\tilde{\boldsymbol{y}}(\nu), L, M/L)$ via (B.15)

for $r = 1, \cdots, R$ **do**

  $\tilde{\boldsymbol{y}}_r = 1/L \ \tilde{\mathbf{Y}}^{\mathsf{T}} \mathbf{c}_r$

  $\hat{\boldsymbol{\theta}}_r = \arg\max_{\boldsymbol{\theta} \in \boldsymbol{\theta}} |\tilde{\boldsymbol{y}}_r^{\mathsf{H}} \bar{\boldsymbol{x}}_r(\boldsymbol{\theta})|^2 / \|\bar{\boldsymbol{x}}_r(\boldsymbol{\theta})\|^2$

end for

Note that the dependence of $\mathbf{H}$ on CFO and AoDs is ignored in the estimation algorithm. In other words, we do not leverage the full potential of the CFO-dependent observations, which is the cost of detangling the effects of CFO and AoD. Therefore, this method is expected to be less accurate than the previous approach, but the complexity is lower and comparable to Algorithm 2.

Once an estimate of the CFO is obtained, it is possible to remove its effect from the observations as in (B.40), and then apply the temporal decoding and R 2-D grid searchs to find estimates of AoDs, as explained in Sec. 5.2.1. The algorithm is summarized in Algorithm 4.

Remark (Operation under the presence of LoS)**:** Note that (B.50) is a valid representation irrespective of whether the LoS path exists or not. In case the LoS exists, the coding matrix will change to $\mathbf{C} = [\mathbf{c}_0, \mathbf{c}_1, \cdots, \mathbf{c}_R]$ and $\mathbf{H} \in \mathbb{C}^{(R+1) \times M/L}$. Theoretically, it is possible to use the approach in Algorithm 4 to estimate the CFO in case LoS exists, but under the assumption of dominant LoS, the performance will be much lower than Algorithm 2.

5.3 Complexity Analysis

A brief complexity analysis is conducted. Assuming a fixed number of grid points G in each dimension, the channel parameter estimation under LoS (Algorithm 2) has a complexity of $\mathcal{O}(GM + RG^2M + R^2)$, where the first term denotes the CFO estimation complexity, the second term corresponds

the AoD estimation complexity and the third term shows the localization time based on (B.33). The NLoS-ML estimation approach (Algorithm 3) has a complexity of $\mathcal{O}(RG^3M+R^2)$ which reflects the fact that we need to perform 3-D estimations. The NLoS low-complexity unstructured estimation approach (Algorithm 4) has a complexity of $\mathcal{O}(GM + RG^2M + R^2)$, which illustrates that the complexity returns to the level of under LoS case with the expense of a reduction in performance which will be demonstrated in Sec. 6.

6 Numerical Results

In this section, we validate the proposed methods for LoS detection, channel estimation and localization in both the presence and absence of the LoS path between the BS and the UE. Several sensitivity studies will also be reported.

6.1 Scenario, Performance Metric and Simulation Setup

We consider a scenario with $R = 2$ RIS, which is the minimal configuration needed to make the localization problem identifiable. The system parameters are summarized in Table 1. First, we will assume that we know whether the LoS exists or not, therefore we will only focus on the performance of the estimators, with and without the presence of LoS. Next, we will relax the aforementioned assumption to assess the performance of the detector together with the estimators.

The path gains (due to propagation loss) α_0, α_1 and α_2 in (B.11) are determined based on the free space path-loss (FSPL) model, containing random phases between $[0, 2\pi)$, similar to [45]:

$$|\alpha_0| = \frac{\lambda}{4\pi d_{\text{BS-UE}}} \tag{B.59}$$

$$|\alpha_r| = \frac{\lambda^2}{16\pi^2 d_{\text{BS-RISr}} d_{\text{RISr-UE}}}, r = 1, 2, \tag{B.60}$$

where the effective area of each RIS element has been assumed to be $\lambda^2/4\pi$, $d_{\text{I-J}}$, I = {BS, RISr}, J = {UE, RISr} is the distance between the entity I and the entity J. In order to assess the performance of the estimators, we calculate the root mean-squared error (RMSE) of our estimates averaged over 100 Monte-Carlo trials, and then compare them with Cramér-Rao bound (CRB)

Table 1: Simulations Parameters

Parameters	**Symbol**	**Value**
Number of RISs	R	2
Wavelength	λ	1 cm
Sampling time	T_s	10 μsec
RIS dimensions	N	64×64
RIS element spacing	d	0.5 cm
Speed of Light	c	3×10^8 m/s
Noise PSD	N_0	-174 dBm/Hz
UE's Noise Figure	n_f	8 dB
Noise power	σ^2	$N_0/T_s \times n_f$ W
Number of Transmissions	M	256
BS position	$\boldsymbol{p}_{\mathrm{b}}$	[0, 0, 0] m
UE position	$\boldsymbol{p}$	[5, 2, 0.5] m
RIS1 position	$\boldsymbol{p}_{\mathrm{RIS},1}$	[10, -10, 0] m
RIS2 position	$\boldsymbol{p}_{\mathrm{RIS},2}$	[0, 10, 0] m
RIS1 rotation matrix	$\boldsymbol{R}_1$	$\boldsymbol{R}_z(\theta = 0)$
RIS2 rotation matrix	$\boldsymbol{R}_2$	$\boldsymbol{R}_z(\theta = \pi)$

as the benchmark. More details on how we derive CRB of different unknowns in our setup are provided in Appendix 2. To assess the performance of the detector, the false alarm probability is calculated over 500 Monte-Carlo trials, and the threshold is chosen numerically to attain a detection probability close to 1. The detection performance turns out to be relatively insensitive to the value of the threshold for the power levels considered in the simulations. To address two NLoS estimation algorithms, we refer to Algorithm 3 as NLoS-ML estimator and Algorithm 4 as NLoS-LC (low complexity) estimator (with respect to NLoS-ML estimator) throughout this section.

6.2 Localization under LoS

In this section, we investigate the accuracy of our proposed estimation algorithm, Algorithm 2, in Sec. 5.1 under the assumption that a dominant LoS path exists between the BS and the UE. To do so, we find the RMSE of the CFO, AoDs, and position, and compare them to the CRBs. For achieving higher precision estimates, we employ the *quasi-Newton* algorithm to perform 1-D CFO refinement and two 2-D AoD refinements.

6.2.1 Channel Parameter Estimation

In Fig. 2, the RMSE of CFO together with the CRB are depicted versus the transmit power P . The CFO is fixed to -40 kHz[5]. Since the LoS is dominant, even at low transmit power we manage to achieve the bound. Fig. 3 shows the RMSE of AoDs versus transmit power for RIS1 and RIS2. We will refer to AoD for RIS1 as AoD1 and AoD for RIS2 as AoD2. It can be observed that the bounds related to the azimuth and elevation angles of AoD2 are smaller than those of AoD1, and with our algorithm it is possible to achieve the CRB at lower transmit power for AoD2 than for AoD1. The reason is as follows: According to Table 1, RIS2 is closer to the BS and the UE than RIS1, suggesting that $\alpha_1 < \alpha_2$. Since the received power at the UE through BS-RIS2-UE path is larger than through BS-RIS1-UE, it is easier to estimate AoD from RIS2 than from RIS1, resulting in lower CRB and RMSE. Overall, Fig. 2 and Fig. 3 demonstrate the effectiveness of the channel estimation algorithm in Algorithm 2, indicating convergence to the theoretical bounds already at low transmit powers.

6.2.2 Localization

Fig. 4 shows the RMSE and the CRB on location estimation against the transmit power. It can be observed that the proposed localization algorithm in Sec. 4.2 can attain the bound at the transmit power for which the RMSE of both AoDs have attained their respective bounds, as expected.

[5]Later, in Fig. 10, we show that the CRB and RMSE from our algorithms remain nearly constant across different CFO values, making the choice of $\nu = -40$ kHz arbitrary.

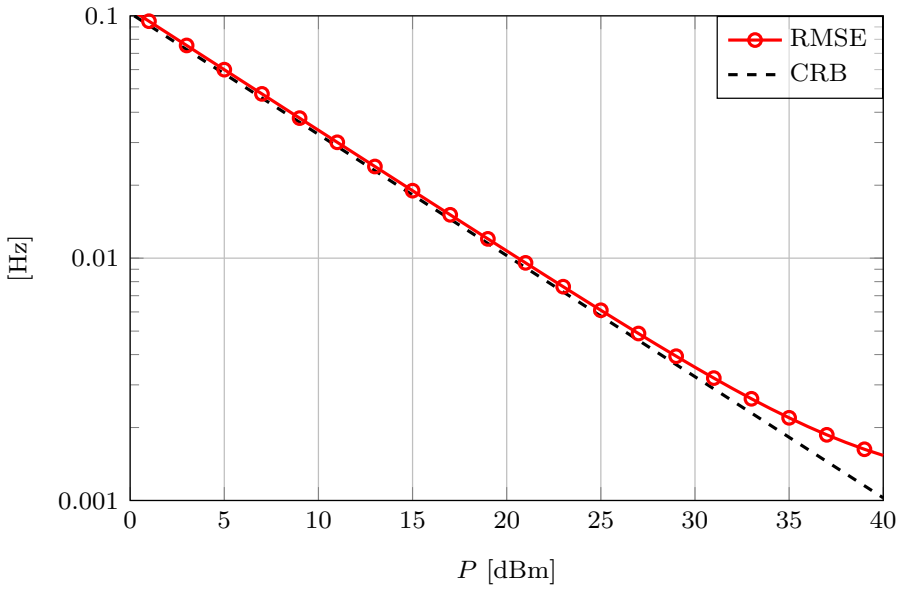

Figure 2: LoS case, CFO estimation performance vs. transmit power.

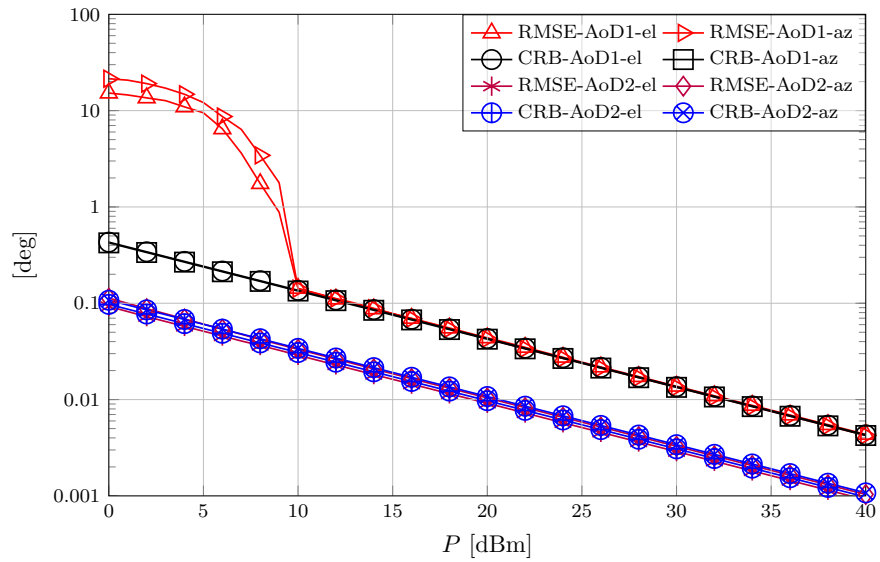

Figure 3: LoS case, AoD1 and AoD2 estimation performance vs. transmit power.

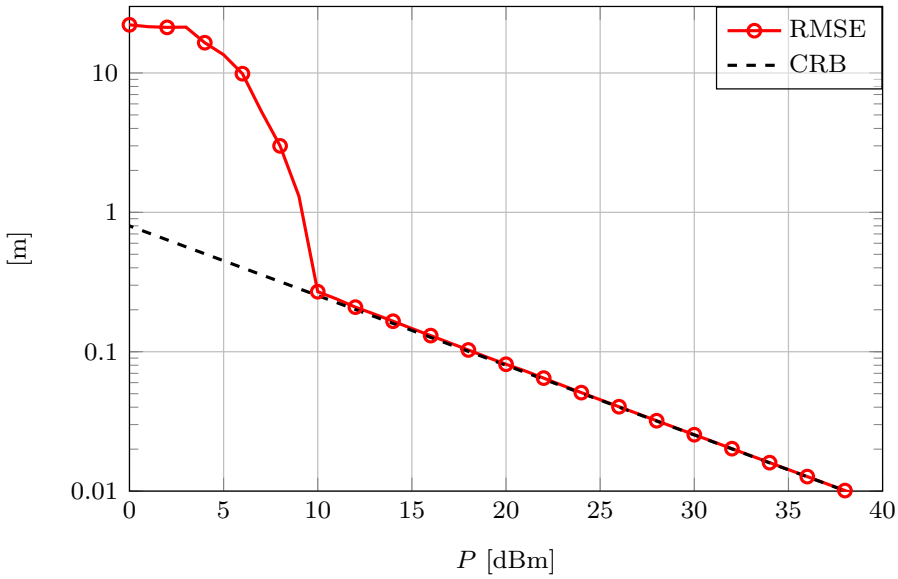

Figure 4: LoS case, position estimation performance vs. transmit power.

6.3 Localization without LoS

In this subsection, we perform the same experiments as explained in the previous subsection for measurements that do not contain the LoS path contribution in (B.11), using the two approaches, Algorithm 3 and Algorithm 4, as explained in Sec. 5.2 and compare the results. To obtain more accurate estimates, we utilize the *quasi-Newton* algorithm to perform 5-D CFO/AoD refinement using the objective function in (B.28).

6.3.1 Channel Parameter Estimation

Fig. 5 and 6 show the RMSE of CFO and AoDs versus transmit power according to the NLoS-ML estimator (Algorithm 3) and low-complexity unstructured (marked by NLoS-LC - Algorithm 4) estimator. The results show that with NLoS-ML estimator, it is possible to touch the bound at lower transmit power (about half) comparing to the NLoS-LC estimator. This advantage is achieved at the expense of higher complexity comparing to the NLoS-LC estimator.

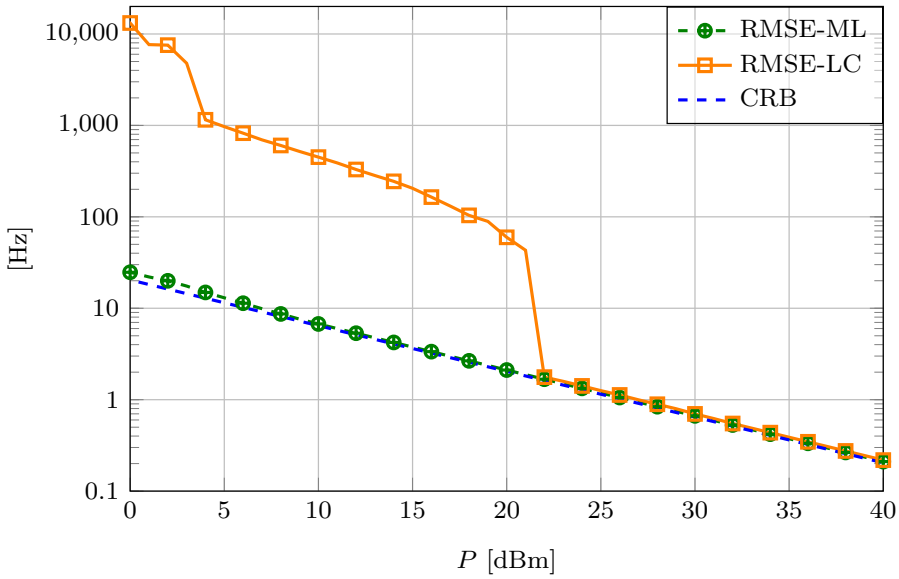

Figure 5: NLoS case, CFO estimation performance vs. transmit power.

6.3.2 Localization

Accordingly, Fig. 7 represents the positional RMSE versus transmit power for two approaches. It can be observed that it is possible to achieve the bound at lower transmit power in NLoS-ML estimator than in NLoS-LC estimator, as previous results suggested. Similar to the results presented in Sec. 6.2 for the scenario with LoS, Fig. 5, Fig. 6 and Fig. 7 reveal the effectiveness of Algorithm 3 and Algorithm 4, as well as the localization algorithm in Sec. 4.2 to solve (B.30).

Remark: The sharp decline in RMSE observed in figures such as Fig. 3, Fig. 4, etc. is attributed to a well-known phenomenon known as waterfall behavior [46], [47]. This phenomenon occurs when increasing the transmit power leads to a point where the signal begins to dominate the noise. Consequently, the RMSE converges to the CRB, resulting in a rapid drop-off in RMSE [6], [23], [28].

Remark: It is worth noting that while the presented optimization problems in Sec. 4 are not globally convex, they exhibit local convexity around the ML estimate. The effectiveness of our proposed initialization methods is

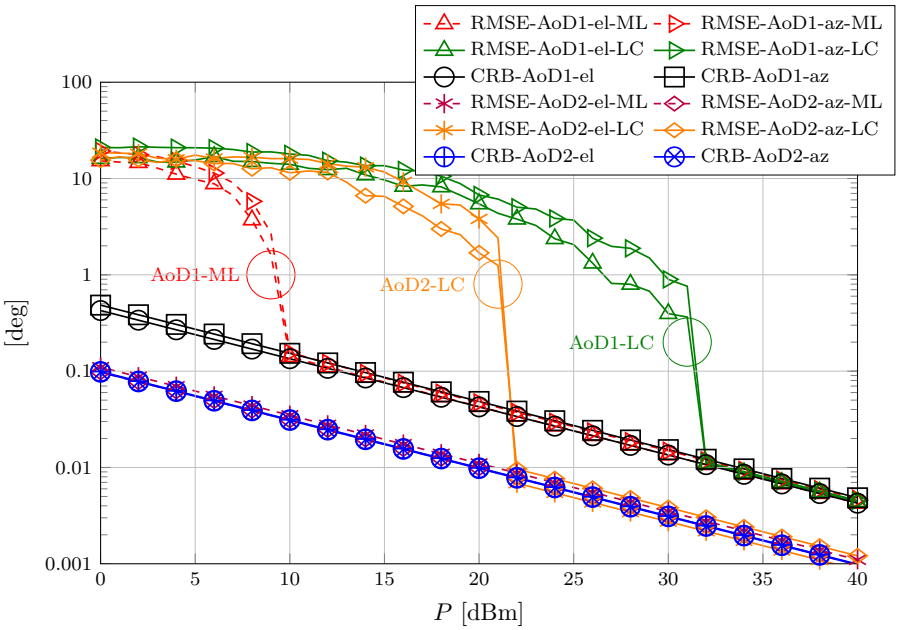

Figure 6: NLoS case, AoD1 and AoD2 estimation performance vs. transmit power.

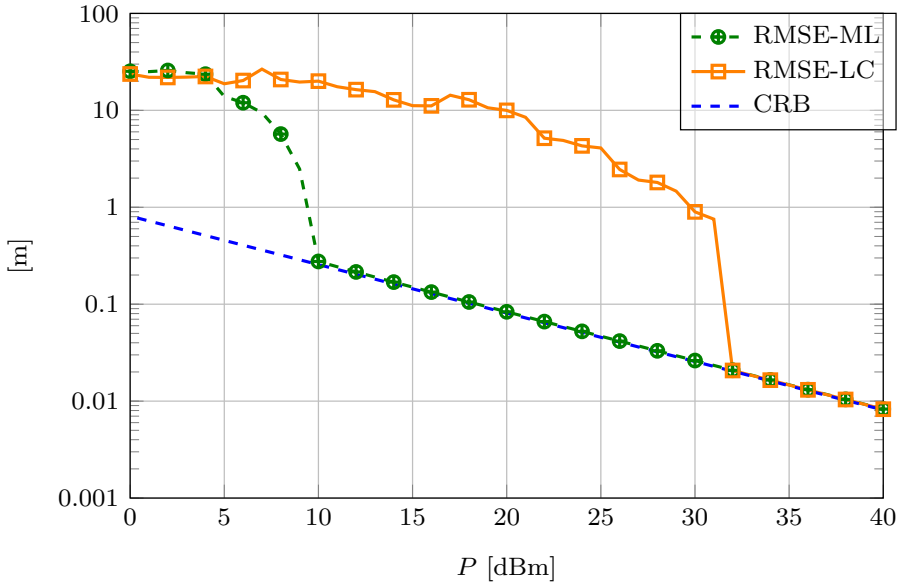

Figure 7: NLoS case, position estimation performance vs. transmit power.

validated by the fact that the final estimates consistently achieve the CRB, confirming that gradient descent successfully converges to the correct solution when initialized appropriately.

6.4 Joint LoS Detection and localization

Here, we analyze the results of the presented LoS detector (Algorithm 1) using two alternative NLoS estimators, i.e. NLoS-ML estimator (Algorithm 3) and NLoS-LC estimator (Algorithm 4).

Fig. 8 shows the false alarm probability vs. transmit power for different estimators presented in Sec. 5.2. By false alarm, we refer to the case that a LoS path does not exist but the detector declares that a LoS path exists. While using NLoS-ML estimator (Algorithm 3) in case of NLoS hypothesis yields almost all zero false alarm probability within the desired transmit power range, using low-complexity approach (Algorithm 4) results in non-zero false alarm probability. This outcome is due to the fact that the quality of our

detector is closely tied to the accuracy of the corresponding estimator, which is noticeably compromised in case of low-complexity estimator.

Fig. 9 presents the positioning RMSE and CRB versus transmit power with LoS and without LoS respectively. It should be pointed out that the CRB in LoS and NLoS scenarios are almost the same, reflecting the fact that the LoS path does not convey any significant localization information. When LoS exists, the performance of the detector using either estimator are similar, since the detector is able to detect the presence of LoS, then the positional RMSE is based on the output of the LoS algorithm and is similar to Fig. 4. On the other hand, when LoS does not exist, by using NLoS-ML estimator the detector is able to verify that LoS path does not exist even at low transmit power (cf. Fig. 8), therefore the positional RMSE is calculated using the output of the NLoS algorithm and the results are similar to Fig. 7 with NLoS-NLoS-ML estimator. In case of using NLoS-LC estimator, we observe non-zero false alarm probability in Fig. 8, but according to Fig. 7, using NLoS-LC estimator already results in poor RMSE at medium transmit power, therefore the non-zero false alarm probability does not considerably affect the estimation accuracy comparing to Fig. 7.

6.5 Comparison with Existing Methods

Here, we compare our proposed CFO-aware localization method to a CFO-agnostic localization method (similar to the one proposed in [23]) to highlight the effect of CFO estimation on the quality of our positioning outcome. The result is shown in Fig. 10 for both the LoS scenario (denoted by the legend 'RMSE-LoS-noCFO') and OLoS scenario (denoted by the legend 'RMSE-NLoS-noCFO'). The transmit power is fixed to $P = 35$ dBm. It can be observed that when we ignore the presence of CFO and bypass the CFO estimation step, the RMSE of the estimated position is close to the bound only for very small CFO and deviates from the CRB for larger CFO, with faster deviation when LoS path exists. The reason is that the LoS component behaves as a strong source of interference when the CFO is not accounted for, resulting in high inter-RIS interference in RIS path separation based on temporal coding, as pointed out in Sec. 3.2. As a result, the quality of the subsequent AoDs and position estimation significantly deteriorates for non-zero CFO. For the sake of comparison, the RMSEs achieved by the proposed estimation algorithms and the corresponding CRBs are also depicted (denoted

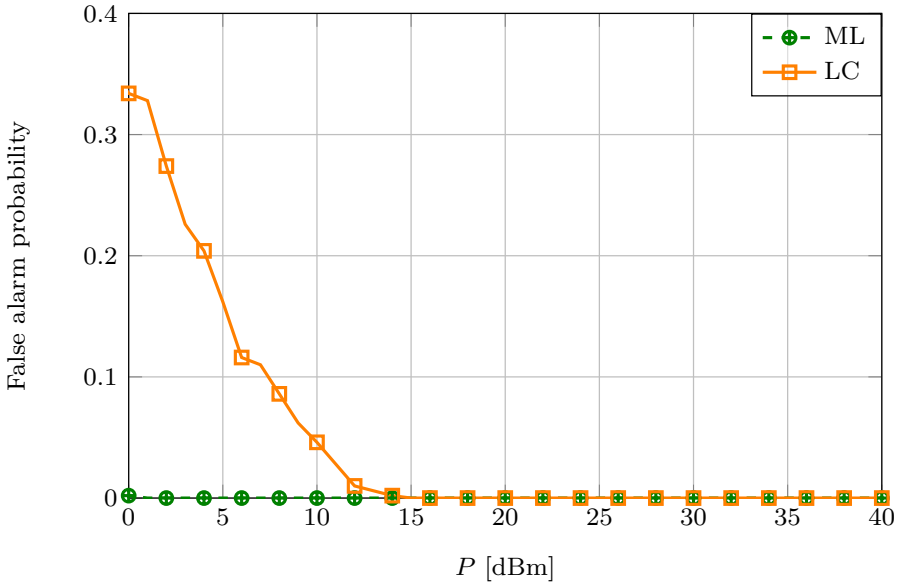

Figure 8: False alarm probability as a function of the transmit power.

by the legends 'RMSE-LoS', 'RMSE-NLoS-ML' for the NLoS-ML estimator and 'RMSE-NLoS-LC' for the NLoS-LC estimator), which shows that using our proposed algorithms, regardless of the value of CFO, it is possible to estimate the position with an accuracy matching the theoretical limits, proving the robustness of our proposed algorithms against increasing CFO values.

6.6 Sensitivity Analysis to Uncontrolled Multipath

Here, we discuss the performance of our estimators in presence of uncontrolled MPCs in the LoS BS-UE channel and the NLoS BS-RIS-UE channel. To account for MPCs, the BS-UE channel and the channel between the RISs and the UE are modeled as Rician [48], [49]. The BS-RIS path is typically regarded as a LoS path because the BS is considered to be directive and the positions of BS and RISs are known [50], [51]. Given our scenario with single-antenna BS and two RISs at different positions, the BS cannot be directive towards both RISs simultaneously. Thus, a more realistic approach would be to consider MPCs in the channel between the BS and the RISs as well. This results in an

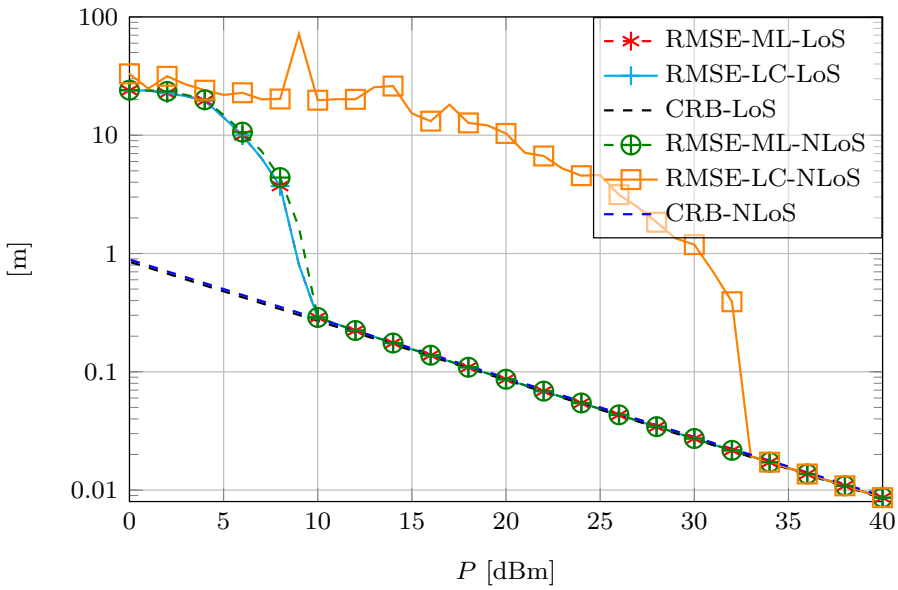

Figure 9: Position estimation performance vs. transmit power, using LoS detector, in LoS and NLoS cases.

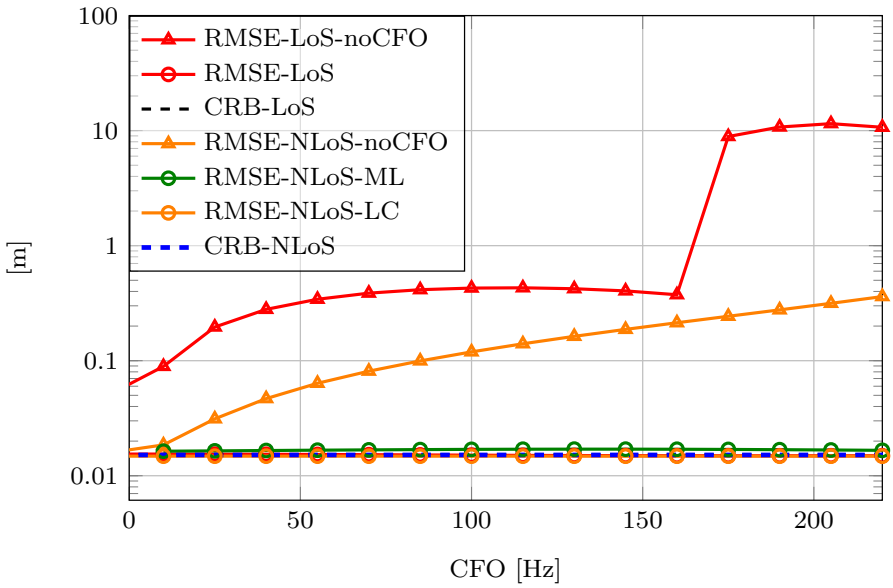

Figure 10: CFO sensitivity analysis, with and without LoS, $P = 35$dBm.

updated version of the received signal in (B.11):

$$\boldsymbol{y} = \boldsymbol{y}_{\text{LoS}}^{\text{MPC}} + \sum_{r=1}^{2} \boldsymbol{y}_{\text{RISr}}^{\text{MPC}} + \boldsymbol{n}, \tag{B.61}$$

where $\boldsymbol{y}_{\text{LoS}}^{\text{MPC}}$ denotes the LoS path including MPCs, defined as

$$\boldsymbol{y}_{\text{LoS}}^{\text{MPC}} = \sqrt{P}\alpha_0 \left(\sqrt{\frac{\kappa_0}{\kappa_0+1}} + \sqrt{\frac{1}{\kappa_0+1}}\tilde{h} \right) \boldsymbol{b}(\nu)\,, \tag{B.62}$$

and $\boldsymbol{y}_{\text{NLoS}}^{\text{MPC}}$ denotes the aggregation of the RIS paths together with their MPCs, given by

$$\begin{aligned} \boldsymbol{y}_{\text{RISr}}^{\text{MPC}} = \sqrt{P}\alpha_r \Big(\Big(\sqrt{\frac{\kappa_{Br}}{\kappa_{Br}+1}} \boldsymbol{W}_r^{\mathsf{T}} + \sqrt{\frac{1}{\kappa_{Br}+1}} \boldsymbol{V}_r^{\mathsf{T}} \Big) \times \\ \Big(\sqrt{\frac{\kappa_{Rr}}{\kappa_{Rr}+1}} \boldsymbol{a}(\boldsymbol{\theta}_r) + \sqrt{\frac{1}{\kappa_{Rr}+1}} \tilde{\mathbf{h}}_r \Big) \Big) \odot \boldsymbol{b}(\nu). \end{aligned} \tag{B.63}$$

Here, κ_0, κ_{Br}, κ_{Rr} are the Rician factors and $\tilde{h} \sim \mathcal{CN}(0,1)$, $\tilde{\mathbf{h}}_{Br} \sim \mathcal{CN}(\mathbf{0},\mathbf{I})$, $\tilde{\mathbf{h}}_r \sim \mathcal{CN}(\mathbf{0},\mathbf{I})$ are the MPC (excluding the direct path) in the BS-UE, BS-r^{th}RIS and r^{th}RIS-UE paths respectively, and $\boldsymbol{V}_r \triangleq [\tilde{\mathbf{h}}_{Br} \odot \boldsymbol{\gamma}_{r,0} \ \cdots \ \tilde{\mathbf{h}}_{Br} \odot \boldsymbol{\gamma}_{r,M-1}] \in \mathbb{C}^{N\times M}$. For sufficiently large κ_0, κ_{Br} and κ_{Rr}, (B.61) will converge to (B.11). The details on how (B.61) is derived are explained in Appendix 3.

Fig. 11 shows the effect of MPC on our estimators, in which we take $\kappa_{Br} = \kappa_{Rr} = \kappa_0 = \kappa$ for the sake of simplicity. The transmit power is chosen to be $P = 35$ dBm. It can be observed that with κ as small as 10, sub-dm accuracy can be achieved and that the proposed algorithms can attain near-optimal performance in the sense of converging to the bounds when the direct paths in the BS-RIS, RIS-UE and BS-UE channels are 20 dB stronger than MPCs (i.e., when $\kappa = 100$).

Operating at a frequency of 30 GHz, we expect the Rician factor to be significant, indicating that the LoS and RIS paths will dominate and that the MPC will generally be weak. However, we must acknowledge that in scenarios where the Rician factor is low, the stochastic nature of NLoS components can lead to performance degradation. For example, strong ground reflections from the RIS may introduce substantial interference, complicating the resolution of multipath effects. This limitation underscores the importance of

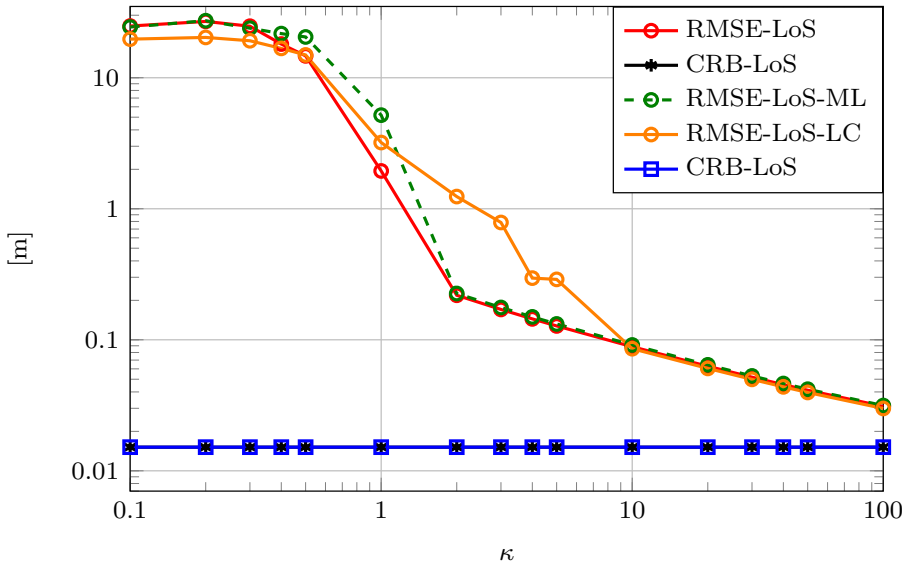

Figure 11: Position estimation performance in presence of MPC vs. κ at $P = 35$ dBm.

considering environmental conditions when interpreting results. Thus, while our findings are promising under typical conditions, they also highlight the challenges posed by strong multipath reflections and the inherent limitations of our approach.

6.7 Sensitivity Analysis to UE Velocity

Here, we analyze the performance of our estimators in the presence of UE mobility with velocity $\boldsymbol{v}$. To account for the impact of UE motion, we extend the received signal model in (B.11) as

$$\boldsymbol{y} = \sqrt{P}\Big(\alpha_0\, \boldsymbol{b}(\nu_0) + \sum_{i=1}^{R} \alpha_i \left(\boldsymbol{W}_i^{\mathsf{T}} \boldsymbol{a}(\boldsymbol{\theta}_i)\right) \odot \boldsymbol{b}(\nu_i)\Big) + \boldsymbol{n}\ , \tag{B.64}$$

where $\nu_0 = v_{\mathrm{b}}/\lambda + \nu, v_{\mathrm{b}} = \boldsymbol{v}^{\mathsf{T}}(\boldsymbol{p}_{\mathrm{b}} - \boldsymbol{p}_0)/\left\|\boldsymbol{p}_{\mathrm{b}} - \boldsymbol{p}_0\right\|$, and $\nu_i = v_{\mathrm{RIS},i}/\lambda + \nu$, $v_{\mathrm{RIS},i} = \boldsymbol{v}^{\mathsf{T}}(\boldsymbol{p}_{\mathrm{RIS},i} - \boldsymbol{p}_0)/\left\|\boldsymbol{p}_{\mathrm{RIS},i} - \boldsymbol{p}_0\right\|$ and $\boldsymbol{p}_0$ represents the UE's initial position. In Fig. 12, we illustrate how the performance of our estimators

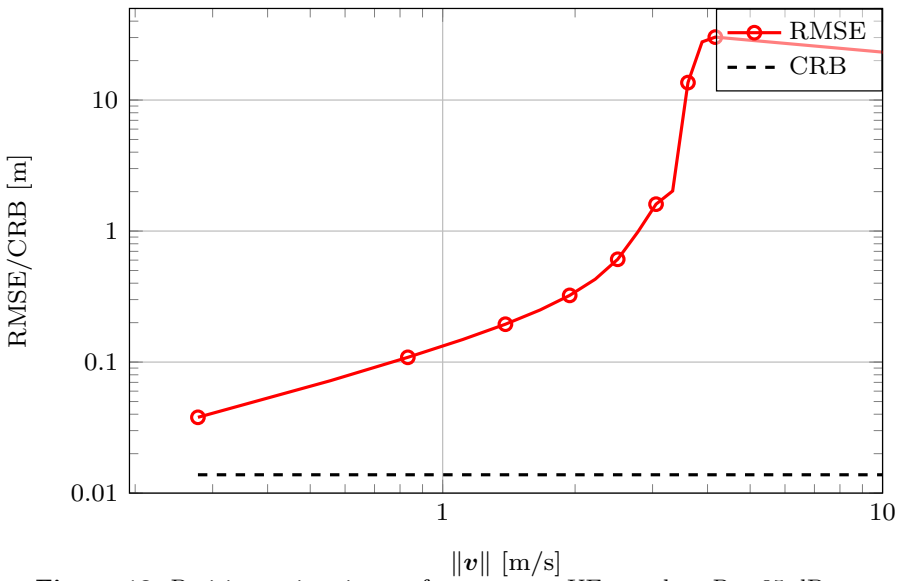

Figure 12: Position estimation performance vs. UE speed at $P = 35$ dBm.

varies with UE speed $\|\boldsymbol{v}\|$ for $R = 2$. The direction of the UE velocity is fixed to $\boldsymbol{v}/\|\boldsymbol{v}\| = [1, 0, 0]^\mathsf{T}$. As expected, our algorithm performs well only for very low UE speeds, as our frugal setup is specifically designed for localizing a stationary UE. Higher UE mobility introduces errors that our approach is not optimized to handle. Hence, the gap between the RMSE and the CRB increases with increasing $\|\boldsymbol{v}\|$ due to mismatch between the assumed model in (B.11) and the true one in (B.64).

6.8 Analysis on Ergodic Capacity

To further evaluate the performance of our proposed RIS-enabled localization and synchronization system, we analyze the ergodic capacity when the RISs are steered towards the estimated UE position while compensating for the AoA from the BS at the same time. The received SNR at the true UE position is then computed using the received signal model. The ergodic capacity is calculated as $\mathbb{E}[\log_2(1 + \mathrm{SNR})]$, where SNR is calculated at the true UE position. In Fig. 13, the capacity under LoS, NLoS-ML and NLoS-LC scenarios/algorithms is shown. In case of LoS, due to the dominance of the

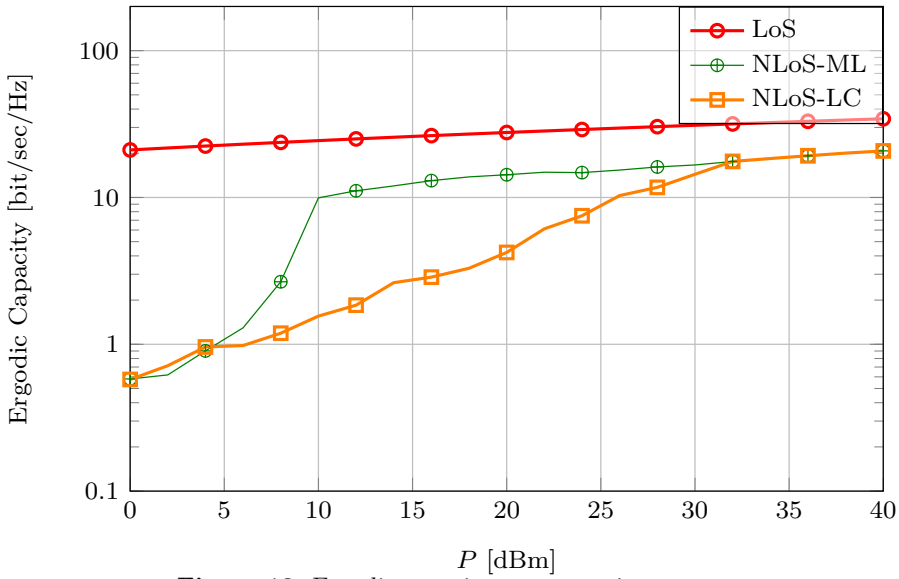

Figure 13: Ergodic capacity vs. transmit power.

LoS path, we cannot observe the effect of accurate localization. In case of NLoS, we can observe an increase in the capacity when accurate positioning is achieved.

6.9 Analysis of Localization Bound with Increasing Number of RISs

In the previous subsections, we have considered the minimal hardware infrastructure necessary for enabling localization and synchronization. Here, we analyze the impact of increasing the number of RISs on the CRB of position estimation, where LoS path exists. The RISs are arranged symmetrically on a square centered at the origin, where the BS is located. The RIS phase profiles are chosen randomly. Fig. 14 shows how the CRB on positioning changes as we add more RISs, in the presence of a LoS path. The results suggest that adding more RISs improves positioning accuracy, especially when going from two to three, where we achieve sub-millimeter precision. This improvement comes from the additional redundant measurements provided by the new RISs. However, after reaching six RISs, the improvement saturates.

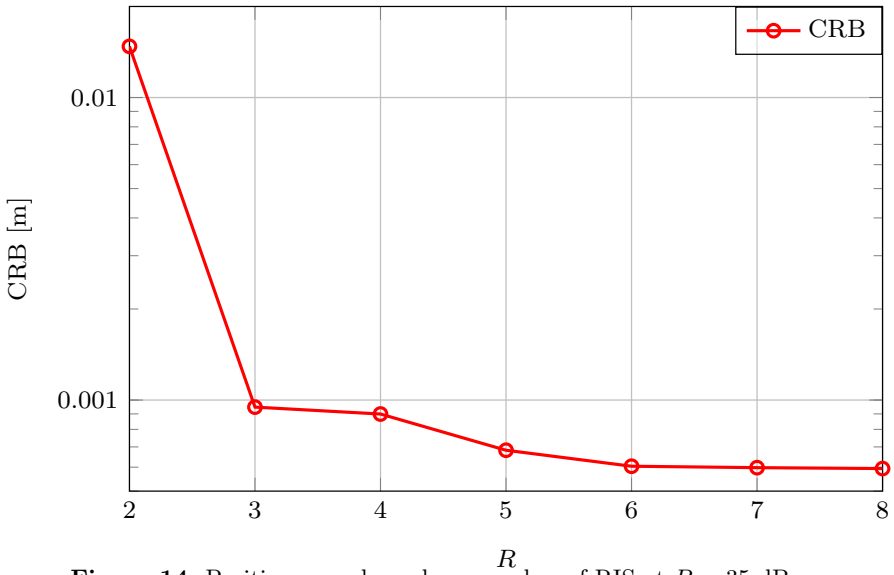

Figure 14: Position error bound vs. number of RIS at $P = 35$ dBm.

7 Conclusion

In this paper, we presented a novel approach for frugal 3-D-localization and frequency synchronization of a single-antenna stationary UE using SISO RIS-enabled communication, even in the absence of a LoS path between the BS and the UE. Our resource-efficient method leverages a single-antenna BS and multiple RISs under NB communication, which significantly reduces the system's complexity and cost.

We developed various estimation algorithms as well as a GLRT-based LoS detector to test the presence of the LoS path. Our approach addresses both LoS and NLoS scenarios with tailored estimation algorithms for each case. Extensive simulation results demonstrated that our method achieves theoretical performance bounds in medium to high transmit power regimes, confirming the feasibility of localizing a single-antenna UE efficiently with minimal spectrum and BS antenna resources.

We also highlighted the critical importance of CFO estimation in accurate positioning by comparing our results with a previous work which is a CFO-agnostic approach. Simulations showed that neglecting CFO estimation leads

to reduced performance, emphasizing the necessity of accurate CFO estimation in our framework. Moreover, we validated the robustness of our approach in a simulated environment with multi-path components, demonstrating near-theoretical performance with a Rician factor as small as 10. Furthermore, we analyzed the impact of UE mobility on our approach and confirmed that while our algorithm remains effective for very low UE speeds, its performance degrades as mobility increases. The results validate that our frugal setup is best suited for stationary UE localization, with higher UE speeds introducing estimation errors beyond its designed capabilities.

The computational efficiency of our estimation algorithms is designed to be practical for real-world applications, with complexities that are quadratic or cubic in relation to the number of grid points. Furthermore, the feasibility of implementing these algorithms will depend on the processing capabilities of the hardware used and the potential for parallel computation, which can significantly enhance their performance in practical scenarios.

Our results show that it is possible to achieve high-accuracy localization of a single-antenna UE with parsimonious use of spectral and spatial resources, making our method highly practical and efficient. This work sets a foundation for developing more resource-efficient localization systems towards sustainable 6G deployments. In a nutshell, our results highlight the potential for frugal usage of hardware and spectral resources to meet localization demands in real-world networks, facilitating cost-effective implementation without compromising accuracy. Future research could explore the frugal localization of mobile UEs, addressing the additional challenges posed by dynamic environments. Investigating these scenarios could enhance the robustness and applicability of RIS-enabled communication systems. We plan to perform real-world experiments to validate the proposed frugal localization approach in realistic scenarios.

1 RIS Phase Profile - Temporal Coding

By applying (B.15) and (B.16) we have

$$
\begin{aligned}
[\boldsymbol{y}_0]_k = &\frac{\sqrt{P}}{4}\alpha_0\big((+1)e^{j2\pi(4k)T_s\nu} + (+1)e^{j2\pi(4k+1)T_s\nu} + \\
&(+1)e^{j2\pi(4k+2)T_s\nu} + (+1)e^{j2\pi(4k+3)T_s\nu}\big) + \\
&\frac{\sqrt{P}}{4}\alpha_1\big(\left(+g_1(\boldsymbol{\phi}_1,\boldsymbol{\theta}_1,k)\right)e^{j2\pi(4k)T_s\nu} + \\
&\left(-g_1(\boldsymbol{\phi}_1,\boldsymbol{\theta}_1,k)\right)e^{j2\pi(4k+1)T_s\nu} + \\
&\left(+g_1(\boldsymbol{\phi}_1,\boldsymbol{\theta}_1,k)\right)e^{j2\pi(4k+2)T_s\nu} + \\
&\left(-g_1(\boldsymbol{\phi}_1,\boldsymbol{\theta}_1,k)\right)e^{j2\pi(4k+3)T_s\nu}\big) + \\
&\frac{\sqrt{P}}{4}\alpha_2\big(\left(+g_2(\boldsymbol{\phi}_2,\boldsymbol{\theta}_2,k)\right)e^{j2\pi(4k)T_s\nu} + \\
&\left(+g_2(\boldsymbol{\phi}_2,\boldsymbol{\theta}_2,k)\right)e^{j2\pi(4k+1)T_s\nu} + \\
&\left(-g_2(\boldsymbol{\phi}_2,\boldsymbol{\theta}_2,k)\right)e^{j2\pi(4k+2)T_s\nu} + \\
&\left(-g_2(\boldsymbol{\phi}_2,\boldsymbol{\theta}_2,k)\right)e^{j2\pi(4k+3)T_s\nu}\big) + [\tilde{\boldsymbol{n}}_0]_k,
\end{aligned}
\tag{B.65}
$$

$$
\begin{aligned}
[\boldsymbol{y}_1]_k = &\frac{\sqrt{P}}{4}\alpha_0\big((+1)e^{j2\pi(4k)T_s\nu} + (-1)e^{j2\pi(4k+1)T_s\nu} + \\
&(+1)e^{j2\pi(4k+2)T_s\nu} + (-1)e^{j2\pi(4k+3)T_s\nu}\big) + \\
&\frac{\sqrt{P}}{4}\alpha_1\big(\left(+g_1(\boldsymbol{\phi}_1,\boldsymbol{\theta}_1,k)\right)e^{j2\pi(4k)T_s\nu} + \\
&\left(+g_1(\boldsymbol{\phi}_1,\boldsymbol{\theta}_1,k)\right)e^{j2\pi(4k+1)T_s\nu} + \\
&\left(+g_1(\boldsymbol{\phi}_1,\boldsymbol{\theta}_1,k)\right)e^{j2\pi(4k+2)T_s\nu} + \\
&\left(+g_1(\boldsymbol{\phi}_1,\boldsymbol{\theta}_1,k)\right)e^{j2\pi(4k+3)T_s\nu}\big) + \\
&\frac{\sqrt{P}}{4}\alpha_2\big(\left(+g_2(\boldsymbol{\phi}_2,\boldsymbol{\theta}_2,k)\right)e^{j2\pi(4k)T_s\nu} + \\
&\left(-g_2(\boldsymbol{\phi}_2,\boldsymbol{\theta}_2,k)\right)e^{j2\pi(4k+1)T_s\nu} + \\
&\left(-g_2(\boldsymbol{\phi}_2,\boldsymbol{\theta}_2,k)\right)e^{j2\pi(4k+2)T_s\nu} + \\
&\left(+g_2(\boldsymbol{\phi}_2,\boldsymbol{\theta}_2,k)\right)e^{j2\pi(4k+3)T_s\nu}\big) + [\tilde{\boldsymbol{n}}_1]_k,
\end{aligned}
\tag{B.66}
$$

$$
\begin{aligned}
[\boldsymbol{y}_2]_k = &\frac{\sqrt{P}}{4}\alpha_0\big((+1)e^{j2\pi(4k)T_s\nu} + (+1)e^{j2\pi(4k+1)T_s\nu} + \\
&(-1)e^{j2\pi(4k+2)T_s\nu} + (-1)e^{j2\pi(4k+3)T_s\nu}\big) + \\
&\frac{\sqrt{P}}{4}\alpha_1\big(\,(+g_1(\boldsymbol{\phi}_1,\boldsymbol{\theta}_1,k))\,e^{j2\pi(4k)T_s\nu} + \\
&(-g_1(\boldsymbol{\phi}_1,\boldsymbol{\theta}_1,k))\,e^{j2\pi(4k+1)T_s\nu} + \\
&(-g_1(\boldsymbol{\phi}_1,\boldsymbol{\theta}_1,k))\,e^{j2\pi(4k+2)T_s\nu} + \\
&(+g_1(\boldsymbol{\phi}_1,\boldsymbol{\theta}_1,k))\,e^{j2\pi(4k+3)T_s\nu}\big) + \\
&\frac{\sqrt{P}}{4}\alpha_2\big(\,(+g_2(\boldsymbol{\phi}_2,\boldsymbol{\theta}_2,k))\,e^{j2\pi(4k)T_s\nu} + \\
&(+g_2(\boldsymbol{\phi}_2,\boldsymbol{\theta}_2,k))\,e^{j2\pi(4k+1)T_s\nu} + \\
&(+g_2(\boldsymbol{\phi}_2,\boldsymbol{\theta}_2,k))\,e^{j2\pi(4k+2)T_s\nu} + \\
&(+g_2(\boldsymbol{\phi}_2,\boldsymbol{\theta}_2,k))\,e^{j2\pi(4k+3)T_s\nu}\big) + [\tilde{\boldsymbol{n}}_2]_k,
\end{aligned}
\tag{B.67}
$$

where $[\tilde{\boldsymbol{n}}_r]_k = 1/4\sum_{l=0}^{3}[\mathbf{c}_r]_l[\boldsymbol{n}]_{4k+l}$.

2 Fisher Information Matrix Analysis

Here, we provide more details about the theoretical limits used to assess the estimation algorithms. We use Fisher information matrix (FIM) analysis and evaluate it for the channel parameters and the positional parameters. The FIM for channel parameters can be found as below [52]

$$
\boldsymbol{F}_{\text{ch}} = \frac{2}{\sigma^2}\sum_{m=0}^{M-1}\Re\left\{\frac{\partial[\boldsymbol{z}]_m}{\partial\boldsymbol{\eta}_{\text{ch}}}\left(\frac{\partial[\boldsymbol{z}]_m}{\partial\boldsymbol{\eta}_{\text{ch}}}\right)^{\text{H}}\right\},
\tag{B.68}
$$

where $\boldsymbol{z}$ is the noiseless part of the received signal in (B.11) and $\boldsymbol{\eta}_{\text{ch}} \in \{\boldsymbol{\eta}_{\text{ch}}^{\text{LoS}}, \boldsymbol{\eta}_{\text{ch}}^{\text{NLoS}}\}$. Then, we can translate $\boldsymbol{F}_{\text{ch}}$ to the positional FIM, $\boldsymbol{F}_{\text{po}}$, accordingly $\boldsymbol{F}_{\text{po}} = \boldsymbol{J}^{\text{T}}\boldsymbol{F}_{\text{ch}}\boldsymbol{J}$, where $\boldsymbol{J}$ is the Jacobian matrix with elements $\boldsymbol{J}_{m,n} = \partial[\boldsymbol{\eta}_{\text{ch}}]_m/\partial[\boldsymbol{\eta}]_n$. and $\boldsymbol{\eta} \in \{\boldsymbol{\eta}^{\text{LoS}}, \boldsymbol{\eta}^{\text{NLoS}}\}$. In case of measurements with LoS, $\boldsymbol{J} \in \mathbb{R}^{10\times 11}$ and $\boldsymbol{F}_{\text{po}} \in \mathbb{R}^{10}$, and in case of measurements without LoS, $\boldsymbol{J} \in \mathbb{R}^{8\times 9}$ and $\boldsymbol{F}_{\text{po}} \in \mathbb{R}^{8}$.

Finally in terms of the error bounds, in case of measurements with LoS, the

position error bound (PEB) can be calculated by

$$\text{PEB} = \sqrt{\text{trace}\left([\boldsymbol{F}_{\text{po}}^{-1}]_{7:9,7:9}\right)}, \tag{B.69}$$

and the error bound on CFO can be found by $\left(\mathbb{E}\left[(\nu-\tilde{\nu})^2\right]\right)^{1/2} \geq \left([\boldsymbol{F}_{\text{po}}^{-1}]_{10,10}\right)^{1/2}$.

In case of measurements without LoS, PEB can be found using PEB $= \left(\text{trace}([\boldsymbol{F}_{\text{po}}^{-1}]_{5:7,5:7})\right)^{1/2}$, and the error bound on CFO can be calculated accordingly using $\left([\boldsymbol{F}_{\text{po}}^{-1}]_{8,8}\right)^{1/2}$. Error bounds on other parameters can be calculated similarly.

3 Received signal model in the presence of multi-path components

The received signal at the m^{th} transmission is

$$\begin{aligned} y_m =& \sqrt{P}\Big(\text{h}_{\text{BS-UE}} + \sum_{r=1}^{2} \mathbf{h}_{\text{BS-RISr}}^{\mathsf{T}}(\boldsymbol{\phi}_r)\text{diag}(\boldsymbol{\gamma}_{r,m})\mathbf{h}_{\text{RISr-UE}}(\boldsymbol{\theta}_r)\Big) \\ &\times e^{j2\pi m T_s \nu} + n_m. \end{aligned} \tag{B.70}$$

Here, $\text{h}_{\text{BS-UE}}$ is the channel between the BS and the UE, $\mathbf{h}_{\text{BS-RISr}}(\boldsymbol{\phi}_r)$ is the channel between the BS and the r^{th}RIS and $\mathbf{h}_{\text{RISr-UE}}(\boldsymbol{\theta}_r)$ is the channel between the r^{th}RIS and the UE as below

$$\text{h}_{\text{BS-UE}} = \alpha_0\Big(\sqrt{\frac{\kappa_0}{\kappa_0+1}} + \sqrt{\frac{1}{\kappa_0+1}}\tilde{h}\Big), \tag{B.71}$$

$$\mathbf{h}_{\text{BS-RISr}}(\boldsymbol{\phi}_r) = \alpha_{Br}\Big(\sqrt{\frac{\kappa_{Br}}{\kappa_{Br}+1}}\boldsymbol{a}(\boldsymbol{\phi}_r) + \sqrt{\frac{1}{\kappa_{Br}+1}}\tilde{\mathbf{h}}_{Br}\Big), \tag{B.72}$$

$$\mathbf{h}_{\text{RISr-UE}}(\boldsymbol{\theta}_r) = \alpha_{Rr}\Big(\sqrt{\frac{\kappa_{Rr}}{\kappa_{Rr}+1}}\boldsymbol{a}(\boldsymbol{\theta}_r) + \sqrt{\frac{1}{\kappa_{Rr}+1}}\tilde{\mathbf{h}}_r\Big), \tag{B.73}$$

and $\alpha_{Br}\alpha_{Rr} = \alpha_r$. Therefore, y_m would be

$$y_m = \sqrt{P}\Big(\mathrm{h}_{\text{BS-UE}} + \sum_{r=1}^{2} \alpha_{Br}\Big(\sqrt{\frac{\kappa_{Br}}{\kappa_{Br}+1}}[\boldsymbol{W}_r]_m^{\mathsf{T}}\mathbf{h}_{\text{RISr-UE}}(\boldsymbol{\theta}_r) + \sqrt{\frac{1}{\kappa_{Br}+1}}(\tilde{\mathbf{h}}_{Br}^{\mathsf{T}} \odot \boldsymbol{\gamma}_{r,m}^{\mathsf{T}})\mathbf{h}_{\text{RISr-UE}}(\boldsymbol{\theta}_r)\Big)\Big)e^{j2\pi m T_s \nu} + n_m, \tag{B.74}$$

where $[\boldsymbol{W}_r]_m$ is the m^{th} column of $\boldsymbol{W}_r$ as introduced in (B.9). Therefore, by defining $\boldsymbol{V}_r$ such that the m^{th} column is $[\boldsymbol{V}_r]_m = \tilde{\mathbf{h}}_{Br} \odot \boldsymbol{\gamma}_{r,m}$, using (B.71) and (B.73) and concatenating all M measurements, (B.61) will be derived.

References

[1] C. de Lima, D. Belot, R. Berkvens, *et al.*, *6G White Paper on Localization and Sensing* (6G Research Visions 12), English. University of Oulu, 2020.

[2] J. A. del Peral-Rosado, R. Raulefs, J. A. López-Salcedo, and G. Seco-Granados, "Survey of cellular mobile radio localization methods: From 1G to 5G," *IEEE Communications Surveys & Tutorials*, vol. 20, no. 2, pp. 1124–1148, 2017.

[3] L. Italiano, B. C. Tedeschini, M. Brambilla, H. Huang, M. Nicoli, and H. Wymeersch, "A tutorial on 5G positioning," *arXiv preprint arXiv:2311.10551*, 2023.

[4] F. Wen, H. Wymeersch, B. Peng, W. P. Tay, H. C. So, and D. Yang, "A survey on 5G massive MIMO localization," *Digital Signal Processing*, vol. 94, pp. 21–28, 2019.

[5] A. Shahmansoori, G. E. Garcia, G. Destino, G. Seco-Granados, and H. Wymeersch, "Position and orientation estimation through millimeter-wave MIMO in 5G systems," *IEEE Transactions on Wireless Communications*, vol. 17, no. 3, pp. 1822–1835, 2017.

[6] H. Wymeersch, J. He, B. Denis, A. Clemente, and M. Juntti, "Radio localization and mapping with reconfigurable intelligent surfaces: Challenges, opportunities, and research directions," *IEEE Vehicular Technology Magazine*, vol. 15, no. 4, pp. 52–61, 2020.

[7] A. Behravan, V. Yajnanarayana, M. F. Keskin, *et al.*, "Positioning and sensing in 6G: Gaps, challenges, and opportunities," *IEEE Vehicular Technology Magazine*, vol. 18, no. 1, pp. 40–48, 2022.

[8] D.-R. Emenonye, H. S. Dhillon, and R. M. Buehrer, "Fundamentals of RIS-aided localization in the far-field," *IEEE Transactions on Wireless Communications*, 2023.

[9] J. He, F. Jiang, K. Keykhosravi, J. Kokkoniemi, H. Wymeersch, and M. Juntti, "Beyond 5G RIS mmwave systems: Where communication and localization meet," *IEEE Access*, vol. 10, pp. 68 075–68 084, 2022.

[10] H. Tataria, M. Shafi, A. F. Molisch, M. Dohler, H. Sjöland, and F. Tufvesson, "6G wireless systems: Vision, requirements, challenges, insights, and opportunities," *Proc. IEEE*, vol. 109, no. 7, pp. 1166–1199, 2021.

[11] E. Basar, M. Di Renzo, J. De Rosny, M. Debbah, M.-S. Alouini, and R. Zhang, "Wireless communications through reconfigurable intelligent surfaces," *IEEE Access*, vol. 7, pp. 116 753–116 773, 2019.

[12] C. Pan, H. Ren, K. Wang, *et al.*, "Reconfigurable intelligent surfaces for 6G systems: Principles, applications, and research directions," *IEEE Communications Magazine*, vol. 59, no. 6, pp. 14–20, 2021.

[13] M. Jian, G. C. Alexandropoulos, E. Basar, *et al.*, "Reconfigurable intelligent surfaces for wireless communications: Overview of hardware designs, channel models, and estimation techniques," *Intelligent and Converged Networks*, vol. 3, no. 1, pp. 1–32, 2022.

[14] Q. Wu, S. Zhang, B. Zheng, C. You, and R. Zhang, "Intelligent reflecting surface-aided wireless communications: A tutorial," *IEEE Trans. Commun.*, vol. 69, no. 5, pp. 3313–3351, 2021.

[15] C. Pan, G. Zhou, K. Zhi, *et al.*, "An overview of signal processing techniques for RIS/IRS-aided wireless systems," *IEEE Journal of Selected Topics in Signal Processing*, vol. 16, no. 5, pp. 883–917, 2022.

[16] C. Pan, H. Ren, K. Wang, *et al.*, "Reconfigurable intelligent surfaces for 6G systems: Principles, applications, and research directions," *IEEE Commun. Mag.*, vol. 59, no. 6, pp. 14–20, 2021.

[17] E. Björnson, H. Wymeersch, B. Matthiesen, P. Popovski, L. Sanguinetti, and E. de Carvalho, "Reconfigurable intelligent surfaces: A signal processing perspective with wireless applications," *IEEE Signal Processing Magazine*, vol. 39, no. 2, pp. 135–158, 2022.

[18] C. De Lima, D. Belot, R. Berkvens, *et al.*, "Convergent communication, sensing and localization in 6G systems: An overview of technologies, opportunities and challenges," *IEEE Access*, vol. 9, pp. 26 902–26 925, 2021.

[19] A. Umer, I. Müürsepp, M. M. Alam, and H. Wymeersch, *Role of reconfigurable intelligent surfaces in 6G radio localization: Recent developments, opportunities, challenges, and applications*, 2023.

[20] M. Li, S. Zhang, Y. Ge, Z. Li, F. Gao, and P. Fan, "STAR-RIS aided integrated sensing and communication over high mobility scenario," *IEEE Transactions on Communications*, 2024.

[21] H. Sun, F. Gao, S. Zhang, S. Jin, and T. J. Cui, "Computational imaging with holographic RIS: Sensing principle and pathloss analysis," *IEEE Journal on Selected Areas in Communications*, 2024.

[22] A. Fascista, M. F. Keskin, A. Coluccia, H. Wymeersch, and G. Seco-Granados, "RIS-aided joint localization and synchronization with a single-antenna receiver: Beamforming design and low-complexity estimation," *IEEE Journal of Selected Topics in Signal Processing*, vol. 16, no. 5, pp. 1141–1156, 2022.

[23] K. Keykhosravi, M. F. Keskin, G. Seco-Granados, P. Popovski, and H. Wymeersch, "RIS-enabled SISO localization under user mobility and spatial-wideband effects," *IEEE Journal of Selected Topics in Signal Processing*, vol. 16, no. 5, pp. 1125–1140, 2022.

[24] Z. Ye, F. Junaid, R. Nilsson, and J. Van De Beek, "Single-antenna sensor localization with reconfigurable intelligent surfaces," in *GLOBECOM 2022-2022 IEEE Global Communications Conference*, IEEE, 2022, pp. 6200–6205.

[25] K. Keykhosravi, B. Denis, G. C. Alexandropoulos, *et al.*, "Leveraging RIS-enabled smart signal propagation for solving infeasible localization problems: Scenarios, key research directions, and open challenges," *IEEE Vehicular Technology Magazine*, vol. 18, no. 2, pp. 20–28, 2023.

[26] K. Keykhosravi, M. F. Keskin, G. Seco-Granados, and H. Wymeersch, "SISO RIS-enabled joint 3D downlink localization and synchronization," in *IEEE Int. Conf. Commun.*, 2021, pp. 1–6.

[27] H. Zhao, N. Zhang, and Y. Shen, "Beamspace direct localization for large-scale antenna array systems," *IEEE Transactions on Signal Processing*, vol. 68, pp. 3529–3544, 2020.

[28] A. B. Baral and M. Torlak, "Joint doppler frequency and direction of arrival estimation for TDM MIMO automotive radars," *IEEE Journal of Selected Topics in Signal Processing*, vol. 15, no. 4, pp. 980–995, 2021.

[29] M. K. Ercan, M. F. Keskin, S. Gezici, and H. Wymeersch, "RIS-aided NLoS monostatic sensing under mobility and angle-doppler coupling," *arXiv preprint arXiv:2401.06544*, 2024.

[30] Z. Gong, L. Wu, Z. Zhang, *et al.*, "Joint TOA and DOA estimation with CFO compensation using large-scale array," *IEEE Transactions on Signal Processing*, vol. 69, pp. 4204–4218, 2021.

[31] B. Yao, W. Wang, and Q. Yin, "Joint AOD and CFO estimation in wireless sensor networks localization system," in *2011 IEEE Wireless Communications and Networking Conference*, IEEE, 2011, pp. 2054–2058.

[32] A. Elzanaty, A. Guerra, F. Guidi, and M.-S. Alouini, "Reconfigurable intelligent surfaces for localization: Position and orientation error bounds," *IEEE Transactions on Signal Processing*, vol. 69, pp. 5386–5402, 2021.

[33] D. Selimis, K. P. Peppas, G. C. Alexandropoulos, and F. I. Lazarakis, "On the performance analysis of RIS-empowered communications over Nakagami-m fading," *IEEE Communications Letters*, vol. 25, no. 7, pp. 2191–2195, 2021.

[34] J. An, C. Xu, L. Gan, and L. Hanzo, "Low-complexity channel estimation and passive beamforming for RIS-assisted MIMO systems relying on discrete phase shifts," *IEEE Transactions on Communications*, vol. 70, no. 2, pp. 1245–1260, 2022.

[35] T. Roman, S. Visuri, and V. Koivunen, "Blind frequency synchronization in OFDM via diagonality criterion," *IEEE Transactions on Signal Processing*, vol. 54, no. 8, pp. 3125–3135, 2006.

[36] L. Liu, Y. L. Guan, G. Bi, and D. Shao, "Effect of carrier frequency offset on single-carrier CDMA with frequency-domain equalization," *IEEE Transactions on Vehicular Technology*, vol. 60, no. 1, pp. 174–184, 2011.

[37] H. Zhang, H. Zhang, B. Di, K. Bian, Z. Han, and L. Song, "Towards ubiquitous positioning by leveraging reconfigurable intelligent surface," *IEEE Communications Letters*, vol. 25, no. 1, pp. 284–288, 2021.

[38] Z. Wang, Z. Liu, Y. Shen, A. Conti, and M. Z. Win, "Location awareness in beyond 5G networks via reconfigurable intelligent surfaces," *IEEE Journal on Selected Areas in Communications*, vol. 40, no. 7, pp. 2011–2025, 2022.

[39] M. A. Richards *et al.*, *Fundamentals of radar signal processing*. Mcgraw-hill New York, 2005, vol. 1.

[40] K. Keykhosravi and H. Wymeersch, *Multi-RIS discrete-phase encoding for interpath-interference-free channel estimation*, 2021.

[41] J. Traa, "Least-squares intersection of lines," *University of Illinois Urbana-Champaign (UIUC)*, p. 50, 2013.

[42] G. C. Alexandropoulos, I. Vinieratou, and H. Wymeersch, "Localization via multiple reconfigurable intelligent surfaces equipped with single receive rf chains," *IEEE Wireless Communications Letters*, vol. 11, no. 5, pp. 1072–1076, 2022.

[43] H. L. Van Trees, *Detection, estimation, and modulation theory, part I: detection, estimation, and linear modulation theory*. John Wiley & Sons, 2004.

[44] K. B. Petersen, M. S. Pedersen, *et al.*, "The matrix cookbook," *Technical University of Denmark*, vol. 7, no. 15, p. 510, 2008.

[45] O. Ozdogan, E. Björnson, and E. G. Larsson, "Intelligent reflecting surfaces: Physics, propagation, and pathloss modeling," *IEEE Wireless Communications Letters*, vol. 9, no. 5, pp. 581–585, 2020.

[46] L. Gaudio, M. Kobayashi, G. Caire, and G. Colavolpe, "Joint radar target detection and parameter estimation with mimo otfs," in *2020 IEEE Radar Conference (RadarConf20)*, IEEE, 2020, pp. 1–6.

[47] J. Rodríguez-Fernández, "Joint synchronization and compressive channel estimation for frequency-selective hybrid mmwave MIMO systems," *IEEE Transactions on Wireless Communications*, vol. 21, no. 1, pp. 548–562, 2021.

[48] E. Björnson and L. Sanguinetti, "Power scaling laws and near-field behaviors of massive MIMO and intelligent reflecting surfaces," *IEEE Open Journal of the Communications Society*, vol. 1, pp. 1306–1324, 2020.

[49] Z. Peng, T. Li, C. Pan, H. Ren, and J. Wang, "RIS-aided D2D communications relying on statistical csi with imperfect hardware," *IEEE Communications Letters*, vol. 26, no. 2, pp. 473–477, 2021.

[50] A. Abrardo, D. Dardari, and M. Di Renzo, "Intelligent reflecting surfaces: Sum-rate optimization based on statistical position information," *IEEE Transactions on Communications*, vol. 69, no. 10, pp. 7121–7136, 2021.

[51] F. Jiang, A. Abrardo, K. Keykhosravi, H. Wymeersch, D. Dardari, and M. Di Renzo, "Two-timescale transmission design and RIS optimization for integrated localization and communications," *IEEE Transactions on Wireless Communications*, vol. 22, no. 12, pp. 8587–8602, 2023.

[52] S. M. Kay, *Fundamentals of statistical signal processing: estimation theory*. Prentice-Hall, Inc., 1993.

PAPER C

Integrated Cellular and LEO-based Positioning and Synchronization under User Mobility

Y. Ettefagh, S. Saleh, MF. Keskin, H. Chen, G. Seco-Granados, and H. Wymeersch

Submitted to IEEE Transactions on Vehicular Technology

The layout has been revised.

Abstract

This paper investigates the localization, synchronization, and speed estimation of a mobile UE leveraging integrated terrestrial and non-terrestrial networks (NTNs), in particular low Earth orbit (LEO) satellites. We focus on a minimal setup in which the UE received signal from only one BS and one LEO satellite. We derive a generic signal model accounting for mobility, clock and frequency offsets, based on which a hierarchy of simplified models are proposed and organized by computational complexity. Estimation algorithms are developed for each model to facilitate efficient and accurate parameter recovery. Rigorous simulations validate the effectiveness of the proposed models, demonstrating their suitability across diverse scenarios. The findings highlight how the trade-off between complexity and performance can be optimized for varying deployment environments and application requirements, offering valuable insights for 6G positioning and synchronization systems under user mobility.

1 Introduction

NON-terrestrial networks (NTNs) are becoming a critical component in the evolution of wireless communication systems, particularly in the transition from 5G to 6G. By integrating satellite systems, high altitude platform station (HAPS), and airborne networks, NTNs aim to provide ubiquitous and seamless global coverage, addressing connectivity gaps in under-served and remote regions [1], [2]. Beyond communication, NTNs have the potential to transform localization services by enabling global, high-precision positioning that is essential for a variety of emerging 6G applications [3], [4]. Among various NTN technologies, low Earth orbit (LEO) satellites stand out due to their low latency, high capacity, and scalability through large constellations [3], [5]. These capabilities make LEO satellites highly effective for critical localization applications such as autonomous driving (AD) and advanced driver-assistance systems (ADAS), where accuracy, reliability, and global availability are essential [2], [5]. By complementing terrestrial systems, NTNs are shaping

the future of integrated localization and communication frameworks, enabling safe and efficient operation of autonomous vehicles, industrial automation, and other next-generation services [1], [3].

Building on these capabilities, recent research has explored integrated positioning frameworks that combine non-terrestrial and terrestrial networks to address the stringent requirements of safety-critical applications [6], [7]. These applications demand high reliability and accuracy to ensure safe operations under diverse conditions, such as urban environments with multipath interference and remote areas with limited terrestrial coverage. Positioning is increasingly central to the vision of 6G, enabling a range of advanced applications [8]. The design of integrated positioning systems leveraging the complementary strengths of terrestrial and non-terrestrial infrastructures has become a key focus in realizing the next-generation communication and sensing ecosystem [2], [9].

Terrestrial cellular networks have been widely utilized for positioning services, but they face several critical limitations that impact accuracy and reliability [10]. Precise synchronization between base stations (BSs) and mobile devices is required for accurate positioning, yet many cellular networks lack the stringent synchronization mechanisms needed for high-precision localization [11]. Another challenge is the limited coverage, as most positioning solutions require connection to at least four BSs, placing high demands on the infrastructure, compared to communication [12]. On the other hand, LEO satellite systems offer global coverage and have been proposed as a solution to enhance positioning services, considering both opportunistic form [13] and as part of 6G [4], [14]. However, they also encounter specific limitations. The high mobility of LEO satellites leads to rapidly changing satellite geometries, causing high Doppler shifts [15]. Furthermore, the beam patterns of LEO satellites, designed for communication purposes, often have narrow beamwidths for maximizing spectral efficiency, which conflicts with the broader, overlapping beams needed for accurate positioning. Interference management between overlapping beams in dense LEO constellations further complicates the system design [4].

Integrating terrestrial and NTN has attracted significant research interest due to the complementary strengths of these systems, both for communication [16]–[18] and for localization [9], [19]–[23]. Cellular networks, with their dense infrastructure and advanced signal processing capabilities, provide re-

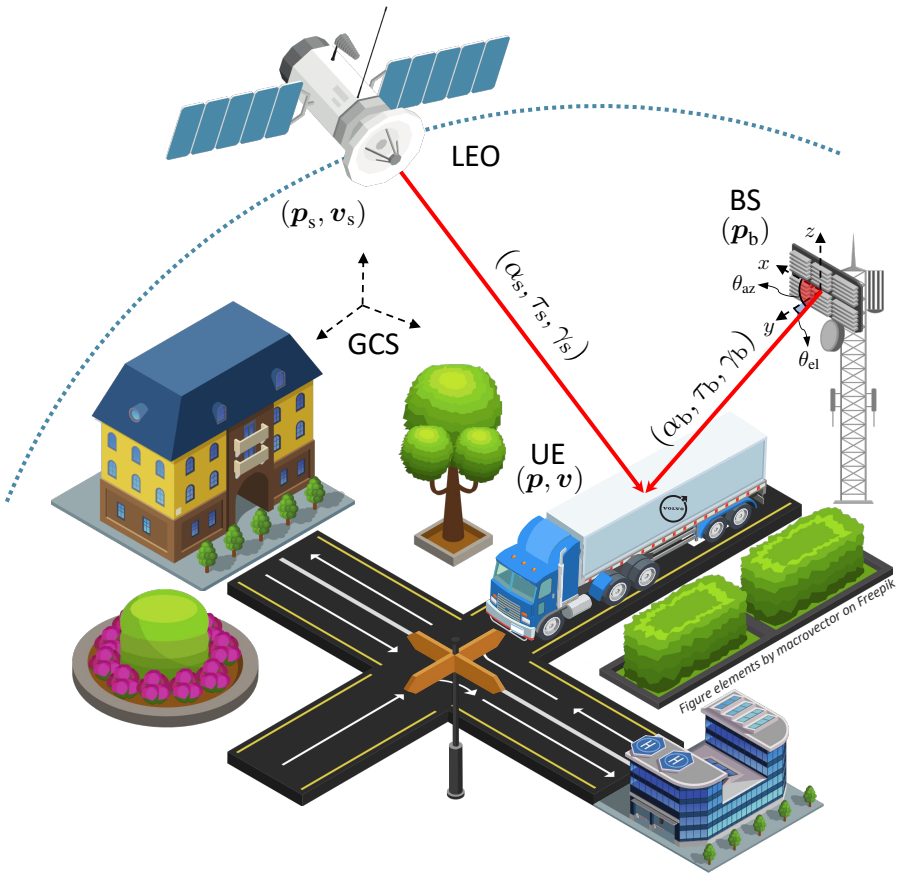

Figure 1: TN-NTN integrated setup to localize the moving UE.

liable positioning in urban areas, whereas NTNs, particularly LEO satellites, offer global coverage and resilience in rural or global navigation satellite system (GNSS)-denied environments. Recent studies have demonstrated the potential of 5G positioning reference signals to support integrated terrestrial-NTN scenarios, addressing challenges like Doppler shifts and interference in LEO-based networks [20], [21]. Fusion-based approaches, such as combining pseudorange and angle-of-arrival (AoA) measurements, have shown promise in enhancing positioning accuracy under low observability [23]. This integrated framework can bridge the performance gaps of individual systems, providing robust, precise positioning for emerging 6G applications.

In this paper, we explore the fusion of NTN positioning, more specifically LEO positioning, with cellular positioning. The setup to be used comprises one multi-antenna BS together with a time and frequency-synchronous single antenna LEO satellite transmitting to a single-antenna mobile user equipment (UE) which has an unknown clock offset and frequency offset with respect to the BS and LEO satellite. The objective is to find the position of the UE as well as the magnitude of velocity (speed), and clock and frequency offsets. The contributions of this paper are listed as follows:

- **Discrete-time channel modeling of the integrated LEO-cellular network:** We derive a sophisticated generative model based on the integration of BS-UE and satellite-UE communication that accounts for the slow-time and fast-time Doppler, intersubcarrier Doppler effect, inter-carrier interference (ICI) as well as time-varying angle-of-departure (AoD) and path gains resulting from the UE's motion. The satellite and BS are assumed to be synchronized; but the UE is not, leading to an unknown initial clock offset as well as an unknown frequency offset.
- **Simplified channel modeling based on the derived generative model:** We developed four simplified models based on the derived generative model in increasing order of complexity. The first one is a conventional communication orthogonal frequency division multiplexing (OFDM) model with a constant phase rotation over the observation window. The second model considers the slow-time Doppler effect on the carrier frequency, where the Doppler is modeled as a phase rotation across OFDM symbols. The third model considers not only the slow-time Doppler effect over the carrier frequency but also over the

subcarriers, which leads to intersubcarrier Doppler effect [24]. Finally, our most complex model considers both slow-time and fast-time Doppler effects, which causes ICI [24], [25].

- **Low complexity positioning and synchronization:** We design low-complexity algorithms for estimating the channel parameters, namely, the propagation delays, Doppler shifts, and AoD. These algorithms enable the estimation of the user's position, velocity magnitude, initial clock offset, and frequency offset based on simplified models.
- **Model Evaluation and Selection:** We assess the simplified models using the Cramér-Rao bound (CRB) and a bias metric derived from the misspecified Cramér-Rao bound (MCRB), which quantifies the performance degradation caused by using a mismatched estimation model instead of the true generative model. This analysis provides insight into how well the simplified models approximate the generative model, achieving acceptable localization performance while keeping estimation complexity low. These results guide the selection of the most suitable simplified model based on application requirements and deployment scenarios.

Notation: Vectors and matrices are shown by bold-face lower-case and bold-face upper-case letters respectively. The notations $(.)^{\mathsf{T}}$ and $(.)^{\mathsf{H}}$ represent transpose and hermitian transpose. All one vector with size n denoted by $\mathbf{1}_n$. The L2 norm of a vector is shown by $\|.\|$. The Hadamard product and convolution are represented by $\odot$ and $*$ respectively. The set of real numbers and complex numbers are shown by $\mathbb{R}$ and $\mathbb{C}$ respectively. The delta Dirac function is represented by $\delta(.)$. The function $\text{rect}(x)$ is defined such that $\text{rect}(x) = 1$ for $0 < x < 1$ and is 0 otherwise. The $(m,n)^{\text{th}}$ element of the matrix $\boldsymbol{A}$ is referred to by $[\boldsymbol{A}]_{(m,n)}$ and the notation $\tilde{(.)}$ represents a passband signal.

2 System Model

2.1 Scenario

We consider a system consisting of a BS equipped with a uniform planar array (UPA) of $\sqrt{L} \times \sqrt{L}$ antennas located at known location $\boldsymbol{p}_{\text{b}} \in \mathbb{R}^3$, a

LEO satellite with a directional antenna with known and varying location and velocity $\boldsymbol{p}_{\mathrm{s}}(t) \in \mathbb{R}^3$ and $\boldsymbol{v}_{\mathrm{s}}(t) \in \mathbb{R}^3$, respectively, and a single-antenna UE. The setup is illustrated in Fig. 1. The UE travels at a constant velocity $\boldsymbol{v} \in \mathbb{R}^3$ with known direction $\boldsymbol{v}/\|\boldsymbol{v}\|$ [1], but unknown speed $\|\boldsymbol{v}\|$ and unknown initial location $\boldsymbol{p}_0 \in \mathbb{R}^3$. As a result, the trajectory of the UE is given by $\boldsymbol{p}(t) = \boldsymbol{p}_0 + \boldsymbol{v}t$. The clock oscillators at the BS and the satellite are assumed to be synchronized to a common global reference. The clock oscillator at the UE is assumed to have an unknown initial clock offset, denoted as $\Delta_{t,0}$, relative to the clock oscillators at the BS and the satellite. Additionally, the UE's clock oscillator introduces a carrier frequency offset (CFO) η which is treated as an unknown.

2.2 Signal and Channel Model

We assume the positioning task is performed using one transmission consisting M OFDM symbols, each comprising N subcarriers (with a subcarrier spacing of Δ_f). We assign the even and the odd subcarriers to the signal transmitted by the BS and the satellite, respectively . The baseband transmit signal at the base station ($\boldsymbol{z}_{\mathrm{b}}(t) \in \mathbb{C}^L$) is

$$\boldsymbol{z}_{\mathrm{b}}(t) = \boldsymbol{w}(t)x_{\mathrm{b}}(t) = \boldsymbol{w}(t)\sum_{m=0}^{M-1} x_{\mathrm{b},m}(t), \tag{C.1}$$

where

$$x_{\mathrm{b},m}(t) = \frac{1}{\sqrt{N}}\sum_{n=0,\text{even } n}^{N-1} x_{n,m}e^{j2\pi n\Delta_f(t-mT_s)}q(t-mT_s). \tag{C.2}$$

Here, $q(t) = \mathrm{rect}(t/T_s)$,[2] $\boldsymbol{w}(t) \in \mathbb{C}^L$ is the time-varying precoding matrix, $x_{n,m}$ is the pilot at the n^{th} subcarrier of the m^{th} symbol. The total symbol duration is $T_s = T_0 + T_{\mathrm{cp}}$, where $T_0 = 1/\Delta_f$ is the elementary symbol duration,

[1] The direction can be estimated using inertial sensors (e.g., inertial measurement units (IMUs)) through dead reckoning or short-term motion tracking, even without reliable GNSS.

[2] In case of using a more practical root-raised cosine (RRC) pulse instead of a rectangular pulse, we need to apply matched filters at the receiver.

and T_{cp} is the cyclic prefix duration. Then the transmit signal upconverted to the carrier frequency f_c is $\tilde{\boldsymbol{z}}_{\text{b}}(t) = \Re\{\boldsymbol{z}_{\text{b}}(t)e^{j2\pi f_c t}\}$.

The time-varying channel between the BS and the UE ($\tilde{\boldsymbol{h}}_{\text{b}}(t,\tau) \in \mathbb{C}^L$) can be expressed as follows, for the l^{th} BS antenna:

$$\tilde{h}_{\text{b},l}(t,\tau) = [\tilde{\boldsymbol{h}}_{\text{b}}(t,\tau)]_l = \alpha_{\text{b}}(t)\delta(\tau - \tau^p_{\text{b},l}(t)), \tag{C.3}$$

Here, $\alpha_{\text{b}}(t)$ denotes the time-varying real-valued channel gain between the BS and the UE and $\tau^p_{\text{b},l}(t)$ [3] expresses the time-varying propagation delay between the l^{th} antenna at the BS and the UE. Therefore, The passband noise-free received signal at the UE can be written as

$$\tilde{y}_{\text{b}}(t) = \alpha_{\text{b}}(t)\Re\Big\{\sum_{l=1}^{L} \tilde{z}_{\text{b},l}(t - \tau^p_{\text{b},l}(t))\Big\}. \tag{C.4}$$

Similar to the BS-UE transmission, the baseband transmit signal at the satellite is $x_{\text{s}}(t) = \sum_{m=0}^{M-1} x_{\text{s},m}(t)$, where

$$x_{\text{s},m}(t) = \frac{1}{\sqrt{N}} \sum_{n=0,\text{odd } n}^{N-1} x_{n,m} e^{j2\pi n \Delta_f (t - mT_s)} q(t - mT_s). \tag{C.5}$$

Here, $x_{n,m}$ is the pilot signal transmitted by the satellite. Then the upconverted transmit signal is $\tilde{s}_{\text{s}}(t) = \Re\{x_{\text{s}}(t)e^{j2\pi f_c t}\}$. Let's denote the time-varying channel between the satellite and the UE by

$$\tilde{h}_{\text{s}}(t,\tau) = \alpha_{\text{s}}(t)\delta(\tau - \tau^p_{\text{s}}(t)), \tag{C.6}$$

where $\alpha_{\text{s}}(t)$ and $\tau^p_{\text{s}}(t)$ denote the time-varying channel gain and propagation delay between the satellite and the UE. Therefore, the noise-free received signal at the UE from the satellite will be

$$\tilde{y}_{\text{s}}(t) = \alpha_{\text{s}}(t)\Re\big\{\tilde{s}_{\text{s}}(t - \tau^p_{\text{s}}(t))\big\}. \tag{C.7}$$

[3] The superscript "p" indicates that the delay is purely due to propagation, distinguishing it from the total effective delay values that will be introduced later.

Finally, the total passband received signal will be

$$\tilde{y}(t) = \tilde{y}_{\mathrm{b}}(t) + \tilde{y}_{\mathrm{s}}(t) + \tilde{n}(t), \tag{C.8}$$

where $\tilde{n}(t)$ is the passband additive white Gaussian noise (AWGN) at the UE, with one-sided power spectral density N_0.

2.3 Geometric Relations

The time-varying propagation delay between the l^{th} antenna of the BS and the UE is given by

$$\tau^p_{\mathrm{b},l}(t) = \tau^p_{\mathrm{b}}(t) + \tau^p_l(t), \tag{C.9}$$

where $\tau^p_{\mathrm{b}}(t) = \|\boldsymbol{p}(t) - \boldsymbol{p}_{\mathrm{b}}\|/c$ is the delay between the BS phase center and the UE, and c is the speed of light. Assuming the UE is located in the far-field region of the BS, the relative delay (or advance) of the l^{th} antenna element with respect to the phase center is $\tau^p_l(t) = -(\mathbf{u}(\boldsymbol{\theta}(t))^{\mathsf{T}}\boldsymbol{q}_l)/c$, where $\boldsymbol{q}_l \in \mathbb{R}^3$ is the known position of the l^{th} antenna element with respect to the BS phase center

The unit direction vector $\mathbf{u}(\boldsymbol{\theta}(t)) \in \mathbb{R}^3$ captures the orientation of the UE with respect to the BS, and is defined as
$\mathbf{u}(\boldsymbol{\theta}(t)) = [\cos(\theta_{\mathrm{el}}(t))\cos(\theta_{\mathrm{az}}(t)),\ \cos(\theta_{\mathrm{el}}(t))\sin(\theta_{\mathrm{az}}(t)),\ \sin(\theta_{\mathrm{el}}(t))]^{\mathsf{T}}$, where $\boldsymbol{\theta}(t) = \left[\theta_{\mathrm{el}}(t), \theta_{\mathrm{az}}(t)\right]^{\mathsf{T}} \in \mathbb{R}^2$ is the time-varying 2D AoD in the global coordinate system. These angles are computed based on the relative position vector $\boldsymbol{r}_{\mathrm{b}}(t) = \boldsymbol{p}(t) - \boldsymbol{p}_{\mathrm{b}}$ from the BS to the UE, as

$$\theta_{\mathrm{el}}(t) = \arcsin\left(\frac{[\boldsymbol{r}_{\mathrm{b}}(t)]_3}{\|\boldsymbol{r}_{\mathrm{b}}(t)\|}\right), \tag{C.10}$$

$$\theta_{\mathrm{az}}(t) = \operatorname{atan2}\left([\boldsymbol{r}_{\mathrm{b}}(t)]_2, [\boldsymbol{r}_{\mathrm{b}}(t)]_1\right). \tag{C.11}$$

Finally, the time-varying propagation delay between the satellite and the UE is given by

$$\tau^p_{\mathrm{s}}(t) = \frac{\|\boldsymbol{p}(t) - \boldsymbol{p}_{\mathrm{s}}(t)\|}{c}. \tag{C.12}$$

2.4 Problem Statement

The UE should determine its initial position $\boldsymbol{p}_0$ and its speed $\|\boldsymbol{v}\|$, from the observation $\tilde{y}(t)$ in (C.8), in the presence of the unknown and time-varying channel parameters, and without being a priori synchronized to the network (the BS and the satellite). The details of the UE-network asynchrony will be elaborated in the next section.

3 Generative and Simplified Models

In this section, we begin by introducing the notion of time-varying clock bias; then, we derive the generative model used to generate observations for the localization task. To assist algorithm development, we propose four distinct simplified models, some of which are widely used in the literature. For ease of reference, the parameters introduced in the following sections are summarized in Table 1.

3.1 Clock and Frequency Offset

Due to the imperfect clock oscillator at the UE, the notion of time at the UE differs from that at the BS and satellite. The time reference of the receiver is denoted by t' and is supposed to be related to the time reference at the transmitter thruoght the below relation

$$t' = t/(1-\eta) + \Delta_{t,0}, \tag{C.13}$$

where t represents the network reference time and $\Delta_{t,0}$ is the initial clock offset. Hence, for $|\eta| \ll 1$ it holds that [26]

$$\Delta_t(t) = t' - t = \eta t + \Delta_{t,0}. \tag{C.14}$$

3.2 Generative Model

3.2.1 Continuous-time Model

The received passband signal in the global time reference t in (C.4) and (C.7) has the below contributions from the BS-UE path and satellite-UE path (see

Table 1: List of Parameters

Symbol	Description
$\boldsymbol{p}_0$	Initial position of the UE
$\boldsymbol{v}$	Velocity vector of the UE
$\|\boldsymbol{v}\|$	Speed of the UE
$\boldsymbol{p}(t)$	Position of the UE at time t
$\boldsymbol{p}_\mathrm{b}$	Position of the BS
$\boldsymbol{p}_\mathrm{s}(t)$	Position of the satellite at time t
$\boldsymbol{v}_\mathrm{s}$	Velocity of the satellite
$\boldsymbol{v}_E$	Earth's rotational velocity
T_s	Total symbol duration
T_cp	Cyclic prefix duration
T_0	Elementary symbol duration
Δ_f	Subcarrier spacing
$\boldsymbol{q}_l$	Position of the l^th BS antenna element
$\boldsymbol{\theta}(t)$	2D AoD (elevation, azimuth) at time t, $[\theta_\mathrm{el}(t), \theta_\mathrm{az}(t)]^\mathsf{T}$
$\boldsymbol{r}_\mathrm{b}(t)$	Vector from the BS to the UE
$\tau^p_{\mathrm{b},l}(t)$	Propagation delay from l^th BS antenna to UE
$\tau^p_\mathrm{b}(t)$	Propagation delay from BS center to UE
$\tau^p_l(t)$	Relative delay from l^th antenna to BS center
$\tau^p_\mathrm{s}(t)$	Propagation delay from satellite to UE
$\Delta_{t,0}$	Initial clock offset of the UE
η	CFO of the UE
t	Global (network) reference time
t'	Local time at the UE
$\Delta_t(t)$	Time-varying clock offset
$\tau^p_i(t)$	Propagation delay from node $i \in \{\mathrm{b}, \mathrm{s}\}$ to UE
τ^p_i	Initial propagation delay from node $i \in \{\mathrm{b}, \mathrm{s}\}$ to UE
ψ_i	First-order Doppler term for node i
μ_i	Second-order Doppler term for node i
γ_i	Effective Doppler shift for node i
ϵ_i	Effective Doppler rate for node i
τ_i	Effective initial delay for node i
$\bar{\psi}_{bs}$	Proxy Doppler term for satellite-BS path
$\boldsymbol{v}_{bs}$	Relative velocity between BS and satellite
τ_{bs}	Estimated delay between BS and satellite
τ_s^res	Initial residual delay after satellite timing advance

Appendix 1):

$$\tilde{y}_{\mathrm{b}}(t) = \Re\{\alpha_{\mathrm{b}}(t)\boldsymbol{a}^{\mathsf{T}}(\boldsymbol{\theta}(t))\boldsymbol{w}(t-\tau_{\mathrm{b}}^{p}(t))x_{\mathrm{b}}\left(t-\tau_{\mathrm{b}}^{p}(t)\right)e^{j2\pi f_c\left(t-\tau_{\mathrm{b}}^{p}(t)\right)}\} \tag{C.15}$$

where the array steering vector $\boldsymbol{a}(\boldsymbol{\theta}(t))$ is given by [27]

$$[\boldsymbol{a}(\boldsymbol{\theta}(t))]_l = e^{j(2\pi/\lambda)\mathbf{u}^{\mathsf{T}}(\boldsymbol{\theta}(t))\boldsymbol{q}_l}, \tag{C.16}$$

and

$$\tilde{y}_{\mathrm{s}}(t) = \Re\big\{\alpha_{\mathrm{s}}(t)x_{\mathrm{s}}\left(t-\tau_{\mathrm{s}}^{p}(t)\right)e^{j2\pi f_c(t-\tau_{\mathrm{s}}^{p}(t))}\big\}. \tag{C.17}$$

It is possible to approximate $\tau_{\mathrm{J}}^{p}(t)$, (with $\mathrm{J}\in\{\mathrm{b},\mathrm{s}\}$) as below: (see Appendix 2)

$$\begin{aligned}\tau_{\mathrm{J}}^{p}(t) &= \frac{\|\boldsymbol{p}(t)-\boldsymbol{p}_{\mathrm{J}}\|}{c} \approx \frac{\|\boldsymbol{p}_0-\boldsymbol{p}_{\mathrm{J}}\|}{c} + \frac{v_{\mathrm{J,u}}}{c}t + \frac{a_{\mathrm{J,u}}}{2c}t^2 \\ &= \tau_{\mathrm{J}}^{p} + \psi_{\mathrm{J}}t + \frac{1}{2}\mu_{\mathrm{J}}t^2,\end{aligned}$$

and $\tau_{\mathrm{J}}^{p} = \|\boldsymbol{p}_0-\boldsymbol{p}_{\mathrm{J}}\|/c$, $\psi_{\mathrm{J}} = v_{\mathrm{J,u}}/c$, $v_{\mathrm{J,u}} = (\boldsymbol{p}_0-\boldsymbol{p}_{\mathrm{J}})^{\mathsf{T}}\boldsymbol{v}_{\mathrm{J,u}}/\|\boldsymbol{p}_0-\boldsymbol{p}_{\mathrm{J}}\|$, $\mu_{\mathrm{J}} = a_{\mathrm{J,u}}/c$, and $a_{\mathrm{J,u}} = (\|\boldsymbol{v}_{\mathrm{J,u}}\|^2 - v_{\mathrm{J,u}}^2)/\|\boldsymbol{p}_0-\boldsymbol{p}_{\mathrm{J}}\|$, in which $\boldsymbol{v}_{\mathrm{b,u}} = \boldsymbol{v}$ and $\boldsymbol{v}_{\mathrm{s,u}} = (\boldsymbol{v}+\boldsymbol{v}_{\mathrm{E}}) - \boldsymbol{v}_{\mathrm{LEO}}$, where $\boldsymbol{v}_{\mathrm{E}}$ denotes the Earth rotational velocity.

We can rewrite the received signal *in the receiver's time domain* t' by substituting $t = (t'-\Delta_{t,0})(1-\eta)$ according to (C.13) as below:

$$\begin{aligned}\tilde{y}'(t') &= \tilde{y}'_{\mathrm{b}}(t') + \tilde{y}'_{\mathrm{s}}(t') + \tilde{n}'(t') \\ &= \Re\big\{\alpha'_{\mathrm{b}}(t')\boldsymbol{a}'^{\mathsf{T}}(\boldsymbol{\theta}'(t'))\boldsymbol{w}'(t_b)x'_{\mathrm{b}}\left(t_b\right)e^{j2\pi f_c t_b} \\ &\quad + \alpha'_{\mathrm{s}}(t')x'_{\mathrm{s}}\left(t_s\right)e^{j2\pi f_c t_s} + \tilde{n}'(t')\big\},\end{aligned} \tag{C.18}$$

where $\alpha'_{\mathrm{b}}(t') = \alpha_{\mathrm{b}}((t'-\Delta_{t,0})(1-\eta))$, $\boldsymbol{\theta}'(t') = \boldsymbol{\theta}((t'-\Delta_{t,0})(1-\eta))$. To ease the notation, we have introduced $t_b = (1-\gamma_b)t' - \tau_b - \epsilon_b t'^2$, $t_s = (1-\gamma_s)t' - \tau_s - \epsilon_s t'^2$

and define $\boldsymbol{w}'(t_b) = \boldsymbol{w}((1-\gamma_b)t' - \tau_b - \epsilon_b t'^2)$, and

$$\gamma_{\mathrm{J}} = \psi_{\mathrm{J}}(1-\eta) + \eta - \mu_{\mathrm{J}}(1-\eta)^2\Delta_{t,0}, \tag{C.19a}$$
$$\epsilon_{\mathrm{J}} = 1/2\mu_{\mathrm{J}}(1-\eta)^2, \tag{C.19b}$$
$$\tau_{\mathrm{J}} = \tau_{\mathrm{J}}^p + \Delta_{t,0}(1-\eta)(1-\psi_{\mathrm{J}}) + 1/2\mu_{\mathrm{J}}\Delta_{t,0}^2(1-\eta)^2, \tag{C.19c}$$

where $\mathrm{J} \in \{b, s\}$. Here, γ_{J}, ϵ_{J}, and τ_{J} can be interpreted as the effective Doppler shift, effective Doppler rate, and effective delay, respectively, in a system affected by clock offset, carrier frequency offset, and time-varying Doppler. This completes the continuous-time generative model, accounting for both first- and second-order Doppler effects as well as the asynchrony between the UE and the network.

3.2.2 Doppler and Time Precompensation

Based on (C.18), the received frequency through the BS-UE path is $f_c(1-\gamma_b)$ and through the satellite-UE path is $f_c(1-\gamma_s)$. This results in a significant Doppler spread of the received signal, which causes limitations in low-pass filtering prior to sampling at the receiver. Although γ_b is unknown and much smaller than γ_s, a significant portion of γ_s can be determined from the known satellite velocity and position, as well as the known BS position, under the assumption that the UE is in close proximity to the BS. Consequently, it is feasible to apply a frequency (Doppler) precompensation at the satellite prior to transmission, thereby rendering the Doppler shifts in the received signals through different paths more comparable and reducing the overall Doppler spread. To achieve this, a proxy for γ_s, denoted by $\bar{\psi}_{\mathrm{bs}}$, can be estimated as follows (where the subscript 'bs' represents satellite-BS path):

$$\bar{\psi}_{\mathrm{bs}} = v_{\mathrm{bs}}/c, \tag{C.20}$$
$$v_{\mathrm{bs}} = (\boldsymbol{p}_{\mathrm{b}} - \boldsymbol{p}_{\mathrm{s}})^{\mathsf{T}}\boldsymbol{v}_{\mathrm{bs}}/\left\|\boldsymbol{p}_{\mathrm{b}} - \boldsymbol{p}_{\mathrm{s}}\right\|, \tag{C.21}$$
$$\boldsymbol{v}_{\mathrm{bs}} = \boldsymbol{v}_{\mathrm{E}} - \boldsymbol{v}_{\mathrm{LEO}}. \tag{C.22}$$

Then, we can utilize $\bar{\psi}_{\mathrm{bs}}$ to adjust the transmit frequency at the satellite to $\bar{f}_c = f_c/(1-\bar{\psi}_{\mathrm{bs}})$. With this Doppler precompensation, the received frequency in the satellite-UE path is changed from $f_c(1-\gamma_s)$ to $f_c(1-\gamma_s)/(1-\bar{\psi}_{\mathrm{bs}})$.

Similarly, in the time domain, the propagation delay experienced by the signal in the satellite-UE path is considerably larger than that in the BS-

UE path. Nevertheless, a significant portion of the satellite-UE propagation delay is already known from the satellite and BS positions, as well as the UE's proximity to the BS. Hence, it is possible to apply timing advance at the satellite to reduce the delay spread in the received signal. Analogous to Doppler precompensation, a rough estimate of τ_{s}^{p} can be obtained as below:

$$\tau_{\mathrm{bs}} = \|\boldsymbol{p}_{\mathrm{b}} - \boldsymbol{p}_{\mathrm{s}}\| / c, \tag{C.23}$$

and we can then apply a timing advance of τ_{bs} to the satellite transmit signal $s(t)$, expressed as follows:

$$\tilde{\tilde{s}}_{\mathrm{s}}(t) = \Re\{x_{\mathrm{s}}(t + \tau_{\mathrm{bs}}) e^{j2\pi f_c (t+\tau_{\mathrm{bs}})}\}. \tag{C.24}$$

In this case, τ_s is replaced by τ_s^{res} in (C.18) defined as follows:

$$\tau_s^{\mathrm{res}} = \tau_{\mathrm{s}} - \tau_{\mathrm{bs}} + \Delta_{t,0}(1-\eta)(1-\psi_{\mathrm{s}}) + 1/2\mu_{\mathrm{s}}\Delta_{t,0}^2(1-\eta)^2. \tag{C.25}$$

3.2.3 Down-Conversion

To downconvert to the baseband, the clock oscillator at the UE generates $e^{-j2\pi f_c t'}$. Consequently, after removing the constant phases, the baseband signal becomes:

$$\begin{aligned} y'(t') &= \alpha'_{\mathrm{b}}(t') z(t') \sum_{m=0}^{M-1} \frac{1}{\sqrt{N}} \sum_{n=0,\ \text{even n}}^{N-1} x_{n,m} \\ &\times e^{j2\pi n \Delta_f (t_b - mT_s)} e^{-j2\pi f_c \left(\gamma_b t' + \epsilon_b t'^2\right)} q(t_b - mT_s) \\ &+ \alpha'_{\mathrm{s}}(t') \sum_{m=0}^{M-1} \frac{1}{\sqrt{N}} \sum_{n=0,\ \text{odd n}}^{N-1} x_{n,m} e^{-j2\pi \bar{f}_c \left(\gamma_s t' + \epsilon_s t'^2\right)} \\ &\times e^{j2\pi n \Delta_f (t_s^{\mathrm{res}} - mT_s)} e^{j2\pi (\bar{f}_c - f_c) t'} q(t_s^{\mathrm{res}} - mT_s) + \tilde{n}'(t'), \end{aligned} \tag{C.26}$$

where $z(t') = \boldsymbol{a}^{\mathsf{T}}(\boldsymbol{\theta}(t'))\boldsymbol{w}'(t_b)$ and $t_s^{\mathrm{res}} = (1-\gamma_s)t' - \tau_s^{\mathrm{res}} - \epsilon_s t'^2$

3.2.4 Discrete-time Model

To obtain the discrete-time received signal, we low-pass filter and sample (C.26) at $t' = mT_s + T_{\text{cp}} + kT_0/N + \tau_0$, where $k = 0, 1, \cdots, N-1$ and

$$\tau_0 = \min(\tau_b/(1-\eta), \tau_s/(1-\eta)), \tag{C.27}$$

denotes the minimum time delay in the receiver time domain making it possible to sample from the first OFDM symbol. Let us assume that τ_0 is detectable (through time acquisition in [28]) and hence we can start the receiver's clock at τ_0. We can take N samples from each OFDM symbol, resulting in $\mathbf{Y} = [\mathbf{y}_0, \cdots, \mathbf{y}_{M-1}] \in \mathbb{C}^{N\times M}$ where $\mathbf{y}_m, m = 0, \cdots, M-1$ is defined as

$$\mathbf{y}_m = \mathbf{y}_{\text{b},m} + \mathbf{y}_{\text{s},m} + \mathbf{n}_m, \tag{C.28}$$

with

$$\begin{aligned}\mathbf{y}_{\text{b},m} = \sqrt{P_{\text{b}}}[\boldsymbol{A}_{\text{b}}]_{(:,m)} \odot [\boldsymbol{Z}]_{(:,m)} \odot \Big(&\mathbf{D}^q_{\text{b}}(\gamma_b, \epsilon_b) \\ &\times \mathbf{F}^q_{m,\text{b}}(\gamma_b, \epsilon_b)\Big(\boldsymbol{i}^q_{m,\text{b}}(\gamma_b, \epsilon_b) \odot \Big(\big(\boldsymbol{q}_{\text{b}}(\gamma_b) \odot \boldsymbol{b}_{\text{b}}(\tau_b)\big) \\ &\times [\mathbf{c}^q_{\text{b}}(\gamma_b, \epsilon_b)]_m\Big)\Big)\Big) \odot \mathbf{H}^q_{\text{b}}(\epsilon_b),\end{aligned} \tag{C.29}$$

$$\begin{aligned}\mathbf{y}_{\text{s},m} = \sqrt{P_{\text{s}}}[\boldsymbol{A}_{\text{s}}]_{(:,m)} \odot \Big(&\mathbf{D}^q_{\text{s}}(\gamma_s, \epsilon_s)\mathbf{F}^q_{\text{s}}(\gamma_s, \epsilon_s)\times \\ &\Big(\boldsymbol{i}^q_{\text{s}}(\gamma_s, \epsilon_s) \odot \Big(\big(\boldsymbol{q}_{\text{s}}(\gamma_s) \odot \boldsymbol{b}_{\text{s}}(\tau^{\text{res}}_s)\big)[\mathbf{c}^q_{\text{s}}(\gamma_s, \epsilon_s)]_m\Big)\Big)\Big) \odot \mathbf{H}^q_{\text{s}}(\epsilon_s).\end{aligned} \tag{C.30}$$

The superscript 'q' is used to underscore that the corresponding matrices/vectors contain quadratic terms, which originate from (C.18). The different matrices defined above are used to capture the different effects:

- *Time variations:* $[\boldsymbol{A}_{\text{b}}]_{(:,m)}$, $[\boldsymbol{A}_{\text{s}}]_{(:,m)}$ and $[\boldsymbol{Z}]_{(:,m)}$ comprise the samples of $\alpha'_{\text{b}}(t')$, $\alpha'_{\text{s}}(t')$ and $z(t')$, respectively.

- *Inter-carrier interference:* The diagonal matrices $\mathbf{D}^q_{\text{b}}(\gamma_b, \epsilon_b) \in \mathbb{C}^{N\times N}$ and $\mathbf{D}^q_{\text{s}}(\gamma_s, \epsilon_s) \in \mathbb{C}^{N\times N}$ denote ICI in the BS-UE and satellite-UE paths,

respectively. The n^{th} diagonal element of each matrix is defined as:

$$[\mathbf{D}_{\text{b}}^{q}(\gamma_b,\epsilon_b)]_{k,k} = e^{-j2\pi f_c(\gamma_b T_0 k/N+\epsilon_b T_0^2 k^2/N^2+2\epsilon_b T_{\text{cp}} T_0 k/N)}, \tag{C.31}$$

$$[\mathbf{D}_{\text{s}}^{q}(\gamma_s,\epsilon_s)]_{k,k} = e^{-j2\pi f_c(1-(1-\gamma_s)/(1-\bar{\psi}_{\text{bs}}))T_0 k/N} \times e^{-j2\pi f_c(\epsilon_s T_0^2/(1-\bar{\psi}_{\text{bs}})k^2/N^2+2\epsilon_s T_{\text{cp}} T_0/(1-\bar{\psi}_{\text{bs}})k/N)}. \tag{C.32}$$

- *Slow-time Doppler:* The slow-time effect in BS-UE path and satellite-UE path are denoted by $\mathbf{c}_{\text{b}}^{q}(\gamma_b,\epsilon_b)$ and $\mathbf{c}_{\text{s}}^{q}(\gamma_s,\epsilon_s)$ respectively and defined as below:

$$[\mathbf{c}_{\text{b}}^{q}(\gamma_b,\epsilon_b)]_m = e^{-j2\pi f_c(\gamma m T_s+\epsilon_b m^2 T_s^2+2\epsilon_b m T_s T_{\text{cp}})}, \tag{C.33}$$

$$[\mathbf{c}_{\text{s}}^{q}(\gamma_s,\epsilon_s)]_m = e^{-j2\pi f_c((1-(1-\gamma_s)/(1-\bar{\psi}_{\text{bs}}))m T_s)} \times e^{-j2\pi f_c(\epsilon_s m^2 T_s^2/(1-\bar{\psi}_{\text{bs}})+2\epsilon_s m T_s T_{\text{cp}}/(1-\bar{\psi}_{\text{bs}}))}. \tag{C.34}$$

- *Delay steering vectors:* For even n, $\boldsymbol{b}_{\text{b}}(\tau) \in \mathbb{C}^{N/2}$ with

$$\boldsymbol{b}_{\text{b}}(\tau_b) = [1, e^{-j2\pi\Delta_f 2\tau_b}, \cdots e^{-j2\pi\Delta_f (N-2)\tau_b}]^{\mathsf{T}}. \tag{C.35}$$

and for odd n,

$$\boldsymbol{b}_{\text{s}}(\tau_s^{\text{res}}) = [e^{-j2\pi\Delta_f \tau_s^{\text{res}}}, e^{-j2\pi\Delta_f 3\tau_s^{\text{res}}}, \cdots e^{-j2\pi\Delta_f (N-1)\tau_s^{\text{res}}}]^{\mathsf{T}}. \tag{C.36}$$

- *Modified Fourier matrices:* For even n, the matrix $\mathbf{F}_{m,\text{b}}^{q}(\gamma_b,\epsilon_b) \in \mathbb{C}^{N\times N/2}$ is defined as

$$[\mathbf{F}_{m,\text{b}}^{q}(\gamma_b,\epsilon_b)]_{k,n} = \frac{1}{\sqrt{N}} \times e^{j2\pi(k/Nn(1-\gamma_b)-\epsilon_b k^2/N^2 nT_0-2\epsilon_b gk/NnT_0-2nm\epsilon_b k/NT_s)}, \tag{C.37}$$

while for odd n

$$[\mathbf{F}^q_{m,\mathrm{s}}(\gamma_s,\epsilon_s)]_{k,n} = \frac{1}{\sqrt{N}}\times \tag{C.38}$$
$$e^{j2\pi(k/Nn(1-\gamma_s)-\epsilon_s k^2/N^2 nT_0-2\epsilon_s gk/NnT_0-2nm\epsilon_s k/NT_s)}.$$

- *Intersubcarrier Doppler effect:* For even n, $\mathbf{I}^q_{\mathrm{b}}(\gamma_b,\epsilon_b)\in\mathbb{C}^{N/2\times M}$, can be expressed as

$$[\mathbf{I}^q_{\mathrm{b}}(\gamma_b,\epsilon_b)]_{n,m} = \tag{C.39}$$
$$e^{-j2\pi(\gamma_b mn(g+1)+nm^2\epsilon_b(1+g)T_s+2mn\epsilon_b gT_s)},$$

while for odd n

$$[\mathbf{I}^q_{\mathrm{s},m}(\gamma_s,\epsilon_s)]_{n,m} = \tag{C.40}$$
$$e^{-j2\pi(\gamma_s mn(g+1)+nm^2\epsilon_s(1+g)T_s+2mn\epsilon_s gT_s)}.$$

- *Intersubcarrier phase offset:* For even n, $\boldsymbol{q}_{\mathrm{b}}(\gamma_b)\in\mathbb{C}^{N/2}$, where

$$\boldsymbol{q}_{\mathrm{b}}(\gamma_b) = [1, e^{-j2\pi\gamma_b g2},\cdots,e^{-j2\pi\gamma_b g(N-2)}]^{\mathsf{T}}, \tag{C.41}$$

while for odd n

$$\boldsymbol{q}_{\mathrm{s}}(\gamma_s) = [e^{-j2\pi\gamma_s g},\cdots,e^{-j2\pi\gamma_s g(N-1)}]^{\mathsf{T}}. \tag{C.42}$$

- *Second-order crossed slow/fast-time Doppler effect*: Finally,

$$[\mathbf{H}^q_{\mathrm{b}}(\epsilon_b)]_{k,m} = e^{-j4\pi f_c\epsilon_b mT_s kT_0/N}, \tag{C.43}$$

$$[\mathbf{H}^q_{\mathrm{s}}(\epsilon_s)]_{k,m} = e^{-j4\pi f_c/(1-\bar{\psi}_{\mathrm{bs}})\epsilon_s mT_s kT_0/N}. \tag{C.44}$$

The received signal in (C.28) represents the 'true' generative model, which is highly complex and challenging to handle. In the following subsection, four simplified models are proposed, arranged in decreasing order of complexity.

3.3 Simplified Models

In this subsection, four simplified models are introduced based on the true model (C.28), arranged in descending order of complexity.

3.3.1 Model with constant channel (gain and AoD) and only first-order Doppler (CCFOD)

This model is derived by neglecting the second-order terms in (C.28). In this model, the assumption is that the channel gains and AoDs remain constant throughout the transmission of M OFDM symbols. Specifically, we set $\mu_{\mathrm{b}} = 0$ and $\mu_{\mathrm{s}} = 0$, which would change γ_b and γ_s in (C.19a) as below

$$\gamma_b = \psi_{\mathrm{b}}(1-\eta) + \eta, \tag{C.45}$$
$$\gamma_s = \psi_{\mathrm{s}}(1-\eta) + \eta. \tag{C.46}$$

Moreover, we consider $\alpha_{\mathrm{b}} = \alpha_{\mathrm{b}}(t=0)$, $\alpha_{\mathrm{s}} = \alpha_{\mathrm{s}}(t=0)$, $\boldsymbol{\theta} = \boldsymbol{\theta}(t=0)$. Under these assumptions, the received signal simplifies to the following form:

$$\begin{aligned}&\mathbf{Y} = \\ &\sqrt{P_{\mathrm{b}}}\alpha_{\mathrm{b}}\mathbf{D}_{\mathrm{b}}(\gamma_b)\mathbf{F}_{\mathrm{b}}\big(\mathbf{I}_{\mathrm{b}}(\gamma_b) \odot (\boldsymbol{b}_{\mathrm{b}}(\tau_b)(\boldsymbol{z}(\boldsymbol{\theta}) \odot \mathbf{c}_{\mathrm{b}}(\gamma_b))^{\mathsf{T}})\big) + \\ &\sqrt{P_{\mathrm{s}}}\alpha_{\mathrm{s}}\mathbf{D}_{\mathrm{s}}(\gamma_s)\mathbf{F}_{\mathrm{s}}(\gamma_{\mathrm{s}})\big(\mathbf{I}_{\mathrm{s}}(\gamma_s) \odot (\boldsymbol{b}_{\mathrm{s}}(\tau_s^{\mathrm{res}})\mathbf{c}_{\mathrm{s}}^{\mathsf{T}}(\gamma_s))\big) + \mathbf{N},\end{aligned} \tag{C.47}$$

where $\mathbf{D}_{\mathrm{b}}(\gamma_b) = \mathbf{D}_{\mathrm{b}}^{q}(\gamma_b, \epsilon_b = 0)$, $\mathbf{D}_{\mathrm{s}}(\gamma_s) = \mathbf{D}_{\mathrm{s}}^{q}(\gamma_s, \epsilon_s = 0)$ as below

$$[\mathbf{D}_{\mathrm{b}}(\gamma_b)]_{k,k} = e^{-j2\pi f_c \gamma_b T_0 k/N}, \tag{C.48}$$
$$[\mathbf{D}_{\mathrm{s}}(\gamma_s)]_{k,k} = e^{-j2\pi f_c (1-(1-\gamma_s)/(1-\bar{\psi}_{\mathrm{bs}}))T_0 k/N}. \tag{C.49}$$

And $\mathbf{F}_{\mathrm{b}} = \mathbf{F}_{\mathrm{b}}^{q}(\gamma_{\mathrm{b}}, \epsilon_{\mathrm{b}} = 0) \approx \mathbf{F}_{\mathrm{b}}^{q}(\gamma_{\mathrm{b}} = 0, \epsilon_{\mathrm{b}} = 0)$, $\mathbf{F}_{\mathrm{s}}(\gamma_{\mathrm{s}}) = \mathbf{F}_{\mathrm{s}}^{q}(\gamma_{\mathrm{s}}, \epsilon_{\mathrm{s}} = 0)$ as below[4]

$$[\mathbf{F}_{\mathrm{b}}]_{k,n} = \frac{1}{\sqrt{N}} e^{j2\pi nk/N}, \text{ for even } n, \tag{C.50}$$

$$[\mathbf{F}_{\mathrm{s}}(\gamma_{\mathrm{s}})]_{k,n} = \frac{1}{\sqrt{N}} e^{j2\pi(1-\gamma_{\mathrm{s}})nk/N}, \text{ for odd } n. \tag{C.51}$$

and $\mathbf{I}_{\mathrm{b}}(\gamma_b) = \mathbf{I}_{\mathrm{b}}^{q}(\gamma_b, \epsilon_b = 0)$, $\mathbf{I}_{\mathrm{s}}(\gamma_s) = \mathbf{I}_{\mathrm{s}}^{q}(\gamma_s, \epsilon_s = 0)$ as following

$$[\mathbf{I}_{\mathrm{b},m}(\gamma_b)]_{n,m} = e^{-j2\pi\gamma_b mn(g+1)}, \text{ for even } n, \tag{C.52}$$

$$[\mathbf{I}_{\mathrm{s},m}(\gamma_s)]_{n,m} = e^{-j2\pi\gamma_s mn(g+1)}, \text{ for odd } n, \tag{C.53}$$

and $\mathbf{c}_{\mathrm{b}}(\gamma_b) = \mathbf{c}_{\mathrm{b}}^{q}(\gamma_b, \epsilon_b = 0)$, $\mathbf{c}_{\mathrm{s}}(\gamma_s) = \mathbf{c}_{\mathrm{s}}^{q}(\gamma_s, \epsilon_s = 0)$ as below

$$[\mathbf{c}_{\mathrm{b}}(\gamma_b)]_m = e^{-j2\pi f_c \gamma_b m T_s}, \tag{C.54}$$

$$[\mathbf{c}_{\mathrm{s}}(\gamma_s)]_m = e^{-j2\pi f_c((1-(1-\gamma_s)/(1-\bar{\psi}_{\mathrm{bs}}))mT_s)}, \tag{C.55}$$

and $[\boldsymbol{z}(\boldsymbol{\theta})]_m = \boldsymbol{w}'^{\mathsf{T}}(t' = mT_s + T_{\mathrm{cp}})\boldsymbol{a}(\boldsymbol{\theta})$.

3.3.2 Model without ICI (CCFODnoICI)

As the next step towards simplifying (C.28), we neglect ICI and Doppler effect on subcarriers over fast time as well. Therefore the received signal can be modeled as

$$\begin{aligned}\mathbf{Y} = &\sqrt{P_{\mathrm{b}}}\alpha_{\mathrm{b}}\mathbf{F}_{\mathrm{b}}\big(\mathbf{I}_{\mathrm{b}}(\gamma_b) \odot (\boldsymbol{b}_{\mathrm{b}}(\tau_b)(\boldsymbol{z}(\boldsymbol{\theta}) \odot \mathbf{c}_{\mathrm{b}}(\gamma_b))^{\mathsf{T}})\big) \\ &+ \sqrt{P_{\mathrm{s}}}\alpha_{\mathrm{s}}\mathbf{F}_{\mathrm{s}}\big(\mathbf{I}_{\mathrm{s}}(\gamma_s) \odot (\boldsymbol{b}_{\mathrm{s}}(\tau_s^{\mathrm{res}})\mathbf{c}_{\mathrm{s}}^{\mathsf{T}}(\gamma_s))\big) + \mathbf{N}.\end{aligned} \tag{C.56}$$

Here, $\mathbf{F}_{\mathrm{s}} = \mathbf{F}_{\mathrm{s}}^{q}(\gamma_s = 0, \epsilon_s = 0)$.

[4]Since γ_{b} is much smaller than γ_{s}, and Doppler precompensation in our setup affects only the carrier frequency, we can approximate $\mathbf{F}_{\mathrm{b}}^{q}(\gamma_{\mathrm{b}}, \epsilon_{\mathrm{b}} = 0) \approx \mathbf{F}_{\mathrm{b}}^{q}(\gamma_{\mathrm{b}} = 0, \epsilon_{\mathrm{b}} = 0) = \mathbf{F}_{\mathrm{b}}$, effectively reducing this matrix to the IDFT matrix. If Doppler precompensation was applied at both the carrier frequency and the subcarrier levels, $\mathbf{F}_{\mathrm{s}}^{q}(\gamma_{\mathrm{s}}, \epsilon_{\mathrm{s}} = 0)$ would similarly reduce to the IDFT matrix.

3.3.3 Model with only Slow Doppler (SlowD)

To further simplify the received signal, we neglect the intersubcarrier Doppler effect as well, leading to

$$\begin{aligned}\mathbf{Y} = &\sqrt{P_{\mathrm{b}}}\alpha_{\mathrm{b}}\mathbf{F}_{\mathrm{b}}(\boldsymbol{b}_{\mathrm{b}}(\tau_b)(\boldsymbol{z}(\boldsymbol{\theta}) \odot \mathbf{c}_{\mathrm{b}}(\gamma_b))^{\mathsf{T}}) \\ &+ \sqrt{P_{\mathrm{s}}}\alpha_{\mathrm{s}}\mathbf{F}_{\mathrm{s}}(\boldsymbol{b}_{\mathrm{s}}(\tau_s^{\mathrm{res}})\mathbf{c}_{\mathrm{s}}^{\mathsf{T}}(\gamma_s)) + \mathbf{N},\end{aligned} \tag{C.57}$$

in which only the slow-time Doppler effect is present, meaning that the phase changes for every OFDM symbol and is constant throughout N subcarriers in each OFDM symbol. This model is common in the OFDM integrated sensing and communication (ISAC) literature [29].

3.3.4 Communication Coherence Interval Model (Comm)

Finally, we derive the simplest model, where mobility is assumed but the CFO and Doppler effects are considered negligible due to their minimal impact over the short observation period. In this model, these effects are treated as a fixed phase over the entire frame, which can be absorbed into the channel gain. Consequently, neither slow nor fast time Doppler nor CFO effects are accounted for, and no phase rotation over time is observed. Under these assumptions, the received signal can be expressed as follows:

$$\mathbf{Y} = \sqrt{P_{\mathrm{b}}}\alpha_{\mathrm{b}}\mathbf{F}_{\mathrm{b}}(\boldsymbol{b}_{\mathrm{b}}(\tau_b)\boldsymbol{z}^{\mathsf{T}}(\boldsymbol{\theta})) + \sqrt{P_{\mathrm{s}}}\alpha_{\mathrm{s}}\mathbf{F}_{\mathrm{s}}(\boldsymbol{b}_{\mathrm{s}}(\tau_s^{\mathrm{res}})\mathbf{1}_M^{\mathsf{T}}) + \mathbf{N}. \tag{C.58}$$

This model is common in the communication literature [30] and also the positioning literature under low mobility [31].

4 Estimation Algorithms

In this section, we present the estimation algorithms corresponding to the proposed simplified models in Section 3.3, starting with the simplest model and progressing to more complex ones.

4.1 Channel Parameter Estimation

4.1.1 Model Comm

The channel-domain parameter vector is

$$\boldsymbol{\chi}_{\mathrm{ch}}^{a} = [\alpha_{\mathrm{R}}, \alpha_{\mathrm{I}}, \alpha_{\mathrm{R}}, \alpha_{\mathrm{I}}, \tau_b, \tau_s^{\mathrm{res}}, \boldsymbol{\theta}^{\mathsf{T}}]^{\mathsf{T}} \in \mathbb{R}^8. \tag{C.59}$$

Since the satellite-UE and BS-UE paths do not share any common unknown parameters, each path can be analyzed independently. Leveraging the structure of model Comm, along with the orthogonal subcarriers employed by the BS and the satellite, the contributions from the BS and satellite can be separated as follows:

$$\tilde{\mathbf{Y}}_{\mathrm{b}} = \mathbf{F}_{\mathrm{b}}^{\mathsf{H}} \mathbf{Y}, \tag{C.60}$$

$$\tilde{\mathbf{Y}}_{\mathrm{s}} = \mathbf{F}_{\mathrm{s}}^{\mathsf{H}} \mathbf{Y}. \tag{C.61}$$

To estimate τ_s^{res}, the following problem needs to be solved:

$$[\hat{\tau}_s^{\mathrm{res}}, \hat{\alpha}_{\mathrm{s}}] = \arg\min_{\tau, \alpha_{\mathrm{s}}} \left\| \tilde{\mathbf{Y}}_{\mathrm{s}} - \alpha_{\mathrm{s}} \sqrt{P_{\mathrm{s}}} \boldsymbol{b}_{\mathrm{s}}(\tau) \mathbf{1}_M^{\mathsf{T}} \right\|^2, \tag{C.62}$$

which results in

$$\hat{\tau}_s^{\mathrm{res}} = \arg\min_{\tau} \left\| \tilde{\mathbf{Y}}_{\mathrm{s}} - \hat{\alpha}_{\mathrm{s}}(\tau) \sqrt{P_{\mathrm{s}}} \boldsymbol{b}_{\mathrm{s}}(\tau) \mathbf{1}_M^{\mathsf{T}} \right\|^2, \tag{C.63}$$

where

$$\hat{\alpha}_{\mathrm{s}}(\tau) = \frac{\left\| \tilde{\mathbf{Y}}_{\mathrm{s}} \mathbf{1}_M \boldsymbol{b}_{\mathrm{s}}^{\mathsf{H}}(\tau) \right\|^2}{\sqrt{P_s} \left\| \boldsymbol{b}_{\mathrm{s}}(\tau) \mathbf{1}_M^{\mathsf{T}} \right\|^2} = \frac{\left\| \tilde{\mathbf{Y}}_{\mathrm{s}} \mathbf{1}_M \boldsymbol{b}_{\mathrm{s}}^{\mathsf{H}}(\tau) \right\|^2}{\sqrt{P_s} MN/2}. \tag{C.64}$$

It follows with (C.63) that

$$\hat{\tau}_s^{\mathrm{res}} = \arg\max_{\tau} \left| \boldsymbol{b}_{\mathrm{s}}^{\mathsf{H}}(\tau) \tilde{\mathbf{Y}}_{\mathrm{s}} \mathbf{1}_M \right|. \tag{C.65}$$

The problem is initially solved by performing a 1D grid search, which can then be refined using a 1D quasi-Newton algorithm to obtain more accurate estimates of τ_s^{res}.

To estimate τ_b and $\boldsymbol{\theta}$, the following problem needs to be solved:

$$[\hat{\tau}_b, \hat{\boldsymbol{\theta}}^{\mathsf{T}}, \hat{\alpha}_{\mathrm{b}}] = \underset{\tau, \boldsymbol{\theta}, \alpha_{\mathrm{b}}}{\arg\min} \left\| \tilde{\mathbf{Y}}_{\mathrm{b}} - \alpha_{\mathrm{b}} \sqrt{P_{\mathrm{b}}} \boldsymbol{b}_{\mathrm{b}}(\tau) \boldsymbol{z}^{\mathsf{T}}(\boldsymbol{\theta}) \right\|^2. \tag{C.66}$$

which results in

$$[\hat{\tau}_b, \hat{\boldsymbol{\theta}}^{\mathsf{T}}] = \underset{\tau, \boldsymbol{\theta}}{\arg\min} \left\| \tilde{\mathbf{Y}}_{\mathrm{b}} - \hat{\alpha}_{\mathrm{b}}(\tau, \boldsymbol{\theta}) \sqrt{P_{\mathrm{b}}} \boldsymbol{b}_{\mathrm{b}}(\tau) \boldsymbol{z}^{\mathsf{T}}(\boldsymbol{\theta}) \right\|^2. \tag{C.67}$$

where

$$\hat{\alpha}_{\mathrm{b}}(\tau, \boldsymbol{\theta}) = \frac{\left\| \tilde{\mathbf{Y}}_{\mathrm{b}} (\boldsymbol{z}(\boldsymbol{\theta})^* \boldsymbol{b}_{\mathrm{b}}^{\mathsf{H}}(\tau)) \right\|^2}{\sqrt{P_{\mathrm{b}}} \left\| \boldsymbol{b}_{\mathrm{b}}(\tau) \boldsymbol{z}^{\mathsf{T}}(\boldsymbol{\theta}) \right\|^2}. \tag{C.68}$$

The estimation problem (C.66) can be solved using a separate 1D and 2D grid search, where the initial search employs non-coherent integration over the OFDM symbols (slow-time) to estimate the delay, as outlined below:

$$\hat{\tau}_b = \arg\max_{\tau} \left| \boldsymbol{b}_{\mathrm{b}}^{\mathsf{H}}(\tau) \tilde{\mathbf{Y}}_{\mathrm{b}} \mathbf{1}_M \right|, \tag{C.69}$$

followed by coherent integration over the sub-carriers to estimate the 2D AoDs

$$\hat{\boldsymbol{\theta}} = \arg\max_{\boldsymbol{\theta}} \left| \boldsymbol{b}_{\mathrm{b}}^{\mathsf{H}}(\hat{\tau}_b) \tilde{\mathbf{Y}}_{\mathrm{b}} \boldsymbol{z}^*(\boldsymbol{\theta}) \right|. \tag{C.70}$$

We can refine our estimates using (C.66) by performing the quasi-Newton algorithm.

4.1.2 Model SlowD

In model SlowD, the channel-domain parameter vector is

$$\boldsymbol{\chi}_{\mathrm{ch}}^b = [\boldsymbol{\chi}_{\mathrm{ch}}^{a\,\mathsf{T}}, \gamma_b, \gamma_s]^{\mathsf{T}} \in \mathbb{R}^{10}. \tag{C.71}$$

Similar to model Comm, the BS-UE and satellite-UE paths can be separated due to the use of orthogonal subcarriers using (C.60) and (C.61). To estimate

τ_s^{res} and γ_s, below problem needs to be solved:

$$[\hat{\tau}_s^{\text{res}}, \hat{\gamma}_s] = \arg\min_{\tau,\gamma} \left\| \tilde{\mathbf{Y}}_{\text{s}} - \hat{\alpha}_{\text{s}}(\tau,\gamma)\sqrt{P_{\text{s}}}\boldsymbol{b}_{\text{s}}(\tau)\mathbf{c}_{\text{s}}(\gamma)^{\mathsf{T}} \right\|^2, \tag{C.72}$$

where

$$\hat{\alpha}_s(\tau,\gamma) = \frac{\left\| \tilde{\mathbf{Y}}_{\text{s}}(\mathbf{c}_{\text{s}}^*(\gamma)\boldsymbol{b}_{\text{s}}^{\mathsf{H}}(\tau)) \right\|^2}{\sqrt{P_s}\left\| \boldsymbol{b}_{\text{s}}(\tau)\mathbf{c}_{\text{s}}(\gamma)^{\mathsf{T}} \right\|^2}. \tag{C.73}$$

Since τ_s^{res} is related to the subcarriers and γ_s is associated with the slow-time samples, these parameters can be estimated independently using separate grid searches. To estimate τ_s^{res}, we can perform non-coherent integration over slow-time and utilize (C.65) to determine $\hat{\tau}_s^{\text{res}}$. Subsequently, this result can be used to perform coherent integration over the sub-carriers and estimate γ_s accordingly:

$$\hat{\gamma}_s = \arg\max_{\gamma} \left| \boldsymbol{b}_{\text{s}}^{\mathsf{H}}(\hat{\tau}_s^{\text{res}})\tilde{\mathbf{Y}}_{\text{s}}\mathbf{c}_{\text{s}}^*(\gamma) \right|. \tag{C.74}$$

For estimating parameters in the BS-UE path, the following problem needs to be solved:

$$[\hat{\tau}_b, \gamma_b, \hat{\boldsymbol{\theta}}^{\mathsf{T}}] = \arg\min_{\tau,\gamma,\boldsymbol{\theta}} \left\| \tilde{\mathbf{Y}}_{\text{b}} - \hat{\alpha}_{\text{b}}(\tau,\gamma,\boldsymbol{\theta})\sqrt{P_{\text{b}}}(\boldsymbol{b}_{\text{b}}(\tau)(\boldsymbol{z}(\boldsymbol{\theta}) \odot \mathbf{c}_{\text{b}}(\gamma))^{\mathsf{T}}) \right\|^2, \tag{C.75}$$

where

$$\hat{\alpha}_{\text{b}}(\tau,\gamma,\boldsymbol{\theta}) = \frac{\left\| \tilde{\mathbf{Y}}_{\text{b}}((\boldsymbol{z}^*(\boldsymbol{\theta}) \odot \mathbf{c}_{\text{b}}^*(\gamma))\boldsymbol{b}_{\text{b}}^{\mathsf{H}}(\tau)) \right\|^2}{\sqrt{P_{\text{b}}}\left\| \boldsymbol{b}_{\text{b}}(\tau)(\boldsymbol{z}(\boldsymbol{\theta}) \odot \mathbf{c}_{\text{b}}(\gamma))^{\mathsf{T}} \right\|^2}. \tag{C.76}$$

It can be observed that while τ_b is associated with subcarrier dimension, both $\boldsymbol{\theta}$ and γ_b vary over slow-time domain. This variation leads to angle-Doppler coupling in the slow-time domain, and to tackle the estimation problem, a 1D grid search followed by a 3D grid search (2D angle + Doppler) is required in the basic approach. The 1D grid search is used to estimate τ_b, and the

subsequent 3D grid search jointly estimates $\boldsymbol{\theta}$ and γ_b. This complexity can be reduced by designing the beamforming matrix with repetitive angles over a subset of the observations, such as the first P samples, similar to the solution in [32]. For this subset, the beamforming matrix remains fixed, meaning no angle information is embedded in these observations. As a result, Doppler can be estimated independently of the angles. Once γ_b is estimated from this subset, the full set of observations can then be used to estimate the angles $\boldsymbol{\theta}$, effectively decoupling the 3D grid search into a 1D Doppler search and a 2D angle search. Therefore, through non-coherent integration over slow-time and a 1D delay search, an estimate for τ_b is obtained using (C.69). Furthermore, an estimate of γ_b can be found by coherently integrating over the sub-carriers, using the estimated delay, and leveraging the first P slow-time samples of $\tilde{\mathbf{Y}}_{\mathrm{b}}$ as below

$$\hat{\gamma}_b = \arg\max_{\gamma} \left| \boldsymbol{b}_{\mathrm{b}}^{\mathsf{H}}(\hat{\tau}_b)[\tilde{\mathbf{Y}}_{\mathrm{b}}]_{(:,1:P)}[\mathbf{c}_{\mathrm{b}}^{*}(\gamma)]_{(1:P)} \right|, \tag{C.77}$$

and then the full set of observations can be utilized with coherent detection to estimate $\boldsymbol{\theta}$ as follows:

$$\hat{\boldsymbol{\theta}} = \arg\max_{\boldsymbol{\theta}} \left| \boldsymbol{b}_{\mathrm{b}}^{\mathsf{H}}(\hat{\tau}_b)\tilde{\mathbf{Y}}_{\mathrm{b}}(\mathbf{c}_{\mathrm{b}}^{*}(\hat{\gamma}_b) \odot \boldsymbol{z}^{*}(\boldsymbol{\theta})) \right|. \tag{C.78}$$

Finally, by performing the quasi-Newton algorithm we can refine our estimates.

4.1.3 Model CCFODnoICI

The channel-domain parameter vector in model CCFODnoICI is identical to that in model SlowD, as $\boldsymbol{\chi}_{\mathrm{ch}}^{b}$. The process begins by separating the BS-UE and satellite-UE contributions, using (C.60) and (C.61). To estimate τ_s^{res} and γ_s, the following problem needs to be solved:

$$\begin{aligned} &[\hat{\tau}_s^{\mathrm{res}}, \hat{\gamma}_s] = \arg\min_{\tau,\gamma} \\ &\left\| \tilde{\mathbf{Y}}_{\mathrm{s}} - \hat{\alpha}_{\mathrm{s}}(\tau,\gamma)\sqrt{P_{\mathrm{s}}}\mathbf{I}_{\mathrm{s}}(\gamma) \odot (\boldsymbol{b}_{\mathrm{s}}(\tau)\mathbf{c}_{\mathrm{s}}(\gamma)^{\mathsf{T}}) \right\|^2, \end{aligned} \tag{C.79}$$

where

$$\hat{\alpha}_s(\tau,\gamma) = \frac{\left\|\tilde{\mathbf{Y}}_{\mathrm{s}}(\mathbf{I}_{\mathrm{s}}^{\mathsf{H}}(\gamma)\odot \mathbf{c}_{\mathrm{s}}^{*}(\gamma)\boldsymbol{b}_{\mathrm{s}}^{\mathsf{H}}(\tau))\right\|^2}{\sqrt{P_s}\left\|\mathbf{I}_{\mathrm{s}}^{\mathsf{H}}(\gamma)\odot(\boldsymbol{b}_{\mathrm{s}}(\tau)\mathbf{c}_{\mathrm{s}}(\gamma)^{\mathsf{T}})\right\|^2}. \tag{C.80}$$

The primary distinction between model CCFODnoICI and model SlowD lies in the inclusion of the intersubcarrier Doppler effect ($\mathbf{I}_{\mathrm{b}}(\gamma_b)$ and $\mathbf{I}_{\mathrm{s}}(\gamma_s)$). Given that a significant portion of γ_s is already known from $\bar{\psi}_{\mathrm{bs}}$, this prior knowledge can be leveraged to partially mitigate the intersubcarrier Doppler effect in the satellite-UE contribution. This can facilitate satellite-UE parameter estimation. We can estimate γ_s using non-coherent integration as below

$$\hat{\gamma}_s = \arg\max_{\gamma}\left|\mathbf{1}_{N/2}^{\mathsf{T}}(\tilde{\mathbf{Y}}_{\mathrm{s}}\odot\mathbf{I}_{\mathrm{s}}^{*}(\bar{\psi}_{\mathrm{bs}}))\mathbf{c}_{\mathrm{s}}^{*}(\gamma)\right|, \tag{C.81}$$

and estimate τ_s^{res} using coherent integration as follows

$$\hat{\tau}_s^{\mathrm{res}} = \arg\max_{\tau}\left|\boldsymbol{b}_{\mathrm{s}}^{\mathsf{H}}(\tau)(\tilde{\mathbf{Y}}_{\mathrm{s}}\odot\mathbf{I}_{\mathrm{s}}^{*}(\hat{\gamma}_s))\mathbf{c}_{\mathrm{s}}^{*}(\hat{\gamma}_s)\right|. \tag{C.82}$$

The term $\mathbf{I}_{\mathrm{s}}(\gamma_s)$ is then utilized to refine these estimates.

To estimate τ_b, γ_b and $\boldsymbol{\theta}$, the following problem needs to be solved:

$$\begin{aligned}[\hat{\tau}_b,\gamma_b,\hat{\boldsymbol{\theta}}^{\mathsf{T}}] = \arg\min_{\tau,\gamma,\boldsymbol{\theta}} ||\tilde{\mathbf{Y}}_{\mathrm{b}} - \\ \hat{\alpha}_{\mathrm{b}}(\tau,\gamma,\boldsymbol{\theta})\sqrt{P_{\mathrm{b}}}\mathbf{I}_{\mathrm{b}}(\gamma)\odot(\boldsymbol{b}_{\mathrm{b}}(\tau)(\boldsymbol{z}(\boldsymbol{\theta})\odot\mathbf{c}_{\mathrm{b}}(\gamma))^{\mathsf{T}})||^2,\end{aligned} \tag{C.83}$$

where

$$\hat{\alpha}_{\mathrm{b}}(\tau,\gamma,\boldsymbol{\theta}) = \frac{\left\|\tilde{\mathbf{Y}}_{\mathrm{b}}(\mathbf{I}_{\mathrm{b}}^{\mathsf{H}}(\gamma)\odot(\boldsymbol{z}^{*}(\boldsymbol{\theta})\odot\mathbf{c}_{\mathrm{b}}^{*}(\gamma))\boldsymbol{b}_{\mathrm{b}}^{\mathsf{H}}(\tau))\right\|^2}{\sqrt{P_{\mathrm{b}}}\left\|\mathbf{I}_{\mathrm{b}}(\gamma)\odot(\boldsymbol{b}_{\mathrm{b}}(\tau)(\boldsymbol{z}(\boldsymbol{\theta})\odot\mathbf{c}_{\mathrm{b}}(\gamma))^{\mathsf{T}})\right\|^2}. \tag{C.84}$$

Coarse estimates can be obtained by initially neglecting the presence of $\mathbf{I}_{\mathrm{b}}(\gamma_b)$ and applying (C.69), (C.77) and (C.78). These estimates can then be refined using (C.83).

4.1.4 Model CCFOD

The channel-domain parameter vector in model CCFOD is the same as the one in model SlowD and model CCFODnoICI. The key difference between

model CCFOD and other simplified models is that due to the existence of ICI represented by $\mathbf{D}_{\mathrm{b}}(\gamma_b)$ and $\mathbf{D}_{\mathrm{s}}(\gamma_s)$, there may be leakage between the BS-UE and satellite-UE paths. As a result, the two paths can only be partially separated using simple processing as outlined in (C.60) and (C.61). To estimate γ_b, τ_b and $\boldsymbol{\theta}$, we need to solve below problem:

$$\begin{aligned}[\hat{\tau}_b, \gamma_b, \hat{\boldsymbol{\theta}}^{\mathsf{T}}] = \underset{\tau,\gamma,\boldsymbol{\theta}}{\arg\min} \, ||\mathbf{F}_{\mathrm{b}}^{\mathsf{H}} \mathbf{D}_{\mathrm{b}}^{\mathsf{H}}(\gamma)\mathbf{Y} - \\ \hat{\alpha}_{\mathrm{b}}(\tau,\gamma,\boldsymbol{\theta})\sqrt{P_{\mathrm{b}}}\mathbf{I}_{\mathrm{b}}(\gamma) \odot (\boldsymbol{b}_{\mathrm{b}}(\tau)(\boldsymbol{z}(\boldsymbol{\theta}) \odot \mathbf{c}_{\mathrm{b}}(\gamma))^{\mathsf{T}})||^2,\end{aligned} \tag{C.85}$$

where

$$\hat{\alpha}_{\mathrm{b}}(\tau,\gamma,\boldsymbol{\theta}) = \frac{\left\|\tilde{\mathbf{Y}}_{\mathrm{b}}(\mathbf{I}_{\mathrm{b}}^{\mathsf{H}}(\gamma) \odot (\boldsymbol{z}^*(\boldsymbol{\theta}) \odot \mathbf{c}_{\mathrm{b}}^*(\gamma))\boldsymbol{b}_{\mathrm{b}}^{\mathsf{H}}(\tau))\right\|^2}{\sqrt{P_{\mathrm{b}}}\left\|\mathbf{I}_{\mathrm{b}}(\gamma) \odot (\boldsymbol{b}_{\mathrm{b}}(\tau)(\boldsymbol{z}(\boldsymbol{\theta}) \odot \mathbf{c}_{\mathrm{b}}(\gamma))^{\mathsf{T}})\right\|^2}. \tag{C.86}$$

To estimate γ_s and τ_s^{res}, following problem needs to get solved:

$$\begin{aligned}[\hat{\tau}_s^{\mathrm{res}}, \hat{\gamma}_s] = \underset{\tau,\gamma}{\arg\min} \, ||\mathbf{F}_{\mathrm{s}}^{\mathsf{H}} \mathbf{D}_{\mathrm{s}}^{\mathsf{H}}(\gamma)\mathbf{Y} - \\ \hat{\alpha}_{\mathrm{s}}(\tau,\gamma)\sqrt{P_{\mathrm{s}}}\mathbf{I}_{\mathrm{s}}(\gamma) \odot (\boldsymbol{b}_{\mathrm{s}}(\tau)\mathbf{c}_{\mathrm{s}}(\gamma)^{\mathsf{T}})||^2,\end{aligned} \tag{C.87}$$

where

$$\hat{\alpha}_s(\tau,\gamma) = \frac{\left\|\tilde{\mathbf{Y}}_{\mathrm{s}}(\mathbf{I}_{\mathrm{s}}^{\mathsf{H}}(\gamma) \odot \mathbf{c}_{\mathrm{s}}^*(\gamma)\boldsymbol{b}_{\mathrm{s}}^{\mathsf{H}}(\tau))\right\|^2}{\sqrt{P_s}\left\|\mathbf{I}_{\mathrm{s}}^{\mathsf{H}}(\gamma) \odot (\boldsymbol{b}_{\mathrm{s}}(\tau)\mathbf{c}_{\mathrm{s}}(\gamma)^{\mathsf{T}})\right\|^2}. \tag{C.88}$$

To tackle (C.85), the presence of $\mathbf{D}_{\mathrm{b}}(\gamma_b)$ and $\mathbf{I}_{\mathrm{b}}(\gamma_b)$ is temporarily neglected. Therefore, we apply (C.60) and (C.61) to partially separate two paths, and then leverage (C.69), (C.77) and (C.78) similar to the procedures model SlowD and model CCFODnoICI to estimate γ_b, τ_b and $\boldsymbol{\theta}$. These estimates are then refined by incorporating $\mathbf{D}_{\mathrm{b}}(\gamma_b)$ and $\mathbf{I}_{\mathrm{b}}(\gamma_b)$ using (C.85), enabling the full reconstruction of the BS path $\tilde{\mathbf{Y}}_{\mathrm{b}}$.

In the next step, we remove the reconstructed BS path from $\mathbf{Y}$ to facilitate separating the satellite-UE contribution. Now to estimate the satellite-UE related parameters (τ_s^{res} and γ_s), similar to the estimation algorithm in model CCFODnoICI, we use $\bar{\psi}_{\mathrm{bs}}$ to eliminate the effect of $\mathbf{D}_{\mathrm{s}}$ and $\mathbf{I}_{\mathrm{s}}$ partly, then we

estimate γ_s and τ_s^{res} as below:

$$\hat{\gamma}_s = \arg\max_{\gamma} \left| \mathbf{1}_{N/2}^{\mathsf{T}} (\mathbf{F}_{\text{s}}^{\mathsf{H}} \mathbf{D}_{\text{s}}^{\mathsf{H}}(\bar{\psi}_{\text{bs}})(\mathbf{Y} - \tilde{\mathbf{Y}}_{\text{b}}) \odot \mathbf{I}_{\text{s}}^{*}(\bar{\psi}_{\text{bs}})) \mathbf{c}_{\text{s}}^{*}(\gamma) \right|, \tag{C.89}$$

$$\hat{\tau}_s^{\text{res}} = \arg\max_{\tau} \left| \boldsymbol{b}_{\text{s}}^{\mathsf{H}}(\tau) (\mathbf{F}_{\text{s}}^{\mathsf{H}} \mathbf{D}_{\text{s}}^{\mathsf{H}}(\hat{\gamma}_s)(\mathbf{Y} - \tilde{\mathbf{Y}}_{\text{b}}) \odot \mathbf{I}_{\text{s}}^{*}(\hat{\gamma}_s)) \mathbf{c}_{\text{s}}^{*}(\hat{\gamma}_s) \right|. \tag{C.90}$$

Remark: All the estimators presented in this section can be improved by considering the first two peaks in the first grid search for each path (e.g., (C.65) and (C.69) in model Comm) to account for potential leakage from the other path when using data from the true model.

Remark: According to (C.55) and the estimation algorithms, where the slow-time terms are primarily utilized to estimate Dopplers, the maximum unambiguous range for estimating γ_s is $(1 - \bar{\psi}_{\text{bs}})/(f_c T_s)$. However, due to the velocities of LEO satellites and the Earth's rotation considered in γ_s, this value may exceed the maximum range in certain scenarios. To address this issue, the known parameter $\bar{\psi}_{\text{bs}}$ is used to determine the integer part corresponding to the unambiguous range within the actual Doppler γ_s. Given that the UE's velocity is significantly smaller than the LEO satellite and Earth's velocities, and that the UE is in close proximity to the BS, the integer factors for $\bar{\psi}_{\text{bs}}$ and γ_s are expected to be identical. Consequently, only the residual Doppler needs to be estimated, after which the known integer factor can be applied to accurately retrieve γ_s.

4.2 Location, Clock Offset, Velocity and CFO Estimation

In all models, the estimators provide $\boldsymbol{p}_0$ and $\Delta_{t,0}$. which are related via

$$\tau_b = \frac{\|\boldsymbol{p}_0 - \boldsymbol{p}_{\text{b}}\|}{c} + \Delta_{t,0}, \tag{C.91}$$

$$\tau_s^{\text{res}} = \frac{\|\boldsymbol{p}_0 - \boldsymbol{p}_{\text{s}}\|}{c} - \tau_{\text{bs}} + \Delta_{t,0}. \tag{C.92}$$

Moreover, we can write the expression for the line passing the BS with AoD $\hat{\boldsymbol{\theta}}$ according to $\boldsymbol{p}_0(\beta) = \boldsymbol{p}_{\text{b}} + \beta \hat{\mathbf{u}}$ where $\hat{\mathbf{u}} = \mathbf{u}(\hat{\boldsymbol{\theta}})$. Therefore we can find $\hat{\boldsymbol{p}}_0$

using $\hat{\boldsymbol{p}}_0 = \boldsymbol{p}_0(\hat{\beta})$ where

$$\hat{\beta} = \arg\min_{\beta} \left| \frac{\|\boldsymbol{p}_0(\beta) - \boldsymbol{p}_\mathrm{b}\|}{c} - \frac{\|\boldsymbol{p}_0(\beta) - \boldsymbol{p}_\mathrm{s}\|}{c} - (\hat{\tau}_b - \hat{\tau}_s^{\mathrm{res}} - \bar{\tau}_{\mathrm{bs}}) \right|, \tag{C.93}$$

and $\hat{\Delta}_{t,0}$ can be found as below

$$\hat{\Delta}_{t,0} = \left(\hat{\tau}_b - \frac{\|\boldsymbol{p}_\mathrm{b} - \hat{\boldsymbol{p}}_0\|}{c}\right) + \left(\hat{\tau}_s^{\mathrm{res}} + \bar{\tau}_{\mathrm{bs}} - \frac{\|\boldsymbol{p}_\mathrm{s} - \hat{\boldsymbol{p}}_0\|}{c}\right). \tag{C.94}$$

In models SlowD, CCFODnoICI, and CCFOD, the Doppler γ_b and γ_s are estimated, so that (C.91) and (C.92) are modified to

$$\tau_b = \frac{\|\boldsymbol{p} - \boldsymbol{p}_\mathrm{b}\|}{c} + \Delta_{t,0}(1-\eta)(1-\psi_\mathrm{b}), \tag{C.95}$$

$$\tau_s^{\mathrm{res}} = \frac{\|\boldsymbol{p} - \boldsymbol{p}_\mathrm{s}\|}{c} - \tau_{\mathrm{bs}} + \Delta_{t,0}(1-\eta)(1-\psi_\mathrm{s}). \tag{C.96}$$

It is possible to neglect the factors $(1-\eta)(1-\psi_\mathrm{b})$ and $(1-\eta)(1-\psi_\mathrm{s})$ due to their small nominal values for simplicity and estimate $\hat{\boldsymbol{p}}_0$ and $\hat{\Delta}_{t,0}$ using (C.93) and (C.94)[5]. As for estimating $\|\boldsymbol{v}\|$ and η, due to the structure of model Comm with neglecting any phase change in the transmission of M OFDM symbols, it is not possible to estimate $\|\boldsymbol{v}\|$ and η. But in models SlowD-CCFOD, it holds that $\gamma_b = \eta + (1-\eta)\psi_\mathrm{b}$ and $\gamma_s = \eta + (1-\eta)\psi_\mathrm{s}$, where

$$\psi_\mathrm{b} = \frac{\|\boldsymbol{v}\|\,(\boldsymbol{p}_0 - \boldsymbol{p}_\mathrm{b})^\mathsf{T}\vec{\boldsymbol{v}}}{c\,\|\boldsymbol{p}_0 - \boldsymbol{p}_\mathrm{b}\|}, \tag{C.97}$$

$$\psi_\mathrm{s} = \frac{\|\boldsymbol{v}\|\,(\boldsymbol{p}_0 - \boldsymbol{p}_\mathrm{s})^\mathsf{T}\vec{\boldsymbol{v}}}{c\,\|\boldsymbol{p}_0 - \boldsymbol{p}_\mathrm{s}\|} - \frac{(\boldsymbol{p}_0 - \boldsymbol{p}_\mathrm{s})^\mathsf{T}(\boldsymbol{v}_{\mathrm{LEO}} - \boldsymbol{v}_\mathrm{E})}{c\,\|\boldsymbol{p}_0 - \boldsymbol{p}_\mathrm{s}\|}, \tag{C.98}$$

[5] A typical value for η is 1ppm, and in case of the UE moving with 80 kph and satellite elevation angle being $\pi/4$, $\left|\psi_\mathrm{b}\right|$ and $\left|\psi_\mathrm{s}\right|$ are in the order of 10^{-6} and 10^{-5} respectively.

according to (C.18) and (C.19a) where $\vec{\boldsymbol{v}} = \boldsymbol{v}/\left\|\boldsymbol{v}\right\|$. Then using estimated $\hat{\boldsymbol{p}}_0$, $\hat{\gamma}_{\mathrm{b}}$ and γ_{s}, we can find $\|\hat{\boldsymbol{v}}\|$ and $\hat{\eta}$ as in below

$$\hat{\eta} = \frac{\hat{\gamma}_s - ((\hat{\psi}_{N,\mathrm{s}}/\hat{\psi}_{N,\mathrm{b}})\hat{\gamma}_b - \tilde{\psi}_{\mathrm{s}})}{1 - ((\hat{\psi}_{N,\mathrm{s}}/\hat{\psi}_{N,\mathrm{b}}) - \tilde{\psi}_{\mathrm{s}})}, \tag{C.99}$$

$$\|\hat{\boldsymbol{v}}\| = \frac{\hat{\gamma}_b - \hat{\eta}}{(1-\hat{\eta})\hat{\psi}_{N,\mathrm{b}}}, \tag{C.100}$$

where

$$\tilde{\psi}_{\mathrm{s}} = \frac{(\hat{\boldsymbol{p}}_0 - \boldsymbol{p}_{\mathrm{s}})^{\mathsf{T}}(\boldsymbol{v}_{\mathrm{LEO}} - \boldsymbol{v}_{\mathrm{E}})}{c\left\|\hat{\boldsymbol{p}}_0 - \boldsymbol{p}_{\mathrm{s}}\right\|}, \tag{C.101}$$

$$\hat{\psi}_{N,\mathrm{s}} = \frac{(\hat{\boldsymbol{p}}_0 - \boldsymbol{p}_{\mathrm{s}})^{\mathsf{T}}\vec{\boldsymbol{v}}}{c\left\|\hat{\boldsymbol{p}}_0 - \boldsymbol{p}_{\mathrm{s}}\right\|}, \tag{C.102}$$

$$\hat{\psi}_{N,\mathrm{b}} = \frac{(\hat{\boldsymbol{p}}_0 - \boldsymbol{p}_{\mathrm{b}})^{\mathsf{T}}\vec{\boldsymbol{v}}}{c\left\|\hat{\boldsymbol{p}}_0 - \boldsymbol{p}_{\mathrm{b}}\right\|}. \tag{C.103}$$

Here, the vector $\vec{\boldsymbol{v}}$ denotes the known UE's heading and the subscript N in (C.102) and (C.103) stands for normalized, with respect to the UE's speed.

4.3 Complexity Analysis

In this subsection, the proposed simplified estimators are compared in terms of computational complexity. Assuming a fixed number of grids G in each dimension, and I iterations for the quasi-Newton algorithm, the channel parameter estimation for the model Comm has the lowest complexity at $\mathcal{O}(GNM + G^2M + I(N+M))$. Here, the first term corresponds to the complexity of estimating the BS and satellite delays; the second term represents the complexity of 2D AoD estimation and the final term accounts for the refinement cost. The estimator for the model SlowD has a complexity of $\mathcal{O}(GM + GP + GNM + G^2M + I(N+M))$ where the terms respectively represent the complexity of satellite Doppler estimation, BS Doppler estimation, BS and satellite delay estimation, AoD estimation, and refinement. For the model CCFODnoICI, the complexity is given as $\mathcal{O}(N^2+GM+GP+GNM+G^2M+I(N+M))$. The first term reflects the additional cost of considering intersubcarrier Doppler effect term in satellite Doppler estimation, while the remaining terms are analogous to those in the model SlowD. Finally, model CCFOD has the highest

complexity at $\mathcal{O}(N^2 + GM + NM + GP + GNM + G^2M + IN^2)$ Here, the third term represents the complexity of reconstructing the BS path, while the other terms are similar to the model CCFODnoICI, with the refinement step contributing $\mathcal{O}(IN^2)$, due to the inclusion of ICI in this model.

5 Simulation Results

In this section, we illustrate the performance of our estimators based on different models considering the data generated from the generative model in (C.28). The goal is to analyze how accurate the simplified models are in different scenarios.

5.1 Simulation Setup and Theoretical Bounds

The system parameters are given in Table. 2. The time-varying channel gains $\alpha_{\mathrm{b}}(t)$ and $\alpha_{\mathrm{s}}(t)$ are modeled based on free space path-loss (FSPL) and given as below:

$$\alpha_{\mathrm{b}}(t) = \sqrt{\cos^q(\boldsymbol{\theta}_{\mathrm{el}}(t))}\frac{\lambda}{4\pi \left\|\boldsymbol{p}(t) - \boldsymbol{p}_{\mathrm{b}}\right\|}, \tag{C.104}$$

where $q = 0.57$ [33, Sec. 9.7.3] and

$$\alpha_{\mathrm{s}}(t) = \frac{\lambda}{4\pi \left\|\boldsymbol{p}(t) - \boldsymbol{p}_{\mathrm{s}}(t)\right\|}. \tag{C.105}$$

We employ two theoretical bounds to evaluate estimation accuracy. The first is the CRB, which represents the minimum achievable variance of an unbiased estimator when the estimation model perfectly matches the true data generation model. However, since the estimators in our scenario are not designed based on the generative model, achieving the CRB is not guaranteed in the presence of significant model mismatch. To address this, we utilize the MCRB as an alternative theoretical bound [34], [35]. The MCRB provides a lower bound on the variance of estimators under model mismatch and incorporates the effect of estimator bias.

The CRB provides a reasonable bound for our mismatched model in the low to medium SNR regime, where estimation errors are mostly due to noise

Table 2: Simulations Parameters

Parameter	**Symbol**	**Value**
Carrier frequency	f_c	2 GHz
Speed of light	c	3×10^8 m/s
Number of subcarriers	N	3300
Subcarrier spacing	Δ_f	30 kHz
Total symbol duration	T_s	35.7 ms
Symbol duration	T_0	33.3 ms
Cyclic prefix duration	T_{cp}	2.3 ms
Number of symbols	M	64
Number of antennas	L	64
LEO satellite velocity	$\|\boldsymbol{v}_{\text{s}}\|$	7800 m/s
Number of beamformer phase repetition	P	4
LEO satellite altitude	h	600 km
Earth rotation velocity	$\|\boldsymbol{v}_{\text{E}}\|$	465 m/s
Earth radius	R	6371 km
BS position	$\boldsymbol{p}_{\text{b}}$	$[0, 0, 5]^{\mathsf{T}}$
UE initial position	$\boldsymbol{p}_0$	$[20, 50, 1.5]^{\mathsf{T}}$
UE heading	$\vec{\boldsymbol{v}}$	$[1, 0, 0]^{\mathsf{T}}$

rather than model mismatches. At high SNR, however, the MCRB becomes more relevant, as the bias term dominates the bound while the variance term approaches zero, making it the appropriate theoretical bound in this regime. The adoption of these bounds in our problem is elaborated in Appendix 3.

5.2 Results and Discussion

5.2.1 Mismatched Estimation Performance

First, we analyze the root mean-squared error (RMSE), CRB and bias terms of estimated UE's position for all simplified models, considering data generated from the true model versus received signal-to-noise ratio (SNR). To better understand the effect of BS and satellite transmit power, two figures are presented to illustrate the trends: Fig. 2 shows the case where the satellite transmit power is fixed at $P_{\text{s}} = 65$ dBm, while Fig. 3 depicts the case where the BS transmit power is fixed at $P_{\text{b}} = 35$ dBm. In Fig. 2 the BS transmit power changes from -40 dBm to 50 dBm, and in Fig. 3 the satellite

transmit power changes from 10 dBm to 80 dBm. In both figures, the velocity magnitude is set to $\|\boldsymbol{v}\| = 15$ kph, the CFO is $\eta = 10^{-8}$ and the satellite is located at an elevation angle of $\boldsymbol{\theta}^{\mathrm{s}}_{\mathrm{el}} = 88°$. It is observed that the CRB for all four models coincides exactly in both figures. The reason is that the combined Doppler and CFO (γ_b and γ_s) contains marginal position information compared to the other channel-domain parameters τ_s, τ_b and $\boldsymbol{\theta}$. The performance of the Comm and SlowD models is very similar, indicating that while accounting for slow-time Doppler is expected to improve AoD estimation and consequently positioning, its impact is overshadowed by the absence of inter-subcarrier Doppler compensation in this scenario. This observation is further reinforced by the performance improvement seen in the CCFODnoICI model compared to Comm and SlowD. The performance of models CCFODnoICI and CCFOD approaches the CRB at high SNR, showing importance of compensating for inter-subcarrier Doppler effect. In contrast, a significant gap is observed between the bias of models Comm and SlowD and the CRB at high SNR, highlighting that the performance of these two models is limited by model mismatch. Notably, except for high SNR, the performance of the CCFODnoICI and CCFOD models is similar, indicating that accounting for ICI has a negligible impact in this scenario at lower SNRs. However, the difference becomes more noticeable at high SNR.

The analyses presented above apply to the specific scenario described. In the following subsections, different scenarios are explored to provide a deeper understanding of the behavior of our algorithm.

5.2.2 Impact of CFO

In Fig. 4, the positioning performance of the four models is analyzed as a function of the CFO. For this evaluation, the satellite is positioned at the zenith, and the user is assumed to be stationary. The transmit powers of the BS and satellite are set to $P_{\mathrm{b}} = 35$ dBm and $P_{\mathrm{s}} = 65$ dBm, respectively. The positioning CRB for all four models coincides, as expected, and all models achieve the CRB at low values of η. Therefore, the bias term is only presented for cases where the RMSE deviates from the CRB. By increasing η, model Comm, then model SlowD and model CCFODnoICI would introduce large estimation errors, but it is model CCFOD that takes the CFO into account in the ICI term as well as in modified Fourier matrix $\mathbf{F}_{\mathrm{s}}(\gamma_{\mathrm{s}})$, therefore, it is more robust towards CFO variations compared to the other models. The

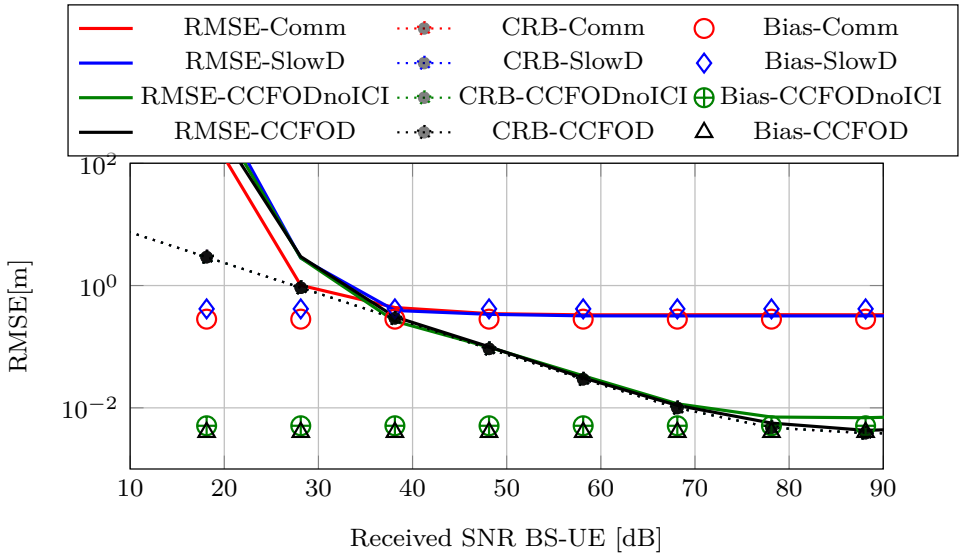

Figure 2: RMSE and CRB of estimated position vs. received SNR in BS-UE path. Since the legends in all figures are similar to that of Fig. 2, they are omitted in the subsequent figures for clarity. Bias values are included where relevant and omitted otherwise.

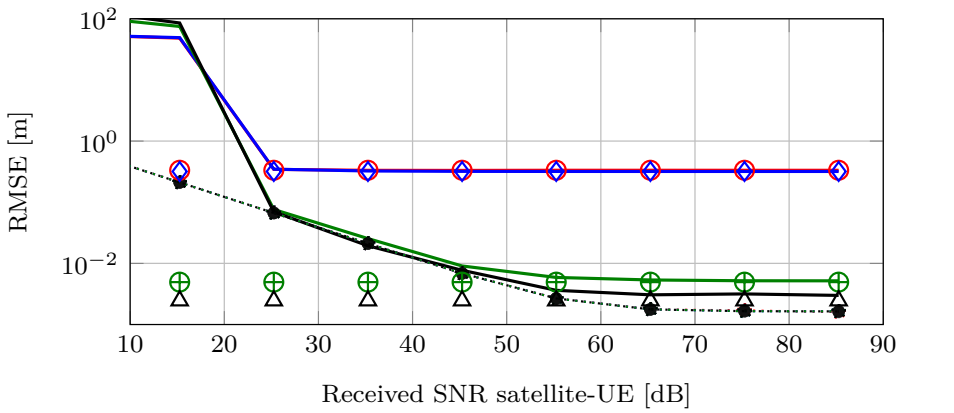

Figure 3: RMSE and CRB of estimated position vs. received SNR in the satellite-UE path.

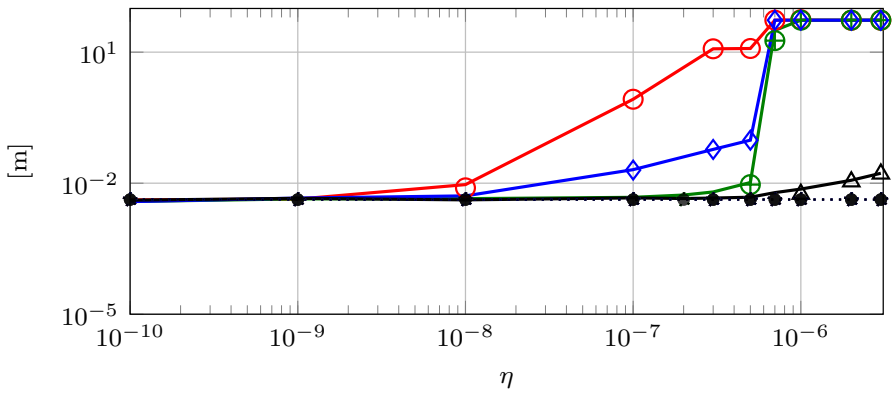

Figure 4: RMSE and CRB of estimated position vs. CFO.

reason is that model Comm entirely ignores the presence of CFO, making it the most susceptible to CFO variations among all models. In contrast, the other models account for CFO to some extent, enabling them to tolerate higher CFO values. Among these, model CCFOD demonstrates the highest robustness. An important observation is that for higher values of CFO, the CCFOD model still achieves performance close to the CRB, resulting in centimeter-level positioning accuracy. This indicates that even for large CFO values, a complex estimation algorithm incorporating time-varying AoDs and second-order terms is not necessary. Instead, our most advanced estimation algorithm is sufficient to achieve centimeter-level positioning accuracy. In case more relaxed requirements on positioning accuracy, other simplified models could be used.

5.2.3 Impact of UE Speed

In Fig. 5, the behavior of our four models is analyzed with varying speeds. We consider $\eta = 0$ in this scenario and the satellite is located at the zenith with the transmit powers of the BS and satellite set to $P_\mathrm{b} = 35$ dBm and $P_\mathrm{s} = 65$ dBm, respectively. Model Comm performs poorly when the velocity is as low as 3 m/s, as expected. In contrast, the other three models demonstrate strong robustness to variations in velocity due to the inclusion of γ_b and γ_s in their models. It is important to note that the impact of CFO and radial velocity is conveyed through Doppler shifts, making their effects similar when

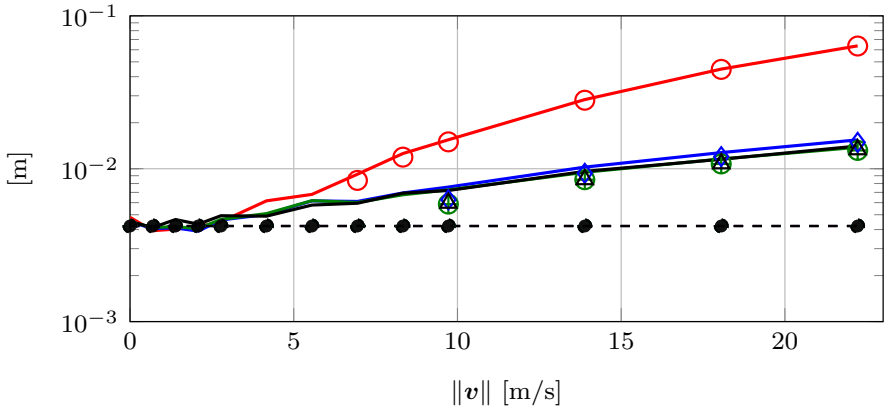

Figure 5: RMSE and CRB of estimated position vs. UE's speed ($\|\boldsymbol{v}\|$).

the satellite is located at the zenith and we investigate the effect of either CFO or radial velocity individually. Specifically in such case, the positioning accuracy when the UE's speed is 15m/s is comparable to that when $\eta = 15/(3 \times 10^8) \approx 0.5 \times 10^{-7}$. Therefore, for practical values of the UE's speed, since the difference between models SlowD, CCFODnoICI and CCFOD is marginal, and model SlowD is sufficient.

5.2.4 Impact of Satellite Elevation

Fig. 6 demonstrates the behavior of our models versus satellite elevation angles. The UE is assumed to be stationary, with $\eta = 0$ and the transmit powers of the BS and satellite are fixed at $P_{\mathrm{b}} = 35$ dBm and $P_{\mathrm{s}} = 65$ dBm, respectively. Under these conditions, all four models perform well when $\boldsymbol{\theta}^{\mathrm{s}}_{\mathrm{el}} = \pi/2$. This is because $\gamma_s \approx 0$ due to the negligible radial velocity between the satellite and the UE, and $\gamma_b = 0$ as the UE is stationary. Consequently, model Comm, which does not account for Doppler effects, performs effectively. With $\gamma_b = 0$, $\gamma_s \approx 0$, $\epsilon_b = 0$, and $\epsilon_s \approx 0$, there is no mismatch between the generative model and any of the simplified models. However, as the satellite elevation angle deviates from $\pi/2$, the performance of models Comm and SlowD deteriorates. Model Comm performs poorly because it entirely neglects γ_s, which increases rapidly as the satellite moves away from the zenith. While model SlowD accounts for γ_s, it only considers it in the slow-time domain,

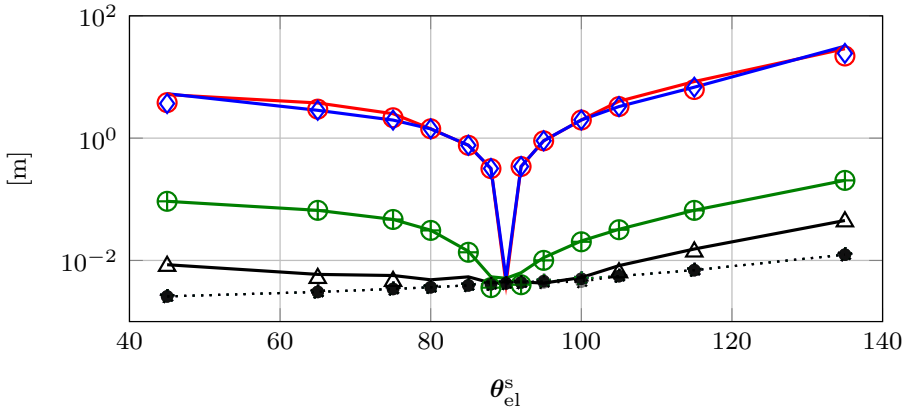

Figure 6: RMSE and CRB of estimated position vs. satellite elevation angle.

leaving delay estimation across subcarriers susceptible to errors. In contrast, models CCFODnoICI and CCFOD consider inter-subcarrier Doppler effects, which spans over the slow time as well as the subcarrier domains. By estimating γ_s and compensating for these terms, models CCFODnoICI and CCFOD significantly outperform models Comm and SlowD.

It is worth noting that γ_s increases as the satellite elevation angle diverges further from the zenith. According to (C.38), a larger γ_s causes the first term in $\mathbf{F}^q_{\mathrm{s}}(\gamma_{\mathrm{s}}, \epsilon_{\mathrm{s}})$ to diverge more substantially from the IDFT matrix, due to the fast-time Doppler effect. In models Comm, SlowD and CCFODnoICI, the IDFT matrix is used to separate BS-UE and satellite-UE contributions based on (C.56), (C.57), and (C.58). This divergence makes it increasingly challenging for the estimators to separate the BS-UE path from the satellite-UE path, ultimately degrading localization performance, whereas model CCFOD (C.47) considers the first term in $\mathbf{F}_{\mathrm{s}}(\gamma_{\mathrm{s}})$ which is the dominant term in $\mathbf{F}^q_{\mathrm{s}}(\gamma_{\mathrm{s}}, \epsilon_{\mathrm{s}})$ for satellite elevation angle away from zenith.

Remark: In general, the choice of the appropriate estimation algorithm depends on factors such as the required positioning accuracy, the expected scenario, and the complexity preferences. Sec. 5.2.2 to 5.2.4 provide a general overview of how different models perform in various scenarios, and the results can serve as a guideline for model selection.

5.2.5 Estimation Performance of Other Parameters

Finally, the estimation performance of $\Delta_{t,0}$, η and $\|\boldsymbol{v}\|$ are illustrated in Figs. 7, 8, and 9, respectively. The UE velocity is set to 15 kph, the BS transmit power is set to $P_{\mathrm{b}} = 35$ dBm, with $\Delta_{t,0} = 1$ ns, $\eta = 10^{-8}$ and the satellite positioned at an elevation angle of $\boldsymbol{\theta}^{\mathrm{s}}_{\mathrm{el}} = 88°$, which is the simulation scenario as the one used in Fig. 3. In Fig. 7, models Comm and SlowD exhibit similar behavior, while model CCFODnoICI outperforms them, with model CCFOD almost achieving the CRB. As for estimation performance of η and $\|\boldsymbol{v}\|$ in Fig. 8 and 9, models CCFODnoICI and CCFOD perform similarly and outperform model SlowD as expected and model Comm is not included since it is not capable of estimating η and $\|\boldsymbol{v}\|$.

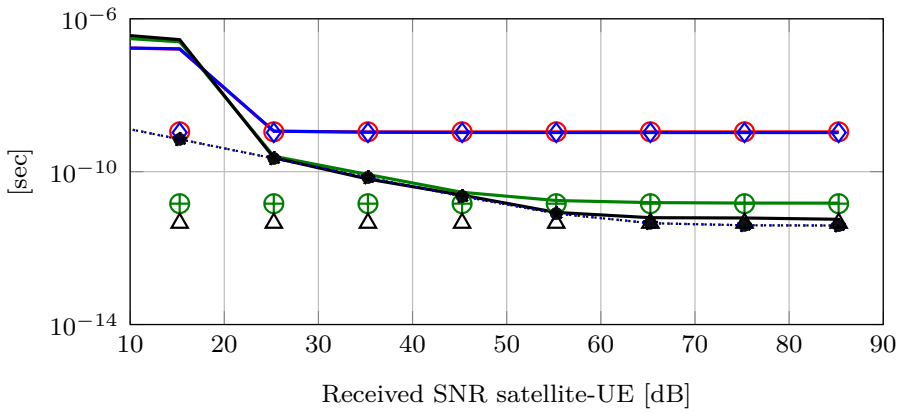

Figure 7: RMSE and CRB of estimated $\Delta_{t,0}$ vs. received SNR.

By comparing Fig. 8 and 9 with Fig. 3, it can be observed that the second-order terms become significant at high SNR, but and only in the estimation of η and $\|\boldsymbol{v}\|$. This is due to the fact that while Doppler conveys negligible positioning information, it conveys significant information for estimating η and $\|\boldsymbol{v}\|$ and specifically the second-order terms (derived based on time-varying Doppler) will be crucial only when we operate at high SNR and we aim at estimating η and $\|\boldsymbol{v}\|$ with very high accuracy. Based on 8 and 9, our CCFODnoICI and CCFOD models would achieve speed and CFO estimation accuracies of sub-1 m/s and sub-0.1 ppm respectively, therefore as long as these values meet the requirements of our application, there is no need to

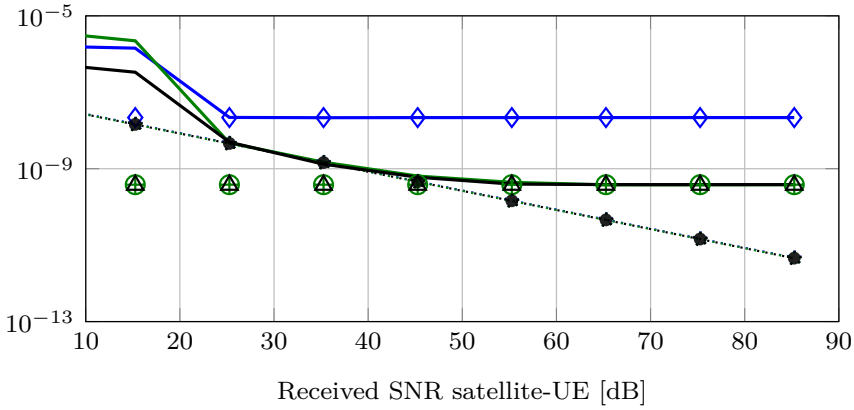

Figure 8: RMSE and CRB of estimated η vs. received SNR.

incorporate second-order terms.

6 Concluding Remarks

This paper presented a comprehensive study on localization, velocity magnitude estimation, and synchronization for a mobile UE in integrated cellular and non-terrestrial networks. We derived a generative model that accounts for the time-varying Doppler and path gains effect, forming the foundation for understanding the positioning system's behavior. Building upon this, we proposed a hierarchy of four simplified models, each offering a distinct trade-off between computational complexity and performance. Estimation algorithms were developed for all the models, enabling accurate estimation of position, velocity magnitude, initial clock bias, and carrier frequency offset.

Through rigorous simulations, we demonstrated the effectiveness of the proposed models across diverse scenarios. By analyzing both the performance and complexity of each model, we can strategically select the most suitable one for different deployment conditions, optimizing processing power while maintaining high accuracy. These insights offer practical guidance for improving 6G positioning and synchronization in mobile scenarios, facilitating the seamless integration of NTNs into future wireless networks.

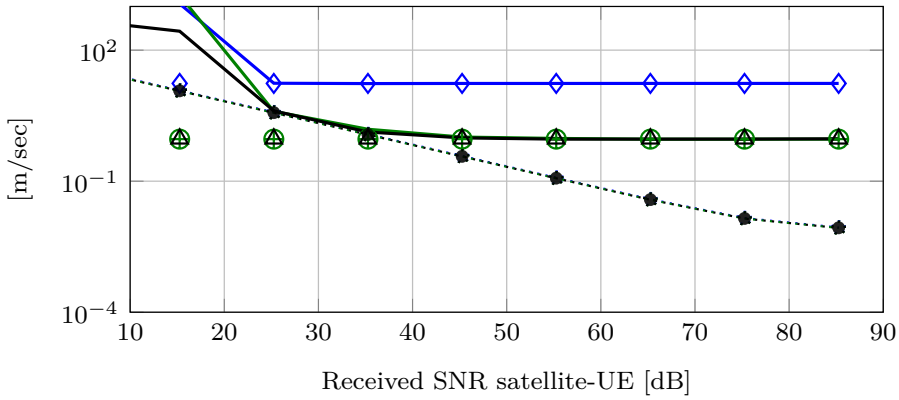

Figure 9: RMSE and CRB of estimated $\|\boldsymbol{v}\|$ vs. received SNR.

1 Derivation of continuous-time generative model

Following (C.4), (C.3) and (C.1), $\tilde{y}_{\mathrm{b}}(t)$ can be written as

$$\begin{aligned}\tilde{y}_{\mathrm{b}}(t) &= \alpha_{\mathrm{b}}(t)\Re\Big\{\sum_{l=1}^{L}\tilde{z}_{\mathrm{b},l}(t-\tau^p_{\mathrm{b},1}(t))\Big\} \\ &= \alpha_{\mathrm{b}}(t)\Re\Big\{\sum_{l=1}^{L}w_l(t-\tau^p_{\mathrm{b},l}(t))x_{\mathrm{b}}(t-\tau^p_{\mathrm{b},l}(t))e^{j2\pi f_c(t-\tau^p_{\mathrm{b},l}(t))}\Big\}.\end{aligned} \tag{C.106}$$

where $w_l(t) = [\boldsymbol{w}(t)]_l$ and $\tilde{z}_{\mathrm{b},l}(t) = [\tilde{\boldsymbol{z}}_{\mathrm{b}}(t)]_l$. Then,

$$\begin{aligned}&\tilde{y}_{\mathrm{b}}(t) \\ &= \Re\{\alpha_{\mathrm{b}}(t)\boldsymbol{a}^{\mathsf{T}}(\boldsymbol{\theta}(t))\boldsymbol{w}(t-\tau^p_{\mathrm{b}}(t))x_{\mathrm{b}}\left(t-\tau^p_{\mathrm{b}}(t)\right)e^{j2\pi f_c\left(t-\tau^p_{\mathrm{b}}(t)\right)}\}.\end{aligned} \tag{C.107}$$

2 Linearizing the delay propagation

We express the propagation delay as

$$\tau(t) = \frac{r(t)}{c} = \frac{\|\boldsymbol{p}(t)-\boldsymbol{p}_{\mathrm{J}}(t)\|}{c}, \tag{C.108}$$

where $\mathrm{J} \in \mathrm{b}, \mathrm{s}$ denotes the transmitter (either the BS or the satellite). The transmitter trajectory is modeled as $\boldsymbol{p}_{\mathrm{J}}(t) = \boldsymbol{p}_{\mathrm{J}} + \boldsymbol{v}_{\mathrm{J}} t$, with $\boldsymbol{p}_{\mathrm{J}}$ and $\boldsymbol{v}_{\mathrm{J}}$ representing its initial 3D position and velocity, respectively. Similarly, the receiver trajectory is given by $\boldsymbol{p}(t) = \boldsymbol{p}_0 + \boldsymbol{v}t$, where $\boldsymbol{p}_0$ and $\boldsymbol{v}$ denote the initial 3D position and velocity of the receiver. Substituting the trajectories into (C.108), the propagation delay can be equivalently rewritten as

$$\tau(t) = \frac{\|\boldsymbol{p}_0 + \boldsymbol{v}_{\mathrm{J,u}} t - \boldsymbol{p}_{\mathrm{J}}\|}{c}, \tag{C.109}$$

where $\boldsymbol{v}_{\mathrm{J,u}}$ denotes the relative velocity between the transmitter and the receiver. Let's expand the nominator of (C.108)

$$\|\boldsymbol{p}_0 + \boldsymbol{v}_{\mathrm{J,u}} t - \boldsymbol{p}_{\mathrm{J}}\| = \|\boldsymbol{p}_0 - \boldsymbol{p}_{\mathrm{J}}\| \frac{\|\boldsymbol{p}_0 + \boldsymbol{v}_{\mathrm{J,u}} t - \boldsymbol{p}_{\mathrm{J}}\|}{\|\boldsymbol{p}_0 - \boldsymbol{p}_{\mathrm{J}}\|} \tag{C.110}$$

$$= \|\boldsymbol{p}_0 - \boldsymbol{p}_{\mathrm{J}}\| \sqrt{\frac{(\boldsymbol{p}_0 + \boldsymbol{v}_{\mathrm{J,u}} t - \boldsymbol{p}_{\mathrm{J}})^{\mathsf{T}} (\boldsymbol{p}_0 + \boldsymbol{v}_{\mathrm{J,u}} t - \boldsymbol{p}_{\mathrm{J}})}{\|\boldsymbol{p}_0 - \boldsymbol{p}_{\mathrm{J}}\|^2}}$$

$$= \|\boldsymbol{p}_0 - \boldsymbol{p}_{\mathrm{J}}\| \sqrt{1 + \frac{2(\boldsymbol{p}_0 - \boldsymbol{p}_{\mathrm{J}})^{\mathsf{T}} \boldsymbol{v}_{\mathrm{J,u}} t + \|\boldsymbol{v}_{\mathrm{J,u}} t\|^2}{\|\boldsymbol{p}_0 - \boldsymbol{p}_{\mathrm{J}}\|^2}}. \tag{C.111}$$

Let's assume that the UE and transmitter displacement during the entire transmission block is much smaller than their initial distance, which is equivalent to the stop-and-hop assumption [36, Ch. 2.7.2]. Then, we can conclude that

$$2(\boldsymbol{p}_0 - \boldsymbol{p}_{\mathrm{J}})^{\mathsf{T}} \boldsymbol{v}_{\mathrm{J,u}} M T_s + \|\boldsymbol{v}_{\mathrm{J,u}} M T_s\|^2 \ll \|\boldsymbol{p}_0 - \boldsymbol{p}_{\mathrm{J}}\|^2 . \tag{C.112}$$

We can then expand (C.111) using the Taylor approximation $\sqrt{1+x} \approx 1 + \frac{x}{2} - \frac{x^2}{8}$ for small x, keeping all constant, linear-in-t, and quadratic-in-t terms:

$$\begin{aligned}
&\|\boldsymbol{p}_0 + \boldsymbol{v}_{\mathrm{J,u}} t - \boldsymbol{p}_{\mathrm{J}}\| \approx \|\boldsymbol{p}_0 - \boldsymbol{p}_{\mathrm{J}}\| \times \\
&\left(1 + \frac{t(\boldsymbol{p}_0 - \boldsymbol{p}_{\mathrm{J}})^{\mathsf{T}} \boldsymbol{v}_{\mathrm{J,u}} + 1/2(\|\boldsymbol{v}_{\mathrm{J,u}} t\|^2 - v_{\mathrm{J,u}}^2 t^2)}{\|\boldsymbol{p}_0 - \boldsymbol{p}_{\mathrm{J}}\|^2}\right) \\
&= \|\boldsymbol{p}_0 - \boldsymbol{p}_{\mathrm{J}}\| + \frac{t(\boldsymbol{p}_0 - \boldsymbol{p}_{\mathrm{J}})^{\mathsf{T}} \boldsymbol{v}_{\mathrm{J,u}} + 1/2(\|\boldsymbol{v}_{\mathrm{J,u}} t\|^2 - v_{\mathrm{J,u}}^2 t^2)}{\|\boldsymbol{p}_0 - \boldsymbol{p}_{\mathrm{J}}\|} \\
&= \|\boldsymbol{p}_0 - \boldsymbol{p}_{\mathrm{J}}\| + v_{\mathrm{J,u}} t + 1/2 a_{\mathrm{J,u}} t^2.
\end{aligned} \tag{C.113}$$

where $v_{\mathrm{J,u}} = (\boldsymbol{p}_0 - \boldsymbol{p}_\mathrm{J})^\mathsf{T}\boldsymbol{v}_{\mathrm{J,u}}/\left\|\boldsymbol{p}_0 - \boldsymbol{p}_\mathrm{J}\right\|$ is the initial radial velocity, and the second-order term denotes the quadratic changes in the radial distance which can be interpreted as the radial pseudo-acceleration $a_{\mathrm{J,u}} = (\left\|\boldsymbol{v}_{\mathrm{J,u}}\right\|^2 - v_{\mathrm{J,u}}^2)/\left\|\boldsymbol{p}_0 - \boldsymbol{p}_\mathrm{J}\right\|$. Therefore, with the above approximation, the radial distance can be written as a constant acceleration kinematic equation, and the radial velocity and the delay will be approximated as

$$\begin{aligned} v_{\mathrm{J,u}}(t) &= v_{\mathrm{J,u}} + a_{\mathrm{J,u}}t, \\ \tau(t) &= r(t)/c = \tau_0 + \psi_0 t + 1/2\mu t^2, \end{aligned} \tag{C.114}$$

where $\tau_0 = \left\|\boldsymbol{p}_0 - \boldsymbol{p}_\mathrm{J}\right\|/c$ is the initial delay, $\psi_0 = v_{\mathrm{J,u}}/c$ is the initial normalized Doppler shift and $\mu = a_{\mathrm{J,u}}/c$ is the normalized Doppler shift rate.

3 FIM and Bias Term in MRCB

The positional parameters are as follows for the model Comm

$$\boldsymbol{\chi}_{\mathrm{pos}}^{a} = [\alpha_\mathrm{R}, \alpha_\mathrm{I}, \alpha_\mathrm{R}, \alpha_\mathrm{I}, \boldsymbol{p}_0^\mathsf{T}, \Delta_{t,0}]^\mathsf{T} \in \mathbb{R}^8, \tag{C.115}$$

while for models k = SlowD, CCFODnoICI, and CCFOD, they are

$$\boldsymbol{\chi}_{\mathrm{pos}}^{\mathrm{Comm}} = [\boldsymbol{\chi}_{\mathrm{pos}}^{\mathrm{Comm}^\mathsf{T}}, \left\|\boldsymbol{v}\right\|, \eta]^\mathsf{T} \in \mathbb{R}^{10} \tag{C.116}$$

The performance bounds Fisher information matrix (FIM) and Bias in MCRB are detailed here. As a basic bound, we use FIM, which is given by[37]

$$\mathbf{F}_{\mathrm{ch}} = \frac{2}{\sigma^2}\sum_{m=0}^{M-1}\sum_{n=0}^{N-1}\Re\left\{\frac{\partial[\boldsymbol{R}]_{n,m}}{\partial\boldsymbol{\chi}_{\mathrm{ch}}^{k}}\left(\frac{\partial[\boldsymbol{R}]_{n,m}}{\partial\boldsymbol{\chi}_{\mathrm{ch}}^{k}}\right)^{\mathrm{H}}\right\}, \tag{C.117}$$

in which $\boldsymbol{R} \in \mathbb{C}^{N\times M}$ is the noise-free part of the received signal, $\boldsymbol{\chi}_{\mathrm{ch}}^{k} \in \mathbb{R}^8$ in case of evaluating model Comm (k = Comm) and $\boldsymbol{\chi}_{\mathrm{ch}}^{k} \in \mathbb{R}^{10}$ (C.59) in case of evaluating model SlowD, CCFODnoICI, and CCFOD (k = SlowD, CCFODnoICI, CCFOD) (C.71). We can convert $\mathbf{F}_{\mathrm{ch}}$ to the positional FIM, $\mathbf{F}_{\mathrm{pos}}$, corresponding to positional vector by using the Jacobian matrix $\mathbf{F}_{\mathrm{po}} = \mathbf{J}^\mathrm{T}\mathbf{F}_{\mathrm{ch}}\mathbf{J}$, where $\mathbf{J}$ is the Jacobian matrix with elements $\mathbf{J}_{m,n} = \partial[\boldsymbol{\chi}_{\mathrm{ch}}^{k}]_m/\partial[\boldsymbol{\chi}_{\mathrm{ch}}^{k}]_n$. In case of k=Comm, $\mathbf{J} \in \mathbb{C}^{8\times 10}$ and in case of k=SlowD, CCFODnoICI, CC-

FOD, $\mathbf{J} \in \mathbb{C}^{10\times 10}$.

In case of mismatched estimation, we can find the positioning bias through MCRB for each model k = Comm, SlowD, CCFODnoICI, CCFOD, which can be found below

$$B_{\text{pos}}^{k} = \sqrt{\text{trace}((\boldsymbol{\chi}_{\text{pos}_{[5:7]}}^{\hat{k}})^{\mathsf{H}}\boldsymbol{\chi}_{\text{pos}_{[5:7]}}^{\hat{k}})}, \tag{C.118}$$

where

$$\boldsymbol{\chi}_{\text{pos}}^{\hat{k}} = \underset{\boldsymbol{\chi}_{\text{pos}}^{k}}{\arg\min}[\left\|\mathbf{Y}_{\text{NF}} - \mathbf{Y}_{\text{NF}}^{k}(\boldsymbol{\chi}_{\text{pos}}^{k})\right\|^{2}]. \tag{C.119}$$

Here, $\mathbf{Y}_{\text{NF}}$ represents the noise-free received signal based on the generative model, $\mathbf{Y}_{\text{NF}}^{k}$ corresponds to the noise-free observations derived from the simplified models. The vector $\boldsymbol{\chi}_{\text{pos}}^{k}$ is given by (C.115) and (C.116). For models SlowD, CCFODnoICI, and CCFOD, the estimator bias for the magnitude of the initial clock bias, velocity, and CFO can be determined as follows:

$$B_{\Delta_{t,0}} = \sqrt{(\boldsymbol{\chi}_{\text{pos}_{[8]}}^{\hat{k}})^{*}\boldsymbol{\chi}_{\text{pos}_{[8]}}^{\hat{k}}}, \tag{C.120}$$

$$B_{\|\boldsymbol{v}\|} = \sqrt{(\boldsymbol{\chi}_{\text{pos}_{[9]}}^{\hat{k}})^{*}\boldsymbol{\chi}_{\text{pos}_{[9]}}^{\hat{k}}}, \tag{C.121}$$

$$B_{\eta} = \sqrt{(\boldsymbol{\chi}_{\text{pos}_{[10]}}^{\hat{k}})^{*}\boldsymbol{\chi}_{\text{pos}_{[10]}}^{\hat{k}}}. \tag{C.122}$$

References

[1] G. Araniti, A. Iera, S. Pizzi, and F. Rinaldi, "Toward 6g non-terrestrial networks," *IEEE Network*, vol. 36, no. 1, pp. 113–120, 2021.

[2] W. Jiang, B. Han, M. A. Habibi, and H. D. Schotten, "The road towards 6g: A comprehensive survey," *IEEE Open Journal of the Communications Society*, vol. 2, pp. 334–366, 2021.

[3] M. M. Azari, S. Solanki, S. Chatzinotas, *et al.*, "Evolution of non-terrestrial networks from 5G to 6G: A survey," *IEEE communications surveys & tutorials*, vol. 24, no. 4, pp. 2633–2672, 2022.

[4] H. K. Dureppagari, C. Saha, H. S. Dhillon, and R. M. Buehrer, "Ntn-based 6g localization: Vision, role of leos, and open problems," *arXiv preprint arXiv:2305.12259*, 2023.

[5] A. Guidotti, A. Vanelli-Coralli, V. Schena, *et al.*, "The path to 5G-advanced and 6G non-terrestrial network systems," in *2022 11th Advanced Satellite Multimedia Systems Conference and the 17th Signal Processing for Space Communications Workshop (ASMS/SPSC)*, IEEE, 2022, pp. 1–8.

[6] J. A. del Peral-Rosado, A. Y. Yildirim, N. C. Klinger, *et al.*, "Preliminary field results of a dedicated 5G positioning network for enhanced hybrid positioning," *Engineering Proceedings*, vol. 54, no. 1, p. 6, 2023.

[7] R. Whiton, "Cellular localization for autonomous driving: A function pull approach to safety-critical wireless localization," *IEEE Vehicular Technology Magazine*, vol. 17, no. 4, pp. 28–37, 2022.

[8] A. Behravan, V. Yajnanarayana, M. F. Keskin, *et al.*, "Positioning and sensing in 6G: Gaps, challenges, and opportunities," *IEEE Vehicular Technology Magazine*, vol. 18, no. 1, pp. 40–48, 2022.

[9] S. Saleh, P. Zheng, X. Liu, *et al.*, *Integrated 6g tn and ntn localization: Challenges, opportunities, and advancements*, 2025.

[10] S. Dwivedi, R. Shreevastav, F. Munier, *et al.*, "Positioning in 5g networks," *IEEE Communications Magazine*, vol. 59, no. 11, pp. 38–44, 2021.

[11] H. Li, L. Han, R. Duan, and G. M. Garner, "Analysis of the synchronization requirements of 5G and corresponding solutions," *IEEE Communications Standards Magazine*, vol. 1, no. 1, pp. 52–58, 2017.

[12] J. A. del Peral-Rosado, R. Raulefs, J. A. López-Salcedo, and G. Seco-Granados, "Survey of cellular mobile radio localization methods: From 1G to 5G," *IEEE Communications Surveys & Tutorials*, vol. 20, no. 2, pp. 1124–1148, 2017.

[13] M. Neinavaie, J. Khalife, and Z. M. Kassas, "Acquisition, doppler tracking, and positioning with starlink LEO satellites: First results," *IEEE Transactions on Aerospace and Electronic Systems*, vol. 58, no. 3, pp. 2606–2610, 2021.

[14] H. K. Dureppagari, C. Saha, H. S. Dhillon, and R. M. Buehrer, "NTN-based 6G localization: Vision, role of LEOs, and open problems," *arXiv preprint arXiv:2305.12259*, 2023.

[15] I. Ali, N. Al-Dhahir, and J. E. Hershey, "Doppler characterization for LEO satellites," *IEEE transactions on communications*, vol. 46, no. 3, pp. 309–313, 1998.

[16] M. Harounabadi and T. Heyn, "Toward integration of 6G-NTN to terrestrial mobile networks: Research and standardization aspects," *IEEE Wireless Communications*, vol. 30, no. 6, pp. 20–26, 2023.

[17] G. Geraci, D. López-Pérez, M. Benzaghta, and S. Chatzinotas, "Integrating terrestrial and non-terrestrial networks: 3d opportunities and challenges," *IEEE Communications Magazine*, vol. 61, no. 4, pp. 42–48, 2022.

[18] G. Charbit, A. Medles, P. Jose, D. Lin, X. Zhu, and I.-K. Fu, "Satellite and cellular networks integration-a system overview," in *2021 Joint European Conference on Networks and Communications & 6G Summit (EuCNC/6G Summit)*, IEEE, 2021, pp. 118–123.

[19] H. Sallouha, S. Saleh, S. De Bast, Z. Cui, S. Pollin, and H. Wymeersch, "On the ground and in the sky: A tutorial on radio localization in ground-air-space networks," *IEEE Communications Surveys & Tutorials*, 2024.

[20] A. Gonzalez-Garrido, J. Querol, and S. Chatzinotas, "5G positioning reference signal configuration for integrated terrestrial/non-terrestrial network scenario," in *2023 IEEE/ION Position, Location and Navigation Symposium (PLANS)*, IEEE, 2023, pp. 1136–1142.

[21] A. Gonzalez-Garrido, J. Querol, H. Wymeersch, and S. Chatzinotas, "Interference analysis and modeling of positioning reference signals in 5G ntn," *IEEE Open Journal of the Communications Society*, 2024.

[22] T. Liang, T. Zhang, and Q. Zhang, "Toward seamless localization and communication: A satellite-UAV NTN architecture," *IEEE Network*, 2024.

[23] T. Jin, P. Zhang, J. Chakwizira, and Y. Wang, "Fusion positioning of gnss-cellular signals of opportunity under low observability," *IEEE Transactions on Instrumentation and Measurement*, 2024.

[24] F. Zhang, Z. Zhang, W. Yu, and T.-K. Truong, "Joint range and velocity estimation with intrapulse and intersubcarrier doppler effects for ofdm-based radcom systems," *IEEE Transactions on Signal Processing*, vol. 68, pp. 662–675, 2020.

[25] R. Prasad, "Ofdm for wireless communications systems," *Artech House Universal Personal Communications Library/Artech House*, 2004.

[26] W. J. Riley and D. A. Howe, "Handbook of frequency stability analysis," 2008.

[27] K. Keykhosravi, M. F. Keskin, G. Seco-Granados, P. Popovski, and H. Wymeersch, "RIS-enabled SISO localization under user mobility and spatial-wideband effects," *IEEE Journal of Selected Topics in Signal Processing*, vol. 16, no. 5, pp. 1125–1140, 2022.

[28] T. ETSI, "138 211-v16. 2.0, 5g nr," *Physical channels and modulation (3GPP TS 38.211 version 16.2. 0 Release 16), ETSI*, 2020.

[29] V. Koivunen, M. F. Keskin, H. Wymeersch, M. Valkama, and N. González-Prelcic, "Multicarrier isac: Advances in waveform design, signal processing, and learning under nonidealities," *IEEE Signal Processing Magazine*, vol. 41, no. 5, pp. 17–30, 2024.

[30] A. Alkhateeb and R. W. Heath, "Frequency selective hybrid precoding for limited feedback millimeter wave systems," *IEEE Transactions on Communications*, vol. 64, no. 5, pp. 1801–1818, 2016.

[31] H. Wymeersch and G. Seco-Granados, "Radio localization and sensing—part i: Fundamentals," *IEEE Communications Letters*, vol. 26, no. 12, pp. 2816–2820, 2022.

[32] M. K. Ercan, M. F. Keskin, S. Gezici, and H. Wymeersch, "RIS-aided NLoS monostatic sensing under mobility and angle-doppler coupling," *arXiv preprint arXiv:2401.06544*, 2024.

[33] W. L. Stutzman and G. A. Thiele, *Antenna theory and design*. John Wiley & Sons, 2012.

[34] S. Fortunati, F. Gini, M. S. Greco, and C. D. Richmond, "Performance bounds for parameter estimation under misspecified models: Fundamental findings and applications," *IEEE Signal Process. Mag.*, vol. 34, no. 6, pp. 142–157, 2017.

[35] C. D. Richmond and L. L. Horowitz, "Parameter bounds on estimation accuracy under model misspecification," *IEEE Trans. Signal Process.*, vol. 63, no. 9, pp. 2263–2278, 2015.

[36] M. A. Richards *et al.*, *Fundamentals of radar signal processing*. Mcgraw-hill New York, 2022, vol. 1.

[37] S. M. Kay, *Fundamentals of statistical signal processing: estimation theory*. Prentice-Hall, Inc., 1993.